

Physics and applications of microresonator solitons and
electro-optic frequency combs

Thesis by
Xu Yi

In Partial Fulfillment of the Requirements for the
degree of
Doctor of Philosophy

Caltech

CALIFORNIA INSTITUTE OF TECHNOLOGY
Pasadena, California

2017
Defended May 23rd 2017

© 2017

Xu Yi

ORCID: 0000-0002-2485-1104

All rights reserved

ACKNOWLEDGEMENTS

To me, Caltech is an ideal place for pursuing a Ph.D. I love its small population, compact campus, close mentor-student relation, and the passion for groundbreaking science and technology. These characteristics really resonates with me and I never hesitated for a second before choosing Caltech for my Ph.D over all other universities.

The five years I have spent here has been, in some way, beyond my wildest imagination. I cannot thank enough my adviser, Prof. Kerry Vahala, for providing so many great research opportunities. I never dreamed of working on exoplanet detection at the Keck telescope in Hawaii after my second year in Caltech. I was involved in so many great projects that I have much better understanding of the value of scientific research and I am much more determined in pursing science in my career than I was five years ago. Prof. Vahala is also very special as an adviser. He is not only a distinguishing scholar, but he also understands and respects the culture that I am from. This means a great deal to me. Studying abroad is never easy and I am really glad Prof. Vahala is my adviser.

During my stay in Pasadena, I have picked up a few hobbies to help me go through the ups and downs in my Ph.D. I want to thank my parents for supporting me to explore my life outside scientific research. My father, who went through a tough medical graduate school 30 years ago, urged me to seek balance between work and life. I also want to thank my wife, Jingyi Fan, for going through these adventures with me. The snowboarding, mountain cycling, skydiving, and rock climbing that we learned together, really made my life special and enjoyable.

I want to thank Qi-Fan Yang and Ki Youl Yang, two of my closest collaborators in the lab. The friendly and healthy collaboration we created was so productive and I benefited a lot from it. I want to thank Dr. Stephanie Liefer, who is like a patient elder sister to me. I want to thank Dr. Scott Diddams; as the co-inventor of frequency comb, a big name in the field, you are super friendly to students and you really spend your time in the lab to help us solve problems. I will always look up to you and Kerry as my role models. I also want to thank Dr. Chas Beichman and Dr. Gautam Vasisht; you are both extremely knowledgeable and generous and I have received a lot of help from you.

The end of my Ph.D is just the beginning of a much longer journey. And may the journal be as pleasant and enjoyable as my Ph.D in Caltech.

ABSTRACT

Frequency combs are having a broad impact on science and technology because they provide a way to coherently link radio/microwave-rate electrical signals with optical-rate signals derived from lasers and atomic transitions. A new, miniature realization, the microcomb, that uses chip-based microresonators can potentially revolutionize instrumentation, time keeping, spectroscopy, and navigation. Microcombs were first demonstrated using a form of cascaded four-wave mixing. However, the recent discovery of dissipative soliton microcombs enables phase-locked spectra with reproducible envelopes, as required in many frequency comb applications. In addition, these solitons are confined in a high-Q microresonator, thereby creating a rich landscape for research in nonlinear optical phenomena. In this thesis, these solitons are demonstrated for the first time in a silica microcavity. Significantly, the device provides a microwave-detectable soliton repetition rate, which is essential to many comb applications. The unusual properties of the solitons are studied from a theoretical viewpoint using a Lagrangian formalism and predictions of the theory are confirmed experimentally. In the course of this work, a new optical soliton, the Stokes soliton, was also discovered. In addition to soliton mode locking, another novel and compact platform, the electro-optical modulation frequency comb, was studied. This type of frequency comb was used to demonstrate a novel electro-optic form of frequency division for stable microwave synthesis. It was also modified to perform astronomical calibration for exoplanet detection at the Keck Observatory in Hawaii.

PUBLISHED CONTENT AND CONTRIBUTIONS

- Li, Jiang, Xu Yi, Hansuek Lee, Scott A Diddams, and Kerry J Vahala (2014). “Electro-optical frequency division and stable microwave synthesis”. In: *Science* 345.6194, pp. 309–313. doi: [10.1126/science.1252909](https://doi.org/10.1126/science.1252909).
X.Y participated in the conception of the project, demonstrated the electro-optics frequency division, and participated in the writing of the manuscript.
- Yang, Qi-Fan, Xu Yi, Ki Youl Yang, and Kerry Vahala (2016). “Spatial-mode-interaction-induced dispersive-waves and their active tuning in microresonators”. In: *Optica* 3, pp. 1132–1135. doi: [10.1364/OPTICA.3.001132](https://doi.org/10.1364/OPTICA.3.001132).
X.Y participated in the discovery of the effect, participated in the measurement, proposed the theoretical model, prepared the data, and participated in the writing of the manuscript.
- Yang, Qi-Fan, Xu Yi, Ki Youl Yang, and Kerry J Vahala (2017). “Stokes solitons in optical microcavities”. In: *Nature Physics* 13, pp. 53–57. doi: [10.1038/nphys3875](https://doi.org/10.1038/nphys3875).
X.Y co-discovered of the effect, co-demonstrated the measurement, analytical model, prepared the data, and participated in the writing of the manuscript.
- Yi, X, K Vahala, J Li, S Diddams, G Ycas, P Plavchan, S Leifer, J Sandhu, G Vasisht, P Chen, P Gao, J Gagne, E Furlan, M Bottom, EC Martin, MP Fitzgerald, G Doppmann, and C Beichman (2016). “Demonstration of a near-IR line-referenced electro-optical laser frequency comb for precision radial velocity measurements in astronomy”. In: *Nature communications* 7.10436. doi: [10.1038/ncomms10436](https://doi.org/10.1038/ncomms10436).
X.Y participated in the conception of the project, demonstrated the line-referenced EOM comb, prepared the data, and participated in the writing of the manuscript.
- Yi, Xu, Qi-Fan Yang, Ki Youl Yang, Myoung-Gyun Suh, and Kerry Vahala (2015). “Soliton frequency comb at microwave rates in a high-Q silica microresonator”. In: *Optica* 2.12, pp. 1078–1085. doi: [10.1364/OPTICA.2.001078](https://doi.org/10.1364/OPTICA.2.001078).
X.Y participated in the conception of the project, demonstrated the soliton generation and measurement, prepared the data, and participated in the writing of the manuscript.
- Yi, Xu, Qi-Fan Yang, Ki Youl Yang, and Kerry Vahala (2016). “Active capture and stabilization of temporal solitons in microresonators”. In: *Optics letters* 41.9, pp. 2037–2040. doi: [10.1364/OL.41.002037](https://doi.org/10.1364/OL.41.002037).
X.Y proposed the conception of the project, demonstrated the soliton capture technique, prepared the data, and participated in the writing of the manuscript.
- Yi, Xu, Qi-Fan Yang, Ki Youl Yang, and Kerry J Vahala (2016). “Theory and measurement of the soliton self-frequency shift and efficiency in optical microcavities”. In: *Optics Letters* 41.15, pp. 3419–3422. doi: [10.1364/OL.41.003419](https://doi.org/10.1364/OL.41.003419).
X.Y participated in the conception of the project, demonstrated the calculation and

measurement of soliton self-frequency shift, prepared the data, and participated in the writing of the manuscript.

Yi, Xu, Qi-Fan Yang, Xueyue Zhang, Ki Youl Yang, Xinbai Li, and Kerry Vahala (2017). “Single-mode dispersive waves and soliton microcomb dynamics”. In: *Nature Communications* 8.14869. doi: [10.1038/ncomms14869](https://doi.org/10.1038/ncomms14869).

X.Y co-discovered of the effect, co-demonstrated the measurement, analytical model, prepared the data, and participated in the writing of the manuscript.

TABLE OF CONTENTS

Acknowledgements	iii
Abstract	iv
Published Content and Contributions	v
Table of Contents	vii
List of Illustrations	ix
Chapter I: Introduction	1
1.1 Thesis outline	1
1.2 Chapter overview	2
Chapter II: Theoretical background of soliton in microresonator	5
2.1 Introduction	5
2.2 Coupled mode equations	5
2.3 Lugiato-Lefever equation	7
2.4 Lagrangian formulation	10
2.5 Method of numerical simulation	15
2.6 summary	16
Chapter III: Soliton generation in silica microresonator	17
3.1 Introduction	17
3.2 Silica wedge resonator and its characterization	18
3.3 Active capture and locking of soliton	25
3.4 Soliton microcomb characterization	30
3.5 Soliton properties: measurement vs. theory	34
3.6 Summary	37
Chapter IV: Soliton self-frequency shift and efficiency in microresonator	39
4.1 Introduction	39
4.2 Raman interaction	40
4.3 Theory of soliton self-frequency shift in microresonator	41
4.4 Experiment of soliton self-frequency shift and efficiency	43
4.5 Summary	45
Chapter V: Stokes soliton	46
5.1 Introduction	46
5.2 Stimulated Raman scattering and group velocity matching	47
5.3 Experimental observation of Stokes soliton	49
5.4 Theory of Stokes soliton	53
5.5 Summary	61
Chapter VI: Spatial-mode-interaction induced soliton dispersive wave	62
6.1 Introduction	62
6.2 Measurement of strong spatial-mode interaction in microresonator	63
6.3 Observation of dispersive wave in microresonator	65
6.4 Phase-matching condition of dispersive wave in microresonator	66

6.5 Formalism of dispersive wave in microresonator	69
6.6 Summary	71
Chapter VII: Single-mode dispersive wave and its nonlinear dynamics in microresonator	73
7.1 Introduction	73
7.2 Observation of single mode dispersive waves	74
7.3 Soliton recoil and hysteresis	76
7.4 Application in soliton repetition rate noise reduction	80
7.5 Detailed theory and simulation of single mode dispersive wave . . .	85
7.6 Summary	94
Chapter VIII: Electro-optical frequency comb	95
8.1 Introduction	95
8.2 Demonstration of electro-optics frequency comb	95
8.3 Summary	100
Chapter IX: Electro-optical frequency division and stable microwave synthesis	101
9.1 Introduction	101
9.2 Electro-optics frequency division (eOFD)	102
9.3 Experiment of frequency division and microwave synthesis	105
9.4 Summary	109
Chapter X: Astronomical calibration and exoplanet detection with electro- optics frequency comb	111
10.1 Introduction	111
10.2 Frequency comb design and stability test	113
10.3 Demonstration of astrocomb in IRTF and Keck observatories . .	121
10.4 Summary	128
Bibliography	129

LIST OF ILLUSTRATIONS

<i>Number</i>	<i>Page</i>
3.1 Imaging of silica wedge-resonator. (a) Top view of a 1-mm diameter of wedge resonator. (b) Scanning electron micrograph of the side view of wedge resonator. Insets are (c) simulated intensity profiles of fundamental modes. Pictures are from group alumni Dr. Hansuek Lee.	19
3.2 (a) Oscilloscope trace of ECDL laser scanning from 1550 nm to 1630 nm. The green line is the transmission and red line is the MZI reference. (b) A magnified figure of panel (a).	20
3.3 (a) Mode spectrum plot of a soliton forming mode in microresonator. $D_1/2\pi = 21.9733$ GHz. Mode numer zero corresponds to wavelength of 1550 nm. (b) FSR measurement of a microresonator. The FSR measured using MZI method is presented in color dots. Different colors correspond to different mode families. The FSR measured using EOM method are illustrated in black dot.	21
3.4 Typical mode spectrum of microresonator (a) before and (b) after optimization. The FSR of both resonators are 22 GHz.	22
3.5 Reproducibility of mode spectrum. Disks in (a) and (b) were fabricated under the same condition. Disk in panel (c) is slightly different than disk in panel (d) in wet etching time.	23
3.6 (a) Measured mode spectra (blue dots) and fitted lines. Green line represents fitting for soliton forming mode. Red and pink lines are fitted for another two high- Q modes. Orange line is fitted for a higher-order transverse mode. $D_1/2\pi$ is 22.0167 GHz. (b) Simulated mode spectra of four transverse electric (TE) modes. Cross-sectional images of the mode spatial intensity distributions are included as insets.	24
3.7 Simulated soliton steps with laser scans from laser-cavity blue-detuned to red-detuned regime.	25

3.8 (a) Schematic of experimental setup. (b) Four phases of feedback-controlled soliton excitation: (I) pump laser scans into cavity resonance from blue-detuned side; (II) laser scan stops and pump power is reduced ($\sim 10 \mu\text{s}$) to trigger solitons, and then increased ($\sim 100 \mu\text{s}$) to extend soliton existence range; (III) servo-control is engaged to actively lock the soliton power by feedback control of laser frequency; (IV) lock sustains and solitons are fully stabilized. The cavity-pump detuning (vertical axis) is relative to the hot cavity resonant frequency.	27
3.9 Complete schematic of soliton generation setup. Channel (CH) 1 to 4 are connected to a fast oscilloscope not showing in this figure.	28
3.10 Demonstration of capture and locking of a soliton state. (a) Soliton excitation with "power kicking" but no active locking is shown. The soliton state destabilizes around 22ms due to thermal transients. Soliton power is shown in red and a Mach Zehnder (MZI) reference is in blue. (b) Soliton excitation with active locking is shown with conditions similar to panel (a).	29
3.11 Zoom-in view of panel (b) in figure 3.10. The four phases are indicated using the same background color scheme as in fig. 3.9.	29
3.12 Optical spectra of soliton frequency comb. (a) The mode spectrum of the soliton-forming mode family. (b) Optical spectrum of single soliton state is shown with a sech^2 envelope (red dashed line) superimposed for comparison. The pump laser is suppressed by 20 dB with an optical Bragg filter. Inset is a zoomed-in spectrum between 1543 nm and 1545 nm.	31
3.13 FROG (a) and autocorrelation trace (b) of the soliton state in fig. 3.12. The optical pulse period is 46 ps and the fitted pulse width is 250 fs (red solid line).	32

- 3.14 Detected phase noise and electrical spectra for three devices. Phase noise spectral density function plotted versus offset frequency from the detected soliton repetition frequency of three different devices. A Rohde Schwarz phase noise analyzer was used in the measurement. Inset shows the electrical spectrum of the soliton repetition frequency (21.92 GHz) for one device. The other devices had similar spectra with repetition frequencies of 22.01 and 21.92 GHz. The phase noise of the fiber pump laser is shown in green and was generated by mixing 2 nominally identical pump lasers to create a 2.7 GHz electrical beatnote. Several features in the pump laser phase noise are reproduced in the soliton phase noise (see features near and above 20 kHz). The black line connecting square dots is the measurement floor of the phase noise analyzer. 32
- 3.15 Three devices with corresponding mode dispersion and soliton data.
(a,b) The mode dispersion spectra and soliton spectra are presented for two of the devices measured in figure 3.14. The third device in figure 3.14 is from figure 3.12. (c) Pump power transmission is plotted versus tuning across a resonance used to generate the soliton spectra in (b). The data show the formation of steps as the pump tunes red relative to the resonance. Both blue-detuned and red-detuned operation of the pump relative to the resonance are inferred from generation of an error signal using a Pound-Drever-Hall system operated open loop. 33

3.16 Control of soliton properties. (a) Measured soliton comb output power is plotted versus measured soliton pulse width (red points) with comparison to eq. (3.4) (dashed red line). The measured power per central comb line is plotted versus pulse width (blue points) with comparison to eq. (3.5) (dashed blue line). (b) The observed soliton spectra at the limits of the measurement in panel a is shown (see arrows A and B in panel a). Solid orange and green curves are simulations using the Lugiato Lefever equation including Raman terms. The indicated wavelength shifts between the pump and the centroid of the soliton spectrum result from Raman interactions with the soliton. The location of the pump line for both spectra is indicated by the dashed black line and has been suppressed by filtering. (c) Measured minimum pump power for soliton existence is plotted versus measured soliton pulse width (red points) with comparison to eqn. (3.6) (dashed red line). Measured efficiency is plotted versus measured soliton pulse width (blue points) with comparison to eqn. (3.7) (dashed blue line). Simulation using Lugiato Lefever equation including Raman terms improves agreement with data (small dashed red and blue lines). 35

- 3.17 Continuous soliton measurement over 19 hours. (a) Soliton power and central comb line power are plotted versus time in hours. The soliton power experiences a slow drift to lower values which is attributed to a slow variation in either the power set point of the electronic control or in the detected power (perhaps due to temperature drift). Central comb line power is approximately constant over the measured period with the exception of a small step increase around 6 hours. This could be associated with anything that changes the resonator coupling efficiency, the resonator Q , or both. Since the resonator is taper coupled any kind of mechanical shock could introduce such a step change in these quantities. (b) Pulse width and Raman self shift (defined as the wavelength center of the soliton spectrum less the pump wavelength) are plotted versus time in hours. A step in these quantities is recorded at the identical moment to that recorded for the central comb line power. It is interesting to note that because soliton power is feedback controlled, from equation (3.2) a step increase (decrease) in coupling η (Q) would be accompanied by a compensating decrease in pump detuning. From equation (3.3), this feedback controlled step in detuning would cause an increase in the soliton pulse width (and decrease in the Raman shift) as observed in the recorded data of panel b. Finally, the operation of the soliton comb proceeded for an additional 5 hours beyond the record presented in this figure. During the additional 5 hours other measurements were performed that required disabling the data recording. 38
- 4.1 Optical spectra measured for a dissipative Kerr cavity soliton at two operating points. The pump power is suppressed using a fiber grating filter. A sech^2 fit is shown as the orange curves and pulse widths inferred from the fitting are shown in the legend. The location of the pump line is indicated as the black line. The centers of the spectra are indicated by the green lines. 44
- 4.2 The measured Raman self-frequency-shift plotted versus $1/\tau_s^4$ for two devices. The red line is a linear fit according to eq. (4.18). 44

4.3 The measured efficiency versus soliton pulse width is plotted (blue points) for two devices and compared with theory. Theory comparison with Raman (solid blue lines) and without Raman (dash blue lines) is presented. There are no free parameters in the comparison. The small deviations between the measurement and the theory could result from the presence of weak avoided mode crossings in the dispersion spectrum (T Herr, V Brasch, J. Jost, Mirgorodskiy, et al., 2014).	45
5.1 The Stokes soliton (red) maximizes Raman gain by overlapping in time and space with the primary soliton (blue). It is also trapped by the Kerr-induced effective optical well created by the primary soliton.	48
5.2 The microcavity (shown as a ring) is pumped with a tunable, continuous-wave (CW) fiber laser amplified by an erbium-doped fiber amplifier (EDFA). An acousto-optic modulator (AOM) is used to control the pump power. The output soliton power is detected with a photo diode (PD) and monitored on an oscilloscope (OSCI). Wavelength division multiplexers (not shown) split the 1550 nm band primary soliton and 1600 nm band Stokes soliton so that their powers can be monitored separately on the oscilloscope. An optical spectrum analyzer (OSA), auto-correlator (A-CORR), and electrical spectrum analyzer (ESA) also monitor the output. In certain measurements (A-CORR and ESA), a fiber Bragg filter was used to remove the pump field from the soliton spectrum.	49

5.3 (a) Free spectral range (FSR) versus wavelength measured for four mode families in a 3 mm disk resonator. The mode families for the primary and Stokes soliton are shown in green and red, respectively. The FSR at the spectral center of the primary soliton is shown as a dashed horizontal line. Extrapolation of the Stokes soliton data (red) to longer wavelengths gives the FSR matching wavelength where the Stokes soliton forms. The background coloration gives the approximate wavelength range of the Raman gain spectrum. (b) Measured primary and Stokes soliton spectra. The Stokes soliton spectral center closely matches the prediction in panel (a). Sech ² envelopes are shown on each spectrum. The primary soliton spectrum features a small Raman self-frequency shift. (c) Dispersion spectra for the Stokes soliton forming mode family measured in three devices (the upper spectrum is the device from panel (a)). Other mode families have been omitted in the plots for clarity. The horizontal dashed lines give the repetition frequency of the primary soliton in each device. Extrapolation of the dispersion data attained by simulation is provided to graphically locate the predicted Stokes soliton wavelength. (d) The measured primary and Stokes soliton spectra corresponding to the devices in panel (c). The spectral locations of the Stokes solitons agree well with the graphical predictions.	50
5.4 Frequency-resolved-optical-gating (FROG) traces of the primary and Stokes solitons. The primary soliton is amplified to 500 mW by an EDFA before coupling into the FROG setup, while the Stokes soliton is amplified to 10 mW by two cascaded semiconductor optical amplifiers with gain centered around 1620 nm. The period of the primary and Stokes solitons are 46 ps, the cavity round trip time. . . .	51
5.5 (a) Electrical spectra of the detected primary soliton pulse stream (blue) and the Stokes pulse stream (red). (b) Beatnote between neighboring comb lines of the primary and Stokes solitons for a device like that in figure 5.3 (a). The beatnote is much noisier than the repetition frequency in panel (a).	52

- 5.6 Stokes soliton spectra, power and threshold measurements. (a) Soliton spectra are plotted below and above threshold. The upper insets show the spatial mode families associated with the primary and Stokes solitons. (b) Measurement of Stokes soliton power and primary soliton peak power versus total soliton power. The primary soliton peak power (blue) versus total power experiences threshold clamping at the onset of Stokes soliton oscillation. The theoretical threshold peak power from eq. (1) is also shown for comparison as the horizontal blue dashed line. 59
- 5.7 Stokes soliton formation in a microresonator. (a) Simulated intracavity comb power during a laser scan over the primary soliton pumping resonance from the blue (left) to the red (right) of the resonance. The detuning is normalized to the resonance linewidth. The initial step corresponds to the primary soliton formation, and the subsequent decrease in power corresponds to the onset of the Stokes soliton. The Stokes soliton power is shown in red. (b) Zoomed-in view of the indicated region from figure panel (a). (c) Experimentally measured primary and Stokes soliton power during a laser scan showing the features simulated in panel (a) and (b). (d) Simulation of the intracavity field in the moving frame of the solitons plotted versus the pump laser detuning. The detuning axis is scaled identically to panel (a). The figure shows the primary soliton step region (below threshold) as well as the onset of the Stokes soliton (above threshold). (e) Temporal overlap of the primary and Stokes solitons is numerically confirmed in the plot of normalized power versus location angle within the resonator. The overlap confirms trapping and co-propagation. (f) Intracavity optical spectra of the primary and Stokes solitons. 60

6.1	Dispersive wave generation by spatial mode interaction. (a) Measured relative-mode-frequencies (blue points) of the soliton-forming mode family and the interaction mode family. Mode number $\mu = 0$ corresponds to the pump laser frequency of 193.45 THz (1549.7 nm). Hybrid mode frequencies calculated from eq. (6.1) are shown in green and the unperturbed mode families are shown in orange. The dashed, horizontal black line determines phase matching for $\omega_{\text{rep}} = D_{1A}$. (b) Measured soliton optical spectrum with dispersive wave feature is shown. For comparison, a Sech ² fitting is provided in red. The pump frequency (black) and soliton center frequency (green) indicate a Raman-induced soliton self-frequency shift.	64
6.2	Measured soliton repetition rate (blue points) is plotted versus soliton self-frequency shift. The dashed blue line is a plot of eq. (6.3). The offset for the repetition rate vertical scale is $D_{1A} = 21.9733$ GHz. A typical microwave beatnote of the photo-detected soliton and dispersive wave is shown in the inset (resolution bandwidth is 10 kHz).	67
6.3	Dispersive wave phase matching condition. (a) Soliton and interaction mode family dispersion curves are shown with phase matching dashed lines (see eq. (6.4)). The black line is the case where $\omega_{\text{rep}} = D_{1A}$ and the green line includes a Raman-induced change in ω_{rep} . The intersection of the soliton branch with these lines is the dispersive wave phase matching point (arrows). (b) Soliton optical spectra corresponding to small (red) and large (blue) cavity-laser detuning ($\delta\omega$). Sech ² fitting of the spectral envelope is shown as the orange curves. (c) Dispersive wave spectra with cavity-laser detuning (soliton power and bandwidth) increasing from lower to upper trace. .	68
6.4	Measured dispersive-wave peak frequencies (red points) are plotted versus soliton self-frequency shift. The dashed red line uses eq. (6.4) to determine the dispersive wave frequency ($\approx \mu_{DW}D_{1A} + \omega_0$) as described in the text.	69

7.1 (a) Measured relative mode frequencies are shown as blue points (Xu Yi, Q.-F. Yang, Ki Youl Yang, Suh, et al., 2015). The green and yellow dashed lines represent the fitted relative mode frequencies ($\Delta\omega_{\mu A}$ and $\Delta\omega_{\mu B}$) of the unperturbed soliton-forming mode family A and crossing mode family B, respectively. Relative mode frequencies for upper and lower branch hybrid-modes are $\Delta\omega_{\mu+}$ and $\Delta\omega_{\mu-}$. The red line illustrates the frequencies of a hypothetical soliton frequency comb. A non-zero slope on this line arises from the repetition rate change relative to the FSR at mode $\mu = 0$. (b) Measured optical spectra at soliton operating points I and II, corresponding to closely matched cavity-pump detuning frequencies, $\delta\omega$. A strong single- mode dispersive wave at $\mu = 72$ is observed for operating point II and causes a soliton recoil frequency shift. This frequency shift adds to the shift resulting from the Raman-induced SSFS.	76
7.2 Dispersive-wave power (a) and soliton spectral center frequency shift (b) versus cavity-pump detuning. Inset in (a): Measured (blue dots) and theoretical (red line) recoil frequency versus the dispersive wave power.	79
7.3 Soliton repetition frequency measurement (a) Measured (blue dots) and theoretical (red) soliton repetition frequency versus pump-cavity detuning. The offset frequency is 22.0167 GHz. The distinct soliton operating points I, II and III refer to phase noise measurements in figure 7.4. Point III is near the quiet operation point. (b) Phase noise of soliton repetition rates at 25 kHz offset frequency plotted versus the cavity-pump detuning. The blue and red dots (lines) denote the experimental (theoretical) phase noise of the upper (blue) and lower (red) branch operating points, respectively.	80
7.4 Soliton phase noise measurement. Phase noise spectra of detected soliton pulse stream at three operating points shown in 7.3. The black line connecting the square dots is the measurement floor of the phase noise analyzer.	81

- 7.5 The experimental setup includes both the soliton generation and characterization setup (Xu Yi, Q.-F. Yang, Ki Youl Yang, Suh, et al., 2015; Xu Yi, Q.-F. Yang, Ki Youl Yang, and Kerry Vahala, 2016a) and a Pound-Drever-Hall (PDH) system operated open loop. The PDH is added to make possible the pump-cavity detuning noise measurement. Components included in the set up are an EOM: electro-optic modulator; EDFA: Erbium-doped fiber amplifier; AOM: acousto-optic modulator; PC: polarization controller; FBG: fiber Bragg grating; PD: photodetector; OSA: optical spectral analyzer; PNA: phase noise analyzer; LO: local oscillator. The OSA and and PNA are shown for completeness. They are used to measure the soliton spectrum and repetition rate phase noise. They are not involved in measuring the detuning frequency noise. 82
- 7.6 Measurements that illustrate the pump-cavity detuning measurement. The green trace is the measured power transmission when scanning the pump laser frequency across a cavity resonance. The pump laser is phase modulated, the transmitted signal is detected, and the resulting photocurrent is then mixed with the PDH local oscillator signal to generate the PDH error signal. Upon laser scan the PDH error signal (as measured on the oscilloscope) is generated as shown in the red trace. The pump laser is filtered using the fiber Bragg grating. The monitoring point for the detuning frequency measurement is indicated by the black dot. In order to convert scanning time into laser frequency, a calibrated Mach-Zehnder interferometer (MZI) records power transmission (blue trace) on an oscilloscope. The free-spectral-range of the MZI is 40 MHz. 83
- 7.7 Existence study for the quiet point. The maximum ratios of $|\partial\Omega_{\text{Recoil}}/\partial\delta\omega|$ to $|\partial\Omega_{\text{Raman}}/\partial\delta\omega|$ at varying normalized modal coupling rate G (see Methods) and normalized crossing-mode damping rate κ_B (dashed curve is unity ratio). The quiet point exists when this ratio is greater than unity (red region). Parameters correspond to a silica resonator. . . 84

7.8	(a) Numerical (blue dots) and analytical (red solid line) soliton total frequency shift versus cavity-pump detuning. Points i, ii, iii, and iv correspond to specific soliton operating points noted in other figure panels. (b) Numerical (blue dots) and analytical (red solid line) dispersive wave power (normalized to total soliton power) versus cavity-pump detuning. Inset: recoil frequency versus the dispersive wave power.	92
7.9	(a) Comb spectra contributions from the two mode families (blue: soliton forming mode family A; red: crossing mode family B). (b) Time domain intracavity power. T_R is the cavity round trip time.(i) to (iv) are indicated in figure 7.8.	93
8.1	Conceptual schematics of a typical EO frequency comb. A continuous pump laser goes through intensity modulation (Int Mod), phase modulation (Ph Mod), single mode fiber (SMF) and forms a train of short pulses with the repetition rate equaling the modulation frequency. The pulses are then amplified by an optical amplifier. The amplifier spontaneous emission (ASE) noise is filtered by a bandpass filter (BPF), or other type of filter. The amplified pulses then go into highly nonlinear fiber (HNLF) and are spectrum broadened.	96
8.2	Detailed schematic of electro-optics modulation. Components in this layout include continuous wave (CW) laser, phase modulator (PM), intensity modulator (IM), microwave source (RF), microwave amplifier (Amp), phase shifter (PS), variable microwave attenuator (VATT) and DC voltage supply (V_{DC}).	96
8.3	Optical spectrum of phase modulation sidebands. The optical spectrum of the 1st, 2nd and 3rd phase modulation are shown in black, red and blue. The optical spectra of the three cascaded phase modulators are presented in green. The modulation frequency is 10 GHz. The contrast of the spectrum is limited by the resolution of this OSA (0.05 nm).	97
8.4	Optical spectrum of EO frequency comb. The parameters of intensity modulators are optimized using the method in main text. The modulation frequency is 10 GHz.	98
8.5	Autocorrelation measurement (blue line) of the EO frequency comb in figure 8.4. The red line is computed with the OSA spectrum in figure 8.4 and assumes flat phase on each comb lines.	99

- 8.6 The optical spectrum of broadened EO frequency comb with different pump laser wavelength. The modulation frequency is 12 GHz and the amplified power is 180 mW. The HNLF is 500 meters long. . . . 100
- 9.1 Conceptual schematics of stable microwave synthesis by use of EOFD.
(a) Two optical reference laser lines are provided by one of several possible methods, including dual-mode laser action, frequency-locking two lasers to distinct optical modes of a reference cavity, or lasers stabilized to atomic transitions. These laser lines are phase-modulated so as to produce sidebands, two of which nearly overlap at the spectral midpoint of the laser lines. The drive frequency is provided by the electrical VCO that is to be stabilized. Optical filtering and detection of the nearly overlapping sidebands gives a beat note that is used to phase-lock the VCO and lower its phase noise. EOM is the electro-optical modulator, OBPF is the optical band-pass filter, and PD is the photodetector. (b) Comparison of conventional, electrical, phase-locked loop control of a VCO with the present method. The conventional method divides the VCO for phase comparison with the low-frequency reference, whereas the present method divides the frequency separation of two lasers so as to stabilize the electrical VCO. 102
- 9.2 Analysis of the relative phase of the inner side bands in the optical spectrum. $\varphi_{1,2}$ and φ_M are the phase fluctuations of the laser field phases and the electrical VCO, respectively. 103
- 9.3 Schematic showing the arrangement used for dual-pumping of the disk resonator Brillouin laser. Lasers 1 and 2 are locked to distinct modes of a high-Q disk resonator. Servo control involves direct frequency tuning of laser 1 and frequency shifting via an acousto-optic modulator (AOM) for laser 2. The reference laser lines provided by the Brillouin oscillation are output to the optical division function. 105

9.4 Schematic of optical frequency division. Depending on the desired division ratio, two pathways are taken (path I and path II). For division up to 30 \times , a pair of phase modulators are synchronously driven, whereas for larger division ratios, the phase modulators are cascaded with a fiber pulse broadener containing an intensity modulator (IM), dispersion compensation (DC), EDFA, and nonlinear fiber (HNLF). The filtered (OBPF) and detected signal is then processed for servo control of the VCO. Also shown are the optical spectrum analyzer (OSA) and electrical phase shifters (PS).	105
9.5 (a) Optical spectra of co-lasing Brillouin lasers at various tuning configurations used in the measurement corresponding to cavity FSR spacings provided in the inset. (b) Optical spectrum of Brillouin laser lines with (red) and without (blue) phase modulation.	106
9.6 SSB phase noise spectrum of the optical reference (red) is shown. For this measurement, the dual SBS lines are tuned to a detectable frequency difference. Also shown are the closed-loop VCO phase noise referenced to dual SBS lines separated by 327 GHz (blue) and 1.61 THz (green), with corresponding division ratios of 30 and 148. The dashed black curve is the phase noise of the free-running VCO. The light blue square markers denote the phase noise sensitivity of the phase noise tester.	108
9.7 (a) VCO RF power spectrum at 10.89 GHz for open-loop and closed-loop conditions in which the Brillouin frequency separation is divided by 18 \times , 30 \times , and 148 \times . Resolution bandwidth is set at 30 Hz. (b) Summary of SSB phase noise levels at 10.89 GHz versus optical division ratio. Cases shown are measured at 1-, 10-, and 100-kHz offset frequencies. The dashed lines give $1/N^2$ trends. Phase noise levels for an Agilent MXG and PSG microwave sources (carrier 11 GHz, 100 kHz offset) are provided for comparison	109

10.1 Conceptual schematics of the line-referenced electro-optic frequency comb for astronomy. Vertically, the first column contains images of key instruments. From (a) to (e), the images are reference laser, Rb clock (left) and phase modulator (right), amplitude modulator, highly-nonlinear fiber and telescope. A simplified schematic setup is in the second column. Third and fourth columns present the comb state in the frequency and temporal domains. The frequency of N -th comb tooth is expressed as $f_N = f_0 + N \times f_m$, where f_0 and f_m are the reference laser frequency and modulation frequency, respectively. N is the number of comb lines relative to the reference laser (taken as comb line $N = 0$), RV is radial velocity and δf , δf_0 and δf_m are the variance of f , f_0 and f_m . (a) The reference laser is locked to a molecular transition, acquiring stability of 0.2 MHz, corresponding to $30 \text{ cm s}^{-1} RV$. (b) Cascaded phase modulation (CPM) comb: the phase of the reference laser is modulated by two phase modulators (PM), creating several tens of sidebands with spacing equal to the modulation frequency. The RF frequency generator is referenced to a Rb clock, providing stability at the sub-Hz level ($\delta f_m < 0.03 \text{ Hz}$ at 100s). (c) Pulse forming is then performed by an amplitude modulator (AM) and dispersion compensation unit (DCU), which could be a long single mode fiber (SMF) or chirped fiber Bragg grating. (d) After amplification by an Erbium Doped Fiber Amplifier (EDFA), the pulse undergoes optical continuum broadening in a highly nonlinear fiber (HNLF), extending its bandwidth $> 100 \text{ nm}$. (e) Finally the comb light is combined with stellar light using a fiber acquisition unit (FAU) and is sent into the telescope spectrograph. The overall comb stability is primarily determined by the pump laser. 114

- 10.2 Detailed setup of line-referenced electro-optic frequency comb. (a) The entire LR-EOFC system sits in a 19 inch instrument rack. Optics and microwave components in the rack are denoted in orange and black, respectively. Small components were assembled onto a breadboard. These included the phase modulators (PM), amplitude modulator (AM), fiber Bragg grating (FBG), photodetector (PD), variable attenuator (VATT), attenuator (ATT), highly nonlinear fiber (HNLF), microwave source, microwave amplifier (Amp), phase shifter (PS) and bandpass filter (BPS). The reference laser, erbium-doped amplifier (EDFA), rubidium (Rb) clock, counter, optical spectrum analyzer (OSA) and servo lock box are separately located in the instrument rack. (b) A simplified schematic of the fiber acquisition unit (FAU) is also shown. Stellar light is focused and coupled into a multi-mode fiber (MMF). The comb light from a single mode fiber (SMF), together with the stellar light in MMF, are focused on the spectrograph slit and sent into the spectrograph. 115
- 10.3 A typical comb spectrum from the 1559.9 nm laser with > 100nm span generated with 600 mW pump power. The insets show the resolved line spacing of 12 GHz or approximately 0.1 nm. 115
- 10.4 Reference laser stability measurement. (a) Experimental setup: BP, optical bandpass filter; PD, photodiode. All beam paths and beam combiners are in single mode fiber. (b) Time series of measured beat frequencies for the two frequency-stabilized lasers with 10 s averaging per measurement. The x-axes are the dates in November of 2013 and May/June of 2014, respectively. (c) Allan deviation, which is a measure of the fractional frequency stability, computed from the time series data of (b). Inset scales give the radial velocity precision. 116
- 10.5 Astrocomb system in a standard 19 inch instrument rack. The comb board is fixed at the top of the instrument rack. The entire system could be move around inside the observatory facilities. 117

10.6 Experimental results at IRTF. (a) Comb spectrum produced using 1559.9 nm reference laser. The insets on the top left and right show the resolved comb lines on the optical spectrum analyzer. Comb spectra taken by the CSHELL spectrograph at 1375 nm, 1400 nm, 1670 nm and 1700 nm are presented as insets in the lower half of the figure. The blue circles mark the estimated comb line power and center wavelength for these spectra. Comb lines are detectable on CSHELL at fW power levels. (b) Comb spectral line power vs. time is shown at five different wavelengths. During the 5 day test at IRTF, no parameter adjustment was made, and comb intensity was very stable even with multiple power-on and off cycling of the optical continuum generation system.	118
10.7 (a) An image of the echelle spectrum from CSHELL on IRTF showing a 4 nm portion of spectrum around 1670 nm. The top row of dots are the laser comb lines while the broad spectrum at the bottom is from the bright M2 II-III giant star β Peg seen through dense cloud cover. (b) Spectra extracted from panel a. The solid red curve denotes the average of 11 individual spectra of β Peg (without the gas cell) obtained with CSHELL on the IRTF. The regular sine-wave like blue lines show the spectrum from the laser comb obtained simultaneously with the stellar spectrum. The vertical axis is normalized flux units. . .	123
10.8 Reduced NIRSPEC image from echelle order 46 to 53, displaying the stabilized laser comb using the 1559.9 nm reference laser. Line brightness represents data counts.	124
10.9 (a) A portion of the extracted comb spectrum from order 48 is plotted versus wavelength. (b) Comb brightness envelope of orders 47 to 50 and orders 48 and 49 when flattened by a waveshaper (ws).	125

C h a p t e r 1

INTRODUCTION

1.1 Thesis outline

The Optical frequency comb has been a revolutionary invention and is having a widespread impact on science and technology (Th Udem, Ronald Holzwarth, and T. W. Hänsch, 2002; S. T. Cundiff and Ye, 2003; S. A. Diddams, 2010; N. R. Newbury, 2011). It was invented around the year 2000 for precise optical metrology (Jones et al., 2000; R Holzwarth et al., 2000; S. A. Diddams, Jones, et al., 2000) and quickly found its application in various fields, including fundamental physics (Bize et al., 2003; Chou et al., 2010), spectroscopy (Thorpe et al., 2006; S. A. Diddams, Leo Hollberg, and Mbele, 2007; Coddington, W. C. Swann, and N. R. Newbury, 2008; Coddington, N. Newbury, and W. Swann, 2016), astronomy (M. Murphy et al., 2007; Steinmetz et al., 2008; C.-H. Li et al., 2008) and was awarded the Nobel prize in physics in 2005 (Hall, 2006; T. W. Hänsch, 2006). An optical frequency comb typically consists of thousands of laser lines with equally spaced frequencies. It resembles the grid of a ruler, or a hair comb, but in frequency domain. It is capable of coherently connecting electrical and optical frequencies through the detection and control of comb repetition frequency and offset frequency (known as carrier envelope frequency). This has led to numerous inventions, including optical clocks (SA Diddams, Th Udem, et al., 2001; SA Diddams, Bergquist, et al., 2004) and optical frequency division (TM Fortier et al., 2011). Traditionally, the optical frequency comb is constructed from mode-locked femtosecond laser. However, this type of conventional frequency combs was typically limited to national labs because of its size, cost and complexity.

Since 2007, microresonator-based frequency comb (microcomb) has been proposed (P Del'Haye et al., 2007) and heavily studied to miniaturize the frequency comb to chip-based microresonator platform (T. J. Kippenberg, Ronald Holzwarth, and SA Diddams, 2011). The Optical microresonator is a dielectric optical structure that confines light in small volume for a long time (K. J. Vahala, 2003). A typical type of resonator is a ring resonator (or whispering-gallery mode resonator) where light is trapped inside the dielectric by total internal reflection (A. B. Matsko and Ilchenko, 2006). The Optical microresonator is widely known for enhancing light-matter

interaction and is intensively studied in cavity quantum electrodynamics (cavity QED) (McKeever et al., 2003; T. Aoki et al., 2006), biosensing (Vollmer and L. Yang, 2012; Vollmer and Arnold, 2008), microlaser (S. Spillane, T. Kippenberg, and KJ Vahala, 2002; Cai et al., 2000), optomechanics (Rokhsari et al., 2005; T. J. Kippenberg and K. J. Vahala, 2008), etc. Here, the microresonator uses Kerr nonlinearity to convert photons from a continuous pump laser to other longitude modes and form optical frequency combs (P Del’Haye et al., 2007). Integrating the frequency comb in a microresonator on photonic chips would revolutionize instrumentation, time keeping, spectroscopy, navigation, and potentially create new mass-market applications.

In this thesis, a new type of microcomb, the dissipated Kerr soliton microcomb, is demonstrated in a silica microresonator for the first time (Xu Yi, Q.-F. Yang, Ki Youl Yang, Suh, et al., 2015). The mode-locked solitary wave is formed in the resonator through the balance between cavity dispersion and Kerr nonlinearity (T Herr, V Brasch, J. Jost, C. Wang, et al., 2014). The development of soliton is a key progress for microcombs, as it is naturally coherent, low noise and has a predictable spectra envelope, which is required for many comb applications. It also provides a rich landscape for research in optical nonlinearity. Several novel phenomena are discovered or modeled for the first time in this thesis, including microresonator soliton self-frequency shift (Xu Yi, Q.-F. Yang, Ki Youl Yang, and Kerry Vahala, 2016b), Stokes soliton (Q.-F. Yang et al., 2017), spatial-mode induced dispersive waves (Q.-F. Yang et al., 2016) and single-mode dispersive waves (Xu Yi, Q.-F. Yang, X. Zhang, et al., 2016). Finally, novel frequency comb applications, including electro-optics frequency division, microwave synthesizer (Jiang Li, Xu Yi, et al., 2014) and astronomical calibration (X Yi et al., 2016), were explored using electro-optics frequency combs.

1.2 Chapter overview

Chapter 2 is an introduction to the theory of microcombs and solitons. The derivation of the widely used coupled mode equations and Lugiato-Lefever equation is included. It also presents the analytical solution of soliton, which will be used frequently throughout the thesis.

Chapter 3 describes the experimental demonstration of soliton microcombs in the silica resonator. The characterization of resonator mode spectrum is described in detail. The active soliton capture, a method developed to overcome thermal

complexity in the microresonator, is also introduced. Soliton measurement including optical spectrum, microwave beatnote and time-domain autocorrelation are also performed. The techniques described in this chapter are used repeatedly through Chapter 4 to Chapter 7.

Chapter 4 investigates the soliton Raman self-frequency shift in microresonator. The soliton self-frequency shift and soliton efficiency is calculated analytically using the Lagrangian variation method. The analytical result is verified by experiments.

Chapter 5 describes the observation of the Stokes soliton induced by stimulated Raman effect. The Stokes soliton is a new type of soliton which harnesses its energy through Raman gain created by the original soliton. The condition of Stokes soliton generation is analyzed and a set of coupled equations is developed to describe this novel observation. The Stokes soliton is demonstrated in multiple silica resonators and the experiment results are compared with theory analysis.

Chapter 6 presents the observation of dispersive waves in microresonator. The dispersive wave in this chapter is induced by spatial-mode interaction, which is confirmed by measurement of the resonator mode spectrum. The phase-matching condition of dispersive wave in resonator is proposed. Furthermore, it is shown that the phase matching condition can be tuned through laser-cavity detuning and soliton self-frequency shift.

In **Chapter 7** the authors investigate a limiting case of dispersive wave: a single-mode dispersive wave. The single-mode dispersive wave occurs when only one longitude mode satisfies the dispersive wave phase matching condition, and is a result of abrupt variation in resonator mode spectrum. The single-mode dispersive wave is capable of recoil the soliton envelope center and introduces nonlinearity of soliton parameters versus laser-cavity detuning. The single-mode dispersive wave is shown to reduce the soliton repetition frequency noise by balancing the Raman self-frequency shift.

Chapter 8 is an introduction to the background of electro-optics (EO) frequency comb. The EO frequency comb is built with off-the-shelf components and is reliable and easy to use. The EO frequency comb will be used in Chapters 9 and 10 for microwave synthesizer and astronomy applications.

Chapter 9 describes an optical frequency divider by using electro-optics (EO) frequency combs. By dividing the frequency difference from two stable stimulated Brillouin lasers to EO comb repetition rate, the divider transfers the stability from

high frequency optical signal to GHz's microwave frequencies and produces stable microwaves. The N-squared-law of frequency division (N being the number of division) is carefully verified.

Chapter 10 presents the implementation of the electro-optics (EO) frequency comb to astronomical calibration and exoplanet detection. The offset frequency of the EO comb from previous chapter is stabilized to a molecular transition, and the repetition frequency is synchronized to a microwave Rubidium clock. The EO comb system is assembled in a 19 inch instrument rack and was demonstrated in NASA IRTF and Keck observatories in Hawaii.

Chapter 2

THEORETICAL BACKGROUND OF SOLITON IN MICRORESONATOR

2.1 Introduction

The dynamics of microcombs involves a series of dissipated optical cavity modes, cavity dispersion, a continuous-wave pump laser, and third order Kerr nonlinearity (four-wave mixing) (P Del'Haye et al., 2007). It can be described by equations in both frequency and time domain. In frequency domain, each line of the frequency comb obeys an equation of motion and is coupled with all other comb lines through four-wave mixing. This set of equations fully describes the dynamics of microcomb and is often referred to as coupled mode equations (Chembo and N. Yu, 2010; T Herr, K Hartinger, et al., 2012). Coupled mode equations are very useful in calculation of parametric oscillation threshold (T. Kippenberg, S. Spillane, and KJ Vahala, 2004) and primary comb sidebands (T Herr, K Hartinger, et al., 2012), where only a few comb lines are generated. However, the complexity increases dramatically once more comb lines are considered. It is therefore more practical to analyze the microcomb in the time domain, in which one Lugiato-Lefever Equation (LLE) fully describes the dynamics (AB Matsko et al., 2011; Chembo and Menyuk, 2013; T Herr, V Brasch, J. Jost, C. Wang, et al., 2014). The LLE equation is equivalent to the coupled-mode equations and will be used extensively in this thesis.

In this chapter, the coupled-mode equations will first be introduced followed by the LLE equation. A Lagrangian perturbation method is then presented to derive the dissipated Kerr cavity (DKC) soliton solution (A. B. Matsko and Maleki, 2013; T Herr, V Brasch, J. Jost, C. Wang, et al., 2014).

2.2 Coupled mode equations

Here, we considered a series of optical cavity modes in the same transverse mode family with resonance frequency of $\{\omega_\mu\}$. The optical field of the μ -th comb line is denoted as $\{A_\mu\}$, with μ being the mode number relative to the mode being pumped by a continuous-wave laser field with frequency ω_p . In the absence of dispersion, $\{\omega_\mu\}$ is equally separated by the free spectral range (FSR) of the microcavity, D_1 . However, when dispersion is considered, the frequency of the modes can be

approximated with Taylor expansion,

$$\omega_\mu = \omega_0 + D_1\mu + \frac{1}{2}D_2\mu^2 + \sum_{j>2} \frac{1}{j!} D_j \mu^j, \quad (2.1)$$

where D_j is the j -th order dispersion.

The equations of motion for the field of μ -th mode A_μ (Chembo and N. Yu, 2010; T Herr, K Hartinger, et al., 2012) can be written as

$$\frac{dA_\mu}{dT} = -(i\omega_\mu + \kappa/2)A_\mu + \delta_{0,\mu}\sqrt{\frac{\kappa_{\text{ext}}P_{\text{in}}}{\hbar\omega_0}}e^{-i\omega_p T} + ig \sum_{\mu_1, \mu_2, \mu_3} A_{\mu_1} A_{\mu_2} A_{\mu_3}^*, \quad (2.2)$$

where κ is the cavity dissipated rate, κ_{ext} is the external coupling rate between cavity mode and tapered fiber (or waveguide), P_{in} is the pump laser power, ω_p is the pump laser frequency, and $g = \hbar\omega_0^2 cn_2/n_0^2 V_{\text{eff}}$ is the equivalent Kerr nonlinear coefficient in microcavity (T. Kippenberg, S. Spillane, and KJ Vahala, 2004; T Herr, K Hartinger, et al., 2012). The equation is normalized by $\hbar\omega_0$ so that $|A_\mu|^2$ is in the unit of photon number. c , n_0 , n_2 , and V_{eff} are the speed of light, refractive index, Kerr nonlinear refractive index and effective cavity mode volume, respectively. The last term in eq. (2.2) is Kerr nonlinear (four wave mixing) term. It is noted that in eq. (2.2) the dissipate rate κ and nonlinear mode volume V_{eff} are independent of mode number μ and this is only valid for microcombs with limited wavelength span. For simplicity, we denote $f \equiv \sqrt{\kappa_{\text{ext}}P_{\text{in}}/\hbar\omega_0}$ in the following derivation.

To eliminate the fast oscillating optical frequency in A_μ , we transform eq. (2.2) to a relative frequency frame where $a_\mu = A_\mu e^{-i(\omega_p + D_1\mu)T}$. It is noted that the pump laser is one of the comb lines and if the comb spacing is the FSR of the cavity, $\omega_p + D_1\mu \equiv \zeta_\mu$ is the frequency of the μ -th comb line. When replacing A_μ with a_μ in eq. (2.2), we obtain

$$\frac{da_\mu}{dT} = -(i\omega_\mu - i\zeta_\mu + \kappa/2)a_\mu + \delta_{0,\mu}f + ig \sum_{\mu_1, \mu_2, \mu_3} a_{\mu_1} a_{\mu_2} a_{\mu_3}^* e^{-iD_1(\mu_1 + \mu_2 - \mu_3 - \mu)T}. \quad (2.3)$$

As eq. (2.3) evolves in the rate of $\kappa \ll D_1$, the four-wave mixing term has nonzero contribution only when $\mu_3 = \mu_1 + \mu_2 - \mu$. Therefore, the coupled mode equations can be further simplified to

$$\frac{da_\mu}{dT} = -(i\omega_\mu - i\zeta_\mu + \kappa/2)a_\mu + \delta_{0,\mu}f + ig \sum_{\mu_1, \mu_2} a_{\mu_1} a_{\mu_2} a_{\mu_1 + \mu_2 - \mu}^*. \quad (2.4)$$

Equation (2.4) is the coupled mode equations governing the dynamics of microcomb. The exact analytical solution to the equations is not known. However, in some

simplified cases, coupled mode equations provide important information about the formation of microcomb. For example, the threshold of parametric oscillation can be obtained (T. Kippenberg, S. Spillane, and KJ Vahala, 2004; Chembo and N. Yu, 2010; T Herr, K Hartinger, et al., 2012) by eq. (2.4) when only considering the equations of $\mu = 0$ (the mode being pumped by laser) and $\mu = \pm m$ (a pair of parametric sidebands),

$$P_{\text{th}} = \frac{\pi n_0 \omega_0 S_{\text{eff}}}{4\eta n_2} \frac{1}{D_1 Q^2}, \quad (2.5)$$

where $S_{\text{eff}} = V_{\text{eff}}/2\pi R$ is the effective mode area, R is the microcavity radius, $Q = \omega_0/\kappa$ is the mode quality factor, and $\eta = \kappa_{\text{ext}}/\kappa$ characterizes the waveguide/tapered-fiber to resonator loading.

The threshold of parametric oscillation is critical to microcombs as it is the characteristic power level of the system. In the silica wedge resonator, the threshold is on the level of 1-2 mW at a detectable repetition rate (Jiang Li et al., 2012b). It shall be noted that in anomalous dispersion cavity ($D_2 > 0$), the threshold of parametric oscillation is finite only when $\omega_0 - \zeta_0 = \omega_0 - \omega_p \equiv \delta\omega < 0$ (T. Kippenberg, S. Spillane, and KJ Vahala, 2004; Chembo and N. Yu, 2010). The variable, $\delta\omega$, is called cavity-pump detuning. The pump laser is said to be in blue-detuned regime when $\delta\omega < 0$, and in red-detuned regime when $\delta\omega > 0$. To generate parametric oscillation and four-wave mixing microcombs (T. Kippenberg, S. Spillane, and KJ Vahala, 2004; P Del'Haye et al., 2007; T Herr, K Hartinger, et al., 2012), the pump laser must be in the blue-detuned regime. However, we will show in the next subsection that to reach soliton operation regime, a transition from blue-detuned to red-detuned is required.

2.3 Lugiato-Lefever equation

In the previous subsection, the microcomb is described in the coordinate of propagation time T and mode number μ (or equivalently frequency ω_μ). Another nature coordinate in microcavity is the position in azimuthal angle ϕ . In this coordinate, instead of considering the optical field $a_\mu(T)$ at each mode number μ , we consider the overall optical amplitude $A(\phi, T)$ at the position of angle ϕ . These two coordinates are linked by discrete Fourier transform,

$$A(\phi, T) = \sum a_\mu(T) e^{i\mu\phi}. \quad (2.6)$$

From eq. (2.6) we can see that $A(\phi, T)$ satisfies the resonator round trip condition with $A(\phi, T) = A(\phi + 2\pi, T)$. It is noted that the ϕ coordinate could be replaced by

the fast time coordinate \tilde{t} as $\phi = -D_1\tilde{t}$ (A. B. Matsko and Maleki, 2013; Xu Yi, Q.-F. Yang, Ki Youl Yang, and Kerry Vahala, 2016b). The minus sign is to keep the wavefront consistent in position and time coordinate.

The Fourier transform of coupled-mode equations can be obtained by multiplying $e^{i\mu\phi}$ onto the μ -th equation in eq. (2.4) and then sum the equations together,

$$\begin{aligned} \sum_{\mu} \frac{da_{\mu} e^{i\mu\phi}}{dT} &= -\frac{\kappa}{2} \sum_{\mu} a_{\mu} e^{i\mu\phi} + f - i \sum_{\mu} (\omega_{\mu} - \zeta_{\mu}) A_{\mu} e^{i\mu\phi} \\ &\quad + ig \sum_{\mu} \sum_{\mu_1, \mu_2} a_{\mu_1} a_{\mu_2} a_{\mu_1 + \mu_2 - \mu}^* e^{i\mu\phi}. \end{aligned} \quad (2.7)$$

Equation (2.7) can be simplified to form the LLE equation. From eq. (2.1), we have $\omega_{\mu} - \zeta_{\mu} = \delta\omega + \sum_{j>1} D_j \mu^j / j!$. At the same time, the j -th derivative of eq. (2.6) over ϕ is $\partial^j A(\phi, t) / \partial \phi^j = i^j \mu^j A_{\mu} e^{i\mu\phi}$. In combination, the third term on the right hand-side of eq. (2.7) can be expressed as $(-i\delta\omega + -i^{1-j} \sum_{j>1} D_j / j! \partial^j / \partial \phi^j) A(\phi, t)$. The four-wave mixing term in eq. (2.7) is equal to $ig \sum_{\mu_1, \mu_2, \mu_3} a_{\mu_1} e^{i\mu_1\phi} a_{\mu_2} e^{i\mu_2\phi} a_{\mu_3}^* e^{-i\mu_3\phi}$, where we have replaced $\mu_1 + \mu_2 - \mu$ with μ_3 as μ_1, μ_2 and μ are independent. In addition, for independent μ_1, μ_2 and μ_3 , the operations of sum and multiply are commutation and the term becomes $ig \sum_{\mu_1} a_{\mu_1} e^{i\mu_1\phi} \sum_{\mu_2} a_{\mu_2} e^{i\mu_2\phi} \sum_{\mu_3} a_{\mu_3}^* e^{-i\mu_3\phi}$. Finally, replace all $\sum_{\mu} a_{\mu} e^{i\mu\phi}$ with $A(\phi, T)$ and keep only the second order dispersion, eq. (2.7) is transformed to

$$\frac{dA(\phi, t)}{dT} = i \frac{D_2}{2} \frac{\partial^2 A}{\partial \phi^2} + ig|A|^2 A - i\delta\omega A - \frac{\kappa}{2} A + f, \quad (2.8)$$

and it is the same form of the Lugiato-Lefever Equation (LLE), a general nonlinear equation proposed in 1987 (Lugiato and Lefever, 1987).

Equation (2.8) and the periodic boundary condition, $A(\phi, T) = A(\phi + 2\pi, T)$, fully describe the dynamics of microcomb and are equivalent to the coupled mode equations (eq. 2.4). In addition, as $A(\phi, T)$ is transformed from the relative frequency frame of $\omega_p + D_1\mu$, and therefore ϕ is a moving coordinate with speed of D_1 relative to the lab coordinate ϕ_l (Chembo and Menyuk, 2013). The optical field in lab coordinate, therefore, can be expressed as $\tilde{A}(\phi_l, T) = A(\phi + D_1T, T) e^{-i\omega_p T}$.

The analytical solutions to eq. (2.8) are only known in the absence of loss and gain ($\kappa, f = 0$). Although loss and gain are always presented in the microcomb system, it is beneficial to take a step back and analyze the simple case without them. The LLE is reduced to an unperturbed soliton equation,

$$\frac{dA(\phi, t)}{dT} - i \frac{D_2}{2} \frac{\partial^2 A}{\partial \phi^2} - ig|A|^2 A + i\delta\omega A = 0, \quad (2.9)$$

with a solution in the form of

$$A = B \operatorname{sech}(\phi/\phi_\tau). \quad (2.10)$$

Here, B is the soliton amplitude, ϕ_τ is the pulse width in ϕ coordinate and Sech is the hyperbolic secant function. $D_1\phi_\tau = \tau_s$ is the soliton pulse width in time coordinate (A. B. Matsko and Maleki, 2013; Xu Yi, Q.-F. Yang, Ki Youl Yang, and Kerry Vahala, 2016b). It is insightful to insert the soliton solution into eq. (2.9) and see how the terms balance each other:

$$\underbrace{\frac{D_2}{2\phi_\tau^2}[1 - 2\operatorname{sech}^2(\phi/\phi_\tau)]}_{\text{2nd order dispersion}} + \underbrace{gB^2\operatorname{sech}^2(\phi/\phi_\tau)}_{\text{Kerr nonlinearity}} - \underbrace{\delta\omega}_{\text{detuning}} = 0. \quad (2.11)$$

For eq. (2.11) to hold for any given ϕ , the Kerr nonlinear term can only be balanced by the second term in dispersion. The remaining first term in dispersion is canceled by the cavity-pump detuning. Therefore, we have

$$D_2/g = B^2\phi_\tau^2, \quad (2.12)$$

$$\delta\omega = D_2/2\phi_\tau^2 = gB^2/2. \quad (2.13)$$

A quick observation of eq. (2.12) and (2.13) is that soliton solution exists only when cavity dispersion is anomalous ($D_2 > 0$) and the pump laser is red-detuned ($\delta\omega > 0$).

There are two common interpretations of the soliton solution. One is that the Kerr nonlinearity balances the overall dispersion in the system, which includes the zero order dispersion (cavity-pump detuning) and the second order anomalous dispersion. This is identical to the understanding of soliton propagation in optical fibers. However, it does not describe why the system would prefer this balanced state. The second interpretation, on the other hand, involves the feature of microresonator. Although the pump laser is off-resonance by the amount of cavity-pump detuning $\delta\omega$, eq. (2.13) suggests that Kerr nonlinearity on average shifts the resonance by the exact amount of $\delta\omega$ so that the soliton is on-resonance with the cavity. In a microresonator, the intracavity field is enhanced when the light is on-resonance with the resonator mode. So in this case, the cavity is acting as an "saturated absorber". It enhances the on-resonance solitary waves, and damps any other waves. This mechanism is similar to the conventional optical frequency combs (SA Diddams, Th Udem, et al., 2001), which uses a mode-locked laser with a saturated absorber. However, a critical

difference is that in the case of soliton microcomb, the microresonator is both the cavity for lasering and the saturated absorber for mode-locking. This fact makes the microcomb structure extremely simple and is very versatile in frequency comb wavelength and repetition frequency.

2.4 Lagrangian formulation

In the complete equation of microcombs, by treating the dissipation and pump as a perturbation, an approximated analytical solution can be calculated with the Lagrangian variation method (A. B. Matsko and Maleki, 2013; T Herr, V Brasch, J. Jost, C. Wang, et al., 2014). In this perturbation method, it is assumed that the soliton maintains its waveform and the perturbation only varies the parameters of the soliton. This treatment is similar to the perturbation theory in quantum mechanics, where the non-perturbed eigenstates are used to calculate the first order correction of eigenvalues. The ansatz of eq. (2.8) can be set as

$$A(\phi, T) = B \operatorname{sech}(\phi/\phi_\tau) e^{i\varphi}, \quad (2.14)$$

where φ is included as the phase of the soliton envelope relative to the pump.

In this subsection, the general method of constructing the Lagrangian and perturbed Euler-Lagrangian equation from a differential equation is explained in detail. This method will be used frequently in the following chapters when the Raman effect and the spatial-mode interactions are further considered.

The principle of least action in Lagrangian method is parallel to Newton's second law in classical mechanics. It states that the physics path from one state to another is the minimum of an action functional defined by the integral of Lagrangian. This variation principle translates into the mathematical form of

$$\delta \int \int \mathcal{L} dT d\phi = 0, \quad (2.15)$$

where \mathcal{L} is the Lagrangian density. Eq. (2.15) can be expanded on the basis of $\{A, A^*, \partial A / \partial T, \partial A^* / \partial T, \partial A / \partial \phi, \partial A^* / \partial \phi\}$,

$$\begin{aligned} \delta \int \int \mathcal{L} dT d\phi &= \int \int dT d\phi \left\{ \frac{\partial \mathcal{L}}{\partial A} \delta A + \frac{\partial \mathcal{L}}{\partial (\frac{\partial A}{\partial T})} \delta \left(\frac{\partial A}{\partial T} \right) + \frac{\partial \mathcal{L}}{\partial (\frac{\partial A}{\partial \phi})} \delta \left(\frac{\partial A}{\partial \phi} \right) \right. \\ &\quad \left. + \frac{\partial \mathcal{L}}{\partial A^*} \delta A^* + \frac{\partial \mathcal{L}}{\partial (\frac{\partial A^*}{\partial T})} \delta \left(\frac{\partial A^*}{\partial T} \right) + \frac{\partial \mathcal{L}}{\partial (\frac{\partial A^*}{\partial \phi})} \delta \left(\frac{\partial A^*}{\partial \phi} \right) \right\}. \end{aligned} \quad (2.16)$$

Similar to all Lagrangian variation calculation, we can use integration by part and symmetric boundary condition to eliminate $\delta \{\partial A / \partial T, \partial A / \partial \phi, \partial A^* / \partial T, \partial A^* / \partial \phi\}$

so that

$$\begin{aligned} \delta \int \int \mathcal{L} dT d\phi &= \int \int dT d\phi \left\{ \left[\frac{\partial \mathcal{L}}{\partial A} - \frac{\partial}{\partial T} \frac{\partial \mathcal{L}}{\partial(\frac{\partial A}{\partial T})} - \frac{\partial}{\partial \phi} \frac{\partial \mathcal{L}}{\partial(\frac{\partial A}{\partial \phi})} \right] \delta A \right. \\ &\quad \left. + \left[\frac{\partial \mathcal{L}}{\partial A^*} - \frac{\partial}{\partial T} \frac{\partial \mathcal{L}}{\partial(\frac{\partial A^*}{\partial T})} - \frac{\partial}{\partial \phi} \frac{\partial \mathcal{L}}{\partial(\frac{\partial A^*}{\partial \phi})} \right] \delta A^* \right\} \quad (2.17) \\ &\equiv \int \int dT d\phi \left(\frac{\partial \mathcal{L}}{\partial A} \delta A + \frac{\partial \mathcal{L}}{\partial A^*} \delta A^* \right). \end{aligned}$$

The Lagrangian only includes terms corresponding to conservative force so that the dissipation and pumping terms must be excluded. Therefore, the Lagrangian density shall be constructed in a way that for any given variation $\{\delta A, \delta A^*\}$, it satisfies the least action principle ($\delta \int \int \mathcal{L} dT d\phi = 0$) and the soliton equation without dissipation and pump (eq. (2.9)). This would require that $\delta \mathcal{L}/\delta A^*$ equals eq. (2.9) and $-\delta \mathcal{L}/\delta A$ equals the conjugate of eq. (2.9),

$$\frac{\partial \mathcal{L}}{\partial A^*} - \frac{\partial}{\partial T} \frac{\partial \mathcal{L}}{\partial(\frac{\partial A^*}{\partial T})} - \frac{\partial}{\partial \phi} \frac{\partial \mathcal{L}}{\partial(\frac{\partial A^*}{\partial \phi})} = \frac{dA(\phi, T)}{dT} - i \frac{D_2}{2} \frac{\partial^2 A}{\partial \phi^2} - ig|A|^2 A + i\delta\omega A. \quad (2.18)$$

Integrate this equation and we arrive at the Lagrangian density of the soliton system,

$$\mathcal{L} = \frac{1}{2} \left(A^* \frac{\partial A}{\partial T} - A \frac{\partial A^*}{\partial T} \right) + i \frac{D_2}{2} \left| \frac{\partial A}{\partial \phi} \right|^2 - \frac{i}{2} g |A|^4 + i\delta\omega |A|^2. \quad (2.19)$$

The method of constructing Lagrangian is universal and can be applied to other differential equation. The dissipation and pumping terms are combined in a perturbation \mathcal{R} , where

$$\mathcal{R} = -\frac{\kappa}{2} A + f. \quad (2.20)$$

In the presence of perturbation, eq. (2.8) is recovered by letting $\delta \mathcal{L}/\delta A^* = \mathcal{R}$ or $\delta \mathcal{L}/\delta A = -\mathcal{R}^*$ (Hasegawa, 2000; A. B. Matsko and Maleki, 2013). This perturbation treatment requires $\delta\omega \gg \kappa/2$.

To calculate the evolution of soliton parameters $\{B, \phi_\tau, \varphi\}$ with T , we first eliminate coordinate ϕ by integrating the Lagrangian density into the Lagrangian

$$L = \int \mathcal{L} d\phi = 2iB^2 \phi_\tau \left(\frac{D_2}{6\phi_\tau^2} - \frac{gB^2}{3} + \delta\omega + \frac{\partial \varphi}{\partial T} \right), \quad (2.21)$$

where we have inserted the ansatz (eq. (2.14)) into the Lagrangian density (eq. (2.19)) and used the chain rule $\partial A/\partial T = \sum_j \frac{\partial A}{\partial r_j} \frac{\partial r_j}{\partial T}$. The coordinate r_j corresponds to the soliton parameter $\{B, \phi_\tau, \varphi\}$. In calculation of eq. (2.21), it is further assumed that the soliton pulse width τ_s is much shorter than the cavity round-trip time $2\pi/D_1$

so that the upper and lower limit of the integration for ϕ can be extended to $\pm\infty$. Insert eq. (2.21) into the equation of variation principle (eq. (2.15)), expand it on the coordinate of $\{r_j, \dot{r}_j\}$ and follow the same procedure as that in eq. (2.16) and (2.17), we can arrive at the Euler-Lagrangian equation

$$\frac{\partial L}{\partial r_j} - \frac{d}{dT} \frac{\partial L}{\partial \dot{r}_j} = 0, \quad (2.22)$$

where $\dot{r}_j \equiv \partial r_j / \partial T$ and no dissipation and pump is included.

In classical mechanics, the first term in eq. (2.22), $\partial L / \partial r_j$, can be understood as a force along with coordinate r_j , and the second term is the inertial. With this in mind, we can integrate the perturbation \mathcal{R} into the Euler-Lagrangian equation. Assign a virtual Lagrangian $L_{\mathcal{R}}$ to perturbation \mathcal{R} , and the force corresponding to \mathcal{R} can be expressed as $\partial L_{\mathcal{R}} / \partial r_j$. In addition, the LLE equation (eq. (2.8)) requires $L_{\mathcal{R}} = L$. Therefore, we can expand the force of \mathcal{R} using the chain rule

$$\frac{\partial L_{\mathcal{R}}}{\partial r_j} = \frac{\partial L}{\partial r_j} = \int \frac{\partial \mathcal{L}}{\partial r_j} d\phi = \int \left(\frac{\delta \mathcal{L}}{\delta A} \frac{\partial A}{\partial r_j} + \frac{\delta \mathcal{L}}{\delta A^*} \frac{\partial A^*}{\partial r_j} \right) d\phi = \int \left(R \frac{\partial A^*}{\partial r_j} - R^* \frac{\partial A}{\partial r_j} \right) d\phi, \quad (2.23)$$

where we have used $L = \int \mathcal{L} d\phi$, $\delta \mathcal{L} / \delta A^* = R$ and $\delta \mathcal{L} / \delta A = -R^*$. Add this perturbation force to the right-hand side of eq. (2.22) and we arrive at the perturbed Euler-Lagrangian equation

$$\frac{\partial L}{\partial r_j} - \frac{d}{dT} \frac{\partial L}{\partial \dot{r}_j} = \int \left(R \frac{\partial A^*}{\partial r_j} - R^* \frac{\partial A}{\partial r_j} \right) d\phi. \quad (2.24)$$

The soliton ansatz (eq. (2.14)), Lagrangian (eq. (2.21)), and the perturbed Euler-Lagrangian equation (eq. (2.24)) are the complete set of equations used to calculate the equation of motion of parameters $\{B, \phi_{\tau}, \varphi\}$.

Take $r_j = B, \phi_{\tau}, \varphi$ and insert eq. (2.14), eq. (2.20), and eq. (2.21) into eq. (2.24), we have

$$\frac{\partial \varphi}{\partial T} = \frac{2gB^2}{3} - \frac{D_2}{6\phi_{\tau}^2} - \delta\omega, \quad (2.25)$$

$$\frac{\partial \varphi}{\partial T} = \frac{gB^2}{3} + \frac{D_2}{6\phi_{\tau}^2} - \delta\omega, \quad (2.26)$$

$$\frac{dB^2 \phi_{\tau}}{dT} = -\kappa B^2 \phi_{\tau} + \pi f B \phi_{\tau} \cos \varphi. \quad (2.27)$$

The steady state solutions of eq. (2.25) to (2.27) give

$$B = \sqrt{\frac{2\delta\omega}{g}}, \quad (2.28)$$

$$\phi_\tau = \sqrt{\frac{D_2}{2\delta\omega}}, \tau_s = \frac{\phi_\tau}{D_1} = \sqrt{-\frac{c\beta_2}{2n_0\delta\omega}} \quad (2.29)$$

$$B\tau_s = \sqrt{\frac{D_2}{gD_1^2}} \quad (2.30)$$

$$\cos\varphi = \frac{\kappa B}{\pi f} = \sqrt{\frac{2\delta\omega}{g}} \frac{\kappa}{\pi f}, \quad (2.31)$$

where we have used the cavity group velocity dispersion $\beta_2 = -n_0 D_2 / c D_1^2$ and it is negative at anomalous dispersion. Eq. (2.28) and (2.29) are identical to eq. (2.12) and eq. (2.13) in unperturbed soliton equation. It is interesting to note that the soliton amplitude B and pulse width $\tau_s = \phi_\tau/D_1$ are only driven by cavity-laser detuning $\delta\omega$, but are independent of pump power f . In addition, eq. (2.31) sets a maximum on detuning ($|\cos\varphi| \leq 1$) as

$$\delta\omega \leq \frac{g\pi^2 f^2}{2\kappa^2}. \quad (2.32)$$

Beyond the maximum detuning $\delta\omega_{\max}$, the soliton is no longer the solution to the LLE equation.

The soliton solution from eq. (2.28) to eq. (2.31) is in ϕ coordinate (or time coordinate). However, as the soliton here is also a frequency comb, it is useful to convert the solution to frequency domain and examine its properties. Inserting the soliton solution of eq. (2.14) and eq. (2.28) to (2.31) into the Fourier transform in eq. (2.6), we obtain

$$a_\mu = \frac{1}{2\pi} \int_{-2\pi}^{2\pi} A(\phi) e^{-i\mu\phi} d\phi = \frac{B\phi_\tau}{2} \operatorname{sech}\left(\frac{\pi\phi_\tau\mu}{2}\right) e^{i\varphi} = \sqrt{\frac{D_2}{4g}} \operatorname{sech}\left(\frac{\pi\phi_\tau}{2}\mu\right) e^{i\varphi}. \quad (2.33)$$

It is interesting to note that in frequency domain, the soliton is also a hyperbolic secant function and its central power (at $\mu = 0$) is independent from cavity-laser detuning and pump laser power. To compare the theory results with the experimental quantities, we further calculate the soliton power output in the waveguide/tapered-fiber using $a_{\mu,\text{ext}} = \delta_{0,\mu} f + i\sqrt{\kappa_{\text{ext}}} a_\mu$. The power for the μ -th comb line ($\mu \neq 0$) is

$$P_\mu = \kappa_{\text{ext}} \hbar \omega_0 |a_\mu|^2 = -\frac{\pi c}{2} \frac{\eta S_{\text{eff}} \beta_2}{n_2} \frac{D_1}{Q} \operatorname{sech}^2\left(\pi D_1 \tau_s \mu / 2\right), \quad (2.34)$$

where we have used $g = \hbar \omega_0^2 c n_2 / n_0^2 V_{\text{eff}}$, $V_{\text{eff}} = 2\pi c S_{\text{eff}} / n_0 D_1$, $\phi_\tau = D_1 \tau_s$, and $\beta_2 = -n_0 D_2 / c D_1^2$. $\eta = \kappa_{\text{ext}} / \kappa$ is the cavity-waveguide/tapered-fiber coupling coefficient. Therefore, the power of the center comb line P_c is purely determined by the

microresonator parameters,

$$P_c = -\frac{\pi c}{2} \frac{\eta S_{\text{eff}} \beta_2}{n_2} \frac{D_1}{Q}. \quad (2.35)$$

In addition, the soliton total power, P_{sol} , can be obtained by taking the sum of eq. (2.34):

$$P_{\text{sol}} = P_c \sum_{\mu} \operatorname{sech}^2(\pi D_1 \tau_s \mu / 2) = -\frac{2c\eta S_{\text{eff}} \beta_2}{n_2 Q} \frac{1}{\tau_s} = \frac{2\eta S_{\text{eff}}}{n_0 Q} \sqrt{-2n_0 c \beta_2 \delta\omega}, \quad (2.36)$$

where we have used $\sum_{\mu} Z(\mu) \rightarrow \int Z(x) dx$ and Z represents any function. The soliton power increases with cavity-laser detuning $\delta\omega$ and it can be used in the experiment to control and stabilize the soliton (Xu Yi, Q.-F. Yang, Ki Youl Yang, Suh, et al., 2015; Xu Yi, Q.-F. Yang, Ki Youl Yang, and Kerry Vahala, 2016a).

The maximum soliton detuning, $\delta\omega_{\text{max}}$, is limited by the power of pump laser, P_{in} . We re-express eq. (2.32) in the unit of cavity dissipation rate κ as

$$\frac{\delta\omega_{\text{max}}}{\kappa} = \frac{\pi\eta n_2 D_1 Q^2}{4n_o S_{\text{eff}} \omega_0} P_{\text{in}} = \frac{\pi^2 P_{\text{in}}}{16 P_{\text{th}}}. \quad (2.37)$$

where we have used the threshold of parametric oscillation in eq. (2.5). Finally, using eq. (2.32) we calculate the minimum pump power, P_{min} , required for a soliton,

$$P_{\text{min}} = \frac{\hbar\omega_0 f_{\text{min}}^2}{\kappa_{\text{ext}}} = \frac{4n_0 S_{\text{eff}}}{\pi\eta n_2 D_1 Q} \delta\omega = -\frac{2c}{\pi} \frac{S_{\text{eff}} \beta_2}{n_2 D_1 Q} \frac{1}{\tau_s^2}. \quad (2.38)$$

Eq. (2.37) and (2.38) are critical in experiments, as they set the boundaries of detuning and pump for the soliton with a certain pulse width (or frequency bandwidth). Furthermore, we define the soliton efficiency, Γ , as the soliton power versus the minimum pump power

$$\Gamma = \frac{P_{\text{sol}}}{P_{\text{min}}} = \pi\eta^2 D_1 \tau_s. \quad (2.39)$$

It is interesting to see that for a soliton with a certain pulse width (or frequency bandwidth), the soliton efficiency is independent of the cavity nonlinear coefficient and the cavity Q -factor. In other words, the soliton efficiency is independent of the material platform of microresonator.

Finally, the LLE equation has one more steady solution. In the limit of $\delta\omega \gg \kappa$, the leading order of the solution is $A_{bc}(\phi, T) = -if/\delta\omega$, and it represents a continuous background field. As the background field is much smaller than the amplitude of the soliton, it does not interfere with the soliton solution. The overall optical field in

the cavity A_{tot} can therefore be expressed as the linear superposition of soliton and the background field

$$A_{\text{tot}} = B \operatorname{sech}(\phi/\phi_\tau) e^{i\phi} - i f / \delta\omega. \quad (2.40)$$

2.5 Method of numerical simulation

In numerical simulation, it is often favored to normalize the differential equation to dimensionless form so that one simulation corresponds to the results of a set of parameters. The LLE equation can be normalized by taking $T = 2\tau/\kappa$, $\phi = \sqrt{2D_2/\kappa}\theta$ and $A = \sqrt{\kappa/2g}\psi$, where τ , θ , and ψ are the normalized time, azimuthal angle, and optical field, respectively (T Herr, V Brasch, J. Jost, C. Wang, et al., 2014). Eq. (2.8) then becomes

$$\frac{d\psi}{d\tau} = \frac{i}{2} \frac{\partial^2 \psi}{\partial \theta^2} + i|\psi|^2 \psi - (i\varsigma + 1)\psi + \tilde{f}, \quad (2.41)$$

where $\varsigma = 2\delta\omega/\kappa$ and $\tilde{f} = \sqrt{8g/\kappa^3}f$ are the normalized detuning and pump laser field. Notice that the Kerr coefficient and cavity dissipation are normalized to 1 so that $|\tilde{f}|^2 = 1$ corresponds to the parametric oscillation threshold in eq. (2.5).

There are several different methods to simulate microcombs numerically. Here, we briefly introduced the split-step (Fourier) method. This method has been widely used in simulation of soliton propagation in fibers and optical supercontinuum (Dudley, Genty, and Coen, 2006). The general idea of this method is based on the fact that the evolution of the Kerr nonlinear term has an analytical solution in the "time" domain (coordinate θ), while the dispersion term has a simple solution in the "frequency" domain (coordinate μ). Therefore, when splitting the evolution into nonlinear and dispersion parts and calculating them separately in the "time" and "frequency" domain, the LLE can be simulated very efficiently. However, as dispersion and Kerr nonlinear operations do not commute, such split-step method has global error on the order of $\Delta\tau$, where $\Delta\tau$ is the evolution step size in normalized time. A modified version, the symmetric split-step Fourier method, was developed to reduce the global error to the order of $\Delta\tau^2$ (Sinkin et al., 2003). In addition, when using fast Fourier transform (FFT) to connect time and frequency domain, the periodic boundary condition of microresonator will be naturally satisfied (Chembo and Menyuk, 2013).

The evolution from $\psi(\theta, \tau)$ to $\psi(\theta, \tau + \Delta\tau)$ can be split into these steps below:

1. Transform $\psi(\theta, \tau)$ to frequency domain (μ coordinate) using fast Fourier transform (FFT) on variable θ :

$$\tilde{\psi}(\mu, \tau) = \text{FFT}_\theta\{\psi(\theta, \tau)\}. \quad (2.42)$$

2. Evolve $\tilde{\psi}(\mu, \tau)$ by $\Delta\tau/2$ with only dispersion by transforming LLE to frequency domain (μ coordinate). Notice in frequency domain, dispersion operator transforms as $\frac{i}{2} \frac{\partial^2 \psi(\theta, \tau)}{\partial \theta^2} = \frac{i}{2} \frac{\partial^2}{\partial \theta^2} \sum_\mu \tilde{\psi}(\mu, \tau) e^{i\mu\theta} = -\frac{i}{2} \sum_\mu \mu^2 \tilde{\psi}(\mu, \tau) e^{i\mu\theta}$. Therefore, we have the differential equation with dispersion as $d\tilde{\psi}_D(\mu, \tau)/d\tau = \frac{-i\mu^2}{2} \tilde{\psi}_D(\mu, \tau)$ and the analytical solution of the $\Delta\tau/2$ evolution is

$$\tilde{\psi}_D(\mu, \tau + \Delta\tau/2) = \exp\left(-\frac{i\mu^2}{2} \frac{\Delta\tau}{2}\right) \tilde{\psi}(\mu, \tau). \quad (2.43)$$

3. Transform $\tilde{\psi}_D(\mu, \tau + \Delta\tau/2)$ back to time domain (θ coordinate) using inversed fast Fourier transform (IFFT) on variable μ :

$$\psi_D(\theta, \tau + \Delta\tau/2) = \text{IFFT}_\mu\{\tilde{\psi}_D(\mu, \tau + \Delta\tau/2)\}. \quad (2.44)$$

4. Evolve $\psi_D(\mu, \tau + \Delta\tau/2)$ by $\Delta\tau$ with Kerr nonlinear, detuning, dissipation and pump terms:

$$\psi_N(\theta, \tau + \Delta\tau) = \exp\{(i|\psi_D(\mu, \tau + \Delta\tau/2)|^2 - i\varsigma - 1)\} \psi_D(\mu, \tau + \Delta\tau/2) + \Delta\tau f. \quad (2.45)$$

5. Repeat step 1, convert $\psi_N(\theta, \tau + \Delta\tau)$ to time domain,

$$\tilde{\psi}_N(\mu, \tau + \Delta\tau) = \text{FFT}_\theta\{\psi_N(\theta, \tau + \Delta\tau)\}. \quad (2.46)$$

6. Repeat step 2, evolve $\Delta\tau/2$ with only dispersion:

$$\tilde{\psi}_{D+N}(\mu, \tau + \Delta\tau) = \exp\left(-\frac{i\mu^2}{2} \frac{\Delta\tau}{2}\right) \tilde{\psi}_N(\mu, \tau + \Delta\tau). \quad (2.47)$$

7. Repeat step 3, convert back to time domain,

$$\psi(\theta, \tau + \Delta\tau) = \text{IFFT}_\mu\{\tilde{\psi}_{D+N}(\mu, \tau + \Delta\tau)\}. \quad (2.48)$$

2.6 summary

In this chapter, we have derived the coupled mode equations and LLE equations for Kerr frequency comb dynamics. The analytical solutions for the LLE equations are introduced. These equations will be repeatedly used in the following chapters.

C h a p t e r 3

SOLITON GENERATION IN SILICA MICRORESONATOR

3.1 Introduction

¹ The optical frequency comb is revolutionizing a wide range of subjects spanning spectroscopy to time standards (Jones et al., 2000; R Holzwarth et al., 2000; SA Diddams, Th Udem, et al., 2001; Th Udem, Ronald Holzwarth, and T. W. Hänsch, 2002; SA Diddams, Bergquist, et al., 2004; N. R. Newbury, 2011; Steinmetz et al., 2008; C.-H. Li et al., 2008; TM Fortier et al., 2011). Since their invention, a miniaturized approach to the formation of a comb of optical frequencies has been proposed in high-Q micro-resonators (P Del'Haye et al., 2007; T. J. Kippenberg, Ronald Holzwarth, and SA Diddams, 2011). These microcombs or Kerr combs have been demonstrated in several material systems (A. A. Savchenkov, A. B. Matsko, Ilchenko, et al., 2008; Grudinin, N. Yu, and Maleki, 2009; Papp and S. A. Diddams, 2011; Hausmann et al., 2014), including certain planar systems suitable for monolithic integration (Levy et al., 2010; Razzari et al., 2010; Ferdous et al., 2011; Jiang Li et al., 2012b; Jung et al., 2013). They have been applied in demonstrations of microwave generation (A. A. Savchenkov, A. B. Matsko, Ilchenko, et al., 2008), waveform synthesis (Ferdous et al., 2011), optical atomic clocks (Papp, Beha, et al., 2014) and coherent communications (Pfeifle et al., 2014). Microcombs were initially realized through a process of cascaded four-wave mixing (P Del'Haye et al., 2007) driven by parametric oscillation (T. Kippenberg, S. Spillane, and KJ Vahala, 2004; A. A. Savchenkov, A. B. Matsko, Strekalov, et al., 2004). However, a recent advance has been the demonstration of mode locking through formation of dissipative Kerr solitons in micro-resonators (T Herr, V Brasch, J. Jost, C. Wang, et al., 2014; V. Brasch et al., 2014). While initial work on microcombs demonstrated phase-locked states (T Herr, K Hartinger, et al., 2012; Jiang Li et al., 2012b; Pascal Del'Haye, Beha, et al., 2014; Pascal Del'Haye, Coillet, Loh, et al., 2015; Papp, Pascal Del'Haye, and S. A. Diddams, 2013) including pulse generation (Saha et al., 2013), solitons are both phase locked and, being pulses, can be readily broadened spectrally (T Herr, V Brasch, J. Jost, C. Wang, et al., 2014). Moreover,

¹Work presented in this chapter has been published in: "Soliton frequency comb at microwave rates in a high-Q silica microresonator", Optica, 2, 1078 (2015) and "Active capture and stabilization of temporal solitons in microresonators", Optics Letters, 41, 2037 (2016).

resonator dispersion can be engineered so as to create coherent dispersive waves that broaden the soliton comb spectrum within the resonator (V. Brasch et al., 2014; S. Wang et al., 2014). Both of these features can simplify the comb self-referencing process. Finally, solitons have a very predictable spectral envelope, which is useful in any application where individual comb teeth are accessed for measurement. Dissipative Kerr solitons balance dispersion with the Kerr nonlinearity while also balancing optical loss with parametric gain from the Kerr nonlinearity (Ankiewicz and Akhmediev, 2008; T Herr, V Brasch, J. Jost, C. Wang, et al., 2014). They have been observed in fiber resonator systems (Leo et al., 2010). In micro-resonators, these solitons have been observed in crystalline (T Herr, V Brasch, J. Jost, C. Wang, et al., 2014; Grudinin and N. Yu, 2015; W Liang, Eliyahu, et al., 2015) and in silicon-nitride based systems (V. Brasch et al., 2014). Crystalline system solitons have also been externally broadened to 2/3 of an octave enabling detection of the comb offset frequency (J. Jost et al., 2014).

To achieve self-referenced operation, these frequencies must be detectable and ideally occur at rates for which low-noise electronics is available. In this chapter, a comb of frequencies is generated by soliton mode locking in a silica resonator. The soliton pulse trains occur at a repetition frequency that is both readily detectable with commercial photo-detectors and that enables use of low-noise electronics. Moreover, the free-running phase noise of the detected pulse train is comparable to a good K-band signal source. Besides being the first observation of soliton frequency combs in a silica micro-resonator, control of soliton properties through a novel locking technique is demonstrated. This technique is used to controllably explore the soliton regime of operation, including measurement of soliton efficiency and existence power, as well as measurement of soliton power and power per line versus soliton pulse width for comparison with theory. Servo-locking also enables stable mode locking indefinitely as well as operation at optimal detuning with respect to comb pumping efficiency. The influence of the Raman process on the soliton is also observed and will be explored in detail in the next chapter. Finally, the silica resonator used here is fabricated on a silicon chip which enables reproducible avoided-mode-crossing control through micro-lithographic control of resonator geometry.

3.2 Silica wedge resonator and its characterization

The silica wedge resonators fabrication process were developed in our group in 2012 (Lee, T. Chen, et al., 2012) (see fig.3.1). The devices were fabricated using float-zone silicon wafers and exhibit a nearly constant finesse over a wide range of

diameters and have previously been applied for comb generation at free-spectral-range (*FSR*) values from 2.6 GHz to 220 GHz, including the formation of stable phase-locked comb states (Jiang Li et al., 2012b; Papp, Beha, et al., 2014). The details of the fabrication techniques were described in Lee, T. Chen, et al., 2012. In the 3 mm diameter devices with an *FSR* of 22 GHz prepared for soliton experiments, the intrinsic Q factors were characterized by linewidth measurement to lie near 400 million. To both characterize the soliton tuning range (see eq.(2.37)) and to provide a separate test of the Q factor, the threshold for parametric oscillation was measured and compared to eq. (2.5) (T. Kippenberg, S. Spillane, and KJ Vahala, 2004; Jiang Li et al., 2012b),

$$P_{\text{th}} = \frac{\pi n_0 \omega_0 S_{\text{eff}}}{4\eta n_2} \frac{1}{D_1 Q^2}, \quad (3.1)$$

where $S_{\text{eff}} \sim 60 \mu\text{m}^2$ is the effective mode area, n_0 is refraction index, n_2 is the Kerr coefficient, D_1 is the *FSR* in rad/s units, $\eta = Q/Q_{\text{ext}}$ characterizes the waveguide to resonator loading, where Q_{ext} is the external or coupling Q-factor and Q is the total Q factor (intrinsic loss and loading included), and ω_0 is the optical frequency. Typical measured threshold powers were around 2.5 mW and were consistent with the measured Q factors.

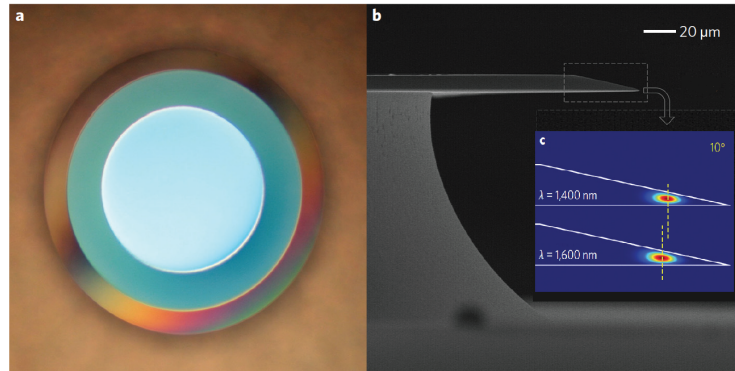


Figure 3.1: Imaging of silica wedge-resonator. (a) Top view of a 1-mm diameter of wedge resonator. (b) Scanning electron micrograph of the side view of wedge resonator. Insets are (c) simulated intensity profiles of fundamental modes. Pictures are from group alumni Dr. Hansuek Lee.

Mode spectrum measurement

It is critical to characterize mode spectrum of the microresonator prior to the experiment of soliton generation. To generate a soliton, the mode family that is phase locked to form the soliton pulse train must feature anomalous dispersion (T. Kippenberg, S. Spillane, and KJ Vahala, 2004) and also minimal distortion of the dispersion

caused by other mode families within the resonator (T Herr, V Brasch, J. Jost, Mirogorodskiy, et al., 2014). To characterize both mode family dispersion and avoided mode crossing behavior, mode frequencies were measured using a tunable laser that was calibrated with a fiber Mach-Zehnder interferometer (MZI). A typical mode spectrum measurement is presented in fig. 3.2 (a) and (b). The cavity resonance appears as Lorentz lineshape dip in transmission (green line), and MZI is a periodic function of laser frequency (red line).

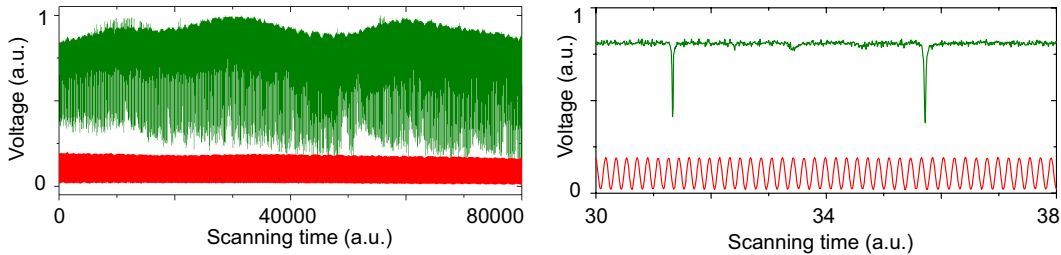


Figure 3.2: (a) Oscilloscope trace of ECDL laser scanning from 1550 nm to 1630 nm. The green line is the transmission and red line is the MZI reference. (b) A magnified figure of panel (a).

The MZI used in this experiment is a fiber interferometer with two unbalanced arms (Lu et al., 2011). A 50/50 fiber coupler splits the laser signal into two optical paths, with one path 5 meters longer than the other. They are then combined by a second 50/50 fiber coupler and sent to a photodetector. The MZI repetition frequency (the frequency difference between two adjacent maximums in MZI signal), $\Delta\omega_{\text{MZI}}$, is subject to fiber dispersion and must be calibrated carefully. The dispersion of MZI can be expressed in a mathematical form of $\Delta\omega_{\text{MZI}}(m) = \Delta\omega_{\text{MZI}0} + d_1 m + d_2 m^2/2$, where m is the number of MZI period relative to a center MZI peak (here we choose the center corresponding to 1550 nm), and d_1 and d_2 are the 1st and 2nd order dispersion of $\Delta\omega_{\text{MZI}}$. The calibration of $\Delta\omega_{\text{MZI}0}$, d_1 , d_2 will be introduced in detail later. The laser scanning time, T , can be associated with a laser frequency $\omega_{\text{MZI}}(m_T) = \sum_{m=0}^{m_T} \Delta\omega_{\text{MZI}}(m)$ relative to the frequency center ($m = 0$), where m_T corresponds to the number of MZI period between time at $m = 0$, T_0 and time T . In our experiment, we set $m = 0$ at the wavelength of 1550 nm, which is the pump laser wavelength in our soliton experiment. Finally, the resonance dips are identified in our "local-extrema-finding" program and each dip is associated with its laser scanning time T , and therefore, an optical frequency $\omega_{\text{MZI}}(m_T)$.

The microresonator mode frequency data are presented in fig.3.3(a) by plotting the *relative-mode-frequency*, $\Delta\omega_\mu \equiv \omega_\mu - \omega_0 - \mu D_1$ versus mode index μ , where

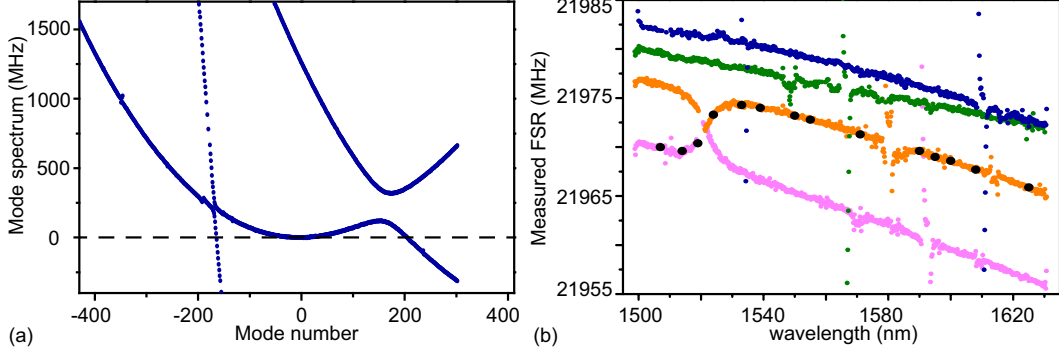


Figure 3.3: (a) Mode spectrum plot of a soliton forming mode in microresonator. $D_1/2\pi = 21.9733$ GHz. Mode numer zero corresponds to wavelength of 1550 nm. (b) FSR measurement of a microresonator. The FSR measured using MZI method is presented in color dots. Different colors correspond to different mode families. The FSR measured using EOM method are illustrated in black dot.

ω_0 and D_1 are specific to the soliton-forming mode family. ω_0 is the frequency of the mode (set to have index $\mu = 0$) that is optically pumped to produce the soliton, and D_1 is the FSR of the soliton-forming mode family at $\mu = 0$ (note: μ is a relative and not an absolute mode index). By plotting the data in this way the second- and higher-order dispersion of the soliton-forming mode family become manifest. A minor mode crossing and a major avoided mode crossing are apparent near $\mu = -180$ and $\mu = 180$. In addition, the microresonator FSR at different wavelengths (or mode number μ) can also be obtained with $D_1(\mu) = D_1 + \Delta\omega_\mu - \Delta\omega_{\mu-1}$, where D_1 , $\Delta\omega_\mu$ and $\Delta\omega_{\mu-1}$ are extracted from fig.3.3(a). The FSR versus wavelength is plotted in fig.3.3(b). Different colors correspond to different mode families. The FSR is a critical quantity in various microresonator experiments, including stimulated Brillouin scattering laser (Lee, T. Chen, et al., 2012) and Stokes soliton (Q.-F. Yang et al., 2017).

Finally, we discuss the calibration of MZI dispersion. One calibration method is to compare the resonator mode spectrum result with results from a secondary method. For this purpose, we measure the microresonator FSR using an electro-optics modulation (EOM) method (Jiang Li, Lee, Ki Youl Yang, et al., 2012; Ki Youl Yang et al., 2016). Only when the MZI parameters $\Delta\omega_{\text{MZI}0}$, d_1 and d_2 are accurate, can the FSR from two different methods equal each other in a wide range of wavelengths. In the EOM method, the input laser (frequency: f_p) is phase modulated in an electro-optics phase modulation before coupling to the microresonator. The modulator is driven by a microwave frequency (f_{eom}) and generates a pair of optical

sidebands at frequency $f_p \pm f_{\text{eom}}$. In a laser frequency scan, if f_{eom} equals the FSR of the cavity mode, then all three laser fields ($f_p - f_{\text{eom}}, f_p, f_p + f_{\text{eom}}$) will be on resonance with mode $\{\mu - 1, \mu, \mu + 1\}$ at the same time and only one resonance dip will show up in transmission. However, if the f_{eom} is slightly different from FSR, three resonance dips can be seen in transmission. In this way, by tuning f_{eom} to merge three transmission dips into one, the FSR of the mode is measured through f_{eom} . In addition, f_{eom} can be easily referenced to a Rb clock or other time standard, which represents an absolute calibration of FSR. The FSR measured with EOM method is plotted in black dots in fig.3.3(b). The uncertainty of this FSR measurement is limited by the resonance linewidth. For a resonator with $Q > 10^8$, the uncertainty is found to be $\sim \pm 100$ kHz. To determine the parameters of our MZI, we fit $\Delta\omega_{\text{MZI}0}$ to match the resonator FSR from two methods at 1550 nm, fit d_1 to match the slope of FSR at 1550 nm and d_2 to match the FSR far from 1550 nm. This fitting is valid because in the Taylor expansion of MZI dispersion, $\Delta\omega_{\text{MZI}0} \gg d_1 m \gg d_2 m^2 / 2$, where $m = 0$ correspond to 1550 nm. Using this method, we obtained $\Delta\omega_{\text{MZI}0}/2\pi = 39.9553$ MHz, $d_1/2\pi = 45$ mHz and $d_2/2\pi = -7.8 \times 10^{-8}$ Hz. With this set of parameters, the FSR from two methods are within ± 100 kHz difference. It shall be noted that the dispersion parameters of each MZI only need to be calibrated once unless there is a dramatic temperature change in the lab.

Mode spectrum optimization

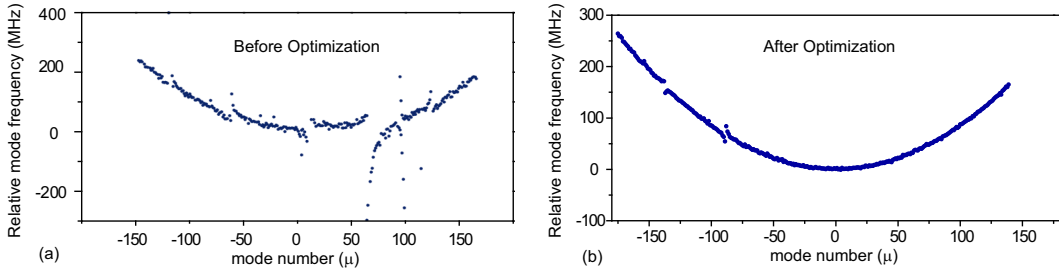


Figure 3.4: Typical mode spectrum of microresonator (a) before and (b) after optimization. The FSR of both resonators are 22 GHz.

Optical microresonator hosts many transverse mode families. They can interact with each other and distort the mode spectrum for soliton generation (T Herr, V Brasch, J. Jost, Mirgorodskiy, et al., 2014). One path to eliminate mode crossing is to reduce the number of transverse mode families in a resonator by limiting the cross-section area of the resonator. This has been successfully demonstrated in MgF (Grudinin, Huet, et al., 2016), SiN (Kordts et al., 2016) and recently our silica

resonator (Ki Y Yang et al., 2016). However, to eliminate mode crossing within soliton wavelength bandwidth, we can also manipulate the geometric parameters of a multimode microresonator so that no other transverse mode crosses the soliton mode in its wavelength range.

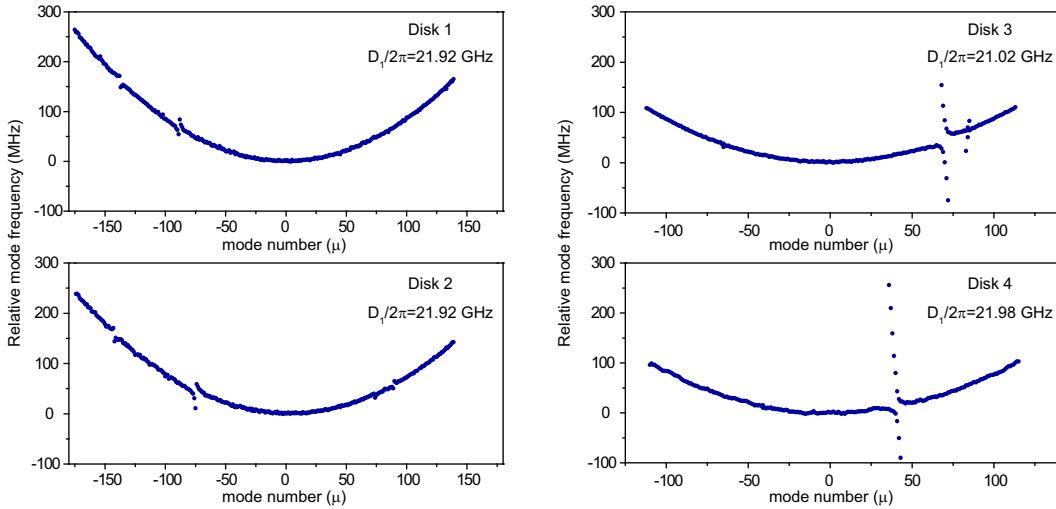


Figure 3.5: Reproducibility of mode spectrum. Disks in (a) and (b) were fabricated under the same condition. Disk in panel (c) is slightly different than disk in panel (d) in wet etching time.

In the effort of eliminating mode-crossing near 1550 nm, my colleague, Ki Youl Yang, fabricated near a hundred of resonators with a systematic control of the fabrication condition. The mode spectrum of these resonators were measured and the results were used to modify the fabrication design. The wedge resonator has three geometric parameters: resonator thickness, diameter and wedge angle. The thickness is determined in the silica oxidation process and it is $7.5 \mu\text{m}$ for all wedge resonators in our experiments. The diameter and wedge angle can be precisely controlled by wet etching time and photoresist adhesion (Lee, T. Chen, et al., 2012). By screening the wedge resonators, we find the combination of diameter and wedge angle that produces mode-crossing free spectrum at 1550 nm. In figure 3.4, we show the comparison of mode spectrum before (panel a) and after disk optimization (panel b). Despite a minor mode-crossing, the mode spectrum in panel b is readily for soliton generation. An important feature of the wedge resonator is that the mode spectrum is well reproducible. In fig. 3.5, disk 1 and 2 show almost identical mode spectrum and minor mode-crossing. In addition, the mode crossing wavelength can be tuned by disk diameter through controlling the wet etching time (disk 3 vs. disk 4). The ability to control mode spectrum is of critical importance in soliton

experiments (Xu Yi, Q.-F. Yang, Ki Youl Yang, Suh, et al., 2015; Q.-F. Yang et al., 2017; Q.-F. Yang et al., 2016; Xu Yi, Q.-F. Yang, X. Zhang, et al., 2016).

Transverse modes identification

²It is often instructive to know which transverse mode is being used for a microcomb experiment. To identify the spatial mode families of the soliton mode and the other mode families, a numerical simulation of the wedge resonator is used (Xu Yi, Q.-F. Yang, Ki Youl Yang, Suh, et al., 2015; Ki Youl Yang et al., 2016). The simulation used the Sellmeier equation for the refractive index of silica and commercial software COSMOL. The measured and simulated mode spectrum of one microresonator are illustrated in figure 3.6.

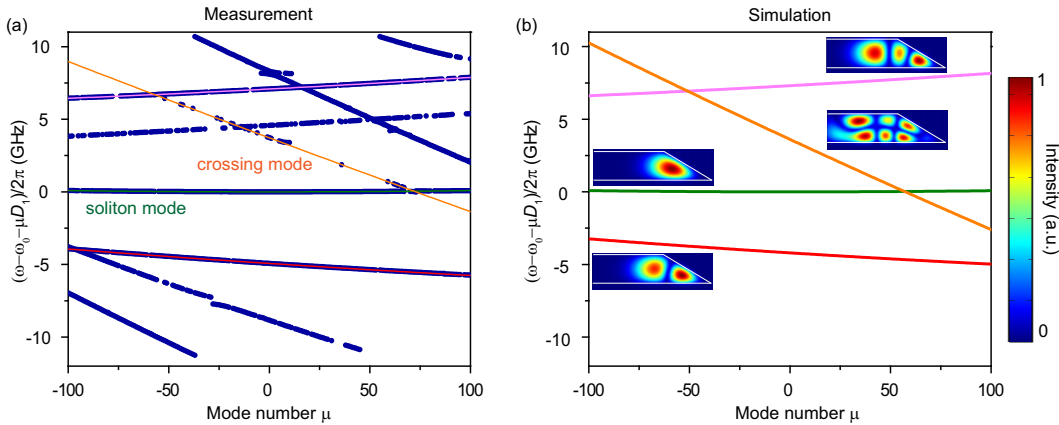


Figure 3.6: (a) Measured mode spectra (blue dots) and fitted lines. Green line represents fitting for soliton forming mode. Red and pink lines are fitted for another two high- Q modes. Orange line is fitted for a higher-order transverse mode. $D_1/2\pi$ is 22.0167 GHz. (b) Simulated mode spectra of four transverse electric (TE) modes. Cross-sectional images of the mode spatial intensity distributions are included as insets.

In the simulation, the geometry of the wedge resonator was first set to the following design parameters: 3 mm diameter, 30° wedge angle and 7.5 μ m silica thickness. These parameters were then slightly tuned to maximize the similarity of measured and simulated mode spectra. In the simulation presented in figure 3.6 (b), the resonator has diameter 2.9826 mm, wedge angle 30.7071° and oxide thickness 7.5154 μ m. The simulated mode spectrum is in reasonable agreement with the measurement. The soliton mode is identified as the fundamental transverse electric (TE) mode and the modes denoted by red, pink and orange lines are the TE10, TE20

²Ki Youl Yang and Xinbai Li performed the simulation. Results in this subsection have been published in the supplementary information of X. Yi et al, Nature Communications, 14869 (2017).

and TE21 mode. The mode spatial distribution in the simulation can be used to calculate the effective area of the transverse mode.

3.3 Active capture and locking of soliton

The soliton formation in microresonator is complicated by cavity thermal effect (Carmon, L. Yang, and Kerry Vahala, 2004). Solitons are formed when an optical pump is tuned from the blue side of a cavity resonance to the red side. Blue detuned operation is thermally stable so that parametric oscillation (T. Kippenberg, S. Spillane, and KJ Vahala, 2004; A. A. Savchenkov, A. B. Matsko, Strekalov, et al., 2004) and cascaded four-wave mixing (FWM) comb formation (T. J. Kippenberg, Ronald Holzwarth, and SA Diddams, 2011; P Del'Haye et al., 2007; A. A. Savchenkov, A. B. Matsko, Ilchenko, et al., 2008; Levy et al., 2010; Razzari et al., 2010; Papp and S. A. Diddams, 2011; W Liang, A. Savchenkov, et al., 2011; Jiang Li et al., 2012b; C. Y. Wang et al., 2013; Jung et al., 2013; Hausmann et al., 2014; Griffith et al., 2015) are readily achieved when the cavity dispersion is anomalous. The FWM process is required to seed the solitons. With continued pump tuning to the red side of the cavity resonance, their formation leads to abrupt, "step-like" features in the intracavity power (see fig. 3.7) (T Herr, V Brasch, J. Jost, C. Wang, et al., 2014) and an accompanying cavity tuning transient. Curiously, while the red-detuned regime is normally unstable, once formed, solitons actually reverse the thermal stability condition of the two thermal regimes. This happens because the average circulating soliton power increases with further red-detuning of the pump laser (i.e., opposite to the normal continuous-wave circulating power detuning dependence). This unusual detuning dependence of soliton power thereby enables red-detuned operation provided that the soliton state persists long enough so as to permit decay of the initial non-soliton (destabilizing) transient.

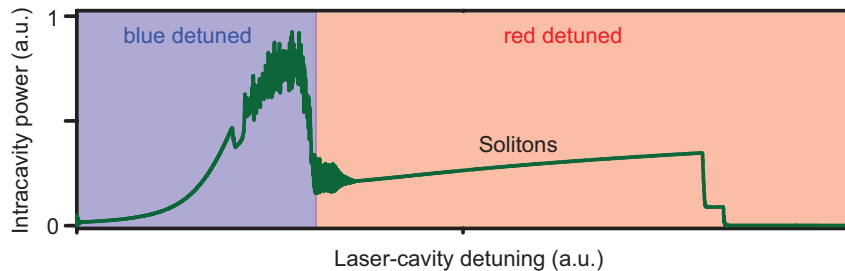


Figure 3.7: Simulated soliton steps with laser scans from laser-cavity blue-detuned to red-detuned regime.

Two passive methods have been demonstrated to overcome thermal destabilization

during soliton formation. In magnesium flouride resonators, where the thermal effect is relatively weak, the red-detuned soliton regime can be achieved by pump laser sweep rate control (T Herr, V Brasch, J. Jost, C. Wang, et al., 2014). In cases where there is a stronger thermal effect, the two-step "power kicking" protocol was developed in silicon nitride resonators (V Brasch et al., 2016) and has also been applied to our silica resonators (Xu Yi, Q.-F. Yang, Ki Youl Yang, Suh, et al., 2015). However, these passive approaches are challenging to implement, requiring a customized pump power time dependence. Also, excitation of a specific soliton state is not guaranteed and, significantly, the soliton power and pulse width still vary as a result of long term drift of the cavity and pump laser frequencies. Ultimately, these drifts result in loss of the soliton state when the cavity-pump detuning drifts to outside of the so-called soliton existence detuning range (AB Matsko et al., 2011; A. B. Matsko and Maleki, 2013; T Herr, V Brasch, J. Jost, C. Wang, et al., 2014; Xu Yi, Q.-F. Yang, Ki Youl Yang, Suh, et al., 2015).

The capture and stabilization method described here is simple to implement, relying on servo-control of the pump laser frequency by measuring the soliton average power. The key parameter in understanding this servo control method is the relative cavity-pump detuning, which for fixed cavity loading determines soliton power and pulse width. The one-to-one relationship between detuning and several soliton properties was recently noted to provide a way to provide long-term locking of the laser-cavity detuning (Xu Yi, Q.-F. Yang, Ki Youl Yang, Suh, et al., 2015). Specifically, the soliton power is given by the following expression (AB Matsko et al., 2011; A. B. Matsko and Maleki, 2013; T Herr, V Brasch, J. Jost, C. Wang, et al., 2014; Xu Yi, Q.-F. Yang, Ki Youl Yang, Suh, et al., 2015):

$$P_{\text{sol}} = \frac{2\eta S_{\text{eff}}}{n_2 Q} \sqrt{-2n_0 c \beta_2 \delta\omega}. \quad (3.2)$$

It is important to note that the typical frequency detuning values for soliton generation are in the range of 10s of cavity linewidths. As a result, it is not clear how conventional locking methods can be applied in these circumstances. On the other hand, leveraging the one-to-one dependence of soliton power on detuning given by eqn. (3.2) avoids the complexities associated with actual measurement of the detuning frequency itself.

The experimental setup in fig. 3.8(a) shows the resonator (a high-Q silica resonator described in references (Lee, T. Chen, et al., 2012; Xu Yi, Q.-F. Yang, Ki Youl Yang, Suh, et al., 2015)) pumped with a continuous-wave fiber laser amplified by

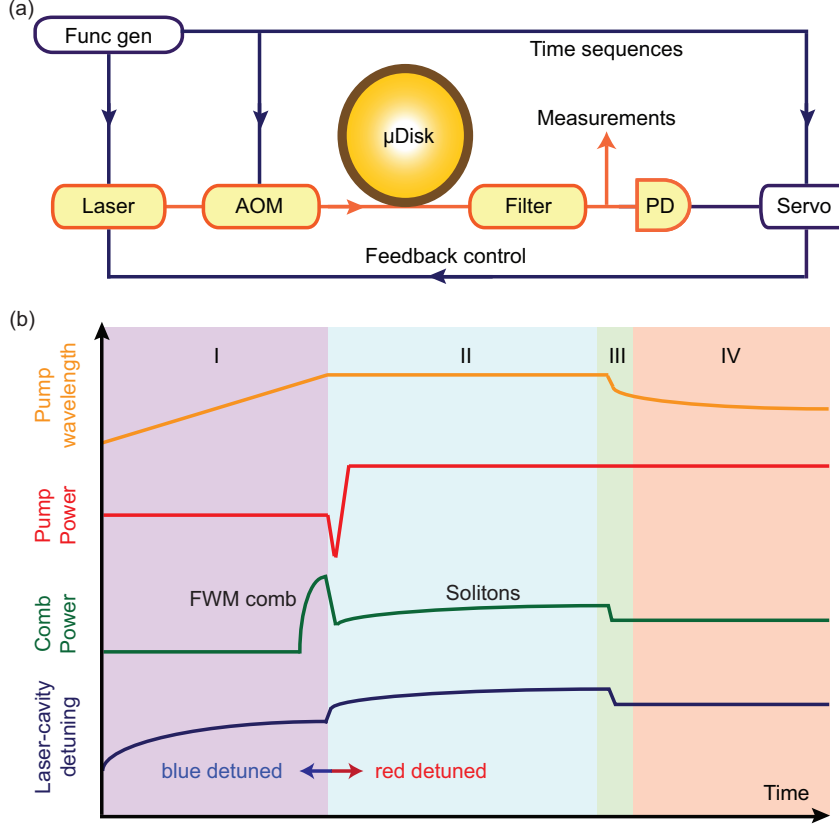


Figure 3.8: (a) Schematic of experimental setup. (b) Four phases of feedback-controlled soliton excitation: (I) pump laser scans into cavity resonance from blue-detuned side; (II) laser scan stops and pump power is reduced ($\sim 10 \mu\text{s}$) to trigger solitons, and then increased ($\sim 100 \mu\text{s}$) to extend soliton existence range; (III) servo-control is engaged to actively lock the soliton power by feedback control of laser frequency; (IV) lock sustains and solitons are fully stabilized. The cavity-pump detuning (vertical axis) is relative to the hot cavity resonant frequency.

an erbium-doped fiber amplifier. The high-Q resonators are 3 mm in diameter and produce solitons at a repetition frequency of approximately 22 GHz. The laser's frequency is piezo controlled by a function generator and also the servo box. An acoustic-optic modulator (AOM) is used to control the pump power coupled into the resonator. At the resonator output port, the comb power is separated from the pump power with a fiber Bragg grating filter and is sent to a photodiode (PD). An error signal is generated from the detected photocurrent after subtracting a set point in the servo control box. The complete setup configuration is shown in fig. 3.9.

The function generator produces signals to create a time sequence for all instruments. The time sequence is composed of four phases illustrated in fig. 3.8(b). The first two are similar to the "power kicking" technique (V Brasch et al., 2016) with the

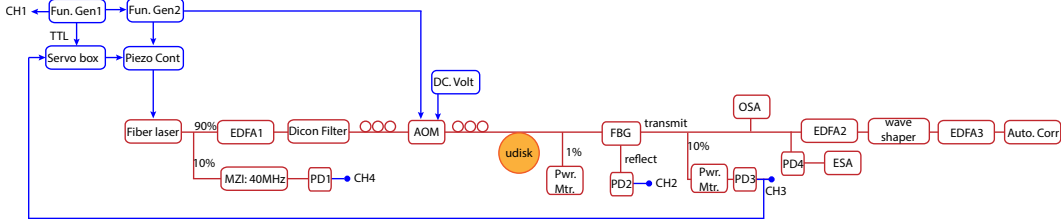


Figure 3.9: Complete schematic of soliton generation setup. Channel (CH) 1 to 4 are connected to a fast oscilloscope not showing in this figure.

exception that the precise shape of the pump power waveform is less important than when power kicking is applied alone. In phase I, the laser is first scanned into resonance from the blue side, causing FWM comb formation (T. J. Kippenberg, Ronald Holzwarth, and SA Diddams, 2011). In phase II, the laser stops scanning and the pump power is decreased over a few microseconds by controlling the acousto-optic modulator. This reduces the intracavity power so that the cavity resonance blue shifts due to the Kerr and thermal effects. At some point, the laser wavelength will reside on the red side of the cavity resonance where soliton formation is possible. The laser power is then ramped to a higher level. Ramp times ranging from $\sim 20 \mu\text{s}$ to $\sim 500 \mu\text{s}$ were used. Ramping the power extends the existence detuning range of the solitons given by $\delta\omega_{\max} = \pi^2 P_{\text{in}} / 16 P_{\text{th}}$ (A. B. Matsko and Maleki, 2013; T Herr, V Brasch, J. Jost, C. Wang, et al., 2014; Xu Yi, Q.-F. Yang, Ki Youl Yang, Suh, et al., 2015), where P_{in} and P_{th} are the pump power and parametric oscillation threshold (Xu Yi, Q.-F. Yang, Ki Youl Yang, Suh, et al., 2015). If the waveform used to control the pump ramp is carefully designed, then the soliton can be stabilized during this phase for extended periods. More typically, however, the soliton will be lost on account of the residual thermal transients and the associated cavity frequency drift, (i.e., cavity-pump detuning frequency drifts beyond the soliton existence range).

To overcome these transients, the servo control is activated in phase III using the function generator. The servo controls the laser frequency to maintain a setpoint for average soliton power. Significantly, the cavity-pump detuning is also locked because it determines the soliton power (see eqn. (3.2)). This frequency locking compensates the short term thermal transients that normally complicate soliton formation, as well as the long term thermal drift of the cavity and the pump laser. The net effect is that the soliton can be reliably captured and sustained indefinitely as illustrated in phase IV. For successful capture of soliton state the soliton free running time in phase II should be longer than the turn-on time of feedback loop. In

the present case it is limited by the speed of laser controller and is around $100\ \mu\text{s}$.

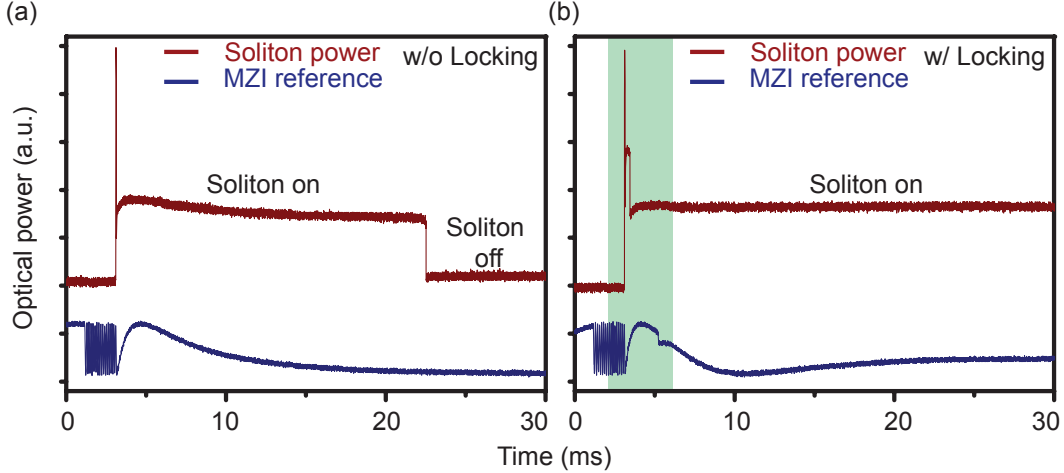


Figure 3.10: Demonstration of capture and locking of a soliton state. (a) Soliton excitation with "power kicking" but no active locking is shown. The soliton state destabilizes around 22ms due to thermal transients. Soliton power is shown in red and a Mach Zehnder (MZI) reference is in blue. (b) Soliton excitation with active locking is shown with conditions similar to panel (a).

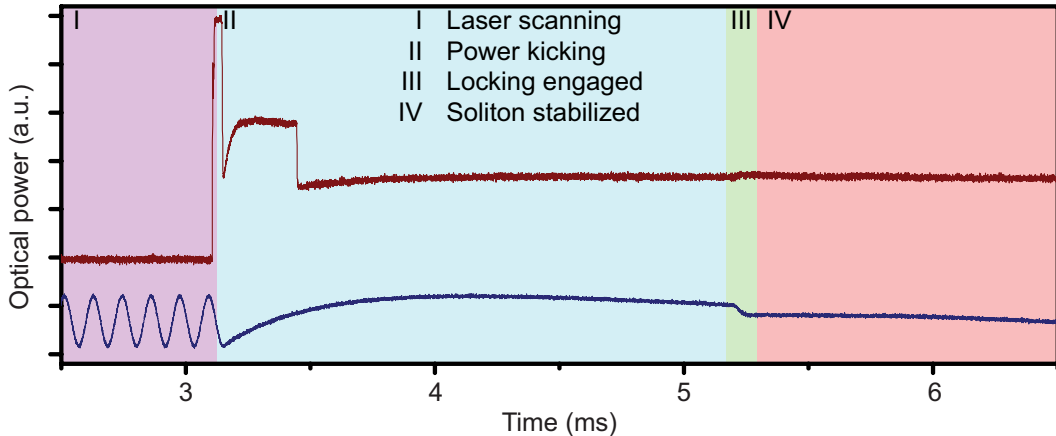


Figure 3.11: Zoom-in view of panel (b) in figure 3.10. The four phases are indicated using the same background color scheme as in fig. 3.9.

The demonstration of active capture and locking of a single soliton is presented in figures 3.10 and 3.11. The comb power is shown in red and a Mach-Zehnder interferometer (MZI) signal in blue is used to track the pump laser frequency (the free spectral range of the interferometer is 40 MHz). The MZI signal gives an indication of tuning of the pump relative to the interferometer (which is stable over the time period of the scan). Soliton excitation without active capture is shown in

fig. 3.10 (a). Here, the power kicking is employed and the soliton persists for about 20 ms before destabilizing. The MZI signal shows that the pump laser is thermally drifting during this period. In fig. 3.10 (b), the feedback loop is switched on around 2 ms after the power kicking. A zoomed-in view is provided in figure 3.11. During phase II, it is interesting to observe the transition from the FWM comb to the soliton step which is accompanied by an abrupt decrease in comb power at ~ 3.2 ms (red trace). Also, in the early part of phase II at ~ 3.5 ms, a further decrease in comb power indicates thermal drift from a two-soliton to a single soliton state. During phase III there is a jump in the MZI signal upon engaging the servo control (~ 5.2 ms) and stable comb power indicates the feedback loop is activated.

3.4 Soliton microcomb characterization

Soliton stability upon locking is confirmed by measuring optical spectra, microwave beatnote and by studying time-domain intensity autocorrelation. Figure 3.12 (b) shows the spectrum measured for a single-soliton state. The square of a hyperbolic secant function is also overlaid onto the spectrum to verify the characteristic single-soliton spectral shape. From this fitting the soliton pulse width τ_s is inferred to be 130 fs where the pulse shape is $\text{sech}^2(t/\tau_s)$. (Note: this definition of pulse width is $0.57 \times$ the FWHM width of the soliton pulse). The presence of small spurs in the spectrum of figure 3.12 (b) correlate with the appearance of avoided crossings in the mode dispersion spectrum in figure 3.12 (a).

Direct confirmation of single-soliton generation is provided by Frequency-Resolved Optical Gating (FROG) and autocorrelation traces (see figure 1d). In these measurements, the pump laser was suppressed by fiber Bragg filters and dispersion compensation of -1.5 ps/nm was applied using a programmable optical filter before the comb was amplified by an Erbium-doped fiber amplifier (EDFA). A pulse width of 250 fs with a pulse period of 46 ps is inferred from this data. The measured pulse width is larger than that fitted from optical spectrum (130 fs) due to the limited wavelength bandwidth of the optical pre-amplifier used in this measurement. The FROG data was also used to reconstruct the phase of the spectrum and showed a constant phase across the comb lines.

An important feature of the soliton states generated in this work is their detectable and stable repetition rate. Figure 3.14 contains phase noise spectra of the detected soliton fundamental repetition frequency measured using single solitons generated with three different resonators. The upper right inset of figure 3.14 is a typical

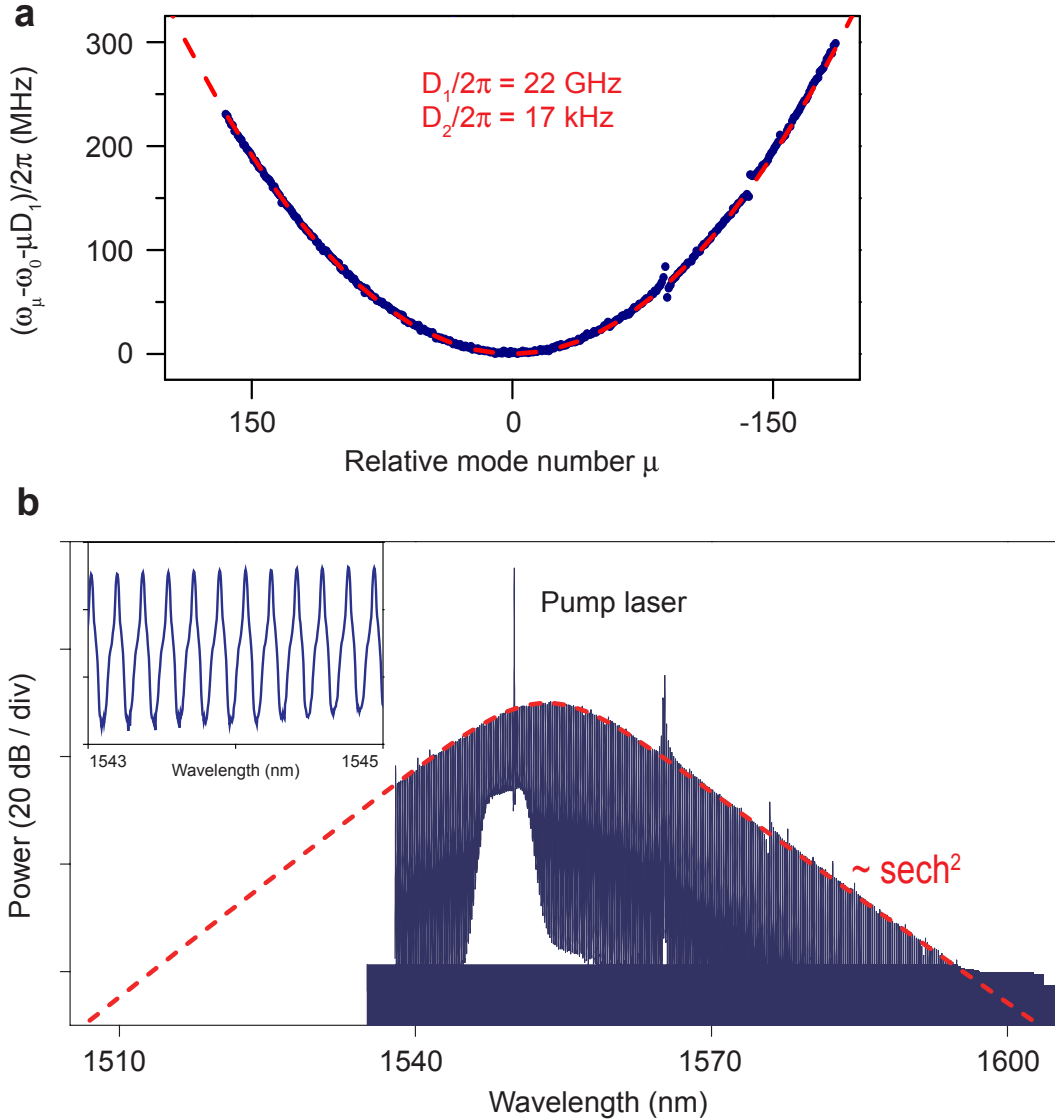


Figure 3.12: Optical spectra of soliton frequency comb. (a) The mode spectrum of the soliton-forming mode family. (b) Optical spectrum of single soliton state is shown with a sech^2 envelope (red dashed line) superimposed for comparison. The pump laser is suppressed by 20 dB with an optical Bragg filter. Inset is a zoomed-in spectrum between 1543 nm and 1545 nm.

radio frequency spectrum of the fundamental repetition frequency. The repetition frequency can be seen to be 21.92 GHz (resolution bandwidth is 10 kHz) and has an excellent stability that is comparable to a good K-band microwave oscillator. For example, one of the devices measured has a phase noise level of -100 dBc/Hz at 10 kHz offset (referenced to a 10 GHz carrier frequency). Some of the variations observable in these spectra are not fundamental, but are related to pump laser noise

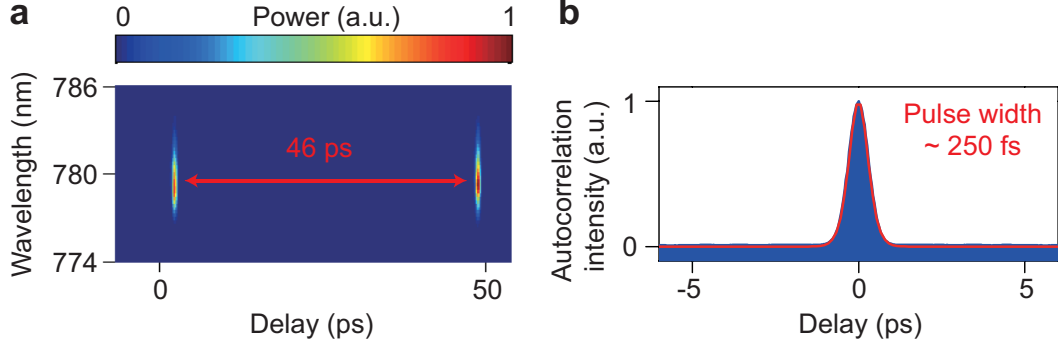


Figure 3.13: FROG (a) and autocorrelation trace (b) of the soliton state in fig. 3.12. The optical pulse period is 46 ps and the fitted pulse width is 250 fs (red solid line).

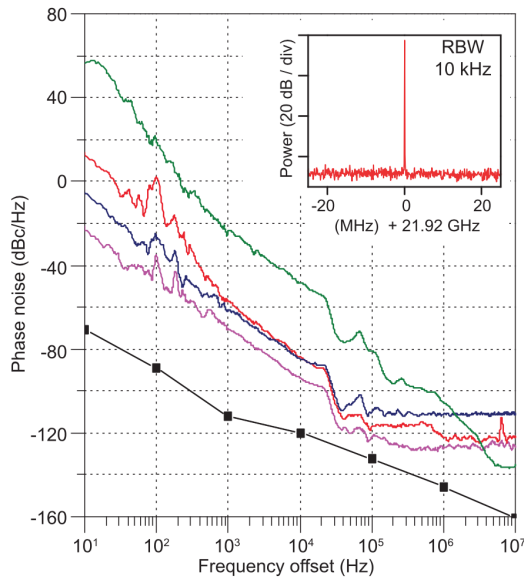


Figure 3.14: Detected phase noise and electrical spectra for three devices. Phase noise spectral density function plotted versus offset frequency from the detected soliton repetition frequency of three different devices. A Rohde Schwarz phase noise analyzer was used in the measurement. Inset shows the electrical spectrum of the soliton repetition frequency (21.92 GHz) for one device. The other devices had similar spectra with repetition frequencies of 22.01 and 21.92 GHz. The phase noise of the fiber pump laser is shown in green and was generated by mixing 2 nominally identical pump lasers to create a 2.7 GHz electrical beatnote. Several features in the pump laser phase noise are reproduced in the soliton phase noise (see features near and above 20 kHz). The black line connecting square dots is the measurement floor of the phase noise analyzer.

and avoided mode crossing (see Chapter VII). For example, the step feature in the spectrum near 20kHz offset frequency also appears in the frequency noise of the

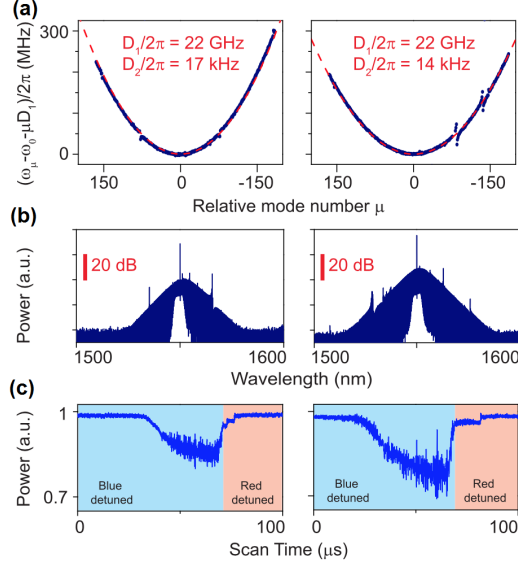


Figure 3.15: Three devices with corresponding mode dispersion and soliton data. (a,b) The mode dispersion spectra and soliton spectra are presented for two of the devices measured in figure 3.14. The third device in figure 3.14 is from figure 3.12. (c) Pump power transmission is plotted versus tuning across a resonance used to generate the soliton spectra in (b). The data show the formation of steps as the pump tunes red relative to the resonance. Both blue-detuned and red-detuned operation of the pump relative to the resonance are inferred from generation of an error signal using a Pound-Drever-Hall system operated open loop.

pump laser (see green curve in figure 3.14).

The ability to reproduce mode family dispersion characteristics in different resonators was investigated. Figure 3.15 (a) and (b) give the results of mode family dispersion measurements and soliton optical spectra on two resonators that are close in size and shape to the device in figure 3.12. There is a high level of consistency in the magnitude of the dispersion and also minimal presence of mode crossings in the measured spectra. This level of consistency was sufficient across many devices to provide ready observation of soliton steps. Nonetheless, there are observable variations in the nature of soliton steps formed in scanning the resonators. The corresponding soliton steps under pump frequency scan are shown in figure 3.15 (c). Also, the microwave phase noise spectra in figure 3.14 were measured on soliton trains using these same three devices and exhibit slight differences.

3.5 Soliton properties: measurement vs. theory

For steady-state soliton generation, it is possible to servo control the laser-cavity detuning. Several soliton properties depend upon the detuning, $\delta\omega \equiv \omega_o - \omega_p$ and it is therefore desirable to control the detuning of the pump relative to the cavity. The technique demonstrated here is identical with the active capture and locking technique described previously. It leverages the dependence of comb power and $\delta\omega$ in eq. (3.2) so that $\delta\omega$ can be servo locked by requiring the comb power to hold a fixed set point. Indeed, implementation of this locking method is a test of the theoretical independence of comb power and pump power. The servo control also has the effect of fixing the soliton pulse width (see eq. (2.29)),

$$\tau_s = \sqrt{-\frac{c\beta_2}{2n_0\delta\omega}}. \quad (3.3)$$

To demonstrate the servo control method and to also test theoretical predictions, several soliton properties were measured. Comb power and the maximum power per comb line were measured at a series of detuning values, $\delta\omega/2\pi$, estimated to range from 12.8 MHz ($\tau_s=187$ fs) to 29.6 MHz ($\tau_s=123$ fs) or approximately 13 to 30 cavity linewidths. At each point the soliton spectrum was also recorded which enables calculation of the soliton pulse width τ_s . The results of these measurements are compiled in figure 3.16 (a). Also, figure 3.16 (b) shows the soliton spectrum measured at the detuning limits presented in figure 3.16 (a). The dashed lines in figure 3.16 (a) give the predicted comb power and maximum comb line power based on the following expressions for comb power and the comb power spectral envelope (T Herr, V Brasch, J. Jost, C. Wang, et al., 2014; Wabnitz, 1993; A. B. Matsko and Maleki, 2013),

$$P_{\text{sol}} = -\frac{2c\eta S_{\text{eff}}\beta_2}{n_2 Q} \frac{1}{\tau_s}, \quad (3.4)$$

$$P(\Delta\omega) = -\frac{\pi c}{2} \frac{\eta S_{\text{eff}}\beta_2}{n_2} \frac{D_1}{Q} \text{sech}^2\left(\frac{\pi\tau_s}{2}\Delta\omega\right), \quad (3.5)$$

where $\Delta\omega$ denotes the comb tooth frequency relative to the pump frequency. Note that the peak power of the spectral envelope (i.e. maximum comb tooth power) is determined entirely by the cavity properties. This feature is apparent in both the data in figure 3.16 (a) and the spectra in figure 3.16 (b).

In units of cavity linewidth, the predicted maximum detuning for soliton existence is given by $\delta\omega_{\text{max}} \equiv \pi^2 P_{\text{in}}/16P_{\text{th}}$ (T Herr, V Brasch, J. Jost, C. Wang, et al., 2014;

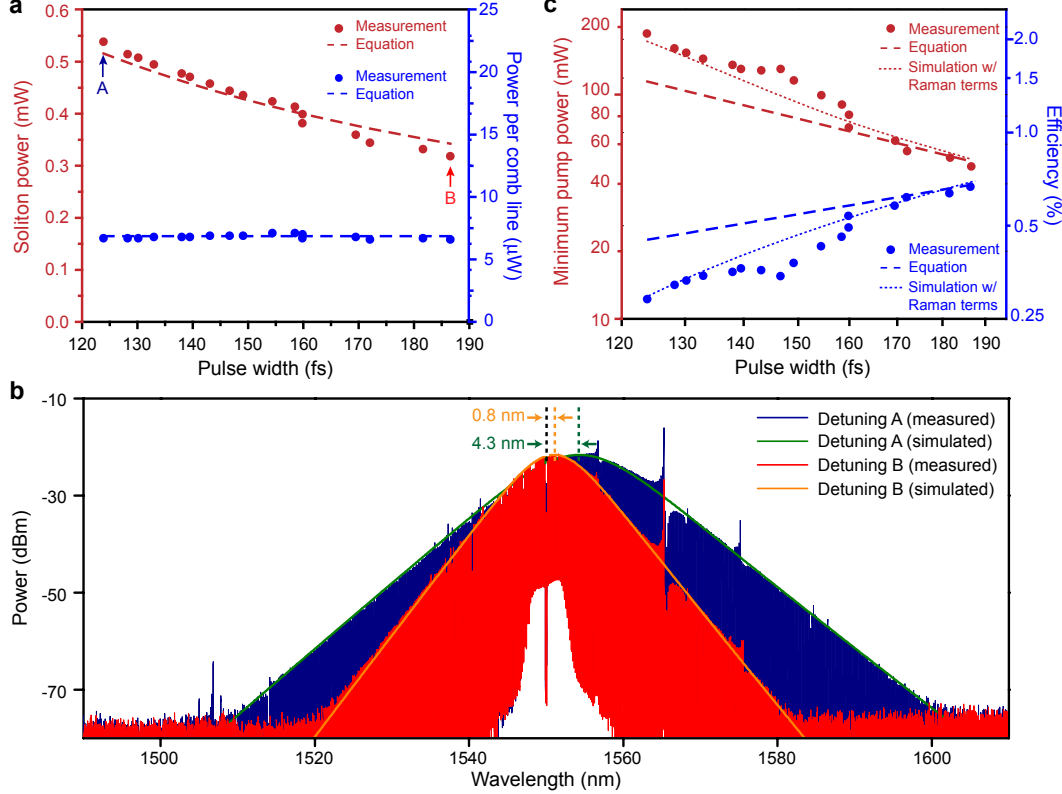


Figure 3.16: Control of soliton properties. (a) Measured soliton comb output power is plotted versus measured soliton pulse width (red points) with comparison to eq. (3.4) (dashed red line). The measured power per central comb line is plotted versus pulse width (blue points) with comparison to eq. (3.5) (dashed blue line). (b) The observed soliton spectra at the limits of the measurement in panel a is shown (see arrows A and B in panel a). Solid orange and green curves are simulations using the Lugiato Lefever equation including Raman terms. The indicated wavelength shifts between the pump and the centroid of the soliton spectrum result from Raman interactions with the soliton. The location of the pump line for both spectra is indicated by the dashed black line and has been suppressed by filtering. (c) Measured minimum pump power for soliton existence is plotted versus measured soliton pulse width (red points) with comparison to eqn. (3.6) (dashed red line). Measured efficiency is plotted versus measured soliton pulse width (blue points) with comparison to eqn. (3.7) (dashed blue line). Simulation using Lugiato Lefever equation including Raman terms improves agreement with data (small dashed red and blue lines).

Wabnitz, 1993; A. B. Matsko and Maleki, 2013) (see eq. (2.38)). This power dependence explains why increased pump power is effective in providing stable, non-locked soliton operation. At higher pumping powers, the solitons can survive over a wider range of tuning values as the pump laser frequency drifts relative to

the cavity resonant frequency. However, as noted above, it is preferable to prevent this relative drift. In addition to the reasons mentioned in the previous section, locking of the detuning frequency, $\delta\omega$, enables operation at a lower (and hence more efficient) pump power setting that is close to the existence power limit for solitons of a desired pulse width.

To measure the minimum existence power, $\delta\omega$ was held constant while pump power was reduced to the point of drop-out of the soliton pulse train. Both this power level and the soliton spectrum were recorded near the point of drop-out. $\delta\omega$ was then reset to a new value and the measurement repeated. Figure 3.16 (c) gives the minimum power measured this way plotted versus the pulse width (as before calculated from the soliton spectrum). Substituting for $\delta\omega$ in eq. (3.3) using $\delta\omega_{max}$ gives the following expression for minimum pump power for soliton existence as a function of pulse width, (T Herr, V Brasch, J. Jost, C. Wang, et al., 2014; Wabnitz, 1993; A. B. Matsko and Maleki, 2013):

$$P_{in}^{\min} = -\frac{2c}{\pi} \frac{A_{eff}\beta_2}{\eta n_2 \tau^2} \frac{1}{QD_1}. \quad (3.6)$$

This expression is plotted in figure 3.16 (c) (dashed red line). A deviation from the predicted dependence is observed. Improved agreement with the data is provided by a simulation (small dashed red line) using the Lugiato-Lefever equation (Lugiato and Lefever, 1987; AB Matsko et al., 2011; Chembo and Menyuk, 2013; T Herr, V Brasch, J. Jost, C. Wang, et al., 2014; A. B. Matsko and Maleki, 2013) (LLE) augmented by Raman terms (Agrawal, 2007; Changjing Bao et al., 2014). In this analysis, a Raman time constant of 2.4 fs was extracted by fitting the data. This time constant closely agrees with a value of 3 fs measured for silica optical fiber (Atieh et al., 1999). The contribution of the Raman terms is both predicted and measured to be stronger for shorter pulses (or equivalently larger $\delta\omega$). These observations are also consistent with modeling which shows modifications to soliton efficiency as a result of the Raman process (Changjing Bao et al., 2014).

It is interesting that the predicted soliton power and power per line do not require a Raman correction (see figure 3.16 (a)). The Raman correction primarily influences the temporal phase of the soliton pulse and not the amplitude (Karpov, Hairun Guo, Kordts, Victor Brasch, M. Pfeiffer, et al., 2015). It would therefore be expected to alter the existence condition which is associated with the phase of the soliton field, and not the power per line or overall comb power.

All of the soliton spectra observed in this work were shifted to the red relative to

the pump wavelength. Raman interaction with dissipative Kerr solitons has recently been shown to cause such self-shifting of the spectrum (Mitschke and Mollenauer, 1986; J. P. Gordon, 1986; Karpov, Hairun Guo, Kordts, Victor Brasch, M. Pfeiffer, et al., 2015). The effect has been observed in silicon nitride resonators (Karpov, Hairun Guo, Kordts, Victor Brasch, M. Pfeiffer, et al., 2015). Like the correction to the minimum power described above, this shift is stronger for shorter pulses and larger detuning frequencies. Shifted soliton spectra can be produced by several mechanisms (L. Zhang et al., 2014) besides Raman effect, including soliton recoil caused by dispersive wave generation (V Brasch et al., 2016). There was no evidence of dispersive wave generation at shorter wavelengths in this work. Consistent with other reports (Karpov, Hairun Guo, Kordts, Victor Brasch, M. Pfeiffer, et al., 2015) the Raman-augmented LLE simulation explains the soliton spectral shift observed here (see orange and green curves in figure 3.16 (b)).

Control of the pump-resonator detuning frequency enables stable operation near an optimal pumping efficiency limit. Defining efficiency (Changjing Bao et al., 2014) as the soliton power divided by the minimum pump power for soliton existence gives the following simple expression:

$$\Gamma \equiv \pi\eta^2 D_1 \tau. \quad (3.7)$$

Comparison of this prediction with measurement is provided in figure 3.16 (c) ($\eta = 0.29$ in this measurement). A deviation between the simple formula (3.7) and the data at small pulse widths occurs on account of Raman effects and has been corrected in the figure (small dashed blue line) using the Raman augmented LLE result. The Raman augmented LLE equation will be discussed in further detail in the next chapter.

An important benefit of the feedback control presented here is that it provides a convenient way to stabilize the mode-locked system indefinitely. For example, the system was operated continuously for over 24 hours. For over 19 hours of this period comb properties were recorded and are presented in figure 3.17.

3.6 Summary

In this chapter, we have demonstrated mode spectrum characterization, soliton generation and soliton characterization. These together formed the foundation for the work in the following chapters (IV to VII). The ability to generate solitons on a chip at rates commensurate with detectors and low-noise electronics is an essential step in the ultimate goal of a fully-integrated comb system. Besides soliton generation,

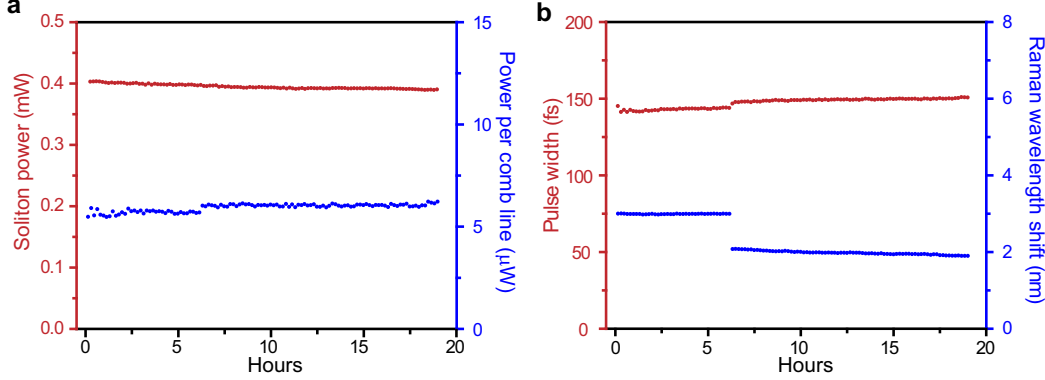


Figure 3.17: Continuous soliton measurement over 19 hours. (a) Soliton power and central comb line power are plotted versus time in hours. The soliton power experiences a slow drift to lower values which is attributed to a slow variation in either the power set point of the electronic control or in the detected power (perhaps due to temperature drift). Central comb line power is approximately constant over the measured period with the exception of a small step increase around 6 hours. This could be associated with anything that changes the resonator coupling efficiency, the resonator Q , or both. Since the resonator is taper coupled any kind of mechanical shock could introduce such a step change in these quantities. (b) Pulse width and Raman self shift (defined as the wavelength center of the soliton spectrum less the pump wavelength) are plotted versus time in hours. A step in these quantities is recorded at the identical moment to that recorded for the central comb line power. It is interesting to note that because soliton power is feedback controlled, from equation (3.2) a step increase (decrease) in coupling η (Q) would be accompanied by a compensating decrease (increase) in pump detuning. From equation (3.3), this feedback controlled step in detuning would cause an increase in the soliton pulse width (and decrease in the Raman shift) as observed in the recorded data of panel b. Finally, the operation of the soliton comb proceeded for an additional 5 hours beyond the record presented in this figure. During the additional 5 hours other measurements were performed that required disabling the data recording.

the silica wedge resonator platform has been used for ultra-narrow linewidth laser sources (Jiang Li et al., 2012a; Loh et al., 2015), high-Q reference cavities (Lee, Suh, et al., 2013) and continuum generation (Oh et al., 2014). These elements are required in both self-referenced combs as well their application to clocks, high-stability microwave sources, and optical synthesizers. The results presented here therefore add to this suite of technologically compatible devices.

Chapter 4

SOLITON SELF-FREQUENCY SHIFT AND EFFICIENCY IN MICRORESONATOR

4.1 Introduction

¹ The frequency shift of the soliton envelope has been observed in several micro-cavity systems (Karpov, Hairun Guo, Kordts, Victor Brasch, M. H. Pfeiffer, et al., 2016; Xu Yi, Q.-F. Yang, Ki Youl Yang, Suh, et al., 2015). Soliton interaction with the Raman nonlinearity causes the so-called self-frequency-shift (SFS). In optical fiber transmission, this effect causes the soliton's central frequency to experience increasing redshifting with propagation distance (Mitschke and Mollenauer, 1986). Intuitively, this is understood as a continuous energy transfer from the blue to red side of the soliton spectrum that is mediated by the Raman interaction (J. P. Gordon, 1986). The effect is of practical importance in supercontinuum generation using optical fibers (Dudley, Genty, and Coen, 2006). It has also been used in difference frequency generation of mid-IR frequency combs (Gambetta, Ramponi, and Marangoni, 2008). Recently, the Raman self-frequency-shift has been numerically modeled (Milián et al., 2015) and observed to influence DKC solitons (Karpov, Hairun Guo, Kordts, Victor Brasch, M. H. Pfeiffer, et al., 2016; Xu Yi, Q.-F. Yang, Ki Youl Yang, Suh, et al., 2015). Here, rather than producing a continuously increasing red shift, the Raman effect produces a constant frequency offset between the optical pump and the soliton spectral maximum (i.e., a frequency locked Raman soliton (Milián et al., 2015)). Without the Raman self-frequency-shift, the optical pump would be centered on the soliton comb spectrum (at the spectral maximum). Instead, the soliton spectral maximum is red-shifted away from the pump. The amount of shift increases with soliton peak power and so far has been numerically calculated (Karpov, Hairun Guo, Kordts, Victor Brasch, M. H. Pfeiffer, et al., 2016; Milián et al., 2015; Xu Yi, Q.-F. Yang, Ki Youl Yang, Suh, et al., 2015) by solving the Lugiato LeFever equation (Lugiato and Lefever, 1987).

In this chapter, a perturbed Lagrangian approach is used to derive simple analytical expressions for the self-frequency-shift and the soliton efficiency. The predicted dependences of these quantities on soliton pulse width are compared with measure-

¹Work presented in this chapter has been published in "Theory and measurement of the soliton self-frequency shift and efficiency in optical microcavities", Optics Letters, 41, 3419 (2016).

ments in a high-Q silica microcavity. The Raman time constant in silica is also inferred. Analytical expressions for the Raman self-frequency-shift and soliton efficiency greatly simplify the prediction of soliton behavior over a wide range of microcavity platforms.

4.2 Raman interaction

The interaction between solitons and the Raman process has been studied in optical fibers using pulse propagation equations (Headley and Agrawal, 1996; Agrawal, 2007). This approach is extended to study the SFS process in microresonators here. The Kerr and Raman interactions can be unified into a single nonlinear term in the pulse propagation equation ((Agrawal, 2007)):

$$\frac{\partial E}{\partial z} + \alpha E + \beta_1 \frac{\partial E}{\partial t} + \frac{i\beta_2}{2} \frac{\partial^2 E}{\partial t^2} = i\gamma E(z, t) \int_0^\infty R(t') |E(z, t - t')|^2 dt', \quad (4.1)$$

where E is the pulse field in optical fiber and $|E|^2$ is normalized to optical power, α is the linear loss, β_1 and β_2 are the group velocity and group velocity dispersion constant for optical fiber. γ and $R(t)$ at the right hand side of eq. (4.1) are the nonlinear coefficient and the normalized nonlinear response function ($\int_0^\infty R(t)dt = 1$). The nonlinear coefficient in optical fiber can be shown as $\gamma = n_2 \omega_0 / c S'_{\text{eff}}$, where n_2 is the Kerr refractive index, and S'_{eff} is the effective mode area of optical fiber (Agrawal, 2007). The nonlinear response function $R(t)$ can be decomposed as

$$R(t) = (1 - f_R)\delta(t) + f_R h_R(t), \quad (4.2)$$

where the δ -function term represents the fast electronic response (Kerr effect) and f_R is the fractional contribution from the Raman effect. $h_R(t)$ is the normalized Raman response function ($\int_0^\infty h_R(t)dt = 1$) and is determined by the interaction between light and vibration of silica molecules.

When the pulse width is much longer than Raman response time (~ 12 fs in silica), equation (4.1) can be further simplified by applying this Taylor expansion:

$$|E(z, t - t')|^2 \approx |E(z, t)|^2 - t' \frac{\partial |E(z, t)|^2}{\partial t}. \quad (4.3)$$

Insert eq. (4.2) and eq. (4.3) into the right-hand side (RHS) of eq. (4.1), and we have

$$\begin{aligned} RHS &= i\gamma |E(z, t)|^2 E(z, t) - i\gamma E(z, t) \frac{\partial |E(z, t)|^2}{\partial t} \int_0^\infty f_R h(t') t' dt' \\ &= i\gamma |E|^2 E - i\gamma \tau_R E \frac{\partial |E|^2}{\partial t}, \end{aligned} \quad (4.4)$$

where we have used the definition of Raman shock time $\tau_R = \int_0^\infty f_R h(t') t' dt'$.

This treatment of pulse propagation in optical fiber can be directly transformed to our soliton equation in microresonator by using $t = -\phi/D_1$. The soliton LLE equation (eq. (2.8)) is then converted into

$$\frac{\partial A(\phi, T)}{\partial T} = -\left(\frac{\kappa_A}{2} + i\delta\omega\right)A + i\frac{D_2}{2}\frac{\partial^2 A}{\partial\phi^2} + f + ig|A|^2A + ig\tau_R D_1 A \frac{\partial|A|^2}{\partial\phi}. \quad (4.5)$$

Equation (4.5) is the LLE equation augmented by the Raman shock term and it is valid when the soliton pulse width τ_s is much longer than the Raman response time.

4.3 Theory of soliton self-frequency shift in microresonator

When including self-frequency shift, the ansatz of soliton could be modified as

$$A(t, T) = B \operatorname{sech}\left(\frac{t - t_c}{\tau_s}\right) e^{-i\Omega(t-t_c)+i\varphi} = A(\phi, T) = B \operatorname{sech}\left(\frac{\phi - \phi_c}{\phi_\tau}\right) e^{i\Omega_\phi(\phi-\phi_c)+i\varphi}, \quad (4.6)$$

where t is the fast time frame and $t = -\phi/D_1$. The frequency shift of the soliton envelope is represented by a frequency oscillation term in the soliton phase. The amount of frequency shift is Ω . In addition, the frequency shift would couple to soliton group velocity and soliton center position (ϕ_c) through dispersion. Finally, the parameters in fast time frame and ϕ -frame are related, as $\Omega_\phi = -\Omega/D_1$ and $t_c = -\phi_c/D_1$.

Similar to Chapter 2, we could use Lagrangian perturbation method to derive the equations of motion for self-frequency shift Ω and other soliton parameters. The Lagrangian density for eq. (4.5) is identical to that of the LLE equation, and the additional term of the Raman effect is treated as perturbation:

$$\mathcal{L} = \frac{1}{2}(A^* \frac{\partial A}{\partial T} - A \frac{\partial A^*}{\partial T}) + i\frac{D_2}{2} \left| \frac{\partial A}{\partial\phi} \right|^2 - \frac{i}{2}g|A|^4 + i\delta\omega|A|^2, \quad (4.7)$$

$$\mathcal{R} = -\frac{\kappa}{2}A + f + ig\tau_R D_1 A \frac{\partial|A|^2}{\partial\phi}. \quad (4.8)$$

The Lagrangian can be calculated by integration of the Lagrangian density over ϕ ,

$$L = \int \mathcal{L} d\phi = 2iB^2\phi_\tau \left(\frac{D_2}{6\phi_\tau^2} - \frac{gB^2}{3} + \delta\omega + \frac{D_2\Omega_\phi^2}{2} - \Omega_\phi \frac{\partial\phi_c}{\partial T} + \frac{\partial\varphi}{\partial T} \right), \quad (4.9)$$

where we have used the soliton ansatz in eq. (4.6). Insert eq. (4.6), (4.8) and (4.9) into the Euler-Lagrangian equation (eq. (2.24)),

$$\frac{\partial L}{\partial r_j} - \frac{d}{dT} \frac{\partial L}{\partial \dot{r}_j} = \int (R \frac{\partial A^*}{\partial r_j} - R^* \frac{\partial A}{\partial r_j}) d\phi, \quad (4.10)$$

and we arrive at the equations of motion of soliton parameter B , ϕ_τ , ϕ_c , Ω_ϕ and φ :

$$\frac{\Omega}{D_1} \frac{\partial \phi_c}{\partial T} - \frac{\partial \varphi}{\partial T} - \delta\omega - \frac{D_2 \Omega^2}{2D_1^2} - \frac{D_2}{6\tau_s^2 D_1^2} + \frac{2}{3} g B^2 = 0 \quad (4.11)$$

$$\frac{\Omega}{D_1} \frac{\partial \phi_c}{\partial T} - \frac{\partial \varphi}{\partial T} - \delta\omega - \frac{D_2 \Omega^2}{2D_1^2} + \frac{D_2}{6\tau_s^2 D_1^2} + \frac{1}{3} g B^2 = 0 \quad (4.12)$$

$$\frac{\partial(B^2 \tau_s \Omega)}{\partial T} = -\kappa B^2 \tau_s \Omega - \frac{8g \tau_R B^4}{15\tau_s} \quad (4.13)$$

$$\frac{\partial \phi_c}{\partial T} = \frac{D_2}{D_1} \Omega \quad (4.14)$$

$$\frac{\partial(B^2 \tau_s)}{\partial T} = -\kappa B^2 \tau_s + f \cos \varphi B \tau_s \pi \operatorname{sech}\left(\frac{\pi \Omega \tau_s}{2}\right), \quad (4.15)$$

where we have substituted $\Omega_\phi = -\Omega/D_1$ and $\tau_s = \phi_\tau/D_1$. Subtracting eq.(4.11) from eq.(4.12) yields

$$B \tau_s = \sqrt{\frac{D_2}{g D_1^2}}, \quad (4.16)$$

which is identical to the non-Raman result in eq. (2.30). Equation (4.16) indicates that the balance between Kerr (soliton peak power) and dispersion (soliton pulse width) is preserved in the presence of the Raman effect. This also explains the agreement between the measurement in fig. 3.16 (a) and equations from the non-Raman derivation.

In steady state, insert eq. (4.14) and (4.16) to eq. (4.12), and we have

$$\delta\omega = \frac{D_2}{2D_1^2} \left(\frac{1}{\tau_s^2} + \Omega^2 \right). \quad (4.17)$$

Equation. (4.17) describes the general relation among cavity-laser detuning, pulse width and soliton frequency shift. The derivation of this equation does not rely on the Raman shock term and therefore can be applied to the soliton frequency shift caused by other effects, e.g. dispersive wave recoil.

The soliton frequency shift Ω can be obtained by the steady state solution of eq. (4.13) and eq. (4.16),

$$\Omega = -\frac{8\tau_R D_2}{15\kappa D_1^2 \tau_s^4} = -\frac{8D_2 Q \tau_R}{15\omega_0 D_1^2 \tau_s^4} \frac{1}{\tau_s^4} = \frac{8c\tau_R Q \beta_2}{15n_0 \omega_0} \frac{1}{\tau_s^4}, \quad (4.18)$$

where we have used $Q = \omega_0/\kappa$ and $\beta_2 = -n_0 D_2/c D_1^2$. In addition, the steady state solution of eq. (4.15) gives the soliton minimum pump power and efficiency at

$$|\cos\varphi| = 1,$$

$$P_{\min} = \frac{\hbar\omega_0 f_{\min}^2}{\kappa_{\text{ext}}} = -\frac{2c}{\pi} \frac{S_{\text{eff}}\beta_2}{\eta n_2 D_1 Q \tau_s^2} \operatorname{sech}^2\left(\frac{\pi\Omega\tau_s}{2}\right) \equiv P_0 \operatorname{sech}^2\left(\frac{\pi\Omega\tau_s}{2}\right), \quad (4.19)$$

$$\Gamma = \frac{P_{\text{sol}}}{P_{\min}} = \pi\eta^2 D_1 \tau_s \operatorname{sech}^2\left(\frac{\pi\Omega\tau_s}{2}\right) \equiv \Gamma_0 \operatorname{sech}^2\left(\frac{\pi\Omega\tau_s}{2}\right), \quad (4.20)$$

where P_0 and Γ_0 are defined as the minimum pump power and soliton efficiency without the Raman effect in eq. (2.38) and (2.39) and the soliton power P_{sol} is identical to eq. (2.36).

Finally, the non-zero soliton frequency shift causes a constant velocity of the soliton position in eq. (4.14). This equivalently changes the group velocity and soliton round trip time in microresonator and therefore the soliton repetition rate. The repetition rate of the soliton can be expressed as follows:

$$\omega_{\text{rep}} = D_1 + \frac{\partial\phi_c}{\partial T} = D_1 + \frac{D_2}{D_1}\Omega. \quad (4.21)$$

The Lagrangian method gives the soliton self-frequency shift Ω , and the corresponding change in soliton efficiency and repetition rate. It shall be noted that, alternatively, the soliton self-frequency shift can also be obtained by the moment analysis method (Karpov, Hairun Guo, Kordts, Victor Brasch, M. H. Pfeiffer, et al., 2016; Xu Yi, Q.-F. Yang, X. Zhang, et al., 2016).

4.4 Experiment of soliton self-frequency shift and efficiency

To test the theory, the soliton was generated using the techniques described in the previous chapter, and a series of soliton spectra of increasing spectral width were obtained using the operating point locking method (Xu Yi, Q.-F. Yang, Ki Youl Yang, and Kerry Vahala, 2016a). The Raman SFS, Ω , and the pulse width, τ_s , were measured by least-squares-fitting of the soliton optical spectrum (see fig. 4.1) to the theoretical soliton spectral envelope $P(\omega) = P_c \operatorname{sech}^2[\pi\tau_s(\omega - \omega_p - \Omega)/2]$ (P_c is the maximum comb tooth power). Figure 4.2 plots the measured Ω versus $1/\tau_s^4$ in two devices. For reference, device I is a device previously characterized (Xu Yi, Q.-F. Yang, Ki Youl Yang, Suh, et al., 2015). A linear fitting to the two sets of data is also provided confirming the predicted theoretical dependence in eq. (4.18). Furthermore, with measured parameters (device I: $Q = 200$ million, $D_1/2\pi = 22$ GHz, $D_2/2\pi = 17$ kHz; and device II: $Q = 235$ million, $D_1/2\pi = 22$ GHz, $D_2/2\pi = 17$ kHz), a value of $\tau_R = 1.8$ fs, both for device I and for device II, is inferred from the linear fitting, which is in a reasonable agreement with the value

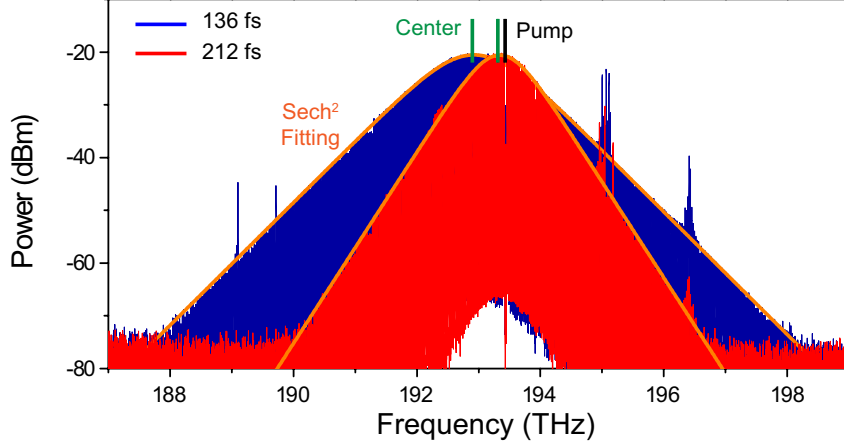


Figure 4.1: Optical spectra measured for a dissipative Kerr cavity soliton at two operating points. The pump power is suppressed using a fiber grating filter. A sech^2 fit is shown as the orange curves and pulse widths inferred from the fitting are shown in the legend. The location of the pump line is indicated as the black line. The centers of the spectra are indicated by the green lines.

of 2-4 fs reported in silica optical fibers (Atieh et al., 1999). The small non-zero intercept of the linear fitting is in the range of 1 free-spectral-range (22 GHz) of the two resonators.

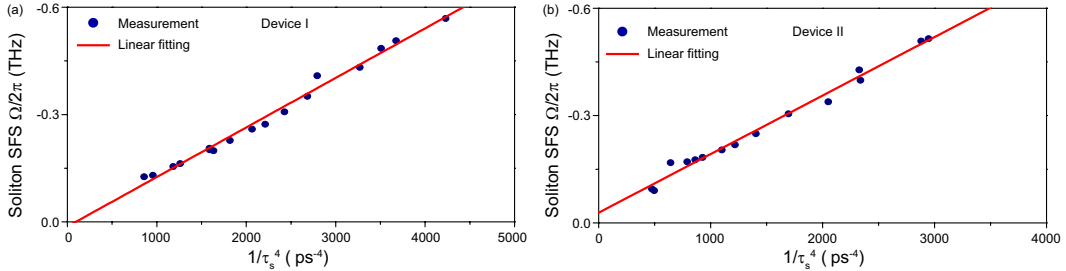


Figure 4.2: The measured Raman self-frequency-shift plotted versus $1/\tau_s^4$ for two devices. The red line is a linear fit according to eq. (4.18).

To measure the soliton efficiency, Γ , the operating point is fixed (i.e., laser-cavity detuning $\delta\omega$ is fixed) while the pump power is decreased until the soliton disappears. Near the disappearance point, the soliton average power, P_{sol} , and the minimum pump power, P_{min} , are recorded and used to obtain efficiency as $\Gamma = P_{\text{sol}}/P_{\text{min}}$. The pulselwidth is obtained from the optical spectrum as before. Measured efficiency is plotted versus the pulse width in fig. 4.3 for devices I and II. The prediction given by eqn. (4.20) is shown as the solid line. The value of τ_R used in the plots is that inferred from the fitting in fig. 4.2. Also, $\eta=0.29, 0.37$ is measured for devices I and

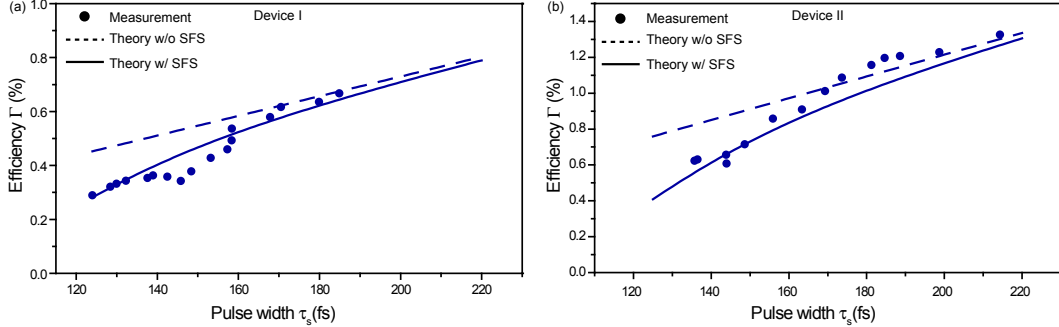


Figure 4.3: The measured efficiency versus soliton pulse width is plotted (blue points) for two devices and compared with theory. Theory comparison with Raman (solid blue lines) and without Raman (dash blue lines) is presented. There are no free parameters in the comparison. The small deviations between the measurement and the theory could result from the presence of weak avoided mode crossings in the dispersion spectrum (T Herr, V Brasch, J. Jost, Mirgorodskiy, et al., 2014).

II. Device II has a higher efficiency as a result of a larger coupling coefficient. The agreement between the theory and measurement in fig. 4.3 is very good, especially considering that there are no free parameters. The dashed lines in the plots give the uncorrected efficiency prediction of eq. (2.39) (i.e., Γ_0 vs. τ_s).

4.5 Summary

In summary, closed-form expressions for the self frequency shift and efficiency of dissipative Kerr cavity solitons have been derived using the Lagrangian perturbation approach. The results are in good agreement with measurements in silica microcavity systems. The expressions should be applicable to predict soliton behavior in any microcavity system. In addition, even though the behavior of the Raman self-frequency-shift in microcavities differs in comparison to conventional soliton propagation in optical fiber (i.e., frequency locking behavior in microcavities (Milán et al., 2015)), it is interesting to note that both systems exhibit an inverse quartic dependence on soliton pulse width (J. P. Gordon, 1986).

Chapter 5

STOKES SOLITON

5.1 Introduction

¹ Temporal solitons are readily formed in optical fiber waveguides (Hasegawa and Tappert, 1973; Mollenauer, Stolen, and J. P. Gordon, 1980; Hermann A Haus and Wong, 1996; Dudley, Genty, and Coen, 2006) and laser resonators (Herman A Haus et al., 2000; S. Cundiff, 2005) and have recently been observed in dielectric microcavities (T Herr, V Brasch, J. Jost, C. Wang, et al., 2014; Xu Yi, Q.-F. Yang, Ki Youl Yang, Suh, et al., 2015; V Brasch et al., 2016). In each of these cases nonlinear compensation of group velocity dispersion is provided by the Kerr effect (nonlinear refractive index). Besides the Kerr nonlinearity, a secondary effect associated with soliton propagation is the so-called soliton self-frequency shift caused by Raman interaction, which induces a continuously increasing red-shift with propagation in a waveguide (Dudley, Genty, and Coen, 2006) or a fixed shift of the soliton spectrum in cavities (Karpov, Hairun Guo, Kordts, Victor Brasch, M. H. Pfeiffer, et al., 2016; Xu Yi, Q.-F. Yang, Ki Youl Yang, and Kerry Vahala, 2016b). More generally, the Raman interaction can produce optical amplification and laser action of waves red-shifted relative to a strong pumping wave or pulse (M. N. Islam, 2002; S. Spillane, T. Kippenberg, and KJ Vahala, 2002; Headley and Agrawal, 1996). In this chapter we report a new Raman-related effect: soliton generation through time and space varying Raman amplification created by the presence of a first temporal soliton. Because the new soliton is spectrally red-shifted relative to the initial soliton we call it a Stokes soliton. It is observed in a silica microcavity and obeys a threshold condition resulting from an optimal balancing of Raman gain with cavity loss when the soliton pulses overlap in space and time. Also, the repetition frequency of both the initial and the Stokes soliton are locked by the Kerr nonlinearity.

The generation of a fundamental soliton by another fundamental soliton in this way is new and also represents a form of mode locking of a soliton laser. It differs from mechanisms like soliton fission which also result in the creation of one or more fundamental solitons (Dudley, Genty, and Coen, 2006). Specifically, soliton fission involves a higher order soliton breaking into multiple fundamental solitons; nor is it a

¹ Work presented in this chapter has been published in "Stokes soliton in microresonators", Nature Physics, 13, 53 (2017).

regenerative process. Also, co-existing and switching dissipative solitons have been observed (Chengying Bao, W. Chang, et al., 2015) and modeled (Chengying Bao, W. Chang, et al., 2015; Soto-Crespo and Akhmediev, 2002) in an erbium-doped mode-locked fiber laser. However, in the present case, the Stokes soliton relies upon the primary soliton for its existence by leveraging spatial-temporal overlap for trapping and optical amplification. Raman gain produced for the Stokes soliton by the primary soliton is also distinctly different from the Raman self-frequency shift (Mitschke and Mollenauer, 1986; J. P. Gordon, 1986), which is an effect of the Raman interaction on the primary soliton (Karpov, Hairun Guo, Kordts, Victor Brasch, M. H. Pfeiffer, et al., 2016; Xu Yi, Q.-F. Yang, Ki Youl Yang, Suh, et al., 2015; Xu Yi, Q.-F. Yang, Ki Youl Yang, and Kerry Vahala, 2016b) (not the Stokes soliton). Also, this new Raman mechanism is responsible for oscillation of the Stokes soliton at a well defined threshold. Raman self shift is, on the other hand, not a thresholding process. Finally, concerning the trapping phenomena that accompanies the Stokes soliton formation, the trapping of temporal solitons belonging to distinct polarization states was proposed in the late 1980s (Menyuk, 1987) and was observed in optical fiber (M. Islam, Poole, and J. Gordon, 1989; S. Cundiff et al., 1999) and later in fiber lasers (Collings et al., 2000). However, trapping of temporal solitons belonging to distinct transverse mode families, as observed here, was proposed even earlier (Hasegawa, 1980; Crosignani and Di Porto, 1981), but has only recently been observed in graded-index fiber waveguides (Renninger and Wise, 2013). Trapping of solitons in microcavities has never been reported. Also, the spatial-temporal formation of a soliton through the Raman process has never before been described. The observation, measurement and modeling of Stokes solitons is now presented.

5.2 Stimulated Raman scattering and group velocity matching

The resonator in this chapter is silica whispering gallery microcavity and the first temporal soliton (see Chapter III) will be referred to as the primary soliton. Consistent with its formation, the primary soliton creates a spatially varying refractive index via the Kerr nonlinearity that serves as an effective potential well. It travels with the primary soliton and counteracts optical dispersion. Moreover, on account of the Raman interaction, the primary soliton creates local Raman amplification that also propagates with the primary soliton. These propagating index and gain profiles are depicted in figure 5.1. The primary soliton is composed of many longitudinal modes belonging to one of the transverse mode families of the cavity. These phase-locked modes form a frequency comb. $\Delta\nu_P$ will denote the longitudinal mode

separation or free spectral range for longitudinal modes near the spectral center of the primary soliton. $\Delta\nu_P$ also gives the approximate round trip rate of the primary soliton around the cavity ($T_{RT} = \Delta\nu_P^{-1}$ is the round trip time).

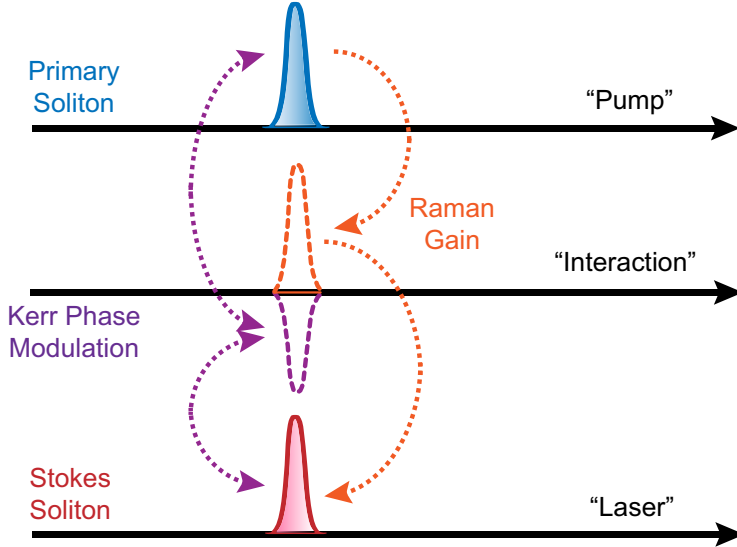


Figure 5.1: The Stokes soliton (red) maximizes Raman gain by overlapping in time and space with the primary soliton (blue). It is also trapped by the Kerr-induced effective optical well created by the primary soliton.

Consider another transverse mode family besides the one that forms the primary soliton. Suppose that some group of longitudinal modes in this family satisfies two conditions: (1) they lie within the Raman gain spectrum created by the primary soliton; (2) they feature a free spectral range (FSR) that is close in value to that of the primary soliton ($\Delta\nu_P$). Any noise in these longitudinal modes will be amplified by Raman gain provided by the primary soliton. If the round trip amplification of a resulting waveform created by a superposition of these modes is sufficient to overcome round trip optical loss, then oscillation threshold is possible. The threshold will be lowest (Raman gain maximal) if the modes of the second family phase lock to form a pulse overlapping in both space and time with the primary soliton. This overlap is possible since the round trip time of the primary soliton and the new pulse are closely matched, i.e., condition (2) above is satisfied. Also, the potential well created by the primary soliton can be shared with the new optical pulse. This latter nonlinear coupling of the primary soliton with the new, Stokes soliton pulse results from Kerr-mediated cross-phase modulation and locks the round trip rates of the two solitons (i.e., their soliton pulse repetition frequencies are locked).

5.3 Experimental observation of Stokes soliton

The experimental setup is shown in figure 5.2. The microcavities are about 3 mm in diameter and have an unloaded optical Q factor of 400 million (Lee, T. Chen, et al., 2012). The cavity is pumped by a continuous-wave fiber laser to induce a primary soliton, which is a DKS with a repetition frequency of 22 GHz and a pulse width that could be controlled to lie within the range of 100-200 fs.

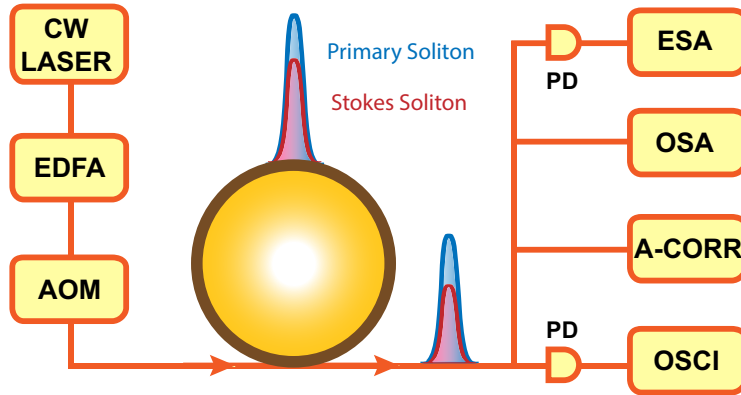


Figure 5.2: The microcavity (shown as a ring) is pumped with a tunable, continuous-wave (CW) fiber laser amplified by an erbium-doped fiber amplifier (EDFA). An acousto-optic modulator (AOM) is used to control the pump power. The output soliton power is detected with a photo diode (PD) and monitored on an oscilloscope (OSCI). Wavelength division multiplexers (not shown) split the 1550 nm band primary soliton and 1600 nm band Stokes soliton so that their powers can be monitored separately on the oscilloscope. An optical spectrum analyzer (OSA), auto-correlator (A-CORR), and electrical spectrum analyzer (ESA) also monitor the output. In certain measurements (A-CORR and ESA), a fiber Bragg filter was used to remove the pump field from the soliton spectrum.

Measurement of the FSR versus wavelength of four transverse mode families in a single resonator is presented in figure 5.3 (a). The measurement is performed by scanning a tunable external cavity diode laser (ECDL) through the spectral locations of optical resonances from 1520 nm to 1580 nm. The resonances appear as minima in the optical power transmitted past the microcavity, and the location of these resonances is calibrated using a fiber-based Mach Zehnder interferometer (see Chapter 3). The resulting data provide the dispersion in the FSR of cavity modes versus the wavelength and readily enable the identification transverse mode families. Other details on this method are described in Chapter 3. The green data plotted in figure 5.3 (a) correspond to the primary soliton forming mode family and the FSR of the pumping mode for that soliton is indicated by the horizontal dashed line. The measured spectrum for the primary soliton is shown in figure 5.3 (b). In

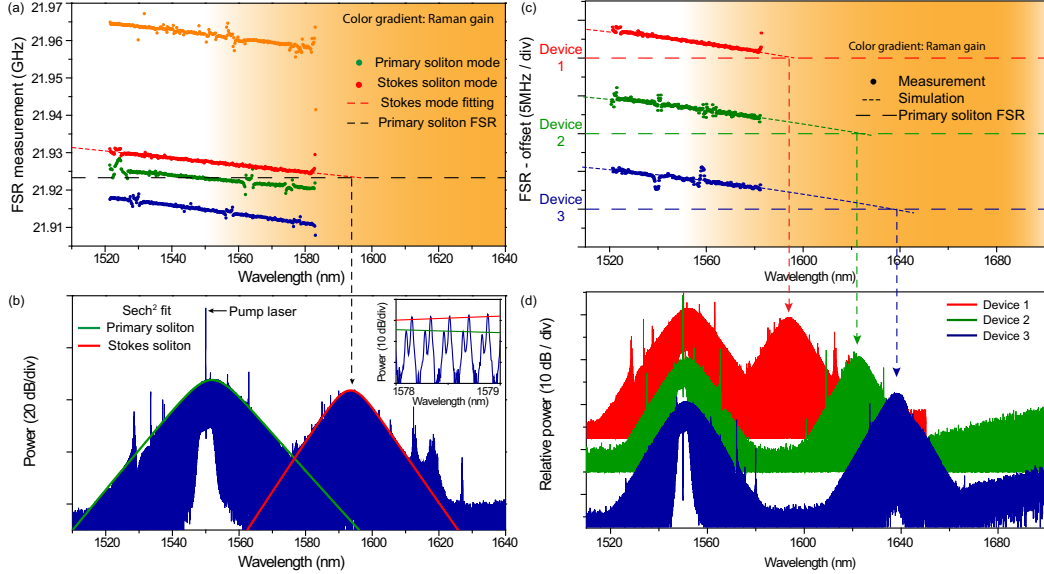


Figure 5.3: (a) Free spectral range (FSR) versus wavelength measured for four mode families in a 3 mm disk resonator. The mode families for the primary and Stokes soliton are shown in green and red, respectively. The FSR at the spectral center of the primary soliton is shown as a dashed horizontal line. Extrapolation of the Stokes soliton data (red) to longer wavelengths gives the FSR matching wavelength where the Stokes soliton forms. The background coloration gives the approximate wavelength range of the Raman gain spectrum. (b) Measured primary and Stokes soliton spectra. The Stokes soliton spectral center closely matches the prediction in panel (a). Sech^2 envelopes are shown on each spectrum. The primary soliton spectrum features a small Raman self-frequency shift. (c) Dispersion spectra for the Stokes soliton forming mode family measured in three devices (the upper spectrum is the device from panel (a)). Other mode families have been omitted in the plots for clarity. The horizontal dashed lines give the repetition frequency of the primary soliton in each device. Extrapolation of the dispersion data attained by simulation is provided to graphically locate the predicted Stokes soliton wavelength. (d) The measured primary and Stokes soliton spectra corresponding to the devices in panel (c). The spectral locations of the Stokes solitons agree well with the graphical predictions.

the spectrum the pump spectral line (near 1550 nm) is indicated as well as the Sech^2 envelope for the soliton (green curve) (T Herr, V Brasch, J. Jost, C. Wang, et al., 2014; Xu Yi, Q.-F. Yang, Ki Youl Yang, Suh, et al., 2015). Returning to figure 5.3 (a), the dispersion for another transverse mode family (red data) is extrapolated to longer wavelengths and crosses the dashed line near 1593 nm. At this wavelength the FSR of the red mode family closely matches that of the primary soliton. Moreover, this wavelength also lies within the Raman gain spectrum produced by the primary

soliton (amber region in figure 5.3 (a) gives the Raman gain band). As a result, conditions 1 and 2 above are satisfied at this wavelength for generation of a Stokes soliton. The corresponding measured Stokes soliton is shown in figure 5.3 (b). Its spectral maximum occurs at a wavelength that agrees well with the prediction based on the FSR measurement in figure 5.3 (a). As an aside, the individual spectral lines of the primary and the Stokes solitons are spaced by approximately 22 GHz and resolved comb lines in the overlapping spectral region between the solitons are provided in the inset to figure 5.3 (b).

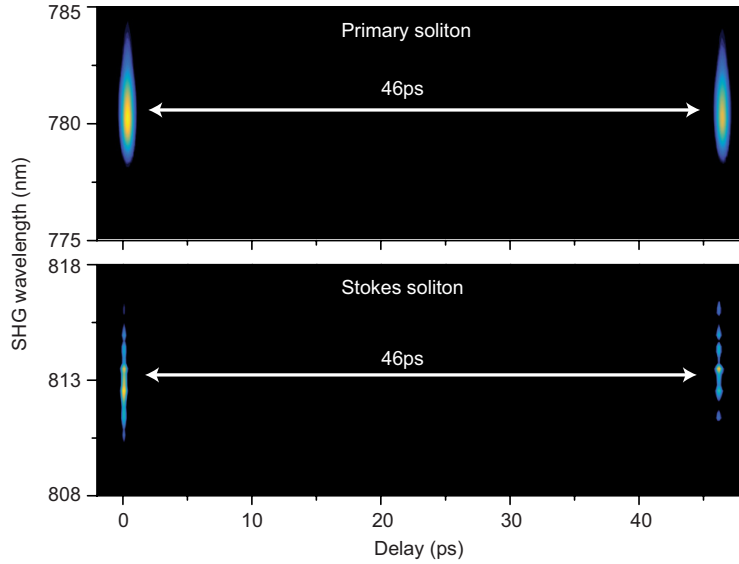


Figure 5.4: Frequency-resolved-optical-gating (FROG) traces of the primary and Stokes solitons. The primary soliton is amplified to 500 mW by an EDFA before coupling into the FROG setup, while the Stokes soliton is amplified to 10 mW by two cascaded semiconductor optical amplifiers with gain centered around 1620 nm. The period of the primary and Stokes solitons are 46 ps, the cavity round trip time.

These results were readily reproduced in other devices. Indeed, the FSR matching wavelength (i.e., condition 2) could be controlled by adjusting the geometry of the resonator. Figure 5.3 (c) shows the FSR dispersion measurements and figure 5.3 (d) shows the corresponding primary and Stokes soliton spectra that are measured using two other devices (green and blue spectra). For clarity, only the Stokes-soliton-forming mode family is presented in figure 5.3 (c) (including the data from figure 5.3 (a), red spectra, for comparison). The FSR of the primary soliton is indicated by the horizontal dashed lines in figure 5.3 (c). The FSR matching wavelengths are indicated by extrapolation of the dispersion data using simulation (Ki Youl Yang et al., 2016) and agree well with the location of the measured Stokes soliton spectral

maximum in figure 5.3 (d).

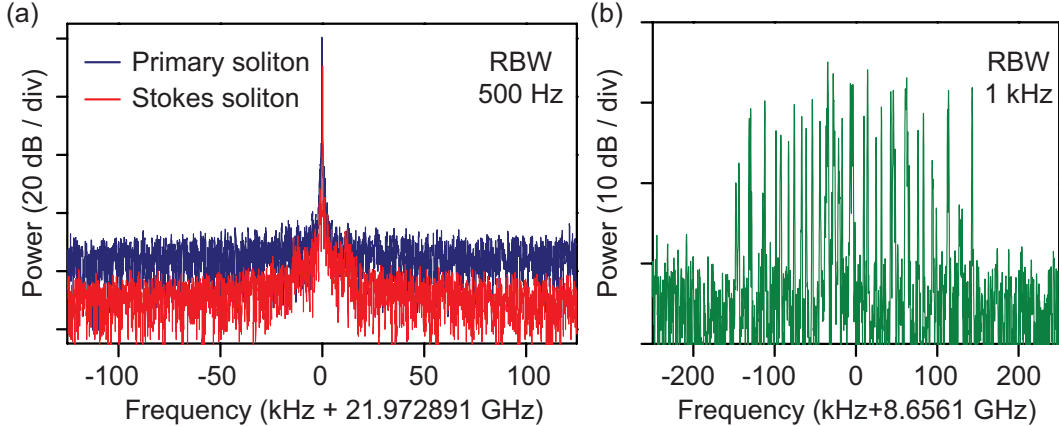


Figure 5.5: (a) Electrical spectra of the detected primary soliton pulse stream (blue) and the Stokes pulse stream (red). (b) Beatnote between neighboring comb lines of the primary and Stokes solitons for a device like that in figure 5.3 (a). The beatnote is much noisier than the repetition frequency in panel (a).

To confirm the temporal pulse nature of the Stokes soliton the frequency resolved optical gate (FROG) method was used to record the correlation traces in figure 5.4. Optical filtering was applied to isolate the primary and Stokes soliton pulse streams. Also, before FROG measurement, the primary soliton stream was amplified by an erbium doped fiber amplifier (EDFA) and the Stokes soliton was amplified using a semiconductor optical amplifier (SOA). The data confirm that both streams consist of pulses. As an aside, the signal-to-noise level for the Stokes soliton measurement was limited by the saturation power of the SOA.

Photodetection of the isolated primary and Stokes soliton pulse streams was also possible. The measured electrical spectrum for each pulse stream is overlaid in figure 5.5 (a). The spectra are observed to align in frequency. As further confirmation of this frequency alignment, the optical pulse streams were simultaneously detected (no filtering to isolate the streams) and the measured electrical spectrum featured a single spectral peak at a resolution of 500 Hz. These results are expected on account of optical trapping of the Stokes soliton by the primary soliton, which causes the line spacing (repetition rate) of the Stokes soliton and the primary soliton to match.

At the same time, the absolute optical frequency of the two solitons is not expected to be locked since the optical potential well depends upon the intensity of the primary soliton. To test this, the relative optical frequency stability of the two soliton streams was measured by using a resonator that featured spectrally overlapping primary and

Stokes solitons such as in figure 5.3 (b). A high resolution optical scan from 1578-1579nm of this overlap region is presented as the inset in figure 5.3 (b) and confirms that the underlying soliton lines are distinct. The beatnote between neighboring spectral lines of the primary and Stokes solitons shows large frequency variations (see figure 5.5 (b)) in comparison to the repetition frequency of each soliton (figure 5.5 (a)). Synchronization of the soliton repetition rates but not of the absolute optical frequencies is thus inferred from these measurements.

5.4 Theory of Stokes soliton

Coupled equations of Stokes soliton

In this section, we will derive the coupled equations governing the primary and Stokes solitons. The derivation of the stimulated Raman process is similar to the derivation of Raman self-frequency shift in Section 4.2. We start with the pulse propagation equation in optical fiber with Raman interactions (eq. 4.1), and then adopted the additional nonlinear terms into microresonator equation. We start with equation 4.1,

$$\frac{\partial E}{\partial z} + \alpha(\lambda)E + \beta_1(\lambda)\frac{\partial E}{\partial t} + \frac{i\beta_2(\lambda)}{2}\frac{\partial^2 E}{\partial t^2} = i\gamma E(z, t) \int_0^\infty R(t')|E(z, t-t')|^2 dt', \quad (5.1)$$

where E is the pulse field in optical fiber and $|E|^2$ is normalized to optical power. The linear loss, α , the group velocity, β_1 , and group velocity dispersion, β_2 , are now functions of wavelength because the primary and Stokes solitons are at different wavelengths and in different transverse mode families. The nonlinear coefficient in optical fiber can be shown as $\gamma = n_2\omega_0/cS'_{\text{eff}}$, where n_2 is the Kerr refractive index, S'_{eff} is the effective mode area of optical fiber (Agrawal, 2007). The field of pulse can be further decomposed as a linear combination of primary soliton field, E_p and Stokes soliton field E_s ,

$$E(z, t) = E_p(z, t) + E_s(z, t)e^{i\omega_{ps}t}, \quad (5.2)$$

where $\omega_{ps} = \omega_p - \omega_s$ denotes the frequency difference between Stokes soliton and primary soliton and eq. (5.2) is in the rotation frame of $e^{-i\omega_p t}$.

From here we only focus on the right-hand-side (RHS) of eq. (5.1), as the left-hand-side terms are all linear and can be directly decomposed to primary soliton field and Stokes soliton field. Insert eq. (5.2) to the RHS of eq. (5.1), and we have

$$\begin{aligned} RHS &= i\gamma(E_p + E_s e^{i\omega_{ps}t}) \int_0^\infty R(t')[|E_p(t-t')|^2 + |E_s(t-t')|^2 + \\ &\quad E_p(t-t')E_s^*(t-t')e^{-i\omega_{ps}(t-t')} + E_s(t-t')E_p^*(t-t')]dt'. \end{aligned} \quad (5.3)$$

We then decompose nonlinear response function $R(t')$ (eq. (4.2))

$$R(t') = (1 - f_R)\delta(t') + f_R h_R(t'). \quad (5.4)$$

Insert eq. (5.4) into eq. (5.3), we have

$$\begin{aligned} RHS &= i(1 - f_R)\gamma[(|E_p|^2 + 2|E_s|^2)E_p + (|E_s|^2 + 2|E_p|^2)E_s e^{i\omega_{ps}t}] \\ &\quad + i f_R \gamma(E_p + E_s e^{i\omega_{ps}t}) \int_0^\infty h_R(t')[|E_p(t-t')|^2 + |E_s(t-t')|^2 + \\ &\quad E_p(t-t')E_s^*(t-t')e^{-i\omega_{ps}(t-t')} + E_s(t-t')E_p^*(t-t')e^{i\omega_{ps}(t-t')}]dt', \end{aligned} \quad (5.5)$$

where we have neglected terms with frequency different from E_p and E_s . Notice the first line are terms corresponding to self-phase modulation and cross-phase modulation. The coefficient shall be different for different transverse mode families and we will add this back later. The form of the right-hand-side second line is identical to the RHS of eq. (4.1), and it is corresponding to the Raman frequency shift. Since Raman-frequency shift is not the main concern here, we apply the same approximation as eq. (4.3) but only keeping the first term. Finally, for the third line in eq. (5.5), we apply the approximation that the variation of the field E_p and E_s is much slower than $h_R(t')$ and $e^{\pm i\omega_{ps}(t-t')}$ and therefore $E_{s,p}(t-t')$ is simplified to $E_{s,p}(t)$. With these approximations, we arrive at

$$\begin{aligned} RHS &= i\gamma[|E_p|^2 E_p + |E_s|^2 E_s e^{i\omega_{ps}t} + (2 - f_R)(|E_s|^2 E_p + 2|E_p|^2 E_s e^{i\omega_{ps}t}) \\ &\quad + \int_0^\infty f_R h_R(t') e^{i\omega_{ps}t'} dt' (|E_p|^2 E_s e^{i\omega_{ps}t} - \frac{\omega_p}{\omega_s} |E_s|^2 E_p)], \end{aligned} \quad (5.6)$$

where the integration gives a constant and its imaginary part can be related to the Raman gain coefficient of silica at frequency ω_{ps} . The factor of $-\omega_p/\omega_s$ in the last term is from the fact that the photon number, instead of photon energy, is conserved in stimulated Raman process (i.e. $\int_0^\infty f_R h_R(t') e^{-i\omega_{ps}t'} dt' = \omega_p/\omega_s \times \int_0^\infty f_R h_R(t') e^{i\omega_{sp}t'} dt'$). Plug eq. (5.6) into eq. (5.1) and separate the equations to E_p and E_s , and we have the coupled equations for pulses in optical fiber augmented by stimulated Raman effect (Agrawal, 2007):

$$\begin{aligned} \frac{\partial E_p}{\partial z} + \alpha_p E_p + \beta_{1p} \frac{\partial E_p}{\partial t} + \frac{i\beta_{2p}}{2} \frac{\partial^2 E_p}{\partial t^2} &= i\gamma[|E_p|^2 + (2 - f_R)|E_s|^2]E_p \\ - \frac{\omega_p}{\omega_s} \gamma f_R \text{Im} \left[\int_0^\infty f_R h_R(t') e^{i\omega_{ps}t'} dt' \right] |E_s|^2 E_p \end{aligned} \quad (5.7)$$

$$\begin{aligned} \frac{\partial E_s}{\partial z} + \alpha_s E_s + \beta_{1s} \frac{\partial E_s}{\partial t} + \frac{i\beta_{2s}}{2} \frac{\partial^2 E_s}{\partial t^2} &= i\gamma[|E_s|^2 + (2 - f_R)|E_p|^2]E_s \\ + \gamma f_R \text{Im} \left[\int_0^\infty f_R h_R(t') e^{i\omega_{ps}t'} dt' \right] |E_p|^2 E_s. \end{aligned} \quad (5.8)$$

This set of coupled equations contains the interactions between two optical pulses in optical fiber. They each obey the dispersion at their wavelengths $\beta_{1p}, \beta_{2p}, \beta_{1s}, \beta_{2s}$, and interact through cross-phase modulation and a stimulated Raman effect that provides gain/loss for longer/shorter wavelength pulse (T. J. Kippenberg, S. M. Spillane, et al., 2004). The coefficient for the Raman gain/loss can be related to the well studied Raman gain coefficient g_R in bulk silica (Agrawal, 2007). The equation for stimulated Raman effect in bulk material can be modeled as (Agrawal, 2007):

$$\frac{dI_s}{dz} = g_R I_p I_s, \quad (5.9)$$

where I_s and I_p are the intensity of the Stokes light and pump light. This equation can be converted to field equation by using $I = \frac{1}{2}c\epsilon_0 n_0 \tilde{E}^2$:

$$\frac{d\tilde{E}_s}{dz} = \frac{1}{4}c\epsilon_0 n_0 g_R |\tilde{E}_p|^2 \tilde{E}_s, \quad (5.10)$$

where \tilde{E} is the field of light and ϵ_0 is the vacuum permittivity. To integrate this equation into the Raman fiber equation, we normalize the electrical field to the same unit as eq. (5.1) such that $|E|^2$ is the optical power in the optical fiber: $|E|^2 = \frac{1}{2} \int \epsilon_0 n_0 c |\tilde{E}|^2 dx dy$, where x, y are the coordinates of optical fiber cross-section. Further separate $\tilde{E}(x, y)$ into $\tilde{E}(x, y) = \xi(x, y)\tilde{E}_{\max}$, where $\xi(x, y)$ carries the mode spatial distribution of optical fiber. This gives us:

$$\tilde{E} = \xi(x, y)\tilde{E}_{\max} = \xi(x, y)E \sqrt{\frac{2}{\epsilon_0 n_0 c \int |\xi(x, y)|^2 dx dy}}. \quad (5.11)$$

Insert eq. (5.11) into eq. (5.10), multiple both side by $\xi_s^*(x, y)$ and integrate over x and y coordinates, we have

$$\frac{dE_s}{dz} = \frac{1}{2}g_R |E_p|^2 E_s \frac{\int |\xi_s(x, y)|^2 |\xi_p(x, y)|^2 dx dy}{\int |\xi_p(x, y)|^2 dx dy \int |\xi_s(x, y)|^2 dx dy} \equiv \frac{g_R}{2S'_{sp}} |E_p|^2 E_s, \quad (5.12)$$

where we have defined the effective nonlinear mode area S'_{sp} . Use the right hand side of eq. (5.12) to replace the stimulated Raman term in eq. (5.7) and (5.8), and we have

$$\begin{aligned} \frac{\partial E_p}{\partial z} + \alpha_p E_p + \beta_{1p} \frac{\partial E_p}{\partial t} + \frac{i\beta_{2p}}{2} \frac{\partial^2 E_p}{\partial t^2} &= i \frac{n_2 \omega_0}{c S'_{eff}} [|E_p|^2 + (2 - f_R) |E_s|^2] E_p \\ &\quad - \frac{\omega_p}{\omega_s} \frac{g_R}{2S'_{sp}} |E_s|^2 E_p \end{aligned} \quad (5.13)$$

$$\begin{aligned} \frac{\partial E_s}{\partial z} + \alpha_s E_s + \beta_{1s} \frac{\partial E_s}{\partial t} + \frac{i\beta_{2s}}{2} \frac{\partial^2 E_s}{\partial t^2} &= i \frac{n_2 \omega_0}{c S'_{eff}} [|E_s|^2 + (2 - f_R) |E_p|^2] E_s \\ &\quad + \frac{g_R}{2S'_{sp}} |E_p|^2 E_s. \end{aligned} \quad (5.14)$$

Notice that the normalization factor between Kerr effect and Raman effect is different, and the normalization ratio is: $2\omega_0 S'_{\text{Raman}}/cS'_{\text{Kerr}}$. This ratio comes from the fact that Kerr refraction index n_2 is in the unit of $[m^2/W]$ while Raman bulk gain coefficient has unit $[m/W]$. When converting eq. (5.13) and eq. (5.14) into microresonator equations, this normalization ratio shall stay the same as both Kerr and Raman terms go through the same normalization procedure from optical fiber to microresonator.

From above, we have known that in microresonator the LLE equation could describe the Stokes soliton behavior by adding cross-phase modulation and Raman gain/loss term:

$$\frac{dA_p}{dT} = i \frac{D_{2p}}{2} \frac{\partial^2 A_p}{\partial \phi^2} - \left(\frac{\kappa_p}{2} + i\Delta\omega_p \right) A_p + i[g_p|A_p|^2 + (2 - f_R)G_p|A_s|^2]A_p - \frac{\omega_p}{\omega_s} R_c |A_s|^2 A_p + \sqrt{\kappa_p^{ext} P_{in}}, \quad (5.15)$$

$$\begin{aligned} \frac{dA_s}{dT} = & -\delta \frac{\partial A_s}{\partial \phi} + i \frac{D_{2s}}{2} \frac{\partial^2 A_s}{\partial \phi^2} - \left(\frac{\kappa_s}{2} + i\Delta\omega_s \right) A_s + i[g_s|A_s|^2 + (2 - f_R)G_s|A_p|^2]A_s \\ & + R_c |A_s|^2 A_p. \end{aligned} \quad (5.16)$$

In this set of equations, it shall be noted that: (1) unlike eq. (2.8), the intracavity fields $|A|^2$ here is normalized to intracavity power instead of photon number; (2) correspondingly, the self-phase modulation coefficient is modified to $g_j = n_2\omega_j D_{1j}/2n_0\pi S_{jj}$, where $j = p, s$; (3) the cross-phase modulation coefficient is $G_j = n_2\omega_j D_{1j}/2n_0\pi S_{ps}$; (4) the nonlinear mode area S_{jk} is defined as

$$S_{jk} = \frac{\iint_{-\infty}^{\infty} |\xi_j(x, y)|^2 dx dy \iint_{-\infty}^{\infty} |\xi_k(x, y)|^2 dx dy}{\iint_{-\infty}^{\infty} |\xi_j(x, y)|^2 |\xi_k(x, y)|^2 dx dy}, \quad (5.17)$$

where ξ_j is the spatial distribution of the mode; (5) $\delta = D_{1s} - D_{1p}$ is the FSR mismatch; and (6) the Raman gain/loss coefficient is $R_c = f_R G_s \text{Im}[\int h_R(\tau) \exp(i\omega_{ps}\tau) d\tau]$ and it could be calculated using the function of $h_R(\tau)$ (Agrawal, 2007). Alternatively, it can also be related to the Raman gain coefficient in bulk silica by making the comparison to eq. (5.13) and (5.14). In equation (5.15) and (5.16), we have $g = \chi' n_2$ and $R_c = \chi'' g_R$, where χ', χ'' are the normalization factor for Kerr and Raman coefficient in microresonator. Notice that the ratio of normalization factor between Kerr and Raman effect shall stay the same with the one in optical fiber, so that $\chi'/\chi'' = 2\omega_j S_{\text{Raman}}/cS_{\text{Kerr}}$. As we know

$\chi' = \omega_j D_{1j} / 2n_0 \pi S_{jj}$ from the expression of g , we have

$$R_c = \frac{c D_{1p} g_R}{4\pi n_0 S_{sp}}, \quad (5.18)$$

where we have neglected the small difference between D_{1p} and D_{1s} . Finally, in bulk silica, the gain coefficient is the function of the frequency difference between pump wave and Stokes wave. The bulk silica Raman gain coefficient is zero at zero frequency and reaches its maximum near 13 THz frequency with $g_R^{\max} = 0.66 \times 10^{-13}$ m/W. In addition, when the frequency is between 0 to 13 THz, the Raman gain coefficient is roughly linear with frequency (Agrawal, 2007).

The coupled LLE equations in eq. (5.15) and (5.16) formed a complete set of equations for Stokes soliton (neglecting Raman self-frequency shift) and all parameters in the equations can be obtained either by experiments or simulation (i.e. mode area). Notice that in the continuous wave limit where both pump and Stokes fields are composed of a single wavelength light, eq. (5.15) and (5.16) will reduce to the equations for stimulated Raman laser and are consistent with previous literatures (S. Spillane, T. Kippenberg, and KJ Vahala, 2002; T. J. Kippenberg, S. M. Spillane, et al., 2004).

Stokes soliton threshold and Weak Stokes limit

Although an exact solution of the coupled solitons cannot be obtained, the near threshold behavior of the Stokes soliton can still be studied analytically. In this limit, the primary soliton is unperturbed by the Stokes soliton since the Stokes soliton is weak (i.e., near threshold). Its solution is therefore given by the $Sech^2$ dissipative Kerr cavity soliton solution (T Herr, V Brasch, J. Jost, C. Wang, et al., 2014). The Stokes soliton equation then uses this solution for the primary soliton. By selecting the carrier frequency of the Stokes soliton such that $\delta = 0$, the equation for the Stokes soliton can be simplified to the following:

$$\frac{\partial A_s}{\partial T} = i \frac{D_{2s}}{2} \frac{\partial^2 A_s}{\partial \phi^2} + i(2 - f_R)G_s |A_s|^2 A_s - \left(\frac{\kappa_s}{2} + i\Delta\omega_s\right)A_s + R_c |A_p|^2 A_s, \quad (5.19)$$

where $A_p = B sech(\phi/\phi_\tau)$ is the uncoupled primary soliton solution (T Herr, V Brasch, J. Jost, C. Wang, et al., 2014) with $|B|^2 = 2\Delta\omega_p/g_p$ and $\phi_\tau = \sqrt{D_{2p}/2\Delta\omega_p}$. The Raman terms containing derivatives cause soliton self frequency shift and subsequently a phase change (Karpov, Hairun Guo, Kordts, Victor Brasch, M. H. Pfeiffer, et al., 2016). However, they minimally affect pulse width and peak power (Xu Yi, Q.-F. Yang, Ki Youl Yang, Suh, et al., 2015). As the primary soliton and

Stokes soliton have no absolute phase coherence, these terms have been omitted. Accordingly, the Stokes soliton can be treated as a wave trapped in a sech²-shape potential well created by the primary soliton (imaginary terms in eq. (5.19)), and also deriving optical gain from the primary soliton (real terms in eq. (5.19)). The bounded solution of the wave function in such a potential (imaginary terms in eq. (5.19)) has the following form:

$$A_s = V \operatorname{sech}^\gamma(\phi/\phi_t au), \quad (5.20)$$

where, consistent with the near threshold assumption, V is a small amplitude satisfying $|V|^2 \ll |B|^2$. Under these assumptions, the exponent γ is a root of the following equation,

$$\gamma(\gamma + 1) = 2(2 - f_R)G_s D_{2p}/g_p D_{2s}. \quad (5.21)$$

As a physical check of this equation, we note that under circumstances of $G_s = g_p/2$ the potential well created by the primary soliton for the Stokes soliton is identical to the primary soliton potential well (note: the factor of 1/2 comes about from cross phase modulation). In this case, assuming identical second-order dispersion ($D_{2s} = D_{2p}$) and also $f_R = 0$, the solution to eq. (5.21) is $\gamma = 1$, which shows that the Stokes soliton acquires the same envelope as the primary soliton.

Once the peak power of the primary soliton reaches a point that provides sufficient Raman gain to overcome Stokes soliton roundtrip loss, the Stokes soliton will begin to oscillate. The threshold condition emerges as the condition for steady-state Stokes soliton power balance. This is readily derived from the real terms in Stokes soliton equation and takes the form

$$\int_0^{2\pi} \partial_t |E_s|^2 d\phi = \int_0^{2\pi} d\phi (\kappa_s - 2R|E_p|^2) |E_s|^2 = 0 \quad (5.22)$$

By substituting the solutions for the primary and Stokes solitons into eqn. (S12), the resulting threshold in primary soliton peak output power is found to be

$$P_{th} = \frac{\kappa_p^{ext} \kappa_s}{2R} \left(1 + \frac{1}{2\gamma}\right). \quad (5.23)$$

Stokes soliton threshold measurement

The thresholding nature of Stokes soliton formation is studied in figure 5.6. The spectra in figure 5.6 (a) show the primary soliton and the corresponding Stokes soliton spectra for pumping levels below and above threshold. The transverse spatial mode profiles on which these solitons are formed are also provided and have

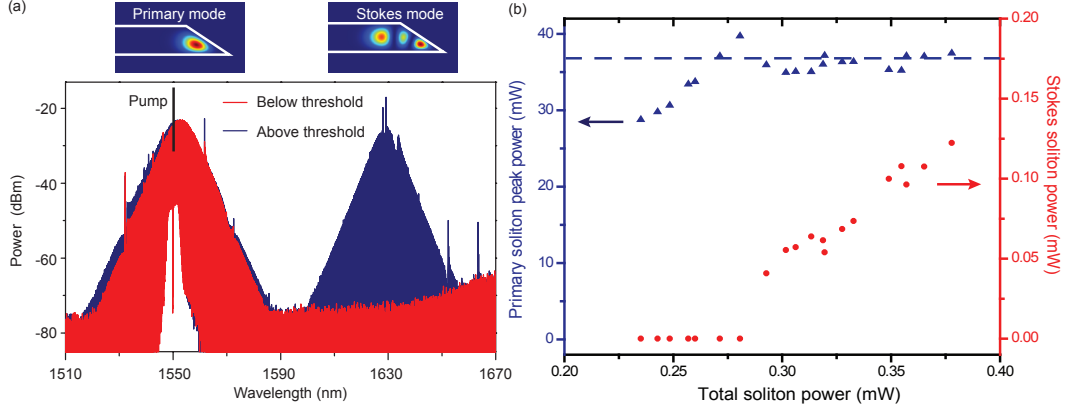


Figure 5.6: Stokes soliton spectra, power and threshold measurements. (a) Soliton spectra are plotted below and above threshold. The upper insets show the spatial mode families associated with the primary and Stokes solitons. (b) Measurement of Stokes soliton power and primary soliton peak power versus total soliton power. The primary soliton peak power (blue) versus total power experiences threshold clamping at the onset of Stokes soliton oscillation. The theoretical threshold peak power from eq. (1) is also shown for comparison as the horizontal blue dashed line.

been inferred by numerical fitting to the dispersion data. In figure 5.6 (b) power data are provided showing the primary soliton peak power and the Stokes soliton power plotted versus the total soliton power. To measure this data, the power in the primary soliton was varied using the locking method described elsewhere (Xu Yi, Q.-F. Yang, Ki Youl Yang, and Kerry Vahala, 2016a). Also, the transmitted pump spectral line was filtered out using a fiber Bragg filter. Power was measured by summing the power of the respective comb lines for the primary and Stokes soliton as measured on the optical spectrum analyzer. Consistent with the thresholding nature of the process, the Stokes soliton power could be increased beyond the primary soliton power (e.g., figure 5.3 (d), blue trace). The threshold peak power predicted by Eq. (5.23) is plotted as the horizontal dashed line in figure 5.6 (b) for comparison to measurements. The values used in this calculation are calculated or measured and are provided here.

The measured parameters are: $\kappa_p/2\pi = 838$ kHz, $\kappa_p^{ext}/2\pi = 222$ kHz, $\lambda_p = 1550$ nm, $D_{1p}/2\pi = 22$ GHz and $D_{2p}/2\pi = 16.1$ kHz. For the Stokes soliton mode family $\kappa_s/2\pi = 3.3$ MHz is measured near 1550 nm and is used for the Stokes soliton loss rate in the 1600 nm band. Calculated parameters (based on mode simulations) are: $D_{2s}/2\pi = 21.7$ kHz, $S_{ss} = 69.8 \mu\text{m}^2$, $S_{pp} = 39.7 \mu\text{m}^2$, $S_{ps} = 120 \mu\text{m}^2$, and $\delta = 0$ when $\lambda_s = 1627$ nm. Other constants are: $n = 1.45$, $n_2 = 2.2 \times 10^{-20} \text{ m}^2/\text{W}$,

$g_R = 3.94 \times 10^{-14}$ m/W, and $\tau_R = 3.2$ fs. $\gamma = 0.55$ is calculated and used in figure 5.6.

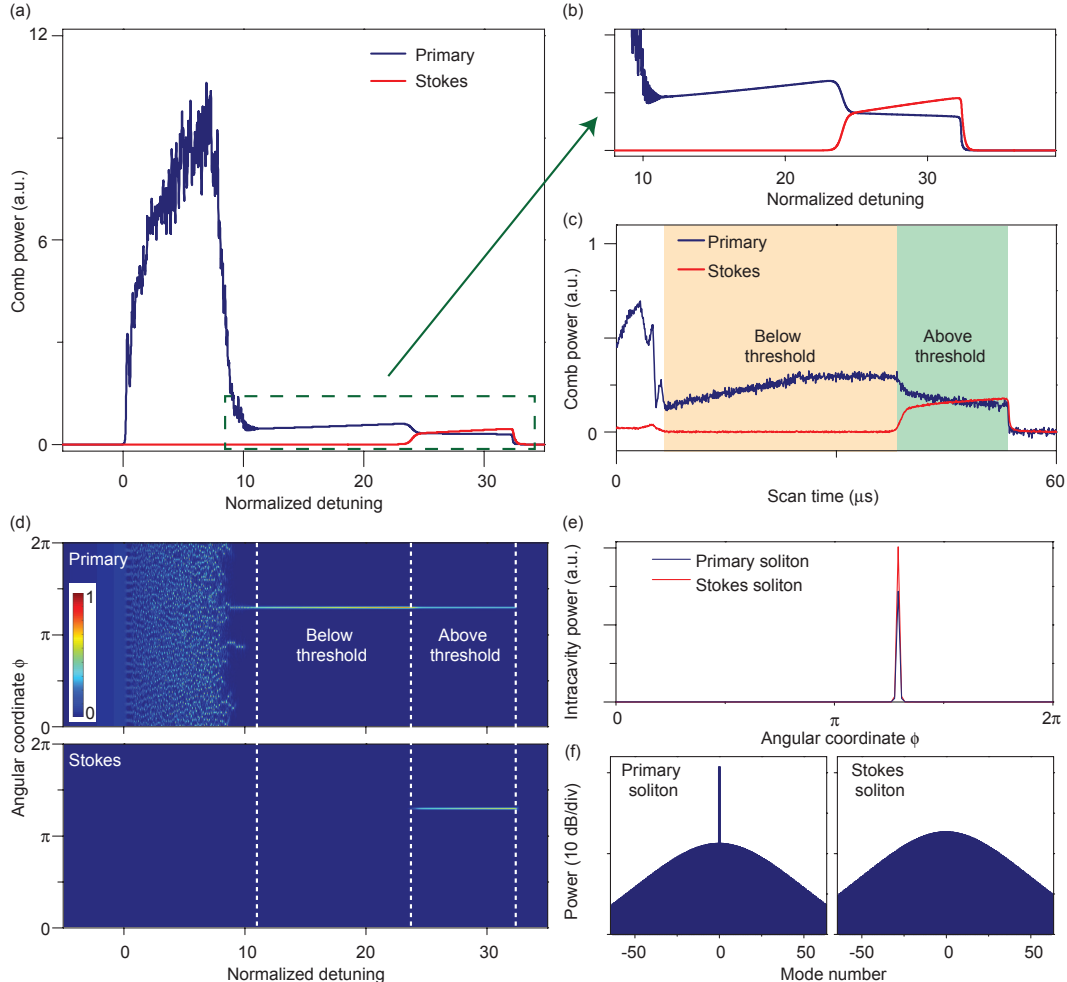


Figure 5.7: Stokes soliton formation in a microresonator. (a) Simulated intracavity comb power during a laser scan over the primary soliton pumping resonance from the blue (left) to the red (right) of the resonance. The detuning is normalized to the resonance linewidth. The initial step corresponds to the primary soliton formation, and the subsequent decrease in power corresponds to the onset of the Stokes soliton. The Stokes soliton power is shown in red. (b) Zoomed-in view of the indicated region from figure panel (a). (c) Experimentally measured primary and Stokes soliton power during a laser scan showing the features simulated in panel (a) and (b). (d) Simulation of the intracavity field in the moving frame of the solitons plotted versus the pump laser detuning. The detuning axis is scaled identically to panel (a). The figure shows the primary soliton step region (below threshold) as well as the onset of the Stokes soliton (above threshold). (e) Temporal overlap of the primary and Stokes solitons is numerically confirmed in the plot of normalized power versus location angle within the resonator. The overlap confirms trapping and co-propagation. (f) Intracavity optical spectra of the primary and Stokes solitons.

Numerical simulation

²Equations (5.15) and (5.16) are numerically simulated to reveal further details on the Stokes soliton formation. In the simulation, a pumping laser is scanning from blue-detuned to red-detuned and 128 modes of primary and Stokes field are employed in the simulation. The formation of a step in the primary comb power (blue) indicates primary soliton formation (T Herr, V Brasch, J. Jost, C. Wang, et al., 2014; Xu Yi, Q.-F. Yang, Ki Youl Yang, Suh, et al., 2015). However, a decrease in power of the primary soliton is next observed that occurs with an increase in power of the Stokes soliton (red). The same features are also observed experimentally (see figure 5.7 (c)). By studying the intracavity field evolution, the simulation shows the correspondence between these features and the soliton formation (see figure 5.7 (d)). Also, the simulation shows that the primary and Stokes pulses overlap in space and time, i.e., confirmation of optical trapping (see figure 5.7 (e)). The calculated spectra for the primary and Stokes solitons are provided in figure 5.7 (f).

5.5 Summary

The Stokes soliton is only the second type of soliton to be observed in microcavities (beyond dissipative Kerr solitons (T Herr, V Brasch, J. Jost, C. Wang, et al., 2014)) and also represents the first time soliton trapping has been observed in any microcavity. It also represents the first observation of trapping by solitons in different transverse modes in a laser. From a practical viewpoint, the Stokes and primary solitons overlap in space and time, and have a frequency separation that can be engineered to fall within the mid IR range. As a result, this soliton system is potentially interesting for mid IR generation by way of difference frequency generation. Not all devices are observed to produce Stokes solitons. However, dispersion engineering techniques are being advanced (Ki Youl Yang et al., 2016) and should enable control of both observation of the Stokes soliton as well as its placement in the optical spectrum. Indeed, the spectral placement of Stokes solitons in figure 5.3 (d) is largely the result of microcavity diameter control to shift the FSR crossing point. Also, engineering of dispersion could permit a Stokes soliton to form within the same mode family as the primary soliton. The specific implementation described here uses a compact microresonator on a silicon wafer which also suggests that monolithic integration will be possible. In an appropriately phase-matched multi-mode waveguide (optical fiber or monolithic) it should also be possible to observe non-cavity-based Stokes solitons.

²Simulation in this subsection was performed by Q.F. Yang.

Chapter 6

SPATIAL-MODE-INTERACTION INDUCED SOLITON DISPERSIVE WAVE

6.1 Introduction

¹ The nonlinear propagation of optical pulses in dielectric waveguides and resonators induces a wide range of remarkable interactions. One example is dispersive wave generation, the optical analog of Cherenkov radiation. These waves play an essential role in fiber-optic spectral broadeners used in spectroscopy and metrology. Dispersive waves form when a soliton pulse begins to radiate power as a result of higher-order dispersion. If the spectrum of a soliton pulse extends into regions where second-order dispersion changes sign, then radiation into a new pulse, the dispersive wave, may occur at a phase matching wavelength (Wai et al., 1986; Akhmediev and Karlsson, 1995). The generation of these waves is analogous to Cherenkov radiation (Cherenkov, 1934) and extends the spectral reach of optical pulses (Dudley, Genty, and Coen, 2006).

The recent ability to control dispersion in microresonators has allowed accurate spectral placement of dispersive waves relative to a radiating cavity soliton (V Brasch et al., 2016). Such dispersion-engineered control has made possible 2f-3f self referencing of frequency microcombs (Victor Brasch et al., 2016) and octave-spanning double-dispersive waves (Q. Li et al., 2015). Dispersive wave generation in optical fibers has traditionally relied upon control of geometrical dispersion in conjunction with the intrinsic material dispersion of the dielectric (Dudley, Genty, and Coen, 2006) and this same method has been successfully demonstrated in microresonators (V Brasch et al., 2016). Recently, spatial-mode-interactions in multimode-fiber have also been used for this purpose (Cheng et al., 2012; G Manili et al., 2012; Modotto et al., 2015).

In this chapter, spatial mode interactions within a microresonator are used to phase match a soliton pulse to a dispersive wave. These mode interactions often frustrate the formation of solitons (T Herr, V Brasch, J. Jost, Mirgorodskiy, et al., 2014) and, as a result, microresonators are typically designed to minimize or exclude

¹Work presented in this chapter has been published in "Spatial-mode-interaction-induced dispersive waves and their active tuning in microresonators", Optica, 3, 1132 (2016).

entirely the resulting modal avoided crossings (T Herr, V Brasch, J. Jost, C. Wang, et al., 2014; V Brasch et al., 2016; Xu Yi, Q.-F. Yang, Ki Youl Yang, Suh, et al., 2015; P.-H. Wang et al., 2016; Joshi et al., 2016). Also, while dispersive-wave phase matching is normally induced by more gradual variations in dispersion, spatial mode interactions produce spectrally abrupt variations that can activate a dispersive wave in the vicinity of a narrow-band soliton. Below, the demonstration of dispersive wave generation by this process is presented after characterizing two strongly interacting spatial mode families. The phase matching of the dispersive wave to the soliton is then studied including for the first time the effect of soliton frequency offset relative to the pump as is caused by soliton recoil or by the Raman-induced soliton self-frequency shift (Milián et al., 2015; V Brasch et al., 2016; Karpov, Hairun Guo, Kordts, Victor Brasch, M. H. Pfeiffer, et al., 2016; Xu Yi, Q.-F. Yang, Ki Youl Yang, Suh, et al., 2015; Xu Yi, Q.-F. Yang, Ki Youl Yang, and Kerry Vahala, 2016b). It is shown that this mechanism enables active tuning control of the dispersive wave by pump tuning.

6.2 Measurement of strong spatial-mode interaction in microresonator

In the experiment, an ultra-high-Q silica micro-resonator with a 22 GHz FSR (3 mm diameter) was prepared (Lee, T. Chen, et al., 2012). Typical intrinsic quality factors were in excess of 200 million. Mode dispersion was characterized from 183.92 THz (1630 nm) to 199.86 THz (1500 nm) by fiber-taper coupling to a tunable external-cavity diode laser from Santec Corporation (J. Liu et al., 2016) and calibrating the laser frequency scan using a Mach-Zehnder interferometer (Xu Yi, Q.-F. Yang, Ki Youl Yang, Suh, et al., 2015). Multiple mode families were observed and their measured frequency dispersion spectra are presented as the blue points in fig. 6.1 (a). In the plot, similar to previous chapters, a linear dispersion term corresponding to the FSR of the soliton-forming mode family ($\Delta\omega_-$) at mode number zero is subtracted so that a *relative-mode-frequency* is plotted. Mode zero is by convention the mode that is optically pumped to form the soliton. Three weak perturbations of the soliton mode family dispersion are observed for $\mu < 0$. The mode family associated with one of the perturbations is plotted as the nearly vertical line of blue points. A much stronger interaction occurs near $\mu = 165$ causing a strong avoided mode crossing that redirects the soliton-forming branch to lower relative mode frequencies.

The dispersion can be accurately modeled using a coupled mode approach. Accordingly, consider two mode families (*A* and *B*) that initially do not interact and that feature frequency dispersion spectra $\omega_{A,B}(\mu)$. An interaction between the mode fam-

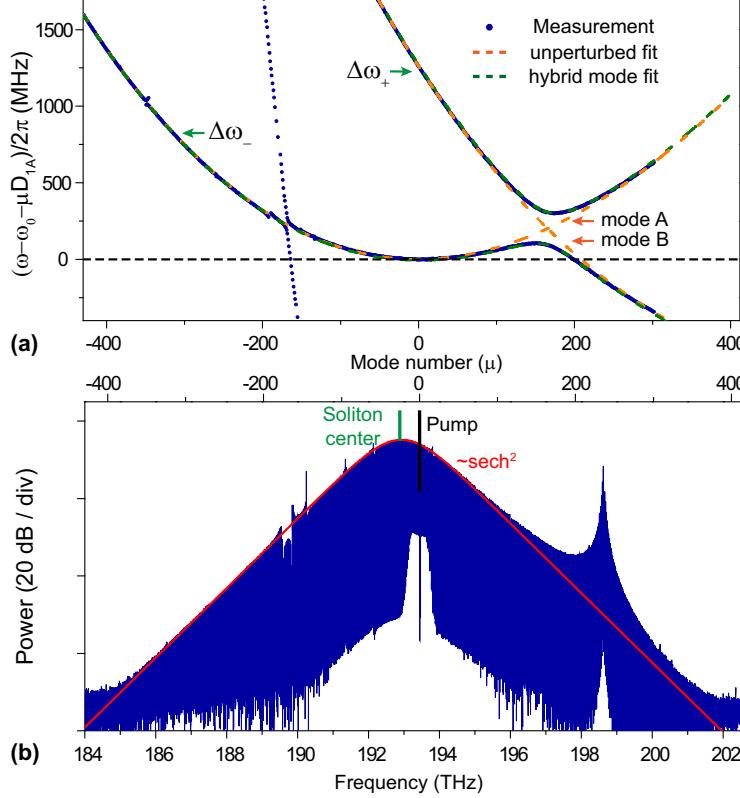


Figure 6.1: Dispersive wave generation by spatial mode interaction. (a) Measured relative-mode-frequencies (blue points) of the soliton-forming mode family and the interaction mode family. Mode number $\mu = 0$ corresponds to the pump laser frequency of 193.45 THz (1549.7 nm). Hybrid mode frequencies calculated from eq. (6.1) are shown in green and the unperturbed mode families are shown in orange. The dashed, horizontal black line determines phase matching for $\omega_{\text{rep}} = D_{1A}$. (b) Measured soliton optical spectrum with dispersive wave feature is shown. For comparison, a Sech^2 fitting is provided in red. The pump frequency (black) and soliton center frequency (green) indicate a Raman-induced soliton self-frequency shift.

ilies is introduced that is characterized by a coupling rate G . The coupling produces two hybrid mode families with upper/lower-branch mode frequencies $\omega_{\pm}(\mu)$ given by the following expression (Hermann A Haus and W. P. Huang, 1991; Wiersig, 2006; Y. Liu et al., 2014),

$$\omega_{\pm}(\mu) = \frac{\omega_A(\mu) + \omega_B(\mu)}{2} \pm \sqrt{G^2 + [\omega_A(\mu) - \omega_B(\mu)]^2/4}. \quad (6.1)$$

Note that in the limit of $|\omega_A(\mu) - \omega_B(\mu)| \gg G$, the frequencies ω_{\pm} approach the frequencies, $\omega_{A,B}(\mu)$, of the non-interacting mode families. This fact is used to determine the form of $\omega_{A,B}(\mu)$ by fitting them within the regions $\mu < 50$ and $\mu > 280$ of the measured dispersion spectra to the following equation: $\omega_{A,B}(\mu) =$

$\omega_{A,B}(0) + D_{1A,B}\mu + D_{2,A,B}\mu^2/2 + D_{3,A,B}\mu^3/6$, which is a third-order Taylor expansion of each mode family about mode number $\mu = 0$. The corresponding fits are shown as the dashed orange curves in fig. 6.1 (a). For mode family A: $D_{1A}/2\pi = 21.9733$ GHz, $D_{2A}/2\pi = 15.2$ kHz, $D_{3A}/2\pi = -14.7$ Hz; and for mode family B: $D_{1B}/2\pi = 21.9654$ GHz, $D_{2B}/2\pi = 18.6$ kHz, $D_{3B}/2\pi = -17.2$ Hz and $\omega_B(0) - \omega_A(0) = 1.261$ GHz. The coupling coefficient, G , is determined by the minimum frequency difference of two branches and gives $G/2\pi=106.5$ MHz. Using these parameters in eq. (6.1), relative-mode-frequencies for the hybrid mode families ($\Delta\omega_{\pm}(\mu) \equiv \omega_{\pm}(\mu) - \omega_0 - \mu D_{1A}$, where $\omega_0 \equiv \omega_A(0)$) are plotted in fig. 6.1 (a) (green) and show good agreement with the measurements (blue points). An improved fitting is possible using a least squares approach in eq. (6.1). As an aside, the mode two families ($\Delta\omega_{\pm}$) were observed to couple nearly equally to the tapered fiber with approximately 20% transmission.

6.3 Observation of dispersive wave in microresonator

The soliton generated here is a dissipative Kerr soliton (DKS) in microresonators (T Herr, V Brasch, J. Jost, C. Wang, et al., 2014; V Brasch et al., 2016; Xu Yi, Q.-F. Yang, Ki Youl Yang, Suh, et al., 2015; P.-H. Wang et al., 2016; Joshi et al., 2016). This type of dissipative soliton (Ankiewicz and Akhmediev, 2008) forms through a double balance of second-order dispersion with the Kerr nonlinearity and cavity loss with Kerr-induced parametric gain (T Herr, V Brasch, J. Jost, C. Wang, et al., 2014). The optical spectrum of a DKS pumped at $\mu = 0$ (193.45 THz or 1549.7 nm) using a fiber laser is presented in fig. 6.1 (b). The soliton is triggered and stabilized using the method described in (Xu Yi, Q.-F. Yang, Ki Youl Yang, Suh, et al., 2015; Xu Yi, Q.-F. Yang, Ki Youl Yang, and Kerry Vahala, 2016a). For comparison, the ideal Sech^2 spectral profile that would occur under conditions of pure second-order dispersion (T Herr, V Brasch, J. Jost, C. Wang, et al., 2014; Xu Yi, Q.-F. Yang, Ki Youl Yang, Suh, et al., 2015; V Brasch et al., 2016) (mode A dashed orange curve in fig. 6.1 (a)) is provided as the red envelope in fig. 6.1 (b). A small soliton self-frequency shift (SSFS) (Milián et al., 2015; V Brasch et al., 2016; Karpov, Hairun Guo, Kordts, Victor Brasch, M. H. Pfeiffer, et al., 2016; Xu Yi, Q.-F. Yang, Ki Youl Yang, Suh, et al., 2015; Xu Yi, Q.-F. Yang, Ki Youl Yang, and Kerry Vahala, 2016b) is apparent in the measured soliton spectrum as indicated by the spectral displacement of the soliton spectral center relative to the pumping frequency. The perturbations to the ideal spectral envelope that are caused by both the weak modal crossings ($\mu < 0$) as well as the strong avoided modal crossing are

apparent. For $\mu > 0$ a dispersive wave feature is apparent (maximum near 198.62 THz or $\mu = 235$). In contrast to the weak avoided crossing induced distortion for $\mu < 0$, the dispersive wave results from a resonance condition (see discussion below) and the comb teeth are accordingly enhanced in strength. The coherence of the soliton and dispersive wave is verified by measuring the electrical spectrum of the detected soliton and dispersive-wave pulse train using a photodetector (figure 6.2).

6.4 Phase-matching condition of dispersive wave in microresonator

When the soliton propagates in a optical fiber or waveguide, it emits a dispersive wave at the wavelength whose group velocity is identical to soliton group velocity. At this wavelength, the momentum is conserved when a soliton photon is converted to a dispersive wave photon, and this greatly enhances the dispersive wave emission. In the microresonator, phase matching between the soliton and the dispersive wave occurs when the μ^{th} soliton line at $\omega_p + \omega_{\text{rep}}\mu$ is resonant with the μ^{th} frequency of the soliton-forming mode family, i.e., $\omega_p + \omega_{\text{rep}}\mu = \omega_-(\mu)$. Under this condition, the dispersive wave emission is enhanced by the resonator. The detailed derivation will be given in section 6.5. As an aside, the Kerr shift for mode μ is much smaller than other terms in this analysis and is neglected in the phase matching condition. So that it is possible to use a graphical interpretation of the phase matching condition based on the relative-mode-frequency of fig. 6.1 (a), $\omega_0 + D_{1A}\mu$ is subtracted from both sides of the phase matching condition to give the following condition:

$$\Delta\omega_-(\mu) = (\omega_{\text{rep}} - D_{1A})\mu - \delta\omega, \quad (6.2)$$

where $\delta\omega \equiv \omega_0 - \omega_p$ is the detuning of the resonator relative to the pump frequency.

If the soliton repetition frequency equals the FSR at $\mu = 0$ (i.e., $\omega_{\text{rep}} = D_{1A}$), then the r.h.s. of eq. (6.2) is the horizontal dashed black line in fig. 6.1 (a) (repeated in fig. 6.3 (a)). Under these circumstances the dispersive wave phase matches to the soliton pulse at the crossing of that line with the soliton-forming mode branch. However, while the mode dispersion profile ($\Delta\omega_-(\mu)$) is determined entirely by the resonator geometry and the dielectric material properties, the soliton repetition rate ω_{rep} depends upon frequency offsets between the pump and the soliton spectral maximum. Defining this offset as Ω , the repetition frequency is given by the following equation (A. B. Matsko and Maleki, 2013; Jang, Erkintalo, Coen, et al., 2015):

$$\omega_{\text{rep}} = D_{1A} + \frac{D_{2A}}{D_{1A}}\Omega. \quad (6.3)$$

The offset frequency Ω can be caused by soliton recoil due to a dispersive wave and also by the Raman-induced soliton self-frequency shift (SSFS) (Milián et al., 2015; V Brasch et al., 2016; Karpov, Hairun Guo, Kordts, Victor Brasch, M. H. Pfeiffer, et al., 2016; Xu Yi, Q.-F. Yang, Ki Youl Yang, Suh, et al., 2015; Xu Yi, Q.-F. Yang, Ki Youl Yang, and Kerry Vahala, 2016b). In this work, Ω is dominated by the Raman interaction, because the typical dispersive wave power is $< 0.2\%$ of the soliton power, causing a negligible dispersive wave recoil (recoil of less than one mode). Photo-thermal-induced change in D_{1A} is another possible contribution that will vary ω_{rep} as pumping is varied (Del'Haye et al., 2008). However, the thermal tuning of D_{1A} is estimated to be ~ -4.5 kHz/mW (by measurement of resonant frequency photo-thermal shift of ~ -40 MHz/mW). With total soliton power less than 1 mW (Xu Yi, Q.-F. Yang, Ki Youl Yang, Suh, et al., 2015), this photo-thermal-induced change in repetition frequency is negligible compared with that caused by the Raman self-frequency-shift.

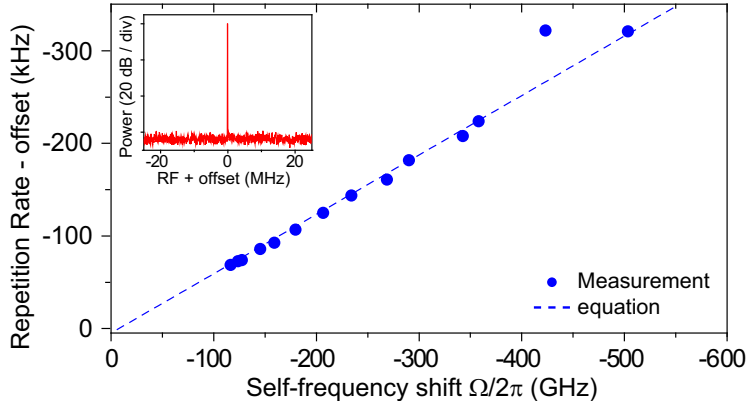


Figure 6.2: Measured soliton repetition rate (blue points) is plotted versus soliton self-frequency shift. The dashed blue line is a plot of eq. (6.3). The offset for the repetition rate vertical scale is $D_{1A} = 21.9733$ GHz. A typical microwave beatnote of the photo-detected soliton and dispersive wave is shown in the inset (resolution bandwidth is 10 kHz).

Combining eqs. (6.2) and (6.3) gives the following phase matching condition:

$$\Delta\omega_-(\mu) = \mu \frac{D_{2A}}{D_{1A}} \Omega - \delta\omega. \quad (6.4)$$

The Raman-induced SSFS is a negative frequency shift ($\Omega < 0$) with a magnitude that increases with soliton bandwidth and average power. Accordingly, with increasing soliton power (and bandwidth), the plot of the r.h.s. of eq. (6.4) versus μ acquires an increasingly negative slope (green dashed line in fig. 6.3 (a)). The phase

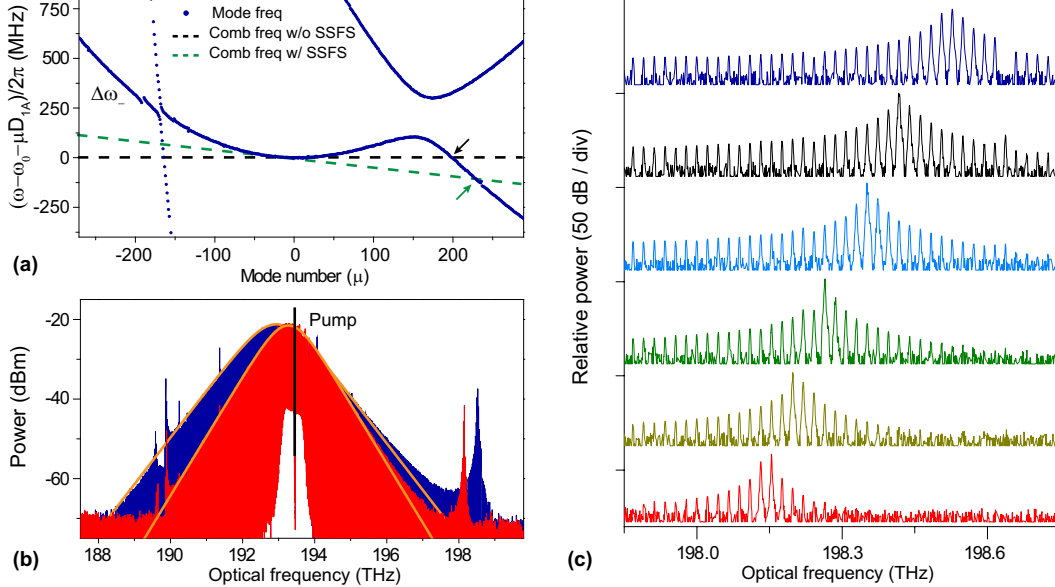


Figure 6.3: Dispersion wave phase matching condition. (a) Soliton and interaction mode dispersion curves are shown with phase matching dashed lines (see eq. (6.4)). The black line is the case where $\omega_{\text{rep}} = D_{1A}$ and the green line includes a Raman-induced change in ω_{rep} . The intersection of the soliton branch with these lines is the dispersive wave phase matching point (arrows). (b) Soliton optical spectra corresponding to small (red) and large (blue) cavity-laser detuning ($\delta\omega$). Sech² fitting of the spectral envelope is shown as the orange curves. (c) Dispersive wave spectra with cavity-laser detuning (soliton power and bandwidth) increasing from lower to upper trace.

matching mode number, $\mu = \mu_{DW}$, therefore also increases (i.e., the dispersive wave shifts to a higher optical frequency) with increasing soliton power. The two soliton spectra presented in fig. 6.3 (b) illustrate this effect (red spectrum is lower power and has the lower dispersive wave frequency). Fig. 6.3 (c) also shows a series of higher-resolution scans of the dispersive wave with soliton power increasing from the lower to upper scans and is, again, consistent with the prediction.

The frequency shift, Ω , repetition frequency, ω_{rep} , and the dispersive wave frequency were measured for a series of soliton powers that were set by controlling the cavity-pump detuning frequency ($\delta\omega$) using the method in ref. (Xu Yi, Q.-F. Yang, Ki Youl Yang, Suh, et al., 2015; Xu Yi, Q.-F. Yang, Ki Youl Yang, and Kerry Vahala, 2016a). ω_{rep} was measured using an electrical spectrum analyzer after photodetection of the resonator optical output. The offset frequency Ω was measured on an optical spectrum analyzer by fitting the center of optical spectrum (see fig. 6.1 (b)) to determine the spectral maximum and then measuring the wavelength offset relative

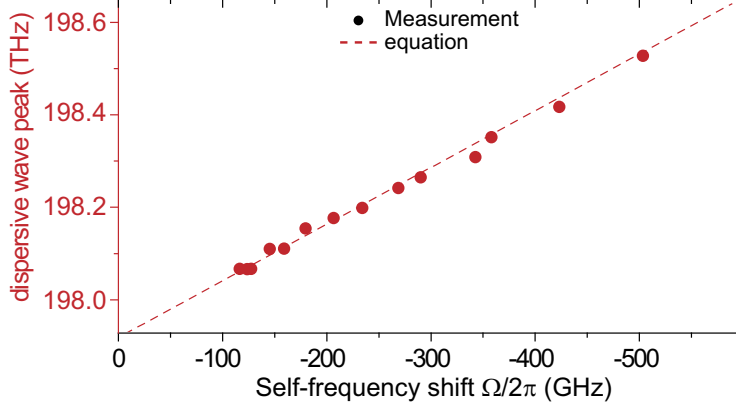


Figure 6.4: Measured dispersive-wave peak frequencies (red points) are plotted versus soliton self-frequency shift. The dashed red line uses eq. (6.4) to determine the dispersive wave frequency ($\approx \mu_{DW} D_{1A} + \omega_0$) as described in the text.

to the pump. This same spectral fitting also allows determination of the soliton pulse width, τ_s (Xu Yi, Q.-F. Yang, Ki Youl Yang, Suh, et al., 2015). Once the soliton pulselwidth is known, the pump-resonator frequency detuning operating point can be inferred using $\delta\omega \approx D_2/2D_1^2\tau_s^2$ (Xu Yi, Q.-F. Yang, Ki Youl Yang, Suh, et al., 2015). $\delta\omega/2\pi$ ranged between 7.8 to 21.1 MHz during the measurement.

The soliton repetition rate is plotted versus Ω in fig. 6.2 and is fitted using eq. (6.3). The intercept closely agrees with D_{1A} and the slope allows determination of $D_{2A}/2\pi = 14.7$ kHz (in good agreement with 15.2 kHz from fitting to the measured dispersion curve in fig. 6.1 (a)). The dispersive wave frequency is also plotted in fig. 6.4 versus Ω and compared with a calculation using eq. (6.4). In this calculation, $\Delta\omega_-(\mu)$ is approximated using a linear expansion in μ near $\mu = 200$. Also, a -60 kHz offset is added to $D_{1A}/2\pi$ in $\Delta\omega_-(\mu)$ due to the calibration uncertainty ($\sim \pm 100$ kHz) of FSR (Jiang Li, Lee, Ki Youl Yang, et al., 2012). No other free parameters are used in the plot.

6.5 Formalism of dispersive wave in microresonator

In this section, we will introduce a toy model to justify the phase matching condition and also calculate dispersive wave power in microresonator. For simplicity, we only consider a transverse mode family that has a mode spectrum capable of producing dispersive wave without spatial-mode interaction (e.g. material or geometry dispersion (V Brasch et al., 2016)). Using eq. (2.4) from Chapter 2, the equation of

motion for the optical field of k -th comb line can be expressed as

$$\frac{da_k}{dT} = -(i\omega_k - i\zeta_k + \kappa/2)a_k + ig \sum_{\mu_1, \mu_2} a_{\mu_1} a_{\mu_2} a_{\mu_1 + \mu_2 - k}^*, \quad (6.5)$$

where ω_k is the frequency of k -th cavity mode and $\zeta_k = \omega_p + \omega_{\text{rep}}k$ is the frequency of k -th comb line. Also since we are considering dispersive wave generation, we have excluded the situation of $k = 0$ and dropped the pump laser term in eq. (2.4).

To calculate the dispersive wave with perturbation method, we further make the assumption that the dispersive wave is relatively weak compared with soliton and does not disturb the Sech² shape of the soliton spectrum. Therefore, we can substitute the non-perturbed soliton from eq. (2.33) in the last term of eq. (6.5),

$$a_{\mu_x,0} = \frac{B_s \tau_s D_1}{2} \operatorname{sech}\left(\frac{\pi \tau_s}{2}(D_1 \mu_x - \Omega)\right) e^{i\varphi}, \quad (6.6)$$

where $a_{\mu_x,0}$ is the non-perturbed soliton field for μ_x -th comb line and τ_s is the soliton pulse width. Insert eq. (6.6) to the last term in eq. (6.5) and calculate the sum by converting it to integral, we have

$$\begin{aligned} f_k &\equiv ig \sum_{\mu_1, \mu_2} a_{\mu_1,0} a_{\mu_2,0} a_{\mu_1 + \mu_2 - k,0}^* \\ &= i \frac{D_2}{4D_1^2} [(D_1 k - \Omega)^2 + \frac{1}{\tau_s^2}] B \tau_s D_1 \operatorname{sech}\left(\frac{\pi \tau_s}{2}(D_1 k - \Omega)\right) e^{i\varphi}, \end{aligned} \quad (6.7)$$

where g has been replaced using equation $B^2 \tau_s^2 = D_2/g D_1^2$, which holds for the soliton (see eq. (4.16)). Finally, by using eq. (4.17): $\delta\omega = \frac{D_2}{2D_1^2} (\frac{1}{\tau_s^2} + \Omega^2)$, f_k can be further reduced to

$$f_k = i(\omega_{k,0} - \zeta_k) a_{k,0}, \quad (6.8)$$

where we have defined $\omega_{k,0}$ as the mode frequency that consists only linear and group velocity dispersion:

$$\omega_{k,0} \equiv \omega_0 + D_1 k + \frac{1}{2} D_2 k^2. \quad (6.9)$$

As a result, we have a steady-state solution of a_k from eq. (6.5):

$$a_k = \frac{i(\omega_{k,0} - \zeta_k)}{i(\omega_k - \zeta_k) + \kappa/2} a_{k,0}. \quad (6.10)$$

As a physical check, equation (6.10) is consistent with the soliton result in Chapters 2 to 4. When resonator has only linear and second order dispersion, we have $\omega_k = \omega_{k,0}$ and a self-consistent result of $a_k = a_{k,0}$ assuming $\omega_k - \zeta_k \gg \kappa$.

When higher order dispersion is considered, we can see that a_k reaches its maximum at $\omega_k - \zeta_k = 0$, where k -th comb frequency is on resonance with k -th mode frequency. This phase matching condition for dispersive wave is identical with eq. (6.2). In addition, the dispersive wave power is enhanced by a factor of $4(\omega_{k,0} - \zeta_k)^2/\kappa^2$ from the non-perturbed soliton solution at the phase matching wavelength. For the dispersive wave presented in figure 6.1, the phase matching is at $k = 235$ and $\omega_{k,0} - \zeta_k$ approximately equals to the frequency difference between unperturbed mode A and lower branch at $\mu = k = 235$, $(\omega_{k,0} - \zeta_k)/2\pi \approx 407 - (-128) = 535$ MHz. Further substitute $\kappa/2\pi = 2$ MHz for loaded $Q = 100$ million, we have arrived at the power enhancement for the dispersive wave as $\approx 3 \times 10^5 \approx 54$ dB. In figure 6.1 (b), the dispersive wave power at $\mu = k = 235$ is 40 dB higher than the Sech² fit, indicating a 40 dB enhancement from unperturbed soliton power. The mismatch between theory and experiment could come from the fact that the dispersive wave in figure 6.1 is formed from spatial-mode interaction, and therefore a significant portion of the optical field is in the upper branch which cannot generate dispersive wave (Andrey Matsko et al., 2016).

6.6 Summary

Spatial mode interactions provide a way to phase match a DKS to a dispersive wave. Interacting mode families must be closely matched in free-spectral-range (i.e., $D_{1A} \approx D_{1B}$) so that the soliton comb lines which initially form on mode family A can transition to mode family B (see fig. 6.1 (a)). As a second condition, the coupling strength G (see eq. (6.1)) must be large enough to create hybrid modes near the modal avoided crossing that are strong admixtures of the A and B modes. For example, this mixing allows the comb of lines to grow along the lower branch (beyond $\mu = 165$ in fig. 6.1 (b)) after initiating near $\mu = 0$. The degree to which these interactions can be engineered and controlled is an active area of investigation. Geometrical control of dispersion over broad spectral spans using microfabrication methods (Ki Youl Yang et al., 2016) could be applicable for dispersive wave control.

As a summary, it has been shown theoretically and through measurement that the dispersive wave frequency can be actively tuned because of coupling to the soliton offset frequency Ω . In the silica microcavities tested here, this offset is dominated by the Raman-induced SSFS and the dispersive wave is predicted and observed to tune to higher frequencies with increasing soliton power and bandwidth. As a further test of the theory, the dependence of repetition frequency on SSFS was combined with measurement to extract resonator dispersion parameters, which compared well

with direct measurements based on resonator dispersion characterization. The dispersion induced by modal interactions in the tested device has been measured and accurately modeled using a coupled-mode formalism. While the soliton existence limitations imposed upon placement of dispersive wave are under investigation, it seems possible that more complex resonator designs could not only engineer the placement of these crossings, but also locate multiple avoided crossings near a soliton so as to induce multiplets of dispersive waves.

Chapter 7

SINGLE-MODE DISPERSIVE WAVE AND ITS NONLINEAR DYNAMICS IN MICRORESONATOR

7.1 Introduction

¹In microcomb research (P Del’Haye et al., 2007; T. J. Kippenberg, Ronald Holzwarth, and SA Diddams, 2011), the dissipated Kerr soliton formation produces phase-locked spectra with reproducible envelopes, as required in frequency comb applications (W Liang, Eliyahu, et al., 2015; Pascal Del’Haye, Coillet, Tara Fortier, et al., 2016; Victor Brasch et al., 2016; Suh et al., 2016; Marin-Palomo et al., 2016). Moreover, their unusual properties and interactions create a rich landscape for research in nonlinear optical phenomena (Jang, Erkintalo, Murdoch, et al., 2013; Xue et al., 2015; V Brasch et al., 2016; Karpov, Hairun Guo, Kordts, Victor Brasch, M. H. Pfeiffer, et al., 2016; Xu Yi, Q.-F. Yang, Ki Youl Yang, and Kerry Vahala, 2016b; Q.-F. Yang et al., 2016; Q.-F. Yang et al., 2017; H Guo et al., 2016; Chengying Bao, Jaramillo-Villegas, et al., 2016; M. Yu et al., 2016; Cole et al., 2016). In the previous chapters, we have gone through a few such phenomena, including the Raman-induced soliton-self-frequency-shift (SSFS) and dispersive-wave generation, which are important to the work in this chapter.

As introduced in Chapter 4, The Raman SSFS causes a spectral red shift of the soliton. In optical fiber systems, this shift continuously increases with propagation distance (Mitschke and Mollenauer, 1986; J. P. Gordon, 1986); however, in microresonators the shift is fixed and depends upon soliton power (Milián et al., 2015; Karpov, Hairun Guo, Kordts, Victor Brasch, M. H. Pfeiffer, et al., 2016; Xu Yi, Q.-F. Yang, Ki Youl Yang, and Kerry Vahala, 2016b; Anderson et al., 2016). Dispersive waves also occur in optical fibre systems (Wai et al., 1986) where they are an important process in continuum generation (Dudley, Genty, and Coen, 2006) and have been used to study general nonlinear phenomena (Mussot et al., 2014). They are formed when a soliton radiates into a spectral region of normal dispersion and can be understood as the optical analog of Cherenkov radiation (Akhmediev and Karlsson, 1995). In microcavities, the Raman SSFS enables controlled fine-tuning of the wavelength of a dispersive wave (Q.-F. Yang et al., 2016). Dispersive waves

¹The work presented in this chapter has been published in "Single-mode dispersive waves and soliton microcomb dynamics", Nature Communications, 8, 14869 (2017).

provide a powerful way to spectrally broaden a soliton within a microresonator as a precursor to self referencing (Q. Li et al., 2015; Victor Brasch et al., 2016). Their formation also induces soliton recoil (Akhmediev and Karlsson, 1995) which, similar to SSFS, causes a frequency shift in the spectral centre of the soliton (V Brasch et al., 2016; Karpov, Hairun Guo, Kordts, Victor Brasch, M. H. Pfeiffer, et al., 2016).

Dispersive waves normally consist of an ensemble of modes that are phase matched to a soliton. As introduced in previous chapter, this phase matching can be assisted by avoided mode crossings in microcavities (A. B. Matsko, Wei Liang, et al., 2016; Q.-F. Yang et al., 2016). In this chapter, an avoided-mode crossing is used to excite a dispersive wave consisting of a single cavity mode. The coupling of this single-mode dispersive wave to the soliton is strongly influenced by the total soliton frequency shift produced by the combined Raman-induced SSFS and the dispersive-wave recoil. The combination is shown to induce hysteresis behavior in soliton properties. Included in this behavior, there is an operating point of improved pulse-rate stability (a quiet point) where the coupling of repetition rate and cavity-pump detuning is greatly reduced. Pulse-rate stability is centrally important in many frequency comb applications (Papp, Beha, et al., 2014; W Liang, Eliyahu, et al., 2015; Suh et al., 2016). Coupling of pulse rate and cavity-pump detuning through avoided-mode-crossing recoil effects has been observed in crystalline resonators (Lucas, J. D. Jost, and T. J. Kippenberg, 2016). Also, the fundamental contributions to phase noise in the pulse train have been considered theoretically (A. B. Matsko and Maleki, 2013). However, technical noise mechanisms are also present. For example, DKS generation using on-chip silica resonators exhibits phase noise that tracks in spectral profile the phase noise of the optical pump (Xu Yi, Q.-F. Yang, Ki Youl Yang, Suh, et al., 2015). The quiet operation point is shown to reduce technical noise contributions to the soliton pulse repetition rate. Both this regime of operation and the hysteresis behavior are measured and modeled theoretically.

7.2 Observation of single mode dispersive waves

A silica whispering-gallery resonator (Lee, T. Chen, et al., 2012) is used for soliton generation. The devices feature a free-spectral-range (FSR) of approximately 22 GHz (3 mm diameter resonator) and have intrinsic Q -factors around 250 million. Specific details on soliton formation in these resonators are given in chapter III. The resonators support multiple, transverse mode families. It is essential that the soliton-forming mode family feature dispersion that is primarily second-order and anomalous (T Herr, V Brasch, J. Jost, Mirgorodskiy, et al., 2014). To characterize

the frequency spectrum of the resonator, mode frequencies were measured from 190.95 THz (1570 nm) to 195.94 THz (1530 nm) using an external-cavity diode laser (ECDL) calibrated by a fiber Mach-Zehnder interferometer (MZI) (Xu Yi, Q.-F. Yang, Ki Youl Yang, Suh, et al., 2015). This provides a set of mode frequencies $\{\omega_{\mu,s}\}$ for each spatial mode family “*s*” with μ as the mode index.

The mode family frequency data are presented in fig. 7.1 (a) by plotting the relative-mode-frequency, $\Delta\omega_{\mu,s} \equiv \omega_{\mu,s} - \omega_0 - \mu D_1$ versus mode index μ where ω_0 and D_1 are specific to the soliton-forming mode family. ω_0 is the frequency of the mode (set to have index $\mu = 0$) that is optically pumped to produce the soliton, and D_1 is the FSR of the soliton-forming mode family at $\mu = 0$ (note: μ is a relative and not an absolute mode index). By plotting the data in this way the second- and higher-order dispersion of the soliton-forming mode family become manifest. To illustrate, the relative-mode-frequency of the soliton mode family is fit with a green, dashed parabolic curve of positive curvature in fig. 7.1 (a) showing that it features anomalous second-order dispersion over a wide range of mode numbers.

A second mode family also appears in fig. 7.1 (a) and causes an avoided-mode-crossing near $\mu = 72$. Hybridization of this “crossing-mode” mode family with the soliton mode family occurs near the avoided crossing (Y. Liu et al., 2014; Q.-F. Yang et al., 2016). The relative-mode-frequencies of the unperturbed soliton-forming mode family and crossing-mode family are denoted as $\Delta\omega_{\mu A}$ and $\Delta\omega_{\mu B}$. Over the range of mode indices measured $\Delta\omega_{\mu A} = \frac{1}{2}D_2\mu^2$ where D_2 is the second-order dispersion at $\mu = 0$. The lower (upper) branch of the hybrid mode family is denoted by $\Delta\omega_{\mu-}$ ($\Delta\omega_{\mu+}$). Avoided mode crossing behavior has been intensively studied in the context of DKS formation and can interfere with soliton generation by creation of distortions in the dispersion spectrum (T Herr, V Brasch, J. Jost, Mirgorodskiy, et al., 2014; Ramelow et al., 2014; S.-W. Huang et al., 2016). In the present system the avoided-mode-crossing induces only minimal distortion in the otherwise parabolic shape of the soliton-forming mode family. Soliton spectra produced on this mode family by pumping at $\mu = 0$ are shown in fig. 7.1 (b) along with theoretical sech^2 spectral envelopes predicted for DKSs. As an aside, the horizontal scales in fig. 7.1 (a) and fig. 7.1 (b) are identical and the location of the $\mu = 0$ pumping mode is indicated by a vertical dashed line in fig. 7.1 (b). At certain cavity-laser detuning, the single-mode dispersive wave is apparent (blue trace in fig. 7.1 (b)).

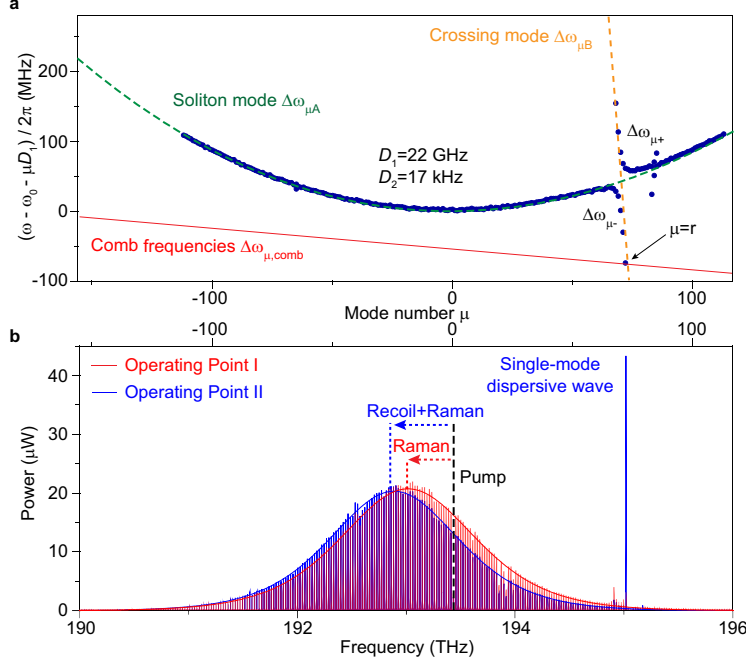


Figure 7.1: (a) Measured relative mode frequencies are shown as blue points (Xu Yi, Q.-F. Yang, Ki Youl Yang, Suh, et al., 2015). The green and yellow dashed lines represent the fitted relative mode frequencies ($\Delta\omega_{\mu A}$ and $\Delta\omega_{\mu B}$) of the unperturbed soliton-forming mode family A and crossing mode family B, respectively. Relative mode frequencies for upper and lower branch hybrid-modes are $\Delta\omega_{\mu+}$ and $\Delta\omega_{\mu-}$. The red line illustrates the frequencies of a hypothetical soliton frequency comb. A non-zero slope on this line arises from the repetition rate change relative to the FSR at mode $\mu = 0$. (b) Measured optical spectra at soliton operating points I and II, corresponding to closely matched cavity-pump detuning frequencies, $\delta\omega$. A strong single-mode dispersive wave at $\mu = 72$ is observed for operating point II and causes a soliton recoil frequency shift. This frequency shift adds to the shift resulting from the Raman-induced SSFS.

7.3 Soliton recoil and hysteresis

Also shown in fig. 7.1 (a) are the comb frequencies associated with a hypothetical soliton spectrum plotted in the relative frequency frame. This comb line is given by

$$\Delta\omega_{\mu,\text{comb}} = \omega_{\mu,\text{comb}} - \omega_0 - D_1\mu = (\omega_{\text{rep}} - D_1)\mu - \delta\omega, \quad (7.1)$$

where $\omega_{\mu,\text{comb}} = \mu\omega_{\text{rep}} + \omega_p$ is the frequency of μ -th comb line, ω_{rep} is the soliton repetition frequency, ω_p is the pump frequency, ω_0 is the frequency of the cavity mode that is being pumped, and $\delta\omega \equiv \omega_0 - \omega_p$ is the cavity-pump detuning frequency. It is necessary to distinguish between relative frequencies for the soliton comb and the resonator modes because the frequency components of the soliton comb are strongly red-detuned relative to the cold-cavity mode frequencies by the Kerr nonlinearity.

Indeed, dispersive waves typically form when a set of modes break this rule and becomes resonant with a set of comb lines. A limiting case of this condition is shown in fig. 7.1 (a), where the occurrence of an isolated resonance between a hybrid mode with relative frequency $\Delta\omega_{r-}$ and a comb line at $\Delta\omega_{r,\text{comb}}$ is illustrated. The equation of motion for the hybrid mode field amplitude h_{r-} is derived in detail in section 7.5 and has have the following form:

$$\frac{dh_{r-}}{dt} = [-i\Delta\omega_{r-} - \frac{\kappa_{r-}}{2}]h_{r-} + f_r e^{-i\Delta\omega_{r,\text{comb}}t}, \quad (7.2)$$

where κ_{r-} is its loss rate and f_r is an effective pumping term associated with the soliton comb line. The pumping term is given by $f_r = i\Gamma(\Delta\omega_{rA} - \Delta\omega_{r,\text{comb}})a_r$, where a_r is the field amplitude of the unperturbed soliton hyperbolic solution at $\mu = r$. Also, the Kerr-effect shift of h_{r-} is of order 10 kHz and is therefore negligible in comparison to κ_{r-} .

Because the damping rate κ_{r-} is low (i.e., the mode has a high optical Q -factor) slight shifts in the slope of the comb frequency line (equivalently, shifts of $\Delta\omega_{r,\text{comb}}$ relative to $\Delta\omega_{r-}$) will cause large changes in the power coupled to the hybrid mode. These changes are observable in fig. 7.1 (b) where a strong spectral line appears in the case of the blue soliton spectrum. Note that scattering from the soliton into the spectral line is strong enough so that the power in the line is greater than the comb line power near the spectral center of the soliton, itself. The strong spectral line can be understood as a single-mode dispersive wave and it induces a recoil in the spectral center of the soliton. This recoil contribution is indicated for the blue soliton spectrum in the figure. In the case of the red soliton spectrum, the operating point was changed and the resonance between the soliton and the mode is diminished. Accordingly, most of the spectral shift in this case results from the Raman SSFS.

A change in the slope of the soliton comb line will occur when the soliton repetition frequency, ω_{rep} , is changed (see eq. (7.1)). On account of second order dispersion ω_{rep} depends linearly on the frequency offset, Ω , of the soliton spectral maximum relative to the pump frequency (A. B. Matsko and Maleki, 2013; Q.-F. Yang et al., 2016). This frequency offset has contributions from both the Raman SSFS, Ω_{Raman} , and the dispersive-wave recoil, Ω_{Recoil} (i.e., $\Omega = \Omega_{\text{Raman}} + \Omega_{\text{Recoil}}$). Accordingly, the soliton repetition rate is given by

$$\omega_{\text{rep}} = D_1 + \frac{D_2}{D_1}(\Omega_{\text{Raman}} + \Omega_{\text{Recoil}}), \quad (7.3)$$

where D_2 (the second order dispersion of soliton-forming mode family at $\mu = 0$) is measured to be 17 kHz from fig. 7.1 (a). Substituting for the repetition rate in the comb line expression (eq. (7.1)) gives

$$\Delta\omega_{\mu,\text{comb}} = \frac{\mu D_2}{D_1}(\Omega_{\text{Raman}} + \Omega_{\text{Recoil}}) - \delta\omega. \quad (7.4)$$

It is shown in derivation in section 7.5 (eq. (7.25)) that the soliton recoil frequency has a linear dependence on the hybrid mode power,

$$\Omega_{\text{Recoil}} = \gamma |h_{r-}|^2 = -r \frac{\kappa_B D_1}{\kappa_A E} |h_{r-}|^2, \quad (7.5)$$

where κ_A and κ_B denote the power loss rates of the family A and family B modes, respectively; and E is the circulating soliton energy.

Solving eq. (7.2) for the steady-state power in the hybrid mode at the soliton comb line frequency and using eq. (7.4)-(7.5) gives the following result:

$$|h_{r-}|^2 = \frac{|f_r|^2}{(\Delta\omega_{r-} + \delta\omega - \frac{r D_2}{D_1} [\Omega_{\text{Raman}} + \gamma |h_{r-}|^2])^2 + \frac{\kappa_r^2}{4}}. \quad (7.6)$$

Equation (7.6) suggests that a bistable state and hysteresis behavior in the dispersive-wave power is possible when varying the soliton operating point. Consistent with this possibility, it is noted that the two soliton spectra in fig. 7.1 (b) (blue and red), which show very different dispersive wave powers, were produced at nearly identical detuning frequencies, $\delta\omega$. A more detailed survey of the dispersive wave power behavior is provided in fig. 7.2 (a) and is again consistent with a hysteresis behaviour versus detuning. Moreover, since the total spectral shift of the soliton is given by $\Omega = \Omega_{\text{Raman}} + \Omega_{\text{Recoil}} = \Omega_{\text{Raman}} + \gamma |h_{r-}|^2$, a corresponding behavior is observed in the overall soliton spectral shift (fig. 7.2 (b)). Theoretical fits are provided in fig. 7.2 (a) and fig. 7.2 (b) using eq. (7.6). The fitting procedure and parameter values are provided in section 7.5.

In plotting the data, the detuning frequency, $\delta\omega/2\pi$, was determined from the measured total soliton spectral shift (Ω) and pulse width (τ_s) using the relation $\delta\omega = (D_2/2D_1^2)(1/\tau_s^2 + \Omega^2)$. This expression is a generalization of a relationship derived elsewhere (Xu Yi, Q.-F. Yang, Ki Youl Yang, and Kerry Vahala, 2016b). The generalization extends the shift Ω to include both the SSFS and the recoil and is derived as eq.(4.17) in chapter IV. As an aside, the pulse width is determined by fitting the soliton optical spectrum (Xu Yi, Q.-F. Yang, Ki Youl Yang, Suh, et al., 2015).

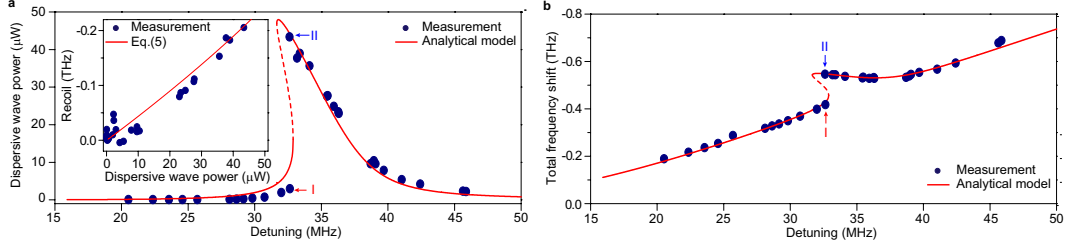


Figure 7.2: Dispersion-wave power (a) and soliton spectral center frequency shift (b) versus cavity-pump detuning. Inset in (a): Measured (blue dots) and theoretical (red line) recoil frequency versus the dispersive wave power.

Likewise, the recoil frequency, Ω_{Recoil} , can also be extracted from the data as $\Omega - \Omega_{\text{Raman}}$ by first using the soliton pulse width to determine the Raman shift using $\Omega_{\text{Raman}} = -8\tau_R D_2 / 15\kappa_A D_1^2 \tau_s^4$. A plot of the recoil shift determined this way versus the dispersive-wave power is given as the inset in fig. 7.2 (a) and verifies the linear dependence (eq.(7.5)). Eq. (7.5) is also plotted for comparison using parameters given in the section 7.5. As an aside, the Raman shift formula noted above is also a generalization of a result proven elsewhere (Xu Yi, Q.-F. Yang, Ki Youl Yang, and Kerry Vahala, 2016b). Curiously, as shown in section 7.5, this formula maintains its previous form in the presence of the dispersive wave.

Within narrow detuning frequency bands in the vicinity of the hysteresis both measurements and calculations show that the total cavity power (soliton and dispersive-wave contributions) can decrease with increasing cavity-pump detuning as opposed to increasing with detuning as is typical for a soliton. Under these special conditions, the pump-cavity detuning will no longer be dynamically stable on account of the thermal nonlinearity (Carmon, L. Yang, and Kerry Vahala, 2004). Evidence of this was observable in the current work as it was not possible to completely map out the theoretically predicted hysteresis curves.

While the present results are produced using a dispersive wave that is blue-detuned relative to the soliton spectral maximum, the hysteresis behaviour is also predicted to occur for a red-detuned dispersive wave. However, in the red-detuned case, the orientation of the curve in fig. 7.2 (a) is reversed with respect to the detuning frequency. The essential feature for appearance of the hysteresis is that the recoil advances and retreats versus detuning. As a result, the existence of hysteresis behaviour predicted in eq. (7.6) is not limited to microresonator materials having a strong Raman SSFS. It is also predicted to occur, for example, in crystalline resonators given an appropriate avoided-mode crossing. The requirements imposed

on the device and mode crossing for this to occur are discussed further below.

7.4 Application in soliton repetition rate noise reduction

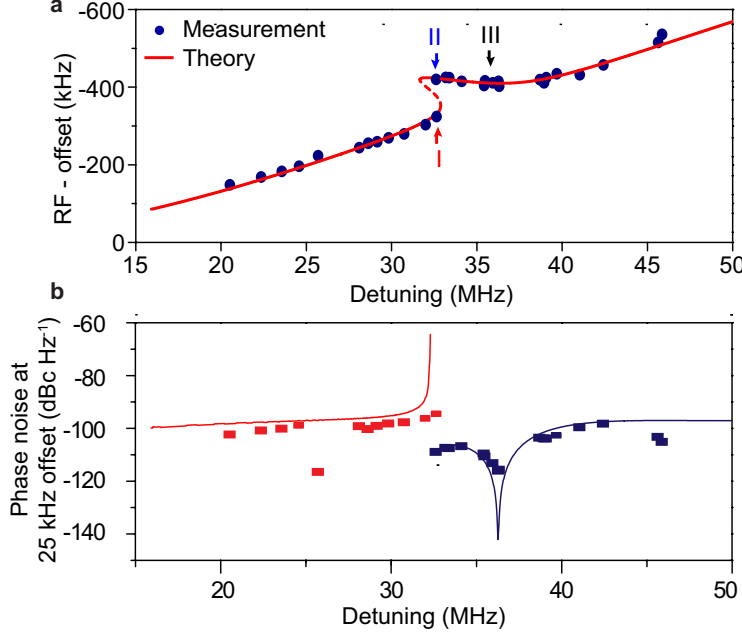


Figure 7.3: Soliton repetition frequency measurement (a) Measured (blue dots) and theoretical (red) soliton repetition frequency versus pump-cavity detuning. The offset frequency is 22.0167 GHz. The distinct soliton operating points I, II and III refer to phase noise measurements in figure 7.4. Point III is near the quiet operation point. (b) Phase noise of soliton repetition rates at 25 kHz offset frequency plotted versus the cavity-pump detuning. The blue and red dots (lines) denote the experimental (theoretical) phase noise of the upper (blue) and lower (red) branch operating points, respectively.

Quiet operation point of soliton repetition rate

The nonlinear behavior associated with soliton coupling to the single-mode dispersive wave can be used to suppress soliton repetition rate noise produced by coupling of pump-laser frequency noise. This noise source is suspected to be a significant contributor to repetition-rate noise in certain frequency-offset regimes (Xu Yi, Q.-F. Yang, Ki Youl Yang, Suh, et al., 2015). From eq. (7.3) the repetition frequency depends linearly on the total soliton spectral-center frequency shift, Ω . However, this total shift frequency versus cavity-pump detuning has a stationary point on the upper hysteresis branch (see fig. 7.2 (b)). As expected from the simple dependence in eq. (7.3), this same stationary point is observed in measurements of the repetition frequency versus detuning (fig. 7.3 (a)). To measure the repetition frequency the

soliton pulse train is directly detected and an electrical spectrum analyzer is used to observe the pulse train spectrum. The theoretical prediction using analysis from eq. (7.3) and (7.6) is also provided for comparison.

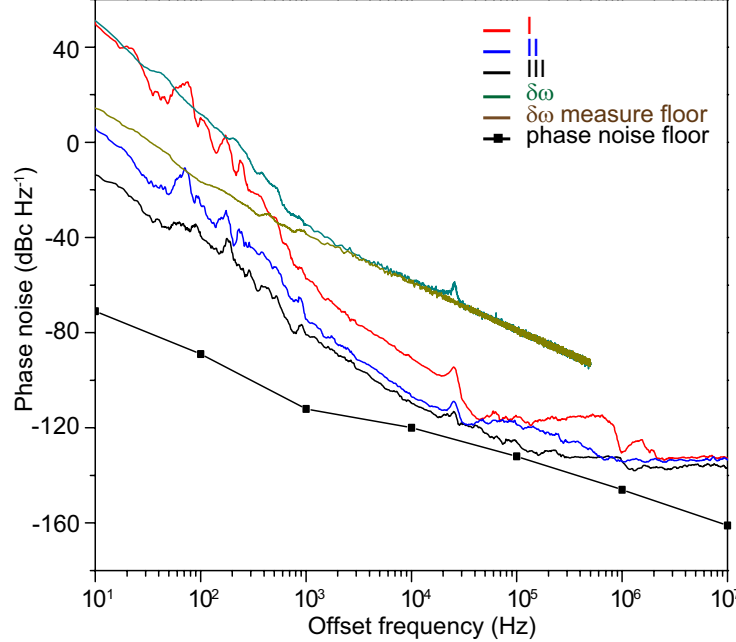


Figure 7.4: Soliton phase noise measurement. Phase noise spectra of detected soliton pulse stream at three operating points shown in 7.3. The black line connecting the square dots is the measurement floor of the phase noise analyzer.

The coupling of pump-laser frequency noise into the soliton repetition rate is expected to be minimal at the stationary point. To verify this prediction, the phase noise of the detected soliton pulse train is measured at different soliton operating points on the upper and lower branches in fig. 7.3 (a) using a phase noise analyzer. Phase noise spectra corresponding to operating points I, II and III in fig. 7.3 (a) are plotted in fig. 7.4. Operating points I and II correspond to nearly identical cavity-pump detuning, but lie on different branches. As expected, operating point II in the upper branch has a lower phase noise level compared to operating point I on account of its reduced slope. Operating point III is close to the zero-slope detuning point in the upper branch. This quiet point has the lowest phase noise among the recorded phase noise spectra. At higher offset frequencies, the phase noise is shot noise limited, while at lower offset frequencies the phase noise indicates $> 0 \text{ dBc Hz}^{-1}$ and is mainly contributed by frequency drift of the repetition rate.

For comparison, the phase noise associated with the detuning frequency $\delta\omega$ was also measured. For this measurement, the error signal of a Pound-Drever-Hall feedback

control system is operated open-loop and recorded using an oscilloscope. Its power spectral density is converted into phase noise in fig. 7.4 . The relatively high noise floor in this measurement is caused by the oscilloscope sensitivity. Nonetheless, a noise bump at 25 kHz offset frequency originates from the laser and provides a laser-noise reference point against which comparison to the soliton phase noise is possible. The soliton phase noise at 25 kHz offset frequency noise is plotted versus detuning in fig. 7.3 (b). The soliton phase noise is calculated in the Methods and the results are presented for comparison using the cavity-pump detuning noise level at 25 kHz offset. The dip of the phase noise occurs at the quiet point. One outlier point (red branch) is believed to have resulted from loss of lock of the phase noise analyzer. For lower offset frequencies, the contributions to noise are believed to originate from thermal contributions within the resonator and are under investigation. Nonetheless, the measured noise contributions at these frequencies show a trend of reduction for operation at the quiet point.

Cavity-laser detuning noise measurement

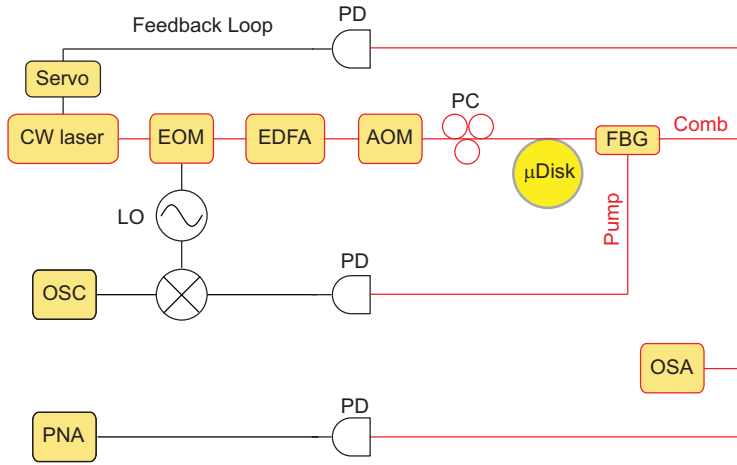


Figure 7.5: The experimental setup includes both the soliton generation and characterization setup (Xu Yi, Q.-F. Yang, Ki Youl Yang, Suh, et al., 2015; Xu Yi, Q.-F. Yang, Ki Youl Yang, and Kerry Vahala, 2016a) and a Pound-Drever-Hall (PDH) system operated open loop. The PDH is added to make possible the pump-cavity detuning noise measurement. Components included in the set up are an EOM: electro-optic modulator; EDFA: Erbium-doped fiber amplifier; AOM: acousto-optic modulator; PC: polarization controller; FBG: fiber Bragg grating; PD: photodetector; OSA: optical spectral analyzer; PNA: phase noise analyzer; LO: local oscillator. The OSA and and PNA are shown for completeness. They are not involved in measuring the detuning frequency noise.

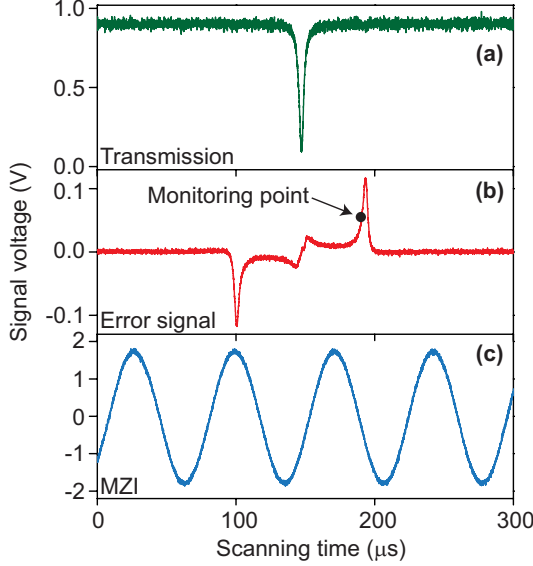


Figure 7.6: Measurements that illustrate the pump-cavity detuning measurement. The green trace is the measured power transmission when scanning the pump laser frequency across a cavity resonance. The pump laser is phase modulated, the transmitted signal is detected, and the resulting photocurrent is then mixed with the PDH local oscillator signal to generate the PDH error signal. Upon laser scan the PDH error signal (as measured on the oscilloscope) is generated as shown in the red trace. The pump laser is filtered using the fiber Bragg grating. The monitoring point for the detuning frequency measurement is indicated by the black dot. In order to convert scanning time into laser frequency, a calibrated Mach-Zehnder interferometer (MZI) records power transmission (blue trace) on an oscilloscope. The free-spectral-range of the MZI is 40 MHz.

To measure the cavity-laser detuning noise, a signal that is linearly proportional to the cavity-laser detuning is required. In this method, a Pound-Drever-Hall (PDH) loop (Drever et al., 1983; T Herr, V Brasch, J. Jost, C. Wang, et al., 2014) is embedded into the setup and operated open loop (see figure 7.5). The pump frequency is red detuned relative to the cavity resonance in order to form the soliton pulse train. Moreover, the amount of cavity-laser detuning required to generate solitons is many cavity linewidths so that the conventional PDH error signal near the resonance frequency cannot be used to monitor the detuning frequency. However, the higher-frequency PDH sideband can be tuned to reside close to the cavity resonance. Path phases in the PDH loop can be adjusted so that a PDH error signal is produced by the interaction of this sideband with the cavity resonance. When the soliton is formed, we tune the PDH local-oscillator (LO) frequency to approximately match the cavity-laser detuning. This is accomplished by monitoring the PDH error signal

(see red trace in figure 7.6). For this measurement the transmitted pump light is filtered from the soliton spectrum using a fibre Bragg filter. By setting this LO frequency to the indicated monitoring point, the corresponding error-signal output will convert detuning frequency to a voltage output. This output can be recorded and then analyzed to produce a noise spectrum. The calibration of voltage into frequency is performed by using the Mach-Zehnder interferometer trace (see blue trace in figure 7.6). This calibration is performed on the resonator at reduced power levels where solitons do not form and where the Lorentzian lineshape of the resonator is unaffected by the Kerr nonlinearity.

Quiet point existence range

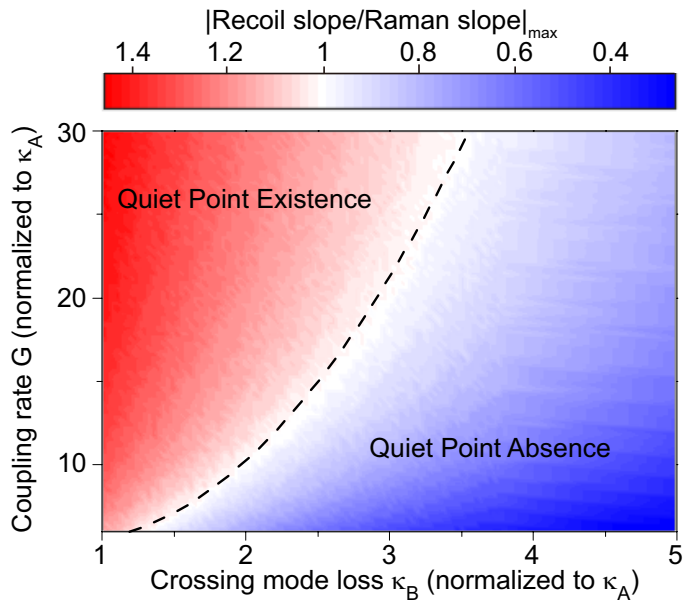


Figure 7.7: Existence study for the quiet point. The maximum ratios of $|\partial\Omega_{\text{Recoil}}/\partial\delta\omega|$ to $|\partial\Omega_{\text{Raman}}/\partial\delta\omega|$ at varying normalized modal coupling rate G (see Methods) and normalized crossing-mode damping rate κ_B (dashed curve is unity ratio). The quiet point exists when this ratio is greater than unity (red region). Parameters correspond to a silica resonator.

An analytical study comparing the detuning response of the Raman and recoil effects was performed to determine conditions required to observe the quiet point. The quiet point occurs when the retreating soliton recoil balances the always advancing SSFS. Accordingly, fig. 7.7 is a contour plot of the maximum ratio of $|\partial\Omega_{\text{Recoil}}/\partial\delta\omega|$ to $|\partial\Omega_{\text{Raman}}/\partial\delta\omega|$ while varying the coupling strength between the soliton-mode and crossing-mode families and the damping rate of the crossing mode (see Methods).

The existence regime for observation of the quiet point corresponds to the ratio > 1 shown in red. Stronger mode interaction and weaker dissipation are required to operate in this regime.

7.5 Detailed theory and simulation of single mode dispersive wave dynamics equation of hybrid mode

The equation of motion in eq. (7.2) can be derived from coupled mode equations that include dispersion, mode interaction and the Kerr nonlinearity. The intracavity field of mode μ in the soliton-forming mode family A can be represented by $A_\mu(t)e^{-i\omega_{\mu A}t+i\mu\phi}$, where $A_\mu(t)$ is the slowly varying amplitude, t is the time and ϕ is the azimuthal angle along the resonator. In the rotation frame of comb frequencies $\omega_{\mu,\text{comb}} = \omega_0 - \delta\omega + \mu\omega_{\text{rep}}$, the intracavity field can be expressed as $a_\mu(t) = A_\mu(t)e^{-i(\omega_{\mu A}-\omega_0+\delta\omega-\mu\omega_{\text{rep}})t}$. We denote the intracavity field in the crossing-mode family B as b_μ and express it in the same reference frame as the soliton-forming mode a_μ . It should be noted that the relative mode number μ is referenced to the mode that is being optically pumped, and does not represent the actual azimuthal index. The intracavity fields can be calculated using the equations of motion with Kerr nonlinearity terms (T Herr, K Hartinger, et al., 2012; Chembo and Menyuk, 2013) and modal-coupling terms(Y. Liu et al., 2014),

$$\begin{aligned} \frac{da_\mu}{dt} = & - \left[\frac{\kappa_A}{2} + i(\omega_{\mu A} - \omega_0 + \delta\omega - \mu\omega_{\text{rep}}) \right] a_\mu + iGb_\mu \\ & + ig \sum_{j,k} a_j a_k a_{j+k-\mu}^* + F\delta(\mu) \end{aligned} \quad (7.7)$$

$$\begin{aligned} \frac{db_\mu}{dt} = & - \left[\frac{\kappa_B}{2} + i(\omega_{\mu B} - \omega_0 + \delta\omega - \mu\omega_{\text{rep}}) \right] b_\mu + iGa_\mu \\ & + ig_B \sum_{j,k} b_j b_k b_{j+k-\mu}^*, \end{aligned} \quad (7.8)$$

where $\kappa_{A,B} = \omega_0/Q_{A,B}$ is the dissipation rate. $g = \hbar\omega_0^2 n_2 D_1 / 2\pi n_0 S_{\text{eff}}$ represents the normalized Kerr nonlinear coefficient with S_{eff} the effective nonlinear mode area. g_B is defined similarly. G is the linear coupling coefficient between the two mode families (Q.-F. Yang et al., 2016) and F is the normalized coupled laser pump field. Also, to calculate eq. (7.2) it is not necessary to include Raman coupling terms in eq.(7.7) and eq.(7.8) since the leading-order contribution to the forcing term, f_r , is from the Kerr nonlinearity.

Modal coupling causes two branches of hybrid modes to form as shown in fig. 7.1 (a). The frequencies of the hybrid modes in the upper (+) and lower (-) branches

are given by (Hermann A Haus and W. P. Huang, 1991; Wiersig, 2006; Y. Liu et al., 2014)

$$\omega_{\mu\pm} = \frac{\omega_{\mu A} + \omega_{\mu B}}{2} \pm \sqrt{G^2 + \frac{1}{4}(\omega_{\mu A} - \omega_{\mu B})^2}, \quad (7.9)$$

where the corresponding field amplitude of the hybrid modes is a linear combination of a_μ and b_μ . In the far-detuned regime where $\omega_{\mu A} - \omega_{\mu B} \gg G$, the field amplitude of the lower branch hybrid mode is approximately given by

$$\tilde{h}_{\mu-} = \frac{Ga_\mu + (\omega_{\mu A} - \omega_{\mu B})b_\mu}{\sqrt{G^2 + (\omega_{\mu A} - \omega_{\mu B})^2}}. \quad (7.10)$$

In this experiment, only one mode was observed to be near resonance with the soliton comb and that mode is assigned mode index $\mu = r$. Consistent with fig. 7.1 (a), the hybridization of mode r is assumed weak (i.e., $|\omega_{rA} - \omega_{rB}| \gg |G|$ and $|\Delta\omega_{rA}| \gg |\Delta\omega_{rB}|$) so that b_r is the dominant contribution to \tilde{h}_{r-} . Also, since the amplitude of b_μ with $\mu \neq r$ is small, the Kerr interaction summation term can be neglected in eq.(7.8) in this calculation.

By taking the time derivative of eq. (7.10) and then substituting using (7.7) and (7.8) the following dynamical equation results for $\tilde{h}_{\mu-}$:

$$\frac{d\tilde{h}_{r-}}{dt} = -\left[\frac{\kappa_{r-}}{2} + i(\omega_{r-} - \omega_0 + \delta\omega - r\omega_{rep})\right]\tilde{h}_{r-} + f_r \quad (7.11)$$

where f_r is the pumping term given by

$$f_r = i\Gamma g \sum_{j,k} a_j a_k a_{j+k-r}^* \quad (7.12)$$

and where $\Gamma = G/\sqrt{|G|^2 + |\omega_{\mu A} - \omega_{\mu B}|^2}$ is the fraction of the family A mode in $\tilde{h}_{\mu-}$ and $\kappa_{r-} \approx \kappa_B$ is assumed for r when $\Gamma \ll 1$. When converting eq. (7.11) into the rotation frame of $(\omega_0 + \mu D_1)$ with $\tilde{h}_{r-} = h_{r-} e^{i\Delta\omega_{r,comb}t}$, the following expression results:

$$\frac{dh_{r-}}{dt} = [-i\Delta\omega_{r-} - \frac{\kappa_{r-}}{2}]h_{r-} + f_r e^{-i\Delta\omega_{r,comb}t}, \quad (7.13)$$

where $\Delta\omega_{r-} = \omega_{r-} - \omega_0 - \mu D_1$ is the relative-mode-frequency of hybrid mode h_{r-} . Equation (7.13) is identical to eq.(7.2) in section 7.3.

Effective pumping term

The pumping term in eq.(7.11) can be expressed in parameters of the resonator and soliton. The soliton field envelope takes the form (T Herr, V Brasch, J. Jost, C. Wang, et al., 2014; Xu Yi, Q.-F. Yang, Ki Youl Yang, and Kerry Vahala, 2016b)

$$A(\phi, t) = B_s \operatorname{sech}[(\phi - \phi_c)/D_1 \tau_s] e^{i\Omega(\phi - \phi_c)/D_1 + i\varphi}, \quad (7.14)$$

where soliton properties are: amplitude B_s , angular position ϕ_c , temporal pulse width τ_s , spectral-centre frequency shift (relative to pump) Ω , and phase relative to the pump laser φ . Also, this solution assumes $\delta\omega \gg \kappa_A$. By applying the Fourier transform to $A(\phi, t)$, a_μ can be expressed in terms of the soliton properties,

$$A(\phi, t) = \sum_{\mu} a_{\mu}(t) e^{i\mu(\phi - \phi_c)} \quad (7.15)$$

$$a_{\mu} = \frac{B_s \tau_s D_1}{2} \operatorname{sech}\left(\frac{\pi \tau_s}{2}(D_1 \mu - \Omega)\right) e^{i\varphi}. \quad (7.16)$$

The pump f_r can therefore be derived by inserting eq.(7.16) into eq.(7.12). The following expression results from simplification of the summation:

$$f_r = i\Gamma \frac{D_2}{4D_1^2} [(D_1 r - \Omega)^2 + \frac{1}{\tau_s^2}] B_s \tau_s D_1 \operatorname{sech}\left(\frac{\pi \tau_s}{2}(D_1 r - \Omega)\right) e^{i\varphi}, \quad (7.17)$$

where g has been replaced using equation $B_s^2 \tau_s^2 = D_2/g D_1^2$, which holds for DKSs (A. B. Matsko and Maleki, 2013; Xu Yi, Q.-F. Yang, Ki Youl Yang, and Kerry Vahala, 2016b) and is also verified in a section below. Finally, by using (Xu Yi, Q.-F. Yang, Ki Youl Yang, and Kerry Vahala, 2016b) $\delta\omega = \frac{D_2}{2D_1^2} (\frac{1}{\tau_s^2} + \Omega^2)$ (see derivation below), f_r can be further reduced to

$$f_r = i\Gamma(\Delta\omega_{rA} - \Delta\omega_{r,comb}) a_r. \quad (7.18)$$

Recoil and Soliton Self Frequency Shift

In addition to the Raman SSFS (Karpov, Hairun Guo, Kordts, Victor Brasch, M. H. Pfeiffer, et al., 2016; Xu Yi, Q.-F. Yang, Ki Youl Yang, and Kerry Vahala, 2016b), the spectral centre of the DKS is also shifted by the single-mode dispersive wave recoil. The effect of the recoil and Raman shift can be calculated using the moment analysis method (Santhanam and Agrawal, 2003; Karpov, Hairun Guo, Kordts, Victor Brasch, M. H. Pfeiffer, et al., 2016). Using the Fourier transform, eq.(7.7) is transformed into the perturbed Lugiato-Lefever equation (LLE) (Chembo and

Menyuk, 2013)

$$\begin{aligned} \frac{\partial A(\phi, t)}{\partial t} = & -\left(\frac{\kappa_A}{2} + i\delta\omega\right)A + i\frac{D_2}{2}\frac{\partial^2 A}{\partial\phi^2} + F + ig|A|^2A \\ & + ig\tau_R D_1 A \frac{\partial|A|^2}{\partial\phi} + iGB, \end{aligned} \quad (7.19)$$

where the Raman shock term has been added (Karpov, Hairun Guo, Kordts, Victor Brasch, M. H. Pfeiffer, et al., 2016; Xu Yi, Q.-F. Yang, Ki Youl Yang, and Kerry Vahala, 2016b) and τ_R is the Raman time constant. The moment analysis method treats the soliton as a particle. The energy E and the spectral centre mode number μ_c are given by,

$$E = \sum_{\mu} |a_{\mu}|^2 = \frac{1}{2\pi} \int_{-\pi}^{+\pi} |A|^2 d\phi = B_s^2 \tau_s D_1 / \pi \quad (7.20)$$

$$\mu_c = \frac{\sum_{\mu} \mu |a_{\mu}|^2}{E} = \frac{-i}{4\pi E} \int_{-\pi}^{+\pi} \left(A^* \frac{\partial A}{\partial\phi} - A \frac{\partial A^*}{\partial\phi} \right) d\phi. \quad (7.21)$$

Taking the time derivative of eq.(7.21) and substituting $\partial A/\partial t$ using eq.(7.19), the following equation of motion for μ_c is obtained:

$$\begin{aligned} \frac{\partial \mu_c}{\partial t} = & -\kappa_A \mu_c - \frac{g\tau_R D_1}{2\pi E} \int_{-\pi}^{+\pi} \left(\frac{\partial|A|^2}{\partial\phi} \right)^2 d\phi \\ & - \frac{1}{2\pi E} \int_{-\pi}^{+\pi} \left(G^* B^* \frac{\partial A}{\partial\phi} - G A^* \frac{\partial B}{\partial\phi} \right) d\phi. \end{aligned} \quad (7.22)$$

The second term on the right-hand-side corresponds to the Raman-induced frequency shift and the third term is the frequency shift caused by recoil.

The Raman term can be calculated by substituting eq.(7.14) into the integral. When calculating the recoil term, B is simplified to $B \approx b_r e^{ir(\phi - \phi_c)}$ as the power in mode B is dominated by the near resonance mode r . In addition, because the integral of ϕ is over 2π , only $a_r e^{ir(\phi - \phi_c)}$ has nonzero contribution. Furthermore, equation (7.8) is used to relate $G a_r$ to b_r and finally leads to

$$\frac{\partial \mu_c}{\partial t} = -\frac{8\tau_R D_2}{15D_1^3 \tau_s^4} - \frac{r\kappa_B}{E} |b_r|^2 - \kappa_A \mu_c. \quad (7.23)$$

The steady-state spectral center mode number is therefore given by

$$\begin{aligned} \mu_c = & -\frac{8\tau_R D_2}{15\kappa_A D_1^3 \tau_s^4} - \frac{r\kappa_B}{\kappa_A E (1 - \Gamma^2)} |h_{r-}|^2 \\ & = \frac{1}{D_1} (\Omega_{\text{Raman}} + \Omega_{\text{Recoil}}), \end{aligned} \quad (7.24)$$

where $|\omega_{\mu A} - \omega_{\mu B}| \gg \kappa_B, \Delta\omega_r$ (equivalent to $|b_r| \gg |a_r|$) is assumed and the recoil and Raman shifts are

$$\Omega_{\text{Recoil}} = \gamma |h_{r-}|^2 = -\frac{r\kappa_B D_1}{\kappa_A E(1 - \Gamma^2)} |h_{r-}|^2, \quad (7.25)$$

$$\Omega_{\text{Raman}} = -\frac{8\tau_R D_2}{15\kappa_A D_1^2 \tau_s^4}. \quad (7.26)$$

In section 7.3, $\Gamma^2 \ll 1$ is assumed. Eq. (7.25) is eq.(7.5) in section 7.3. The form for the Raman SSFS, Ω_{Raman} , is identical to the form previously derived in the absence of the dispersive-wave coupling (Xu Yi, Q.-F. Yang, Ki Youl Yang, and Kerry Vahala, 2016b).

Soliton parameters with Raman and mode-coupling effects

In the presence of recoil and Raman, the relations between soliton parameters in eq.(7.14) can be derived from the Lagrangian approach (Xu Yi, Q.-F. Yang, Ki Youl Yang, and Kerry Vahala, 2016b; A. B. Matsko and Maleki, 2013; T Herr, V Brasch, J. Jost, C. Wang, et al., 2014). In addition, the Lagrangian approach verifies the expression for Ω_{Recoil} obtained above as well as providing a path for calculation of the repetition-rate phase noise (A. B. Matsko and Maleki, 2013). As detailed in previous literature (A. B. Matsko and Maleki, 2013; Xu Yi, Q.-F. Yang, Ki Youl Yang, and Kerry Vahala, 2016b), the perturbation Lagrangian method is applied to the LLE equation of A (eq. 7.19). However, now an additional perturbation term is added to account for the mode coupling to the crossing-mode family. Taking $B \approx b_r e^{ir(\phi - \phi_c)}$, produces the following equations of motion:

$$\frac{\Omega}{D_1} \frac{\partial \phi_c}{\partial t} - \frac{\partial \varphi}{\partial t} - \delta\omega - \frac{D_2 \Omega^2}{2D_1^2} - \frac{D_2}{6\tau_s^2 D_1^2} + \frac{2}{3} g B_s^2 = 0 \quad (7.27)$$

$$\frac{\Omega}{D_1} \frac{\partial \phi_c}{\partial t} - \frac{\partial \varphi}{\partial t} - \delta\omega - \frac{D_2 \Omega^2}{2D_1^2} + \frac{D_2}{6\tau_s^2 D_1^2} + \frac{1}{3} g B_s^2 = 0 \quad (7.28)$$

$$\frac{\partial(B_s^2 \tau_s \Omega)}{\partial t} = -\kappa_A B_s^2 \tau_s \Omega - \frac{8g\tau_R B_s^4}{15\tau_s} - \kappa_B \pi r |b_r|^2 \quad (7.29)$$

$$\frac{\partial \phi_c}{\partial t} = \frac{D_2}{D_1} \Omega \quad (7.30)$$

$$\frac{\partial(B_s^2 \tau_s)}{\partial t} = -\kappa_A B_s^2 \tau_s + f \cos \varphi B_s \tau_s \pi \operatorname{sech}(\Omega \tau_s \frac{\pi}{2}) \quad (7.31)$$

where we have assumed the mode r is far from the mode centre $\mu_c = \Omega/D_1$ and the coupling coefficient G is smaller than or around the same order of magnitude with

$\delta\omega$. Also, higher order terms are neglected. Subtracting eq. (7.28) from eq. (7.27) yields

$$B_s \tau_s = \sqrt{\frac{D_2}{g D_1^2}}. \quad (7.32)$$

This equation was previously verified in the presence of Raman-only interactions (Xu Yi, Q.-F. Yang, Ki Youl Yang, and Kerry Vahala, 2016b).

An additional relation between $\delta\omega$, τ_s and Ω is derived for steady state by substituting eq. (7.30) and (7.32) into eq. (7.27)

$$\delta\omega = \frac{D_2}{2D_1^2} \left(\frac{1}{\tau_s^2} + \Omega^2 \right), \quad (7.33)$$

where Ω can be obtained from (7.29) and (7.32),

$$\Omega = \Omega_{\text{Raman}} + \Omega_{\text{Recoil}} = -\frac{8D_2\tau_R}{15\kappa_A D_1^2 \tau_s^4} - \frac{r\kappa_B D_1}{\kappa_A E(1-\Gamma^2)} |h_{r-}|^2. \quad (7.34)$$

This result provides an independent confirmation of eq. (7.24). Also, eq. (7.33) is identical in form to an expression which included only the Raman SSFS (Xu Yi, Q.-F. Yang, Ki Youl Yang, and Kerry Vahala, 2016b). Significantly, however, eq. (7.33) is more general since Ω is the total spectral centre shift provided by the combined effects of Raman SSFS and dispersive-wave recoil.

Phase noise transfer function

The repetition rate of the soliton can be expressed as follows (Q.-F. Yang et al., 2016),

$$\omega_{\text{rep}} = D_1 + \frac{\partial \phi_c}{\partial t} = D_1 + \frac{D_2}{D_1} \Omega. \quad (7.35)$$

The variation in both D_1 and Ω contribute to fluctuations in the repetition rate. While D_1 is subject to thermo-refractive noise and fluctuations from the environment, a significant contributor to fluctuations in Ω results from fluctuations in the pump-laser frequency detuning frequency, $\delta\omega$. The noise conversion from cavity-pump detuning to repetition rate can be calculated by linearizing eqs. (7.27)-(7.31) using the small signal approximation (A. B. Matsko and Maleki, 2013). Accordingly, all soliton parameters (X) can be expressed as $X = X_0 + \Delta X$, where X_0 is the steady-state value and ΔX is a small-signal fluctuation. For simplicity, we further denote the Raman and recoil terms in eq. (7.29) as $-8g\tau_R B_s^4 / 15\tau_s - \kappa_B \pi r |b_r|^2 \equiv \kappa_A B_s^2 \tau_s F(\delta\omega)$ so that $\Omega = F(\delta\omega)$ is the function of detuning measured in fig. 7.2 (b) (i.e., steady-state Ω versus $\delta\omega$).

In the following derivation, τ_s in eqs. (7.27)-(7.31) is eliminated using eq. (7.32). Equation (7.29) can therefore be expressed as

$$\frac{\partial B_s \Omega}{\partial t} = -\kappa_A B_s [\Omega - F(\delta\omega)]. \quad (7.36)$$

Applying the small-signal approximation and Fourier transform to eq. (7.36) gives the result,

$$(1 + i\omega/\kappa_A) \Delta \tilde{\Omega}(\omega) = \frac{\partial F}{\partial \delta\omega} \Delta \tilde{\delta\omega}(\omega) - \frac{i\omega \Omega_0}{\kappa_A B_{s0}} \Delta \tilde{B}_s(\omega), \quad (7.37)$$

where $\Delta \tilde{X}(\omega)$ is the Fourier transform of ΔX , ω is the Fourier frequency (i.e., offset frequency in the phase or frequency-noise spectrum) and where the Fourier transform of $\partial \Delta X / \partial t$ equals $i\omega \Delta \tilde{X}(\omega)$. $\Delta \tilde{\delta\omega}(\omega)$ represents the cavity-pump detuning noise. Similarly, eq. (7.27) can be transformed to

$$g B_{s0} \Delta \tilde{B}_s(\omega) = \Delta \tilde{\delta\omega}(\omega) - \frac{D_2 \Omega_0}{D_1^2} \Delta \tilde{\Omega}(\omega), \quad (7.38)$$

where the contribution from $i\omega \Delta \tilde{\varphi}(\omega)$ is neglected as it is of order $(\omega/\delta\omega)$ smaller compared to the leading-order terms.

In the limit of $\omega^2/\kappa_A^2 \ll 1$ and $\Omega^2 \tau_s^2 \omega/\kappa_A \ll 1$, eq. (7.37) and eq. (7.38) are solved for $\Delta \tilde{\Omega}(\omega)$ in terms of $\Delta \tilde{\delta\omega}(\omega)$. The result is substituted into the Fourier transform of eq. (7.35) to give the following result:

$$\widetilde{\Delta \omega_{\text{rep}}}(\omega) = \frac{D_1}{D_2} \Delta \tilde{\Omega}(\omega) = \frac{\Delta \tilde{\delta\omega}(\omega)}{1 + i\omega/\kappa_A} \left(\frac{\partial \omega_{\text{rep}}}{\partial \delta\omega} - \frac{i\omega}{\kappa_A} \Omega D_1 \tau_s^2 \right), \quad (7.39)$$

where sources of noise associated with D_1 in eq. (7.35) are ignored.

The soliton repetition rate noise can be expressed as $\widetilde{\Delta \omega_{\text{rep}}}(\omega) = \alpha(\omega) \Delta \tilde{\delta\omega}(\omega)$, where $\alpha(\omega)$, the noise transfer function, is the coefficient of $\Delta \tilde{\delta\omega}(\omega)$ in eq. (7.39). Accordingly, the phase noise of repetition rate is $S_\phi(\omega) = |\alpha(\omega)|^2 S_{\phi, \delta\omega}(\omega)$.

Typically, for the resonators in this study $\omega < \kappa_A$ so that the first term in eq. (7.39) expresses the trivial result that the slope of the plot in fig. 7.3 (a) acts as a transfer function of fluctuations in $\delta\omega$ into repetition-rate fluctuations. However, when $\partial \omega_{\text{rep}} / \partial \delta\omega$ approaches zero (the quiet point), the first term in eq. (7.39) vanishes and the noise transfer function reaches a minimum determined by the second term. The phase noise plots in fig. 7.3 (c) were fitted using the same parameters as in analytical fitting in fig. 7.2 (c), (d) and 7.3 (a), and $\partial \omega_{\text{rep}} / \partial \delta\omega$ extracted numerically from the fitting curves in fig. 7.3 (a).

Analytical model fitting and parameters

²Measurements are compared with the analytical model in figures 7.2 (a), (b) and 7.3 (a). Measured parameters used for the analytical model are: $\kappa_A/2\pi = 2.12$ MHz, $D_1/2\pi = 22$ GHz, $D_2/2\pi = 17$ kHz, $G/2\pi = 42.4$ MHz. $\tau_R = 2.49$ fs can be extracted from the measured Ω in the regime without the mode recoil effect ($\delta\omega/2\pi < 30$ MHz and $\delta\omega/2\pi > 40$ MHz). Two free parameters are used to optimize the fitting in figure 7.2, 7.3 and 7.4 and they are in reasonable agreement with the measurement: $\Delta\omega_{r-} = -62.2$ MHz (-75 ± 7 MHz in measurement) and $\kappa_{r-}/2\pi = 3.6$ MHz (6 MHz in measurement). The procedure for fitting is as follows: a detuning frequency, $\delta\omega$, (horizontal axis in fig. 7.2 (a), (b) and 7.3 (a) plots) is selected. By eliminating Ω in eq. (7.33) and eq. (7.34) a single condition relating τ_s and $|h_{r-}|^2$ results. Likewise, with $\delta\omega$ selected a second condition relating τ_s and $|h_{r-}|^2$ results from eq. (7.6) by replacing Ω_{Raman} using eq. (7.26). This pair of equations is solved for τ_s and $|h_{r-}|^2$ from which Ω is determined by eq. (7.34) and ω_{rep} is determined by eq. (7.3).

Numerical simulation

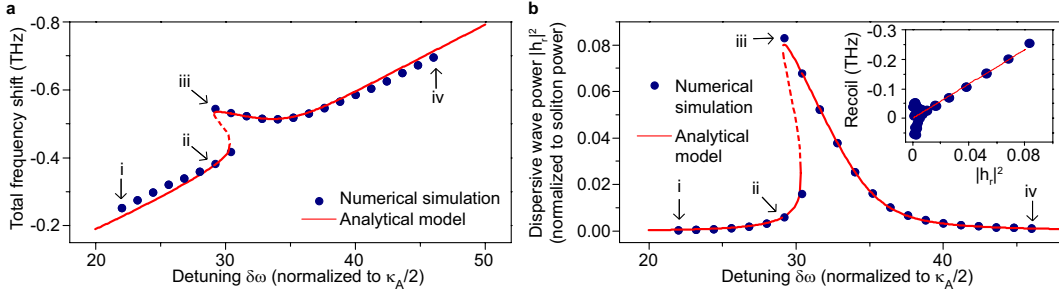


Figure 7.8: (a) Numerical (blue dots) and analytical (red solid line) soliton total frequency shift versus cavity-pump detuning. Points i, ii, iii, and iv correspond to specific soliton operating points noted in other figure panels. (b) Numerical (blue dots) and analytical (red solid line) dispersive wave power (normalized to total soliton power) versus cavity-pump detuning. Inset: recoil frequency versus the dispersive wave power.

To further investigate the single-mode dispersive wave phenomena, we perform numerical simulations based on the coupled Lugiato-Lefever equation of mode family A and B (eq. (7.19) and Fourier transform of eq. (7.8)). The two mode families are coupled using a model studied in detail in previous chapter. The coupling is char-

²The analytical model fitting and numerical simulation were performed by Xueyue Zhang and Qi-Fan Yang.

acterized by a rate constant G and is designed to induce an avoided-mode-crossing around mode index $\mu = 72$, similar to the experimental mode family dispersion. Figures 7.8 and 7.9 show the results of the numerical simulation including 2048 modes. The hysteresis behavior in the soliton total frequency shift and the dispersive-wave power resembles the experimental observation and is also in agreement with the analytical model (see fig. 7.8 (a),(b)). As predicted by eq. (7.5) (and observed in the fig. 7.2 (a) inset), the recoil is numerically predicted to vary linearly with the dispersive wave power (fig. 7.8 (b) inset).

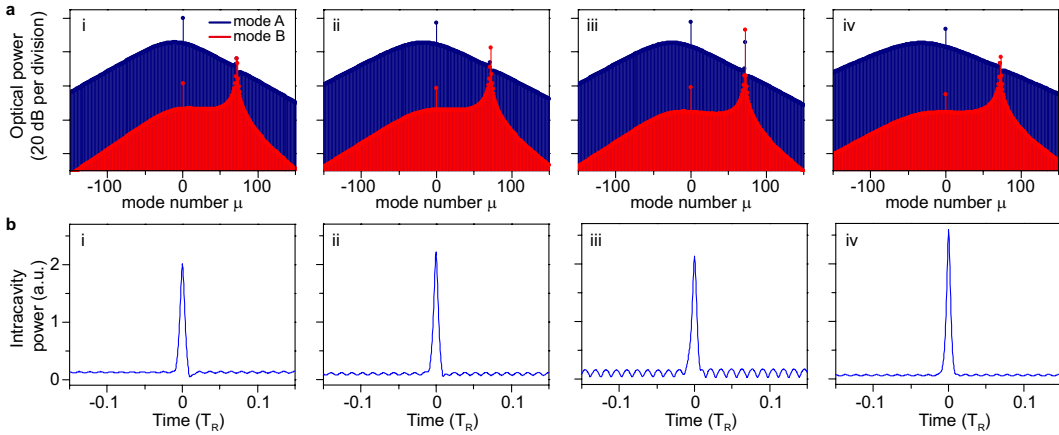


Figure 7.9: (a) Comb spectra contributions from the two mode families (blue: soliton forming mode family A; red: crossing mode family B). (b) Time domain intracavity power. T_R is the cavity round trip time.(i) to (iv) are indicated in figure 7.8.

Frequency and time domain features of the soliton (blue) and dispersive wave (red) are also studied in fig. 7.9 in units of intracavity power. They show that the dispersive wave emerges on mode family B and consists primarily of a single mode. The single-mode dispersive wave leads to a modulated background field in the resonator with a period determined by the beating between the pump and the dispersive wave. This modulation is observable in fig. 7.9 (b). Spectral recoil of the soliton is also observable in the numerical spectra. The combined power of mode A and B spectra in fig. 7.9 (a) is the total intracavity power.

Finally, the simulations are implemented with the split-step Fourier method (Agrawal, 2007) where 2048 modes in the frequency domain are taken into account. The parameters for two mode families used in figure 7.7, 7.8 and 7.9 are $\kappa_A/2\pi = 2.12$ MHz, $\kappa_B/2\pi = 3.4$ MHz, $D_1/2\pi = 22$ GHz for mode A, $D_{1B}/2\pi = D_1/2\pi + 50.9$ MHz for mode B, $D_2/2\pi = 17$ kHz for both mode A

and B , $\tau_R = 2.489$ fs, $g = g_B = 9.8 \times 10^{-4}$ rad s $^{-1}$ and $G/2\pi = 42.4$ MHz.

7.6 Summary

Coupling of a dissipative Kerr soliton to a single-mode dispersive wave has been shown to produce hysteresis behavior in both the dispersive-wave power and in the soliton properties. These properties include the frequency shift of the soliton spectral center relative to the pumping frequency and the soliton repetition frequency. The hysteresis results from the dependence of the dispersive-wave phase matching condition upon the dispersive-wave power. The hysteresis behavior of the dispersive wave also leads to an operating point wherein coupling of laser pump frequency noise into the soliton repetition rate is greatly reduced. This reduction was modeled and measured, and the requirements for quiet point existence were also studied. The operating point for quiet soliton operation is of potential use for ultra-low-noise microwave generation.

ELECTRO-OPTICAL FREQUENCY COMB

8.1 Introduction

In this chapter, we will introduce a different type of frequency comb, electro-optics (EO) frequency comb (Murata et al., 2000; Fujiwara et al., 2001; C.-B. Huang et al., 2008; Metcalf et al., 2013). The EO frequency comb has relatively simple structure comparing with the conventional mode-locked laser comb and the newly developed microcomb. It uses the electro-optics modulation to create equally spaced sidebands from a continuous-wave pump laser. The EO comb uses off-the-shelf components from telecommunication industry and therefore has great reliability. The repetition rate of EO comb is versatile and set by the modulation frequency. The reliability and flexible repetition rate make EO comb a suitable candidate for certain comb applications. The EO comb described in this chapter will be used for optical frequency division and astronomical calibration in the next two chapters. It shall be also noted that dual comb spectroscopy (Millot et al., 2015) and self-referencing (Beha, Cole, Del'Haye, et al., 2017) using EO comb has been recently demonstrated elsewhere.

8.2 Demonstration of electro-optics frequency comb

Electro-optics modulation

A typical EO frequency comb schematic is presented in figure 8.1. The detailed modulation layout is shown in figure 8.2. A continuous-wave laser is sent into electro-optics phase modulator (PM) to create equally spaced sidebands at the modulation frequency. The modulation frequency is set by the microwave source, and can be tuned from MHz to a few tens GHz. A few PMs can be cascaded to increase the modulation depth and the number of sidebands. The phase shifter is used to synchronize the modulation. The intensity modulator (IM) following the PMs is used to gate the signal and provide a linear chirp to the frequency. The laser field after the cascaded PMs and IM can be expressed as

$$E(t) = E_0 e^{-i\omega t} \times e^{i \sum_k V_k \cos(\omega_m t + \varphi_k)} \times [e^{i\varphi_{DC}} + e^{iV_{IM} \cos(\omega_m t + \varphi_{IM})}], \quad (8.1)$$

where the insertion loss of modulators has been neglected. ω and ω_m are the pump laser frequency and modulation frequency. V_k and φ_k are the modulation depth

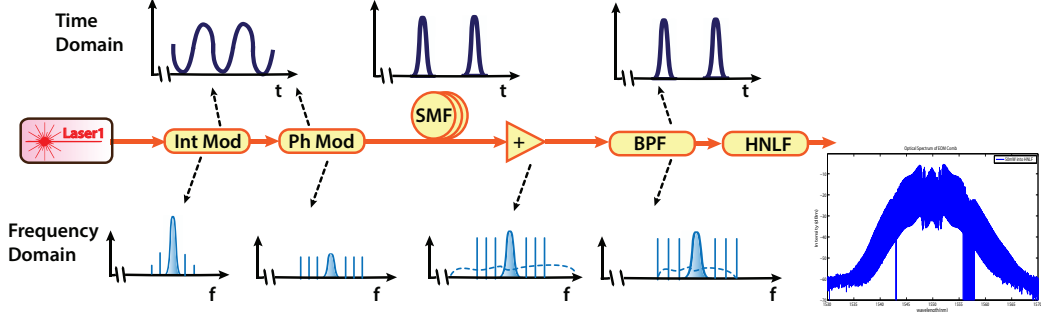


Figure 8.1: Conceptual schematics of a typical EO frequency comb. A continuous pump laser goes through intensity modulation (Int Mod), phase modulation (Ph Mod), single mode fiber (SMF) and forms a train of short pulses with the repetition rate equaling the modulation frequency. The pulses are then amplified by an optical amplifier. The amplifier spontaneous emission (ASE) noise is filtered by a bandpass filter (BPF), or other type of filter. The amplified pulses then go into highly nonlinear fiber (HNLF) and are spectrum broadened.

and phase of k -th phase modulator. V_{IM} , φ_{IM} , and φ_{DC} are the modulation depth, modulation phase, and bias phase of intensity modulator.

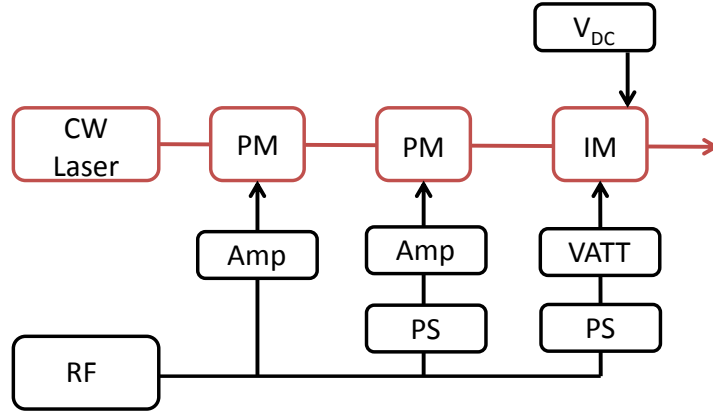


Figure 8.2: Detailed schematic of electro-optics modulation. Components in this layout include continuous wave (CW) laser, phase modulator (PM), intensity modulator (IM), microwave source (RF), microwave amplifier (Amp), phase shifter (PS), variable microwave attenuator (VATT) and DC voltage supply (V_{DC}).

To obtain the maximum number of modulation sidebands, the phase of PM φ_k shall be synchronized through microwave phase shifter. In figure 8.3, the optical spectrum of three independent phase modulators are shown. When three phase modulators are cascaded and synchronized ($\varphi_k = 0$), the number of modulation sidebands are roughly the sum of the numbers of three independent phase modulators. The optical

spectrum of phase modulation could be obtained by Fourier transform and is related to Bessel function (Yariv, 1976). However, the exact spectrum of phase modulation is not critical here. The number of sidebands from phase modulation could be estimated by the time-bandwidth limit. In time domain, the phase is varying at the rate of $1/V_k \omega_m$. Correspondingly, the frequency domain bandwidth shall be $V_k \times \omega_m$ and therefore the number of sidebands is roughly V_k .

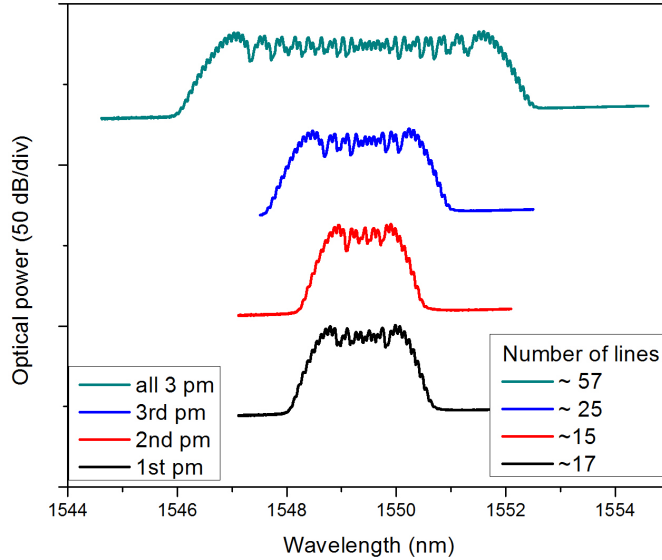


Figure 8.3: Optical spectrum of phase modulation sidebands. The optical spectrum of the 1st, 2nd and 3rd phase modulation are shown in black, red and blue. The optical spectra of the three cascaded phase modulators are presented in green. The modulation frequency is 10 GHz. The contrast of the spectrum is limited by the resolution of this OSA (0.05 nm).

To provide a linear chirp to the phase modulation sidebands, the intensity modulation is used to gate out the center of the phase modulation: $t \in (-\pi/2\omega_m, \pi/2\omega_m)$. The linear chirp of frequency could be understood through the Taylor expansion of the phase term $\varphi = \cos\omega_m t \sim 1 - 0.5(\omega_m t)^2$ at $t = 0$ and frequency $\omega' = \partial\varphi/\partial t$. Such gating could be achieved by setting the modulation phase to $\varphi_{IM} = \varphi_k = 0$, and modulation depth as $V_{IM} = \pi$. Then $\varphi_{DC} = \pi$ and $\varphi_{DC} = 0$ correspond to negative chirp (gate $t \in (-\pi/2\omega_m, \pi/2\omega_m)$) or positive chirp (gate $t \in (\pi/2\omega_m, 3\pi/2\omega_m)$). In the experiment, $\varphi_{IM} = 0$ can be tuned through phase shifter. When $\varphi_{IM} = 0$ or π , the optical spectrum of EO comb is symmetric along the pump laser wavelength. The modulation depth $V_{IM} = \pi$ could be set by a variable attenuator. The accurate

value can be obtained by measuring the average optical output power. Assume the maximum average output power is P_0 when there is no modulation (maximum power achieved by varying φ_{DC}). It can be calculated that when $V_{IM} = \pi$, the maximum average output power shall be $0.75P_0$. Therefore, by varying the modulation input power to the intensity modulation and observing the average optical output power, we could tune the modulation depth to $V_{IM} = \pi$. Finally, φ_{DC} can be set through a DC voltage supply. When it is near 0 or π , the optical spectrum will be relatively flat around the pump wavelength with two small wings (see figure 8.4).

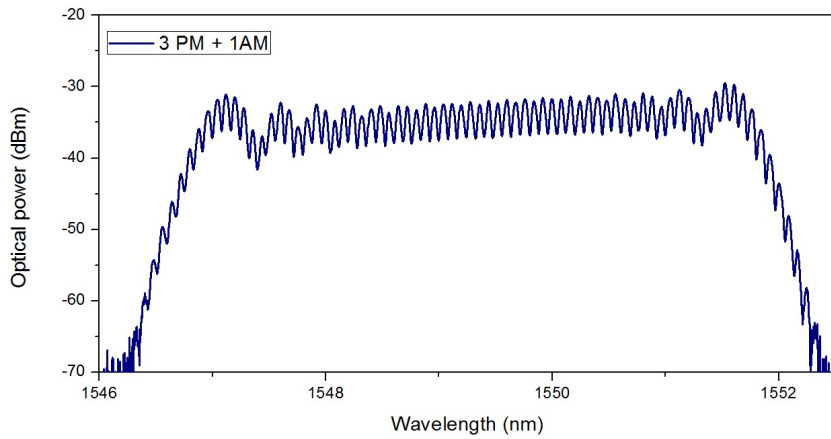


Figure 8.4: Optical spectrum of EO frequency comb. The parameters of intensity modulators are optimized using the method in main text. The modulation frequency is 10 GHz.

The linear chirp of modulation sidebands could be compensated with any dispersive components, including single mode fibers, dispersion compensation Bragg grating, and line-by-line waveshaping. The compensation of dispersion will flatten the phase of sidebands and form a temporal pulse. The formation of this temporal pulse could be verified by intensity autocorrelation measurement. In figure 8.5, a 10.3 ps/nm dispersion is applied to the optical spectrum in figure 8.4 by using waveshaper, and a pulse with < 2 ps pulse width is measured. In addition, the optical pulse is near Fourier-transform-limited. Its autocorrelation trace overlap very well with the trace calculated by assuming a flat phase of the optical spectrum (figure 8.5).

Optical spectrum broadening of EO frequency comb

Optical spectrum broadening, or supercontinuum, of an optical frequency comb has been a well developed technology (Dudley, Genty, and Coen, 2006). By using micro-structured highly nonlinear fiber, the self-phase modulation of optical pulses

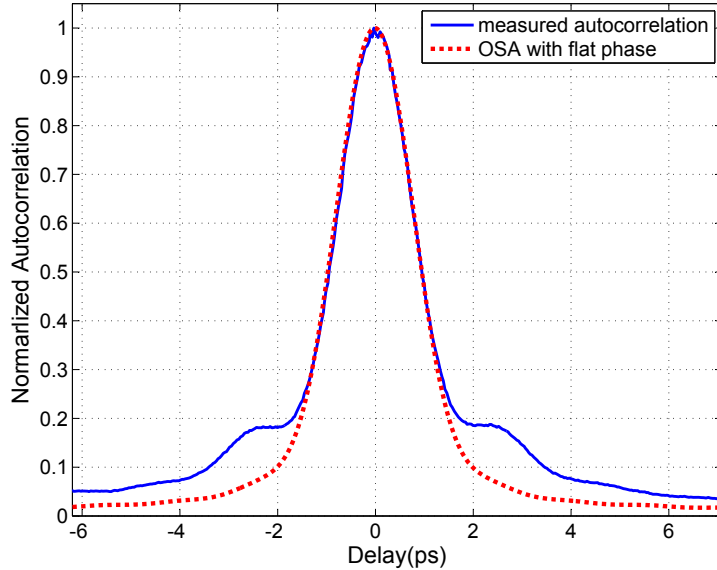


Figure 8.5: Autocorrelation measurement (blue line) of the EO frequency comb in figure 8.4. The red line is computed with the OSA spectrum in figure 8.4 and assumes flat phase on each comb lines.

is greatly enhanced and new comb lines are created through four-wave mixing. Supercontinuum is especially useful for EO frequency comb. The EO frequency comb has bandwidth of a few nanometers, much smaller than the conventional mode-lock laser comb and microcomb. However, supercontinuum can broaden the comb to more than a hundred nanometer, or even to an octave span (Beha, Cole, Del’Haye, et al., 2017).

Due to the high duty cycle of EO frequency comb, the supercontinuum requires at least a high power erbium doped fiber amplifier (EDFA) and a highly nonlinear optical fiber (HNLF). Typically, the EDFA amplify the average power of EO combs to a few Watts. Then the EO comb pulses are launched into the HNLF. The result of spectrum broadening is closely related to many factors: the optical polarization, the EDFA power level, the amplifier spontaneous emission (ASE) noise, the HNLF dispersion, HNLF length, etc. It is found that the best spectrum broadening effect can be achieved when the wavelength of EO comb is near the EDFA maximum gain wavelength (near 1560nm, see figure 8.6). At this wavelength, the signal to noise ratio (EO comb power versus ASE noise power) is maximized and less noise will be amplified in the self-phase modulation in HNLF. Further suppression of ASE noise can be achieved by using bandpass filter or Fabry–Pérot cavity filter (Beha, Cole, Del’Haye, et al., 2017). In addition, using short HNLF can further minimize the

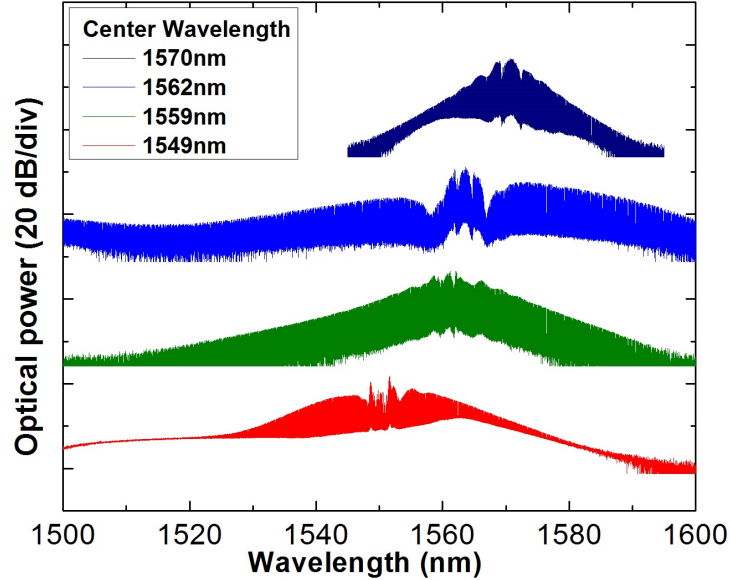


Figure 8.6: The optical spectrum of broadened EO frequency comb with different pump laser wavelength. The modulation frequency is 12 GHz and the amplified power is 180 mW. The HNLF is 500 meters long.

tension-induced polarization drift in HNLF fiber spool (see Chapter 10). The effect of HNLF dispersion on spectrum broadening has been studied elsewhere (G. G. Ycas et al., 2012).

8.3 Summary

In this chapter, we have shown the basic of electro-optics frequency comb. The EO frequency comb will be further used in Chapter 9 and 10.

Chapter 9

ELECTRO-OPTICAL FREQUENCY DIVISION AND STABLE MICROWAVE SYNTHESIS

9.1 Introduction

¹The photomixing of two highly coherent laser signals is a well-known approach to generate a stable radio frequency (RF) or microwave signal (Seeds and Williams, 2006; Yao, 2009). Recently, however, a different approach to all-optical signal generation has been demonstrated that may revolutionize applications that require high-stability microwaves. Rather than photomixing stabilized laser signals to directly produce a microwave signal, the approach uses an octave-spanning, self-referenced frequency comb to divide a stable optical reference frequency down to microwave or RF rates (TM Fortier et al., 2011). Frequency dividers are widely used in electronics to generate new frequencies from a single base oscillator or to coherently link different frequency bands. As an ancillary benefit, all frequency dividers reduce the phase noise spectral density of the output signal relative to the input by the square of the division ratio. The new optical frequency dividers perform division by a factor of $\sim 50,000$ (the ratio of optical to microwave frequencies), so that phase-noise reduction is greater than 10^9 . Moreover, reference-cavity stabilized lasers exhibit a superior, fractional frequency stability in comparison with electrical oscillators (Young et al., 1999; Kessler et al., 2012). Optical dividers applied to such signals thereby generate microwave signals with an exceedingly low phase noise level (TM Fortier et al., 2011).

In this chapter, we present a way to generate high-performance microwave signals through optical frequency division (OFD) by using a cascade of direct phase modulation and self-phase modulation to create an optical comb (Murata et al., 2000; Fujiwara et al., 2001; C.-B. Huang et al., 2008; Metcalf et al., 2013). Because the spectral line spacing is set by the electrical oscillator used to drive the phase modulators (as opposed to an optical resonator), the method of microwave synthesis has similarities to conventional microwave synthesizers while also leveraging the power of OFD so as to reduce phase noise.

¹The work presented in this chapter has been published in "Electro-optical frequency division and stable microwave synthesis", Science, 345, 309 (2014). The dual Brillouin-laser generation was demonstrated by Jiang Li, Caltech.

9.2 Electro-optics frequency division (eOFD)

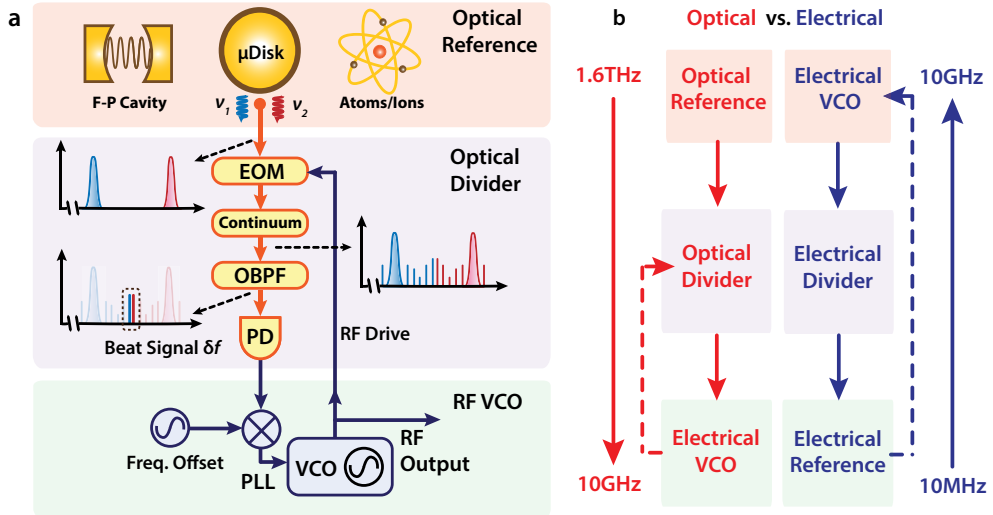


Figure 9.1: Conceptual schematics of stable microwave synthesis by use of EOFD. (a) Two optical reference laser lines are provided by one of several possible methods, including dual-mode laser action, frequency-locking two lasers to distinct optical modes of a reference cavity, or lasers stabilized to atomic transitions. These laser lines are phase-modulated so as to produce sidebands, two of which nearly overlap at the spectral midpoint of the laser lines. The drive frequency is provided by the electrical VCO that is to be stabilized. Optical filtering and detection of the nearly overlapping sidebands gives a beat note that is used to phase-lock the VCO and lower its phase noise. EOM is the electro-optical modulator, OBPF is the optical bandpass filter, and PD is the photodetector. (b) Comparison of conventional, electrical, phase-locked loop control of a VCO with the present method. The conventional method divides the VCO for phase comparison with the low-frequency reference, whereas the present method divides the frequency separation of two lasers so as to stabilize the electrical VCO.

In our approach, two laser lines having good relative frequency stability provide an optical reference for the microwave source (figure 9.1). These laser lines are produced by Brillouin oscillation in a single high-quality-factor (Q) microcavity. However, the lines could also result from any stable optical references, including various types of dual-mode lasers (Pillet et al., 2008; Geng, Staines, and S. Jiang, 2008; Pan and Yao, 2009; Gross et al., 2010; Callahan, Gross, and Dennis, 2011; Carpintero et al., 2012), two lasers locked to distinct optical modes of a reference cavity (W. C. Swann et al., 2011), or lasers stabilized to atomic transitions (Papp, Beha, et al., 2014). The laser lines enter the frequency divider portion of the signal generator, where they are phase-modulated by a pair of modulators at a frequency set by a voltage-controlled electrical oscillator (VCO). The sideband spectrum created

by the phase modulators is further broadened through pulse-forming and self-phase modulation in an optical fiber (C.-B. Huang et al., 2008; Morohashi, Sakamoto, Sotobayashi, Kawanishi, and Hosako, 2009; Ishizawa et al., 2013). The comb of lines extending from each laser line results in a pair of sidebands near the midpoint of the frequency span. These are optically filtered and detected. The detected beat-note signal contains the phase noise of the VCO, but magnified by the optical division factor. It therefore provides a suitable error signal for phase-lock loop control of the VCO.

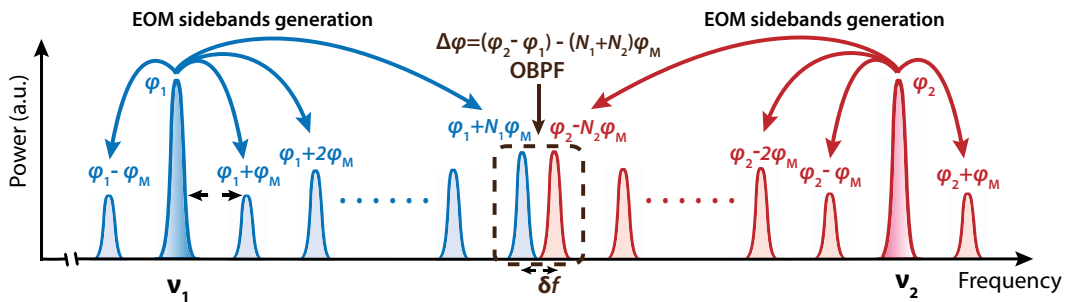


Figure 9.2: Analysis of the relative phase of the inner side bands in the optical spectrum. $\varphi_{1,2}$ and φ_M are the phase fluctuations of the laser field phases and the electrical VCO, respectively.

In our method, we contrast this microwave source that is based on electro-optical frequency division (eOFD) with a conventional microwave source that is based on electrical frequency division of a VCO (Rohde, 1997). In the conventional approach (figure 9.1 (b)), the VCO provides the highest frequency in the system. It is stabilized through electrical frequency division and phase comparison with a lower-frequency reference oscillator, such as a quartz oscillator. A consequence is that the stabilized VCO has a phase noise level that is always higher than the reference oscillator phase noise by the square of their frequency ratio (the frequency division ratio). In contrast, our optical version reverses the positions of the reference and the VCO in the frequency domain. Specifically, the reference is provided by the frequency difference of the laser lines, and this frequency difference is made much greater than the frequency of the VCO (in the present implementation, this is a non-detectable rate set at ~ 150 times the VCO frequency). Moreover, this reference frequency is divided down to the VCO frequency, as opposed to dividing the VCO frequency down to the reference frequency rate. By making this reversal, the present device benefits from the stability of optical oscillators and the power of OFD to quadratically reduce the phase noise of optical oscillators by the division

factor. Also, because the divider derives its rate from the electrical VCO, it is continuously tunable. In particular, the frequency output is set by the tuning range of the electrical VCO and the frequency separation of the reference laser lines and is not fixed by a cavity repetition rate. Additionally, by obtaining the output of the electro-optical frequency divider directly from the VCO, this approach greatly relaxes the linearity constraints of high-bandwidth photodetection that have posed challenges for OFD based on mode-locked lasers (Ivanov, S. A. Diddams, and Leo Hollberg, 2005; Taylor et al., 2011).

In addition, the use of a frequency difference as opposed to an absolute frequency to derive a reference for microwave generation has been demonstrated by using mode-locked laser frequency combs. In that case, the mode-locked frequency comb optical divider is implemented by locking a comb at two frequencies of a reference cavity (W. C. Swann et al., 2011). This two-point lock approach has also been implemented by using two atomic lines and a frequency microcomb (Papp, Beha, et al., 2014). Cascaded phase modulation, other than being applied for pulse generation (Murata et al., 2000; Fujiwara et al., 2001; C.-B. Huang et al., 2008; Metcalf et al., 2013), has also been used to stabilize the frequency difference (in the millimeter wave domain) of a dual-frequency laser (Rolland et al., 2011) and to create continuously tunable microwave signals through sideband-injection locking (Schneider et al., 2013).

To understand phase noise reduction in this divider, one should consider the accumulated phase noise contributions in the side bands as being tracked from the laser sources to the phase difference of the detected sidebands (figure 9.2). By adjusting the VCO phase to nullify the phase difference, $\Delta\varphi$, the VCO fluctuations are reduced to $\varphi_M^2 = (\varphi_1 - \varphi_2)^2 / (N_1 + N_2)^2$, where φ_1 , φ_2 and φ_M are the phase fluctuations of the laser field phases and the electrical VCO. Also, N_1 and N_2 are the number of sidebands produced by modulation (sidebands are higher in frequency for laser 1 and lower in frequency for laser 2). As a result, within the servo control bandwidth, the phase noise of the VCO is given by the relative phase noise of the two laser fields reduced by the division factor squared, $(N_1 + N_2)^2$. Clearly, to reduce phase noise of the electrical VCO, the laser frequency separation should be made as large as possible. In the present system, this value is set by the span of the dual-pumped Brillouin lasers. It is the relative phase noise of the laser sources that determines the phase noise reference level (before OFD). Because these lasers are co-lasing within the same resonator, the common-mode laser noise (such as pump noise, microphonics, or cavity noise) is largely suppressed, leaving primarily fundamental sources of

laser noise, such as Schawlow-Townes noise.

9.3 Experiment of frequency division and microwave synthesis

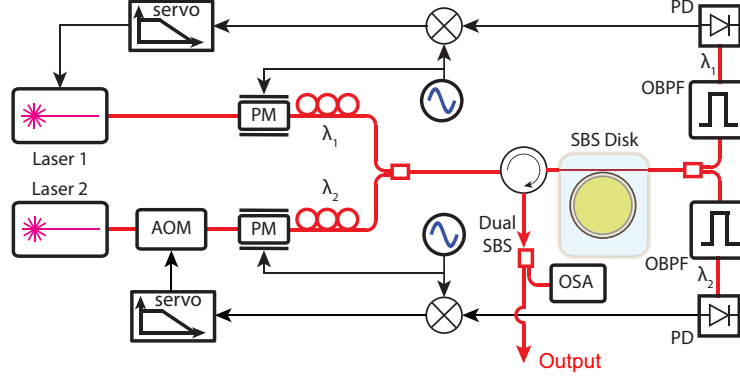


Figure 9.3: Schematic showing the arrangement used for dual-pumping of the disk resonator Brillouin laser. Lasers 1 and 2 are locked to distinct modes of a high-Q disk resonator. Servo control involves direct frequency tuning of laser 1 and frequency shifting via an acousto-optic modulator (AOM) for laser 2. The reference laser lines provided by the Brillouin oscillation are output to the optical division function.

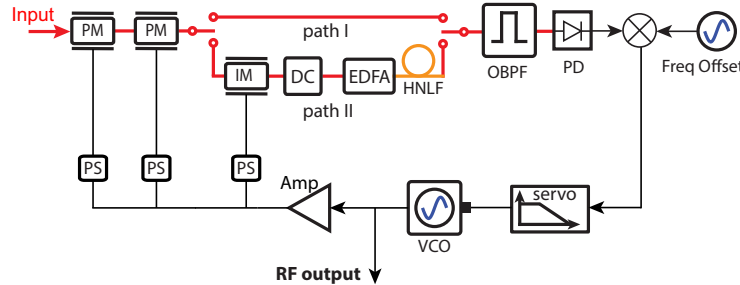


Figure 9.4: Schematic of optical frequency division. Depending on the desired division ratio, two pathways are taken (path I and path II). For division up to 30 \times , a pair of phase modulators are synchronously driven, whereas for larger division ratios, the phase modulators are cascaded with a fiber pulse broadener containing an intensity modulator (IM), dispersion compensation (DC), EDFA, and nonlinear fiber (HNLF). The filtered (OBPF) and detected signal is then processed for servo control of the VCO. Also shown are the optical spectrum analyzer (OSA) and electrical phase shifters (PS).

The detailed experimental setup is provided in figure 9.3 and 9.4. The reference laser signals are provided by Brillouin-laser lines co-lasing within a single silica-on-silicon high-Q disk resonator (figure 9.3). The coherence properties of the individual Brillouin laser lines is excellent (Lee, T. Chen, et al., 2012; Jiang Li et al., 2012a). The silica disk resonators are designed and fabricated with a free spectral

range (FSR) of 10.890 GHz that matches the Brillouin shift frequency in silica near 1550 nm. We used a frequency modulation technique to measure the FSR (Jiang Li, Lee, Ki Youl Yang, et al., 2012). In prior work, a single pump configuration was used to demonstrate microwave synthesis up to K-band (22 GHz) rates by the photomixing of cascaded Brillouin laser lines (Jiang Li, Lee, and K. J. Vahala, 2013). Here, the Brillouin lines must be separated by a much larger frequency, and a dual pump configuration is used. Each pump laser is locked to the disk resonator by using the Pound-Drever-Hall (PDH) technique (Drever et al., 1983) and excites its own Brillouin laser in the backward-propagating direction. In the experiment, the stimulated Brillouin scattering (SBS) lines are separated by as much as 1.61 THz by dual pumping on cavity modes separated by 148 FSR. The maximum separation of 1.61 THz is currently set by the tuning range of the pump lasers. The optical spectra of the dual SBS lines at several frequency differences appears in figure 9.5. Besides inherent stability from co-lasing within the same cavity, the two SBS laser signals share the same fiber optical path, suppressing path-length variation effects.

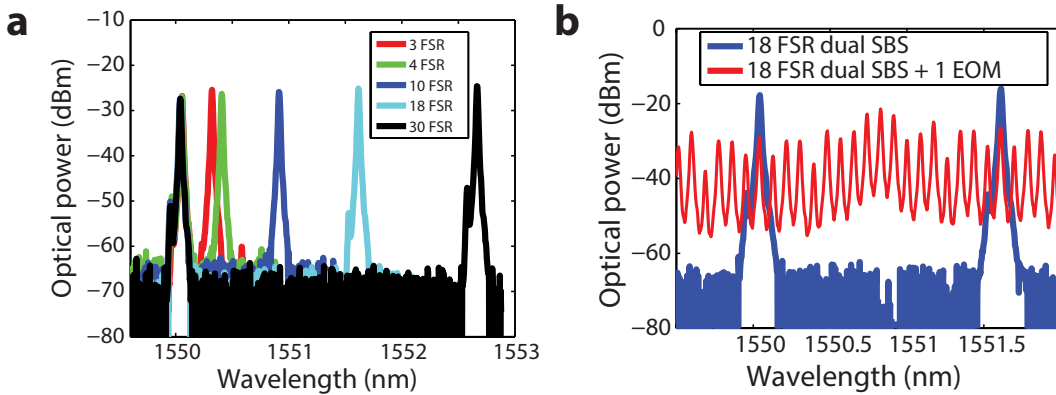


Figure 9.5: (a) Optical spectra of co-lasing Brillouin lasers at various tuning configurations used in the measurement corresponding to cavity FSR spacings provided in the inset. (b) Optical spectrum of Brillouin laser lines with (red) and without (blue) phase modulation.

The laser signals are coupled to the optical divider section by use of a circulator. In order to increase the comb bandwidth and the division factor, two phase modulators with low $V_\pi \sim 3.9$ (at 12 GHz) are cascaded and phase-synchronized with a RF phase shifter. The phase modulators were driven at 32.5 and 30.7 dBm, corresponding to a total phase-modulation amplitude up to 6π ($\approx \pi V_{\text{drive}}/V_\pi$), which is also approximately equal to half of the number of sidebands produced by the modulators (Sakamoto, Kawanishi, and Izutsu, 2007). In the experiment, up to 30 electro-optic

modulator (EOM) sidebands can be created by using the phase modulators alone, enabling optical division by around a factor of 30. An optical spectrum showing both the original SBS laser lines (18 FSR frequency separation) and the resulting phase modulation sidebands is shown in figure 9.5 (b). To further enhance the sideband spectral width, nonlinear spectral broadening was performed by introducing an intensity modulator, dispersion compensation, erbium-doped fiber amplifier (EDFA), and nonlinear fiber (C.-B. Huang et al., 2008; Morohashi, Sakamoto, Sotobayashi, Kawanishi, and Hosako, 2009; Ishizawa et al., 2013). The inner sidebands are optically filtered, and their beat note is detected on an amplified photodetector. The beat note frequency was set near 10 MHz and phase-compared with a 10-MHz oven-controlled crystal oscillator (OCXO) in order to generate the error signal used for phase-locking the VCO. The phase noise of the OCXO is very low (compared with the optical frequency reference) and is further divided down in the control loop (supplementary materials). As such, it does not introduce any limitation on the final VCO phase noise. The residual phase noise levels of the amplifier used here [MicroSemi (Aliso Viejo, CA) model L0612-35-T977] are well below the phase noise levels attained through loop control of the VCO and therefore do not present any limitation to the measurement. The sum of the free-running VCO phase noise and the residual phase noise of the RF power amplifier is suppressed by the servo loop. As a result, by taking the electrical output signal at the output of the amplifier, there is no phase noise limitation set by the RF power amplifier.

The phase noise reference level is provided by the relative phase noise of the co-lasing Brillouin laser lines. This phase noise level is expected to be relatively insensitive to the frequency difference (Jiang Li et al., 2012a; Jiang Li, Lee, and K. J. Vahala, 2013). Therefore, this noise level was measured by pumping the two lasers on modes that were three cavity FSR apart, enabling direct detection of the beat signal at 32.7 GHz by a fast photodetector. We then analyzed this detected signal using a phase noise analyzer in order to obtain the single sideband (SSB) phase noise spectrum (figure 9.6, red curve). For offset frequencies higher than 100 Hz, this spectrum is limited by Schawlow-Townes noise, whereas at offset frequencies less than 100 Hz a technical noise component is present (Jiang Li, Lee, and K. J. Vahala, 2013). The white phase noise floor above 1 MHz offset is due to the thermal noise of the fast photodetector. We measured the SSB phase noise spectrum using a commercial phase noise tester [Rohde Schwartz (Munich, Germany) model FSUP26; sensitivity limit given as the light blue squares in figure 9.6] based on the phase detector method, with dual-channel cross-correlations so as to further improve the phase

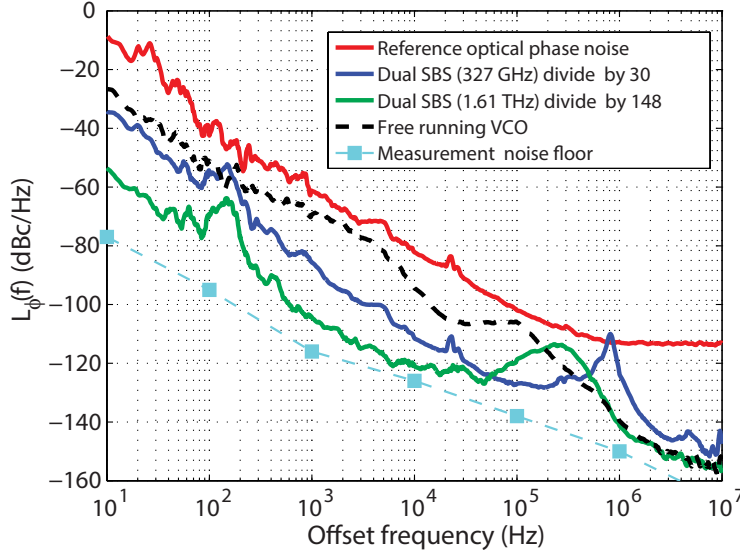


Figure 9.6: SSB phase noise spectrum of the optical reference (red) is shown. For this measurement, the dual SBS lines are tuned to a detectable frequency difference. Also shown are the closed-loop VCO phase noise referenced to dual SBS lines separated by 327 GHz (blue) and 1.61 THz (green), with corresponding division ratios of 30 and 148. The dashed black curve is the phase noise of the free-running VCO. The light blue square markers denote the phase noise sensitivity of the phase noise tester.

noise sensitivity.

To test the optical divider, we locked the VCO to the divided optical reference using the VCO control/tuning port (figure 9.4). The blue and green curves in fig. 9.6 are the corresponding phase noise spectra of the VCO at 10.89 GHz when optically dividing by 30 and 148 times relative to the initial frequency separation of the dual SBS lines at 327 GHz and 1.61 THz, respectively. The microwave carrier frequency is held at 10.89 GHz in these measurements by adjusting the frequency separation of the Brillouin laser lines with the tunable pump lasers. Decrease of the phase noise with the increase of the division ratio is clear in the data. For division by 148 \times , the achieved phase noise level is -104 dBc/Hz at 1 kHz and -121 dBc/Hz at 10 kHz. For comparison, the dashed black curve in fig. 9.6 gives the phase noise of the free-running VCO. The servo-locking bandwidth can be seen from the servo bumps in the phase noise spectra, which are located at 820 kHz for the blue curve (adopting path I in fig. 9.4) and 300 kHz for the green curve (adopting path II in fig. 9.4). As an aside, the locking bandwidth is determined by the loop delay, which includes both optical and electrical path lengths (~ 20 m for path I and ~ 50 m for

path II) and the FM response of the VCO. For frequencies beyond the servo control bandwidth, the phase noise level is set by the free-running VCO.

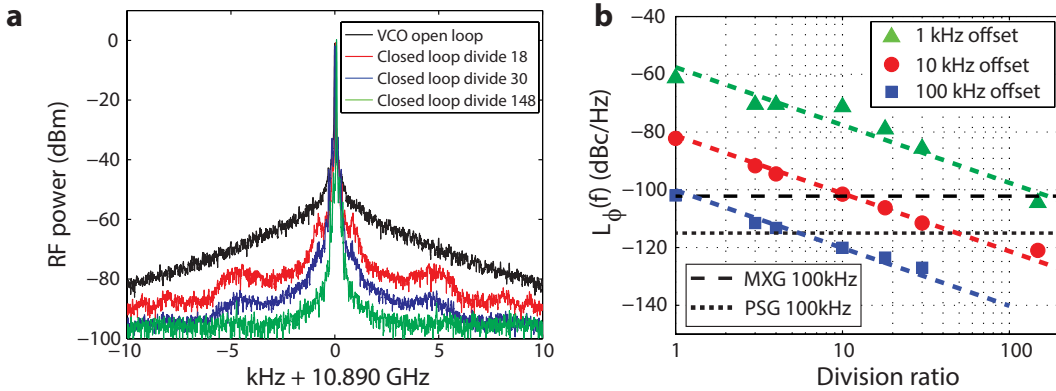


Figure 9.7: (a) VCO RF power spectrum at 10.89 GHz for open-loop and closed-loop conditions in which the Brillouin frequency separation is divided by 18 \times , 30 \times , and 148 \times . Resolution bandwidth is set at 30 Hz. (b) Summary of SSB phase noise levels at 10.89 GHz versus optical division ratio. Cases shown are measured at 1-, 10-, and 100-kHz offset frequencies. The dashed lines give $1/N^2$ trends. Phase noise levels for an Agilent MXG and PSG microwave sources (carrier 11 GHz, 100 kHz offset) are provided for comparison

In the measured RF power spectra of the VCO at 10.89 GHz (20 kHz span and 30 Hz resolution bandwidth) (figure 9.7 (a)), the black curve is the free- running VCO spectrum, and the red, blue, and green curves are the spectra of the phase-locked VCO when dividing down 18, 30, and 148 times, respectively, from corresponding SBS frequency separations of 196 GHz, 327 GHz, and 1.61 THz. These results are summarized in figure 9.7 (b) by giving the measured phase noise at 1 kHz, 10 kHz, and 100 kHz offset frequencies plotted versus division ratios of 1, 3, 4, 10, 18, 30, and 148. The dashed lines give $1/N^2$ trend lines. For comparison, the phase noise of an Agilent (Santa Clara, CA) MXG microwave synthesizer (carrier 11 GHz, offset 100 kHz, Agilent online data sheet, Literature number 5989-7572EN) and a high-performance Agilent PSG microwave synthesizer (carrier 11 GHz, offset 100 kHz, Agilent online data sheet, Literature number 5989-0698EN, option UNX) are shown as black, dashed, and dotted lines.

9.4 Summary

The optical division factor can be scaled to higher values for additional phase noise improvement. Although the frequency reference might be based on some other system, for simplicity we considered the use of one SBS laser operating at 1.55 mm

(current system) and another at 1 mm [recently demonstrated by using silica high-Q disks (Jiang Li, Lee, and K. J. Vahala, 2014)]. Matching the Brillouin shift at these wavelengths within the same disk is possible by designing the system to oscillate at a multiple cavity free spectral range. For example, a disk diameter of ~12 mm (FSR of ~5.4 GHz, which is half of the Brillouin shift at 1.55 mm and one third of the Brillouin shift at 1 mm) would enable simultaneous SBS oscillation at 1.55 and 1 mm. To extend the comb over this span would require about one half of an octave. Spectrally broadened EOM combs with more than 500 nm bandwidth have previously been demonstrated (Suzuki et al., 2013). An electro-optical frequency divider spanning 1- and 1.55-mm SBS lines is therefore feasible. This example system does not necessarily represent a fundamental limit but nonetheless would feature a division factor of ~7000. Assuming that relative phase noise of the co-lasing optical lines does not degrade beyond what has been demonstrated in the present work, this hypothetical system could provide phase noise performance close to levels demonstrated by conventional OFD.

This new photonic architecture for OFD provides a route to improve the phase noise of a common VCO. In the present configuration, dual SBS lasers have been co-generated in a single, chip-based resonator to establish a stable reference as high as 1.61 THz. Although dual-pumped SBS laser lines provide an excellent reference frequency, it should also be possible to lock two lasers to a resonator to establish the reference. Because the current frequency separation is limited by the pump lasers, much larger division ratios and potentially lower phase noise levels should be possible. In comparison with conventional OFD by use of a self-referenced frequency comb, this technique does not presently offer as large a division ratio. However, it is simple and relatively low-cost and also provides tuning of the electrical carrier. More-over, it relies on a reference signal derived from the relative phase of two lasers as opposed to the absolute phase of a single laser. This can potentially improve the robustness with respect to microphonics and other sources of technical noise.

ASTRONOMICAL CALIBRATION AND EXOPLANET DETECTION WITH ELECTRO-OPTICS FREQUENCY COMB

10.1 Introduction

¹The earliest technique for the discovery and characterization of planets orbiting other stars (“exoplanets”) is the Doppler or Radial Velocity (RV) method whereby small periodic changes in the motion of a star orbited by a planet are detected via careful spectroscopic measurements (Perryman, 2011). So far, the RV technique has identified hundreds of planets ranging in mass from a few times the mass of Jupiter to less than an Earth mass, and in orbital periods from less than a day to over 10 years (Marcy and A, 2011). However, the detection of Earth-like at orbital separations suitable for the presence of liquid water at the planet’s surface, i.e. in the “Habitable Zone” (HZ) (Kasting, Whitmire, and Reynolds, 1993), remains challenging for stars like the Sun with RV signatures $< 0.1 \text{ m s}^{-1}$ ($\Delta V/c < 3 \times 10^{-10}$) and periods of a year ($\sim 10^8$ sec to measure three complete periods). For cooler, lower luminosity stars (spectral class M), however, the Habitable Zone moves closer to the star which, by application of Kepler’s laws, implies that a planet’s radial velocity signature increases, $\sim 0.5 \text{ m s}^{-1}$ ($\Delta V/c < 1.5 \times 10^{-9}$), and its orbital period decreases, ~ 30 days ($\sim 10^7$ sec to measure three periods). Both of these effects make the detection easier. But for M stars, the bulk of the radiation shifts from the visible wavelengths, where most RV measurements have been made to date, into the near-infrared. Thus, there is considerable interest among astronomers in developing precise RV capabilities at longer wavelengths.

Critical to precision RV measurements is a highly stable wavelength reference (Pepe, Ehrenreich, and Meyer, 2014). Recently a number of groups have undertaken to provide a broadband calibration standard that consists of a “comb” of evenly spaced laser lines accurately anchored to a stable frequency standard and injected directly into the spectrometer along with the stellar spectrum (M. Murphy et al., 2007; Steve Osterman et al., 2007; C.-H. Li et al., 2008; Braje et al., 2008; Glenday et al., 2015). While this effort has mostly been focused on visible wavelengths, there

¹Work presented in this chapter has been published in “Demonstration of a near-IR line-referenced electro-optical laser frequency comb for precision radial velocity measurements in astronomy”, Nature Communications, 7, 10436 (2016).

have been successful efforts at near-IR wavelengths as well (Steinmetz et al., 2008; G. G. Ycas et al., 2012; F Quinlan et al., 2010). In all of these earlier studies, the comb has been based on a femtosecond mode-locked laser that is self-referenced (Jones et al., 2000; S. T. Cundiff and Ye, 2003; S. A. Diddams, 2010), such that the spectral line spacing and common offset frequency of all lines are both locked to a radio frequency standard. Thus, laser combs potentially represent an ideal tool for spectroscopic and radial velocity measurements.

However, in the case of mode-locked laser combs, the line spacing is typically in the range of 0.1-1 GHz, which is too small to be resolved by most astronomical spectrographs. As a result, the output spectrum of the comb must be spectrally filtered to create a calibration grid spaced by >10 GHz, which is more commensurate with the resolving power of a high-resolution astronomical spectrograph (Braje et al., 2008). While this approach has led to spectrograph characterization at the cm sec⁻¹ level (Wilken et al., 2012), it nonetheless increases the complexity and cost of the system.

In light of this, there is interest in developing photonic tools that possess many of the benefits of mode-locked laser combs, but that might be simpler, less expensive, and more amenable to “hands-off” operation at remote telescope sites. Indeed, in many radial velocity measurements, other system-induced errors and uncertainties can limit the achievable precision, such that a frequency comb of lesser precision could still be equally valuable. For example, one alternative technique recently reported is to use a series of spectroscopic peaks induced in a broad continuum spectrum using a compact Fabry-Perot interferometer (Wildi et al., 2010; Halverson et al., 2014; Bauer, Zechmeister, and Reiners, 2015). While the technique must account for temperature-induced tuning of the interferometer, it has the advantage of simplicity and low cost. Another interesting alternative is the so-called Kerr comb or microcomb, which has the distinct advantage of directly providing a comb with spacing in the range of 10-100 GHz, without the need for filtering (T. J. Kippenberg, Ronald Holzwarth, and SA Diddams, 2011). While this new type of laser comb is still under development, there have been promising demonstrations of full microcomb frequency control(Del’Haye et al., 2008; Papp, Beha, et al., 2014) and in the future it could be possible to fully integrate such a microcomb on only a few square centimeters of silicon, making a very robust and inexpensive calibrator. Another approach that has been proposed is to create a comb through electro-optical modulation of a frequency stabilized laser (Suzuki et al., 2013; Kotani et al., 2014).

In the following paragraphs, we describe a successful effort to implement this approach. We produce a line-referenced, electro-optical-modulation frequency comb (LR-EOFC) around 1559.9 nm in the astronomical H band (1500-1800 nm). We discuss the experimental setup, laboratory results and proof of concept demonstrations at the NASA Infrared Telescope Facility (IRTF) and the W. M. Keck observatory (Keck) 10 m telescope.

10.2 Frequency comb design and stability test

Frequency comb generation

A line-referenced electro-optic frequency comb (LR-EOFC) is a spectrum of lines generated by electro-optic modulation of a continuous-wave (CW) laser source (Imai, Kourogi, and Ohtsu, 1998; Fujiwara et al., 2001; C.-B. Huang et al., 2008; Morohashi, Sakamoto, Sotobayashi, Kawanishi, Hosako, and Tsuchiya, 2008; Ishizawa et al., 2013) which has been stabilized to a molecular or atomic reference (e.g. $f_0 = f_{\text{atom}}$). The position of the comb teeth ($f_N = f_0 \pm Nf_m$, N is an integer) has uncertainty determined by the stabilization of f_0 and the microwave source that provides the modulation frequency f_m . However, the typical uncertainty of a microwave source can be sub-Hertz when synchronized with a compact Rb clock and moreover can be GPS-disciplined to provide long-term stability (F Quinlan et al., 2010). Thus, the dominant uncertainty in comb tooth frequency in the LR-EOFC is that of f_0 .

The schematic layout for LR-EOFC generation is illustrated in fig. 10.1 and a detailed layout is shown in fig. 10.2. All components are commercially available off-the-shelf telecommunications components. Pictures of the key components are shown in the left column of fig. 10.1. The frequency-stabilized laser is first pre-amplified to 200 mW with an Erbium Doped Fiber Amplifier (EDFA, model: Amonics, AEDFA-PM-23-B-FA) and coupled into two tandem lithium niobate (LiNbO_3) phase modulators ($V_\pi = 3.9$ V at 12 GHz, RF input limit: 33 dBm). The phase modulators are driven by an amplified 12 GHz frequency signal at 32.5 dBm and 30.7 dBm, and synchronized by using microwave phase shifters. This initial phase modulation process produces a comb having approximately 40 comb lines ($\approx 2\pi \times V_{\text{drive}}/V_\pi$), or equivalently 4 nm bandwidth. This comb is then coupled into a LiNbO_3 amplitude modulator (AM) with 18-20 dB distinction ratio, driven at the same microwave frequency by the microwave power recycled from the phase modulator external termination port. The modulation index of $\pi/2$ is set by an attenuator and the phase offset of two AM arms is set and locked to $\pi/2$. Microwave phase shifters are used to align the drive phase so

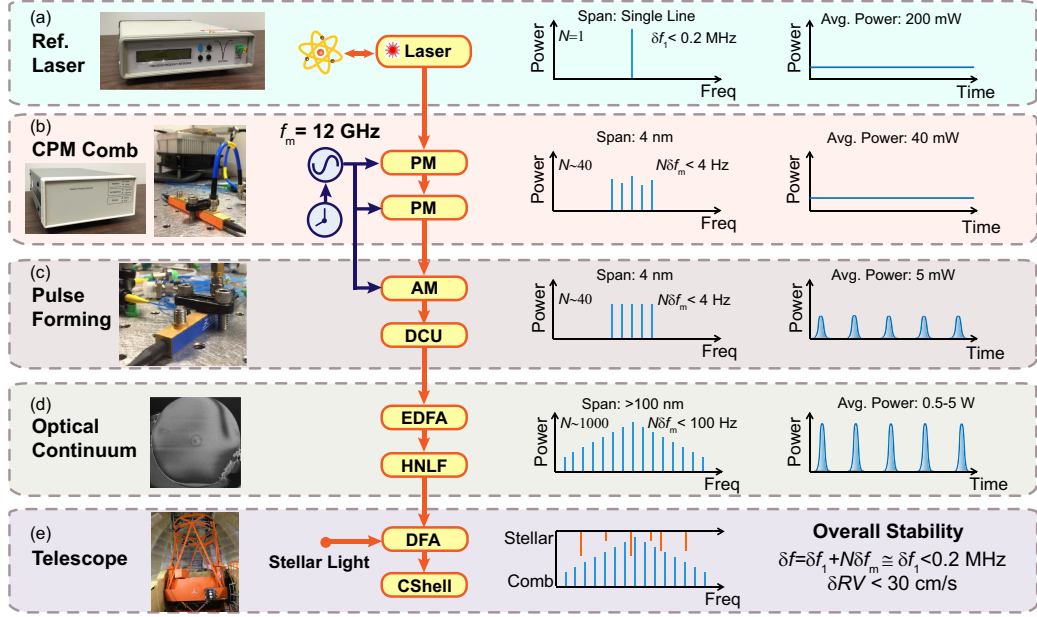


Figure 10.1: Conceptual schematics of the line-referenced electro-optic frequency comb for astronomy. Vertically, the first column contains images of key instruments. From (a) to (e), the images are reference laser, Rb clock (left) and phase modulator (right), amplitude modulator, highly-nonlinear fiber and telescope. A simplified schematic setup is in the second column. Third and fourth columns present the comb state in the frequency and temporal domains. The frequency of N -th comb tooth is expressed as $f_N = f_0 + N \times f_m$, where f_0 and f_m are the reference laser frequency and modulation frequency, respectively. N is the number of comb lines relative to the reference laser (taken as comb line $N = 0$), RV is radial velocity and δf , δf_0 and δf_m are the variance of f , f_0 and f_m . (a) The reference laser is locked to a molecular transition, acquiring stability of 0.2 MHz, corresponding to $30 \text{ cm s}^{-1} RV$. (b) Cascaded phase modulation (CPM) comb: the phase of the reference laser is modulated by two phase modulators (PM), creating several tens of sidebands with spacing equal to the modulation frequency. The RF frequency generator is referenced to a Rb clock, providing stability at the sub-Hz level ($\delta f_m < 0.03 \text{ Hz}$ at 100s). (c) Pulse forming is then performed by an amplitude modulator (AM) and dispersion compensation unit (DCU), which could be a long single mode fiber (SMF) or chirped fiber Bragg grating. (d) After amplification by an Erbium Doped Fiber Amplifier (EDFA), the pulse undergoes optical continuum broadening in a highly nonlinear fiber (HNLF), extending its bandwidth $> 100 \text{ nm}$. (e) Finally the comb light is combined with stellar light using a fiber acquisition unit (FAU) and is sent into the telescope spectrograph. The overall comb stability is primarily determined by the pump laser.

that the amplitude modulator gates-out only those portions of the phase modulation that are approximately linearly chirped with one sign (i.e., parabolic phase variation

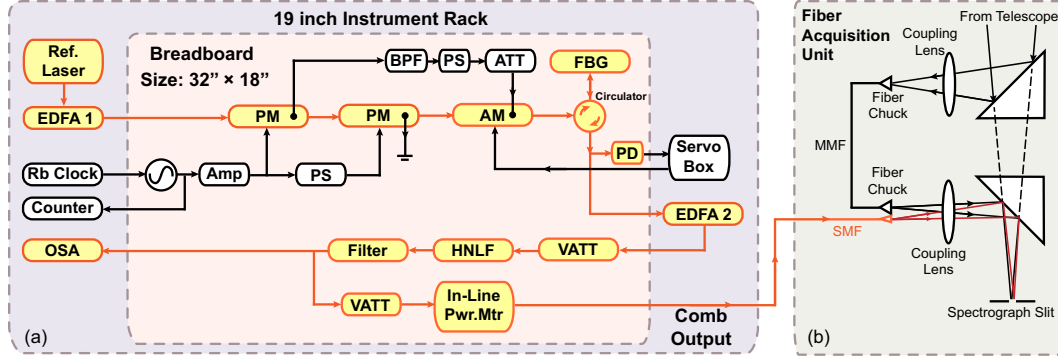


Figure 10.2: Detailed setup of line-referenced electro-optic frequency comb. (a) The entire LR-EOFC system sits in a 19 inch instrument rack. Optics and microwave components in the rack are denoted in orange and black, respectively. Small components were assembled onto a breadboard. These included the phase modulators (PM), amplitude modulator (AM), fiber Bragg grating (FBG), photodetector (PD), variable attenuator (VATT), attenuator (ATT), highly nonlinear fiber (HNLF), microwave source, microwave amplifier (Amp), phase shifter (PS) and bandpass filter (BPF). The reference laser, erbium-doped amplifier (EDFA), rubidium (Rb) clock, counter, optical spectrum analyzer (OSA) and servo lock box are separately located in the instrument rack. (b) A simplified schematic of the fiber acquisition unit (FAU) is also shown. Stellar light is focused and coupled into a multi-mode fiber (MMF). The comb light from a single mode fiber (SMF), together with the stellar light in MMF, are focused on the spectrograph slit and sent into the spectrograph.

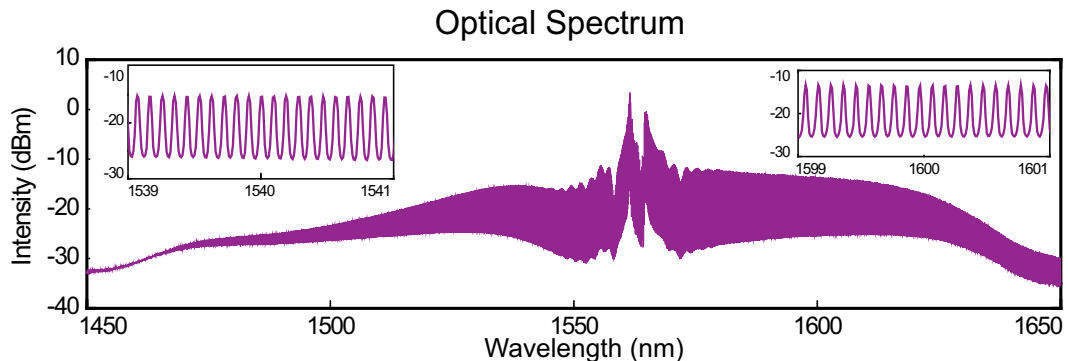


Figure 10.3: A typical comb spectrum from the 1559.9 nm laser with > 100nm span generated with 600 mW pump power. The insets show the resolved line spacing of 12 GHz or approximately 0.1 nm.

in time). A nearly transform-limited pulse is then formed when this parabolic phase variation is nullified by dispersion compensation unit using a chirped fiber Bragg grating with 8ps nm^{-1} dispersion. A 2 ps FWHM pulse is measured after the fiber grating using an autocorrelator. Owing to this pulse formation, the duty cycle of

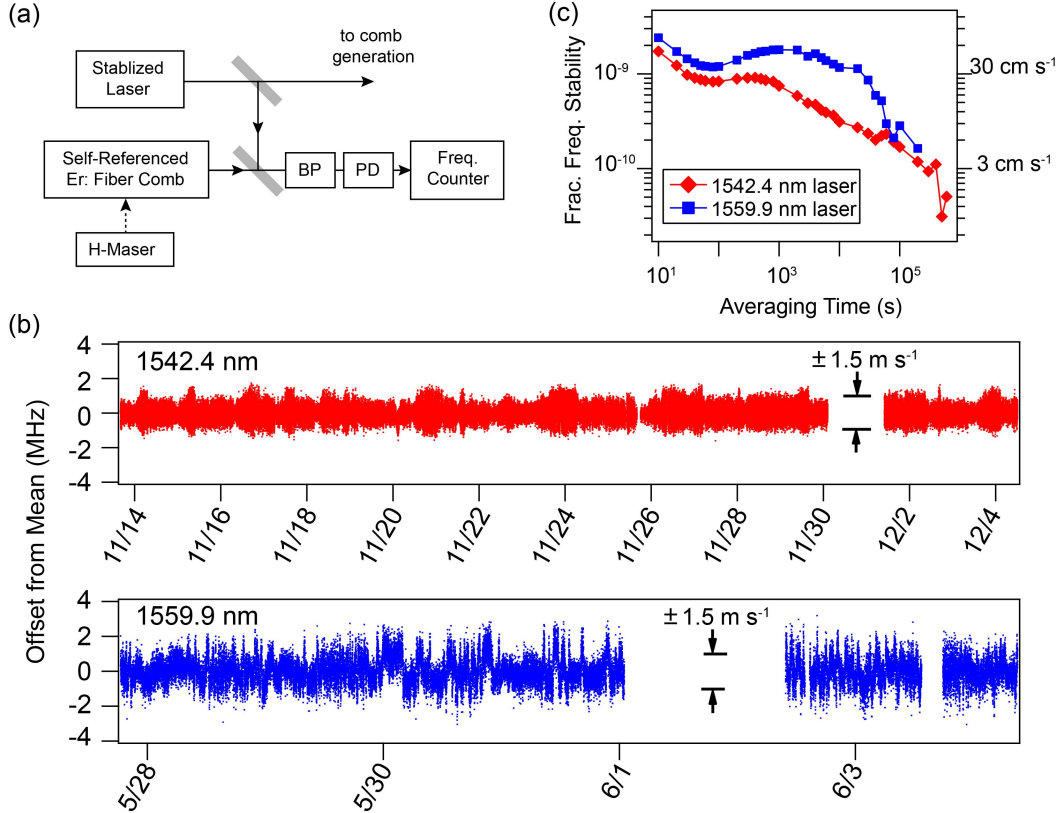


Figure 10.4: Reference laser stability measurement. (a) Experimental setup: BP, optical bandpass filter; PD, photodiode. All beam paths and beam combiners are in single mode fiber. (b) Time series of measured beat frequencies for the two frequency-stabilized lasers with 10 s averaging per measurement. The x-axes are the dates in November of 2013 and May/June of 2014, respectively. (c) Allan deviation, which is a measure of the fractional frequency stability, computed from the time series data of (b). Inset scales give the radial velocity precision.

the pulse train reaches below 2.5%, boosting the peak intensity of the pulses. These pulses are then amplified in a second EDFA (IPG Photonics, EAR-5K-C-LP). For an average power of 1 W, peak power (pulse energy) is 40 W (83 pJ). The amplified pulses are then coupled into a 20 m length of highly-nonlinear fiber (HNLF) with $0.25 \pm 0.15 \text{ ps nm}^{-1} \text{ km}^{-1}$ dispersion and dispersion slope of $0.006 \pm 0.004 \text{ ps nm}^{-2} \text{ km}^{-1}$. Propagation in the HNLF causes self-phase modulation and strong spectral broadening of the comb (Dudley, Genty, and Coen, 2006). Comb spectra span and envelope can be controlled by the pump power launched into the HNLF. A typical comb spectrum with >600 mW pump power from the 1559.9 nm laser is shown in fig. 10.3, with >100 nm spectral span. Moreover, by using different nonlinear fiber and spectral flattening methods, broad combs with level power are possible (Mori,

2005).



Figure 10.5: Astrocomb system in a standard 19 inch instrument rack. The comb board is fixed at the top of the instrument rack. The entire system could be move around inside the observatory facilities.

The LR-EOFC system is mounted on an aluminum breadboard (18" \times 32", or equivalently 45.7 cm \times 81.3 cm) in a standard 19 inch instrument rack (see fig. 10.2 and 10.5) for transport and implementation with the spectrograph at the NASA Infrared telescope facility (IRTF) and at Keck II on Mauna Kea in Hawaii. The system is designed to provide operational robustness matching the requirements of astronomical observation. All optical components prior to the HNLF are polarization maintaining fiber-based, so as to eliminate the effect of polarization drift on spectral broadening in HNLF. Moreover, no control-locking loops are involved in the system and no temperature control is required at the two telescope facilities. As a result, the comb is able to maintain its frequency, bandwidth and intensity without the need to adjust

any parameters. During a 5 day run at IRTF, the comb had zero failures and the intensity of individual comb teeth was measured to deviate less than 2 dB, including multiple power-off and on cycling of the optical continuum generation system (see fig. 10.6(b)).

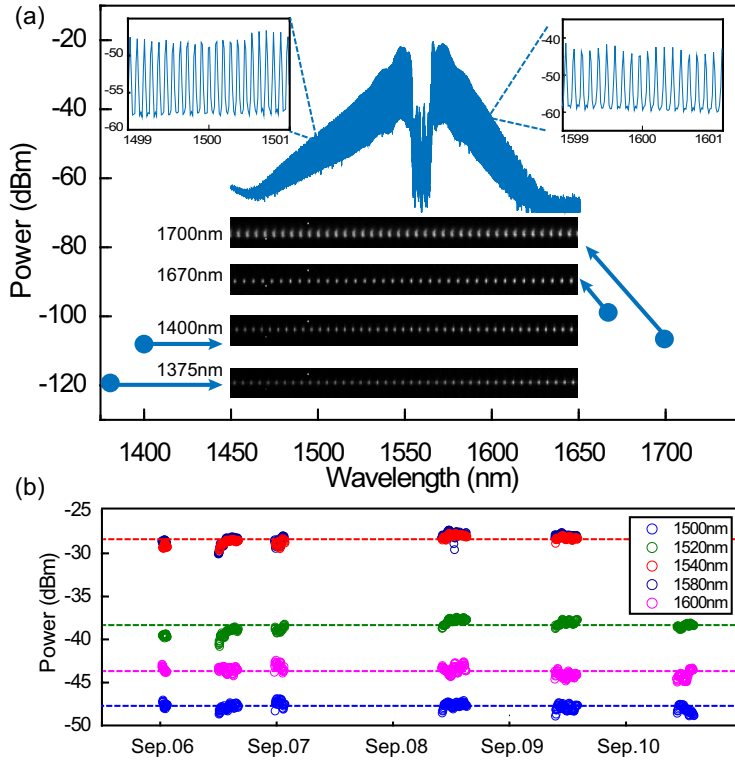


Figure 10.6: Experimental results at IRTF. (a) Comb spectrum produced using 1559.9 nm reference laser. The insets on the top left and right show the resolved comb lines on the optical spectrum analyzer. Comb spectra taken by the CSHELL spectrograph at 1375 nm, 1400 nm, 1670 nm and 1700 nm are presented as insets in the lower half of the figure. The blue circles mark the estimated comb line power and center wavelength for these spectra. Comb lines are detectable on CSHELL at fW power levels. (b) Comb spectral line power vs. time is shown at five different wavelengths. During the 5 day test at IRTF, no parameter adjustment was made, and comb intensity was very stable even with multiple power-on and off cycling of the optical continuum generation system.

Comb stability

²As noted above, the frequency stability of the LR-EOFC is dominated by the stability of the reference laser f_0 . We explored the use of two different

²The work presented in this subsection was performed by Gabriel Ycas and Scott Diddams in NIST, Boulder.

commercially-available lasers (Wavelength References) that were stabilized respectively to Doppler- and pressure-broadened transitions in acetylene (C_2H_2) at 1542.4 nm, and in hydrogen cyanide ($H^{13}C^{15}N$) at 1559.9 nm. We note that the spectroscopy related to the locking of the reference laser to the molecular resonances is done internally to the commercial laser system, so that our experiments only assess the stability of these commercial off-the-shelf (COTS) lasers. To assess the stability, the stabilized laser frequencies were measured relative to an Er:fiber based self-referenced optical frequency comb (Gabriel Ycas, Steve Osterman, and Scott Diddams, n.d.; G. G. Ycas et al., 2012). Fiber-coupled light from a reference laser was combined into a common optical fiber with light from the Er:fiber comb. Then the heterodyne beat between a single comb line and the line-stabilized reference was filtered, amplified, and counted with a 10 s gate time using a frequency counter that was referenced to a hydrogen maser (see fig. 10.4 (a)). The Er:fiber comb was stabilized relative to the same hydrogen maser, such that the fractional frequency stability of the measurement was $< 2 \times 10^{-13}$ at all averaging times. The drift of the hydrogen maser frequency is $< 1 \times 10^{-15}$ per day, thereby providing a stable reference at levels corresponding to a radial velocity uncertainty $\ll 1 \text{ cm sec}^{-1}$. Thus, the frequency of the counted heterodyne beat accurately represents the fluctuations in the reference laser.

The series of 10 s measurements of the heterodyne beat was recorded over 20 days in 2013 for the case of the 1542.4 nm laser and more than 7 days in 2014 for the case of the 1559.9 nm laser, as shown in fig. 10.4 (b). Gaps in the measurements near 11/31 and 6/4 are due to unlocking of the Er:fiber comb from the hydrogen maser reference. From these time series, we calculate the Allan deviation, which is a measure of the fractional frequency fluctuations (instability) of the reference laser as a function of averaging time. As seen in fig. 10.4 (c), the instability of the 1542.2 nm laser is $< 10^{-9}$ (30 cm s^{-1} RV, or corresponding to 200 kHz in frequency) at all averaging times greater than ~ 30 s. The 1559.9 nm laser is less stable, but provides a corresponding RV precision of $< 60 \text{ cm s}^{-1}$ for averaging times greater than 20 s. This difference in stability was to be expected because of the difference in relative absorption line strength between the acetylene and HCN stabilized lasers. In both cases, the stability improves with averaging time, although at a rate slower than predicted for white frequency noise. As an aside, we note that despite the lower stability of the 1559.9 nm laser, this wavelength ultimately produced wider and flatter comb spectra owing to the better gain performance of the fiber amplifier used in this work. We did not explore the noise mechanisms that

lead to the observed Allan deviation, as they arise from detail of the spectroscopy internal to the COTS laser, to which we did not have access.

Additional analysis included an estimate of the drift of the frequencies of the two reference lasers obtained by fitting a line to the full multi-day counter time series. From these linear fits, an upper limit of the drift over the given measurement period was determined to be $< 9 \times 10^{-12}$ per day for the acetylene-referenced laser and $< 4 \times 10^{-11}$ for the hydrogen cyanide-referenced laser. This corresponds to equivalent RV drifts of $< 0.27 \text{ cm s}^{-1}$ and $< 1.2 \text{ cm s}^{-1}$ per day for the two references. Finally, we attempted to place a bound on the repeatability of the 1542.4 nm reference laser during re-locking and power cycling. Although only evaluated for a limited number of power cycles and re-locks, in all cases, we found that the laser frequency returned to its predetermined value within $< 100 \text{ kHz}$, or equivalently, with a RV precision of $< 15 \text{ cm s}^{-1}$.

While these calibrations are sufficient for the few-day observations reported below, confidence in the longer term stability of the molecularly-referenced CW lasers would be required for observations that could extend over many years. Likewise, frequency uncertainty of the molecular references should be examined. Properly addressing the potential frequency drifts on such a multi-year time scale would require a more thorough investigation of systematic frequency effects due to a variety of physical and operational parameters (e.g. laser power, pressure, temperature, and electronic offsets). Alternatively, narrower absorption features, as available in non-linear Doppler-free saturation spectroscopy, could provide improved performance. For example, laboratory experiments have shown fractional frequency instability at the level of 10^{-12} and reproducibility of 1.5×10^{-11} for lasers locked to a Doppler-free transition in acetylene (Edwards et al., 2004). Most promising of all, self-referencing of an EOFC comb has been demonstrated recently (Beha, Cole, Pascal Del'Haye, et al., 2015), enabling full stabilization of the frequency comb to a GPS-disciplined standard. This would eliminate the need for the reference laser to define f_0 , and thereby provide comb stability at the level of the GPS reference (e.g. $< 10^{-11}$ or equivalently $< 0.3 \text{ cm s}^{-1}$) on both long and short timescales.

10.3 Demonstration of astrocomb in IRTF and Keck observatories

IRTF demonstrations

³To demonstrate that the laser comb is portable, robust, and easy-to-use as a wavelength calibration standard, we shipped the laser comb to the NASA Infrared Telescope Facility (IRTF). IRTF is a three-meter diameter infrared-optimized telescope located at the summit of Mauna Kea, Hawaii. The telescope is equipped with a cryogenic echelle spectrograph (CSHELL) operating from 1-5.4 microns. CSHELL is a cryogenic, near-infrared traditional slit-fed spectrograph, with a resolution (Greene et al., 1993; Tokunaga et al., 1990) of $R \sim \lambda/\Delta\lambda = 46,000$ and it images an adjustable single ~ 5 nm wide order spectrum on a 256×256 InSb detector. We have modified the CSHELL spectrograph to permit the addition of a fiber acquisition unit (FAU) for the injection of starlight and laser frequency comb light into a fiber array and focusing on the spectrograph entrance slit. A simple schematic of the FAU is shown in fig. 10.2 (b) and the details are described elsewhere (P. P. Plavchan, Anglada-Escude, et al., 2013; P. P. Plavchan, Bottom, et al., 2013). Before the star-light reaches the CSHELL entrance slit, it can be switched to pass through an isotopic methane absorption gas cell to introduce a common optical path wavelength reference (P. P. Plavchan, Bottom, et al., 2013). A pickoff mirror is next inserted into the beam to re-direct the near-infrared starlight to a fiber via a fiber-coupling lens. A dichroic window re-directs the visible light to a guide camera to maintain the position of the star on the entrance of the fiber tip. For the starlight, we made use of a specialized non-circular core multi-mode fiber (MMF), with a 50×100 micron rectangular core. These fibers “scramble” the near-field spatial modes of the fiber so that the spectrograph is evenly illuminated by the output from the fiber, regardless of the alignment, focus, or weather conditions of the starlight impinging upon the input to the fiber. We additionally made use of a dual-frequency agitator motor to vibrate the 10-meter length of the fiber to provide additional mode mixing, distributing the starlight evenly between all modes. Finally, a lens and a second pickoff mirror are used to relay the output of the starlight from the fiber output back to the spectrograph entrance slit. A single mode fiber (SMF) carrying the laser comb is added next to the non-circular core fiber carrying the star light. This was accomplished by replacing the output single fiber SMA fiber chuck with a custom 3-D printed V-groove array ferrule. This allowed us to send the light from both the star and frequency comb to

³The telescope operation and data process in this subsection were performed by Peter Plavchan (Caltech/JPL), Peter Gao (Caltech), Elise Furlan (Caltech), Michael Bottom (Caltech) and was assisted by Stephanie Liefer (Caltech/JPL), Charles Beichman (Caltech and Caltech/JPL) and IRTF staff.

the entrance slit of the CSHELL spectrograph when rotated in the same orientation as the slit.

Finally, the laser comb and associated electronics rack were set up in the room temperature ($\sim \pm 5^\circ\text{C}$) control room. A 50-meter length of single mode fiber was run from the control room to the telescope dome floor, and along the telescope mount to the CSHELL spectrograph to connect to the V-groove array and FAU. The unpacking, setup and integration of the comb fiber with CSHELL were straightforward, and required only 2 days working at an oxygen-deprived elevation of 14,000 feet in preparation for the observing run. Because the CSHELL spectrometer has a spectral window < 5 nm, there was no effort made to generate spectrally flat combs. Comb lines are well resolved on CSHELL from 1375 nm to 1700 nm (fig. 10.6(a)), with power adjusted by tunable optical attenuators to match the power of star light and 6.7 pixels per comb line spacing at 1670 nm wavelength. Also, comb line power was monitored (fig. 10.6(b)) periodically during the observing run and was stable.

Three partial nights of CSHELL telescope time in September 2014 were used for this first on-sky demonstration of the laser comb. Unfortunately, the observing run was plagued by poor weather conditions, with 5-10 magnitudes of extinction due to clouds. Consequently, we observed the bright M2 II-III star β Peg ($H=-2.1$ mag), which is a pulsating variable star ($P=43.3$ days). Typical exposure times were 150 seconds, and multiple exposures were obtained in sequence.

The star was primarily observed at 1670 nm, with and without the isotopic methane gas cell to provide a wavelength calibration comparison for the laser comb. Other wavelengths were also observed to demonstrate that the spectral grasp of the comb is much larger than the spectral grasp of the spectrograph itself. Given the low SNR (signal-to-noise ratio) on β Peg from the high extinction due to clouds and CSHELL's limited spectral grasp, the SNR of these data is inadequate to demonstrate that the comb is more stable than the gas cell, as shown above.

One critical aspect of demonstrating the usability of the comb for astrophysical spectrographs is the comb line spacing. As seen in fig. 10.7 (a) and (b), the spectra clearly demonstrate that the individual comb lines are resolved with the CSHELL spectrograph without the need for additional line filtering (S Osterman et al., 2011). Thus this comb operates at a frequency that is natively well-suited for astronomical applications with significantly less hardware complexity compared to “traditional” laser frequency combs.

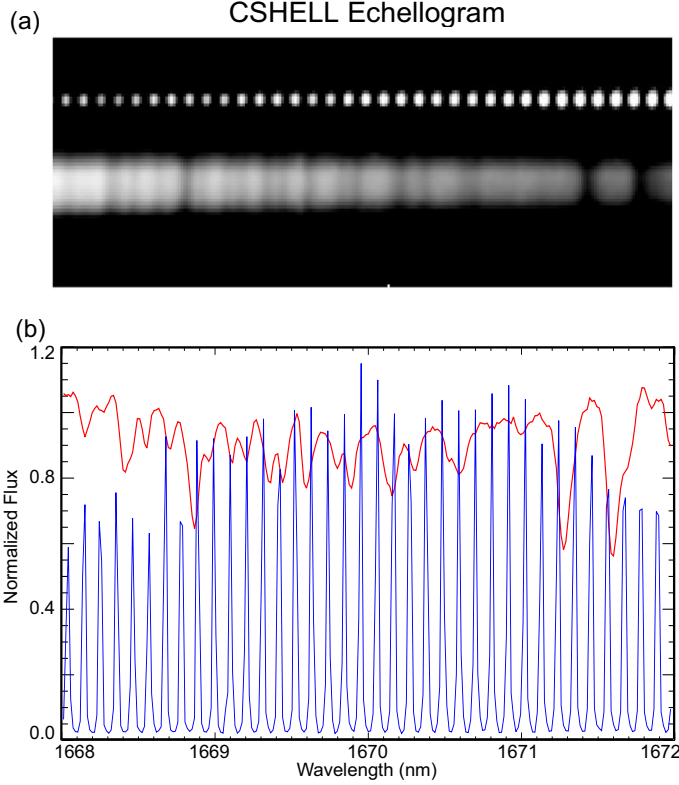


Figure 10.7: (a) An image of the echelle spectrum from CSHELL on IRTF showing a 4 nm portion of spectrum around 1670 nm. The top row of dots are the laser comb lines while the broad spectrum at the bottom is from the bright M2 II-III giant star β Peg seen through dense cloud cover. (b) Spectra extracted from panel a. The solid red curve denotes the average of 11 individual spectra of β Peg (without the gas cell) obtained with CSHELL on the IRTF. The regular sine-wave like blue lines show the spectrum from the laser comb obtained simultaneously with the stellar spectrum. The vertical axis is normalized flux units.

Keck Demonstration

⁴We were able to use daytime access to the near infrared cryogenic echelle spectrograph (NIRSPEC) on the Keck-II telescope McLean et al., 1998 to demonstrate our laser comb. NIRSPEC is a cross-dispersed echelle capable of covering a large fraction of the entire H-band in a single setting with a spectral resolution of $R \sim 25,000$. Observations were taken on May 18 and 19, 2015, with the comb set up in the Keck-II control room in the same configuration as at the IRTF. The apparatus was

⁴Operation of NIRSPEC and data processing were performed by Emily Martin (UCLA), Mike Fitzgerald (UCLA), Greg Doppmann (Keck), Charles Beichman (Caltech, Caltech/JPL) and were assisted by Gautam Vasisht (Caltech/JPL), Stephanie Liefer (Caltech/JPL) and Keck observatory staff.

reassembled after almost 8 months of storage from the time of the IRTF experiment and was fully operational within a few hours. The fiber output from the comb was routed through a cable wrap up to the Nasmyth platform where NIRSPEC is located. We injected the comb signal using a fiber feed into the integrating sphere at the input to the NIRSPEC calibration subsystem. While this arrangement did not allow for simultaneous stellar and comb observations, we were able to measure the comb lines simultaneously with the arc lamps normally used for wavelength calibration and to make hour-long tests of the stability of the NIRSPEC instrument at the sub-pixel level.

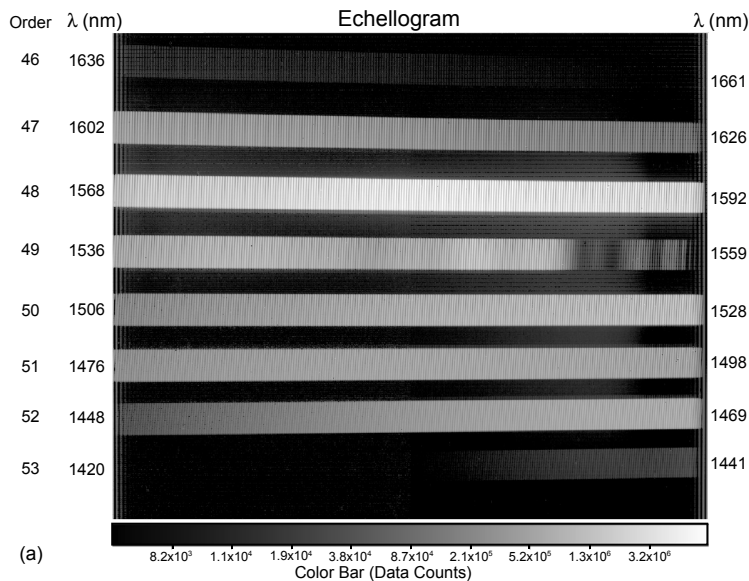


Figure 10.8: Reduced NIRSPEC image from echelle order 46 to 53, displaying the stabilized laser comb using the 1559.9 nm reference laser. Line brightness represents data counts.

Figure 10.8(a) shows the laser comb illuminating more than 6 orders of the high-resolution echellogram. The echelle data were reduced in standard fashion, correcting for dark current and flat field variations. Under this comb setting, a spectral grasp of approximately 200 nm is covered, from 1430 nm to 1640 nm. A zoomed-in spectral extraction (fig. 10.9 (a)) shows that individual comb lines are well resolved at NIRSPEC's resolution and spaced approximately 4 pixels apart (0.1 nm), consistent with the higher resolution IRTF observations described above. The spectral intensity of the comb lines can be made more uniform with a flattening filter to allow constant illumination over the entire span. In this demonstration, we were

also able to implement a programmable optical filter (Waveshaper 1000s) from 1530 to 1600 nm, greatly reducing comb intensity variation (fig. 10.9 (b)). If desired, a customized filter could increase the bandwidth of the flattened regime to cover the entire comb span.

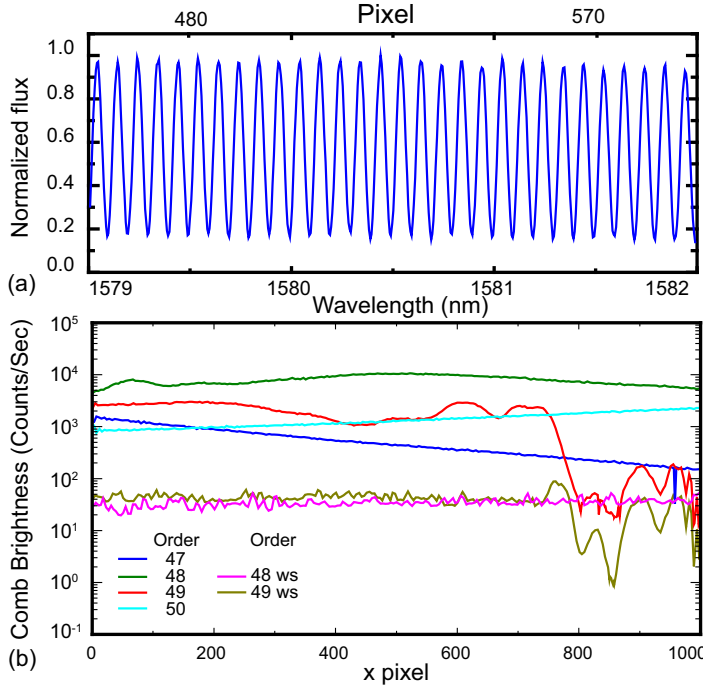


Figure 10.9: (a) A portion of the extracted comb spectrum from order 48 is plotted versus wavelength. (b) Comb brightness envelope of orders 47 to 50 and orders 48 and 49 when flattened by a waveshaper (ws).

We used a series of 600 spectra taken over a ~ 2 hour time period to test the instrumental stability of NIRSPEC. Order 48, which had the highest signal-to-noise comb lines, was reduced following a standard procedure to correct for dark current and flat field variations. Due to the quasi-Littrow configuration of the instrument, the slits appear tilted on the detector and the spectra have some curvature. We performed a spatial rectification using a flat-field image taken with a pinhole slit to mimic a bright compact object on the spectrum in order to account for this curvature. Wavelength calibration and spectral rectification to account for slit tilting were applied using the Ne, Kr, Ar, and Xe arc lamps and the rectification procedure in the REDSPEC software written for NIRSPEC.

Instrumental stability was tested by performing a cross-correlation between the first comb spectrum in the 600 image series and each successive comb spectrum. The

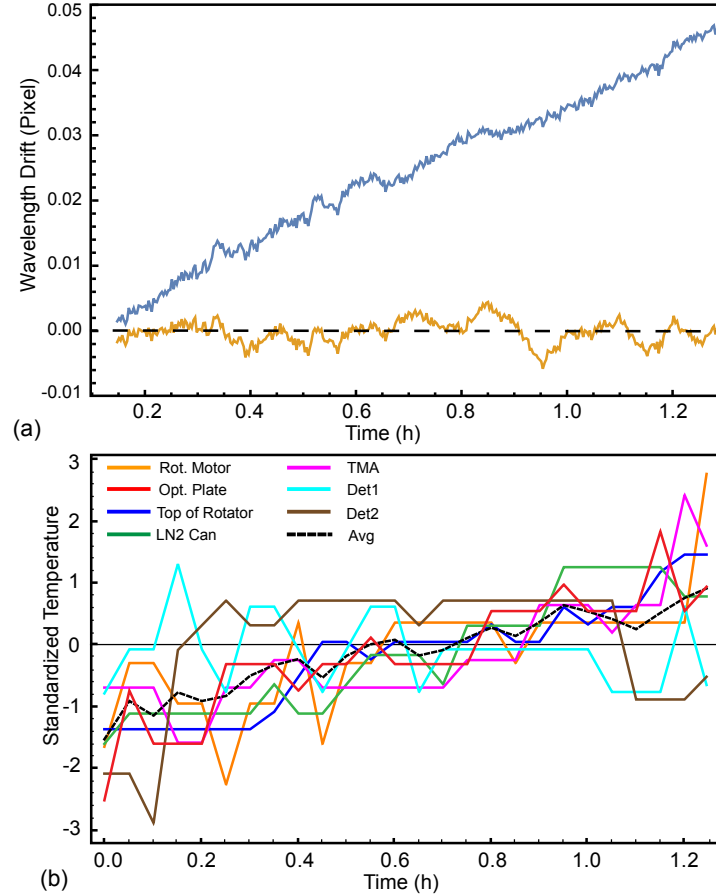


Figure 10.10: Measurement of wavelength and temperature drift on the Keck II NIRSPEC spectrometer. (a) The blue curve shows the drift in the pixel location of individual comb lines in order 48 as measured with the cross-correlation techniques described in the text. The yellow curve shows the residual shifts after de-correlating the effects of the internal NIRSPEC temperatures. (b) Five internal NIRSPEC temperatures are shown as a function of time. For ease of plotting, the individual temperatures have been standardized with respect to the means and standard deviations of each sensor. The black dashed curve shows the average of these standardized temperatures. The effect of the quantization of the temperature data at the 10 mK level (as recorded in the available telemetry) is evident in the individual temperature curves.

peak of the cross correlation function corresponded to the drift, measured in pixels, between the images. Figure 10.10 (a) demonstrates the power of the laser comb to provide a wavelength standard for the spectrometer. Over a period of roughly an hour the centroid of each comb line in Order 48 moved by about 0.05 pixel, equivalent to 0.0114 Å. By examining various internal NIRSPEC temperatures it is possible to show that this drift correlates to changes inside the instrument. Figure

10.10 (b) shows changes in the temperatures measured at five different points within the instrument: the grating mechanism motor, an optical mounting plate, the top of the grating rotator mechanism, the base of the (unused) LN₂ container and the three mirror anastigmat assembly (TMA) (McLean et al., 1998). At these locations the temperatures range from 50 to 75 K and have been standardized to fit onto a single plot: $\Theta_i(t) = (T_i(t) - \langle T \rangle)/\sigma(T)$. Average values of each temperature show drifts of order 15-35 mK over this 1-hr period. In its present configuration NIRSPEC is cooled using a closed cycle refrigerator without active temperature control — only the detector temperature is maintained under closed cycle control to ~ 1 mK.

Examination of the wavelength and temperature drifts in the two figures reveals an obvious correlation. A simple linear fit of the wavelength drift to the five standardized temperatures reduces the temperature-induced wavelength drifts from 0.05 pixel hr⁻¹ to a near-constant value with a standard deviation of $\sigma = 0.0017$ pixel for a single comb line (bottom curve in figure 10.10 (a)). While other mechanical effects may manifest themselves in other or longer time series, this small dataset indicates the power of the laser comb to stabilize the wavelength scale of the spectrometer. At the present spectral resolution of NIRSPEC, $R \sim 25,000$, and with over 240 comb lines in just this one order, we can set a limit on the velocity drift due to drifts within NIRSPEC of $\sim c/R \times \sigma / \sqrt{\#lines} < 1.5$ m s⁻¹ where c is the speed of light.

Thus, operation with a laser comb covering over 200 nm with more than 2000 lines in the H-band would allow much higher radial velocity precision than is presently possible using, for example, atmospheric OH lines, as a wavelength standard. NIRSPEC's ultimate RV precision will depend on many factors, including the brightness of the star, NIRSPEC's spectral resolution (presently 25,000 but increasing to 37,500 after a planned upgrade) and the ability to stabilize the input stellar light against pointing drifts and line profile variations. We anticipate that in an exposure of 900 sec NIRSPEC should be able to achieve an RV precision ~ 1 m s⁻¹ for stars brighter than H=7 mag and < 3 m s⁻¹ for stars brighter than H<9 mag. A detailed discussion of the NIRSPEC error budget is beyond the scope of this paper, but a stable wavelength reference, observed simultaneously with the stellar spectrum, is critical to achieving this precision.

10.4 Summary

Many challenges remain to achieving the high precision RV capability needed for the study of exoplanets orbiting late M dwarfs, jitter-prone hotter G and K spectral types, or young stars exhibiting high levels of RV noise in the visible. Achieving adequate signal to noise on relatively faint stars requires a large spectral grasp on a high-resolution spectrometer on a large aperture telescope. Injecting both the laser comb and starlight into the spectrograph with a highly stable line spread function demands carefully designed interfaces between the comb light and star light at the entrance to the spectrograph. Extracting the data from the spectrometer requires careful attention to flat-fielding and other detector features. Finally, reducing the extracted spectra to produce RV measurements at the required level of precision requires sophisticated modeling of complex stellar atmospheres and telluric atmospheric absorption. The research described here addresses only one of these steps, namely the generation of a highly stable wavelength standard in the NIR suitable for sub m s^{-1} RV measurements.

BIBLIOGRAPHY

- Agrawal, Govind P (2007). *Nonlinear fiber optics*. Academic press.
- Akhmediev, Nail and Magnus Karlsson (1995). “Cherenkov radiation emitted by solitons in optical fibers”. In: *Phys. Rev. A* 51.3, p. 2602.
- Anderson, Miles H et al. (2016). “Measurement of the Raman Self-Frequency Shift of a Temporal Cavity Soliton”. In: *Nonlinear Photonics*. Optical Society of America, NW4A–4.
- Ankiewicz, Adrian and Nail Akhmediev (2008). *Dissipative Solitons: From Optics to Biology and Medicine*. Springer.
- Aoki, Takao et al. (2006). “Observation of strong coupling between one atom and a monolithic microresonator”. In: *Nature* 443.7112, pp. 671–674.
- Atieh, AK et al. (1999). “Measuring the Raman Time Constant (T_R) for Soliton Pulses in Standard Single-Mode Fiber”. In: *Journal of lightwave technology* 17.2, p. 216.
- Bao, Changjing et al. (2014). “Nonlinear conversion efficiency in Kerr frequency comb generation”. In: *Opt. Lett.* 39.21, pp. 6126–6129.
- Bao, Chengying, Wonkeun Chang, et al. (2015). “Observation of Coexisting Dissipative Solitons in a Mode-Locked Fiber Laser”. In: *Physical review letters* 115.25, p. 253903.
- Bao, Chengying, Jose A Jaramillo-Villegas, et al. (2016). “Observation of Fermi-Pasta-Ulam Recurrence Induced by Breather Solitons in an Optical Microresonator”. In: *Physical Review Letters* 117.16, p. 163901.
- Bauer, Florian F, Mathias Zechmeister, and Ansgar Reiners (2015). “Calibrating echelle spectrographs with Fabry-Perot etalons”. In: *arXiv preprint arXiv:1506.07887*.
- Beha, Katja, Daniel C Cole, Pascal Del’Haye, et al. (2015). “Self-referencing a continuous-wave laser with electro-optic modulation”. In: *arXiv preprint arXiv:1507.06344*.
- Beha, Katja, Daniel C Cole, Pascal Del’Haye, et al. (2017). “Electronic synthesis of light”. In: *Optica* 4.4, pp. 406–411.
- Bize, S et al. (2003). “Testing the Stability of Fundamental Constants with the H g+ 199 Single-Ion Optical Clock”. In: *Physical review letters* 90.15, p. 150802.
- Braje, DA et al. (2008). “Astronomical spectrograph calibration with broad-spectrum frequency combs”. In: *The European Physical Journal D* 48.1, pp. 57–66.
- Brasch, Victor et al. (2016). “Self-referencing of an on-chip soliton Kerr frequency comb without external broadening”. In: *arXiv preprint arXiv:1605.02801*.

- Brasch, V. et al. (2014). “Photonic chip based optical frequency comb using soliton induced Cherenkov radiation”. In: *ArXiv e-prints*. arXiv: 1410 . 8598 [physics.optics].
- Brasch, V et al. (2016). “Photonic chip-based optical frequency comb using soliton Cherenkov radiation”. In: *Science* 351.6271, pp. 357–360.
- Cai, Ming et al. (2000). “Fiber-coupled microsphere laser”. In: *Optics letters* 25.19, pp. 1430–1432.
- Callahan, Patrick T, Michael C Gross, and Michael L Dennis (2011). “Frequency-independent phase noise in a dual-wavelength Brillouin fiber laser”. In: *IEEE Journal of Quantum Electronics* 47.8, pp. 1142–1150.
- Carmon, Tal, Lan Yang, and Kerry Vahala (2004). “Dynamical thermal behavior and thermal self-stability of microcavities”. In: *Opt. Express* 12.20, pp. 4742–4750.
- Carpintero, Guillermo et al. (2012). “95 GHz millimeter wave signal generation using an arrayed waveguide grating dual wavelength semiconductor laser”. In: *Optics letters* 37.17, pp. 3657–3659.
- Chembo, Yanne K and Curtis R Menyuk (2013). “Spatiotemporal Lugiato-Lefever formalism for Kerr-comb generation in whispering-gallery-mode resonators”. In: *Physical Review A* 87.5, p. 053852.
- Chembo, Yanne K and Nan Yu (2010). “Modal expansion approach to optical-frequency-comb generation with monolithic whispering-gallery-mode resonators”. In: *Physical Review A* 82.3, p. 033801.
- Cheng, Ji et al. (2012). “Intermodal Čerenkov radiation in a higher-order-mode fiber”. In: *Opt. Lett.* 37.21, pp. 4410–4412.
- Cherenkov, Pavel A (1934). “Visible emission of clean liquids by action of γ radiation”. In: *Doklady Akademii Nauk SSSR* 2, p. 451.
- Chou, Chin-Wen et al. (2010). “Optical clocks and relativity”. In: *Science* 329.5999, pp. 1630–1633.
- Coddington, Ian, Nathan Newbury, and William Swann (2016). “Dual-comb spectroscopy”. In: *Optica* 3.4, pp. 414–426.
- Coddington, Ian, William C Swann, and Nathan R Newbury (2008). “Coherent multiheterodyne spectroscopy using stabilized optical frequency combs”. In: *Physical Review Letters* 100.1, p. 013902.
- Cole, Daniel C et al. (2016). “Soliton crystals in Kerr resonators”. In: *arXiv preprint arXiv:1610.00080*.
- Collings, Brandon C et al. (2000). “Polarization-locked temporal vector solitons in a fiber laser: experiment”. In: *J. Opt. Soc. Am. B* 17.3, pp. 354–365.
- Crosignani, Bruno and Paolo Di Porto (1981). “Soliton propagation in multimode optical fibers”. In: *Opt. Lett.* 6.7, pp. 329–330.

- Cundiff, ST (2005). “Soliton dynamics in mode-locked lasers”. In: *Dissipative Solitons*. Springer, pp. 183–206.
- Cundiff, Steven T and Jun Ye (2003). “Colloquium: Femtosecond optical frequency combs”. In: *Reviews of Modern Physics* 75.1, p. 325.
- Cundiff, ST et al. (1999). “Observation of polarization-locked vector solitons in an optical fiber”. In: *Phys. Rev. Lett.* 82.20, p. 3988.
- Del’Haye, Pascal, Katja Beha, et al. (2014). “Self-injection locking and phase-locked states in microresonator-based optical frequency combs”. In: *Phys. Rev. Lett.* 112.4, p. 043905.
- Del’Haye, Pascal, Aurélien Coillet, Tara Fortier, et al. (2016). “Phase-coherent microwave-to-optical link with a self-referenced microcomb”. In: *Nature Photonics* 10, pp. 516–520.
- Del’Haye, Pascal, Aurélien Coillet, William Loh, et al. (2015). “Phase steps and resonator detuning measurements in microresonator frequency combs”. In: *Nat. Commun.* 6, p. 5668.
- Del’Haye, Pascal et al. (2008). “Full stabilization of a microresonator-based optical frequency comb”. In: *Physical Review Letters* 101.5, p. 053903.
- Del’Haye, P et al. (2007). “Optical frequency comb generation from a monolithic microresonator”. In: *Nature* 450.7173, pp. 1214–1217.
- Diddams, SA, JC Bergquist, et al. (2004). “Standards of time and frequency at the outset of the 21st century”. In: *Science* 306.5700, pp. 1318–1324.
- Diddams, SA, Th Udem, et al. (2001). “An optical clock based on a single trapped $^{199}\text{Hg}^+$ ion”. In: *Science* 293.5531, pp. 825–828.
- Diddams, Scott A (2010). “The evolving optical frequency comb [Invited]”. In: *JOSA B* 27.11, B51–B62.
- Diddams, Scott A, Leo Hollberg, and Vela Mbele (2007). “Molecular fingerprinting with the resolved modes of a femtosecond laser frequency comb”. In: *Nature* 445.7128, pp. 627–630.
- Diddams, Scott A, David J Jones, et al. (2000). “Direct link between microwave and optical frequencies with a 300 THz femtosecond laser comb”. In: *Physical Review Letters* 84.22, p. 5102.
- Drever, RWP et al. (1983). “Laser phase and frequency stabilization using an optical resonator”. In: *Applied Physics B* 31.2, pp. 97–105.
- Dudley, John M, Goëry Genty, and Stéphane Coen (2006). “Supercontinuum generation in photonic crystal fiber”. In: *Reviews of modern physics* 78.4, p. 1135.
- Edwards, Christopher S et al. (2004). “Absolute frequency measurement of a 1.5- μm acetylene standard by use of a combined frequency chain and femtosecond comb”. In: *Optics letters* 29.6, pp. 566–568.

- Ferdous, Fahmida et al. (2011). “Spectral line-by-line pulse shaping of on-chip microresonator frequency combs”. In: *Nature Photon.* 5.12, pp. 770–776.
- Fortier, TM et al. (2011). “Generation of ultrastable microwaves via optical frequency division”. In: *Nature Photonics* 5.7, pp. 425–429.
- Fujiwara, M et al. (2001). “Flattened optical multicarrier generation of 12.5 GHz spaced 256 channels based on sinusoidal amplitude and phase hybrid modulation”. In: *Electronics Letters* 37.15, pp. 967–968.
- Gambetta, Alessio, Roberta Ramponi, and Marco Marangoni (2008). “Mid-infrared optical combs from a compact amplified Er-doped fiber oscillator”. In: *Opt. Lett.* 33.22, pp. 2671–2673.
- Geng, Jihong, Sean Staines, and Shibin Jiang (2008). “Dual-frequency Brillouin fiber laser for optical generation of tunable low-noise radio frequency/microwave frequency”. In: *Optics letters* 33.1, pp. 16–18.
- Glenday, Alexander G et al. (2015). “Operation of a broadband visible-wavelength astro-comb with a high-resolution astrophysical spectrograph”. In: *Optica* 2.3, pp. 250–254.
- Gordon, James P (1986). “Theory of the soliton self-frequency shift”. In: *Optics letters* 11.10, pp. 662–664.
- Greene, Thomas P et al. (1993). “CSHELL: a high spectral resolution 1-5- μm cryogenic echelle spectrograph for the IRTF”. In: *Optical Engineering and Photonics in Aerospace Sensing*. 313–324.
- Griffith, Austin G et al. (2015). “Silicon-chip mid-infrared frequency comb generation”. In: *Nature communications* 6, p. 6299.
- Gross, Michael C et al. (2010). “Tunable millimeter-wave frequency synthesis up to 100 GHz by dual-wavelength Brillouin fiber laser”. In: *Optics express* 18.13, pp. 13321–13330.
- Grudinin, Ivan S, Vincent Huet, et al. (2016). “High-contrast Kerr Frequency Combs”. In: *arXiv preprint arXiv:1612.00820*.
- Grudinin, Ivan S and Nan Yu (2015). “Towards efficient octave-spanning comb with micro-structured crystalline resonator”. In: *SPIE LASE*. International Society for Optics and Photonics, 93430F–93430F.
- Grudinin, Ivan S, Nan Yu, and Lute Maleki (2009). “Generation of optical frequency combs with a CaF₂ resonator”. In: *Opt. Lett.* 34.7, pp. 878–880.
- Guo, H et al. (2016). “Universal dynamics and deterministic switching of dissipative Kerr solitons in optical microresonators”. In: *Nature Physics*, doi:10.1038/nphys3893.
- Hall, John L (2006). “Nobel Lecture: Defining and measuring optical frequencies”. In: *Reviews of Modern Physics* 78.4, p. 1279.

- Halverson, Samuel et al. (2014). “Development of fiber Fabry-Perot interferometers as stable near-infrared calibration sources for high resolution spectrographs”. In: *Publications of the Astronomical Society of the Pacific* 126.939, pp. 445–458.
- Hänsch, Theodor W (2006). “Nobel lecture: passion for precision”. In: *Reviews of Modern Physics* 78.4, p. 1297.
- Hasegawa, Akira (1980). “Self-confinement of multimode optical pulse in a glass fiber”. In: *Opt. Lett.* 5.10, pp. 416–417.
- (2000). “Soliton-based optical communications: An overview”. In: *IEEE Journal of Selected Topics in Quantum Electronics* 6.6, pp. 1161–1172.
- Hasegawa, Akira and Frederick Tappert (1973). “Transmission of stationary nonlinear optical pulses in dispersive dielectric fibers. I. Anomalous dispersion”. In: *Appl. Phys. Lett.* 23.3, pp. 142–144.
- Haus, Herman A et al. (2000). “Mode-locking of lasers”. In: *IEEE J. Sel. Topics Quantum Electron.* 6.6, pp. 1173–1185.
- Haus, Hermann A and Weiping P Huang (1991). “Coupled-mode theory”. In: *Proc. IEEE* 79.10, pp. 1505–1518.
- Haus, Hermann A and William S Wong (1996). “Solitons in optical communications”. In: *Rev. Mod. Phys.* 68.2, p. 423.
- Hausmann, BJM et al. (2014). “Diamond nonlinear photonics”. In: *Nat. Photon.* 8.5, pp. 369–374.
- Headley, Clifford and Govind P Agrawal (1996). “Unified description of ultrafast stimulated Raman scattering in optical fibers”. In: *JOSA B* 13.10, pp. 2170–2177.
- Herr, T, V Brasch, JD Jost, I Mirgorodskiy, et al. (2014). “Mode spectrum and temporal soliton formation in optical microresonators”. In: *Phys. Rev. Lett.* 113.12, p. 123901.
- Herr, T, V Brasch, JD Jost, CY Wang, et al. (2014). “Temporal solitons in optical microresonators”. In: *Nat. Photon.* 8.2, pp. 145–152.
- Herr, T, K Hartinger, et al. (2012). “Universal formation dynamics and noise of Kerr-frequency combs in microresonators”. In: *Nature Photonics* 6.7, pp. 480–487.
- Holzwarth, R et al. (2000). “Optical frequency synthesizer for precision spectroscopy”. In: *Phys. Rev. Lett.* 85.11, p. 2264.
- Huang, Chen-Bin et al. (2008). “Nonlinearly broadened phase-modulated continuous-wave laser frequency combs characterized using DPSK decoding”. In: *Optics express* 16.4, pp. 2520–2527.
- Huang, S-W et al. (2016). “Smooth and flat phase-locked Kerr frequency comb generation by higher order mode suppression”. In: *Scientific reports* 6, p. 26255.

- Imai, K, M Kourogi, and M Ohtsu (1998). “30-THz span optical frequency comb generation by self-phase modulation in an optical fiber”. In: *IEEE journal of quantum electronics* 34.1, pp. 54–60.
- Ishizawa, Atsushi et al. (2013). “Phase-noise characteristics of a 25-GHz-spaced optical frequency comb based on a phase-and intensity-modulated laser”. In: *Optics express* 21.24, pp. 29186–29194.
- Islam, MN, CD Poole, and JP Gordon (1989). “Soliton trapping in birefringent optical fibers”. In: *Opt. Lett.* 14.18, pp. 1011–1013.
- Islam, Mohammed N (2002). “Raman amplifiers for telecommunications”. In: *IEEE J. Sel. Topics Quantum Electron.* 8.3, pp. 548–559.
- Ivanov, Eugene N, Scott A Diddams, and Leo Hollberg (2005). “Study of the excess noise associated with demodulation of ultra-short infrared pulses”. In: *IEEE transactions on ultrasonics, ferroelectrics, and frequency control* 52.7, pp. 1068–1074.
- Jang, Jae K, Miro Erkintalo, Stéphane Coen, et al. (2015). “Temporal tweezing of light through the trapping and manipulation of temporal cavity solitons”. In: *Nat. Commun.* 6.
- Jang, Jae K, Miro Erkintalo, Stuart G Murdoch, et al. (2013). “Ultraweak long-range interactions of solitons observed over astronomical distances”. In: *Nat. Photon.* 7.8, pp. 657–663.
- Jones, David J et al. (2000). “Carrier-envelope phase control of femtosecond mode-locked lasers and direct optical frequency synthesis”. In: *Science* 288.5466, pp. 635–639.
- Joshi, Chaitanya et al. (2016). “Thermally controlled comb generation and soliton modelocking in microresonators”. In: *Opt. Lett.* 41.11, pp. 2565–2568.
- Jost, JD et al. (2014). “Microwave to Optical Link Using an Optical Microresonator”. In: *arXiv preprint arXiv:1411.1354*.
- Jung, Hojoong et al. (2013). “Optical frequency comb generation from aluminum nitride microring resonator”. In: *Opt. Lett.* 38.15, pp. 2810–2813.
- Karpov, Maxim, Hairun Guo, Arne Kordts, Victor Brasch, Martin HP Pfeiffer, et al. (2016). “Raman self-frequency shift of dissipative Kerr solitons in an optical microresonator”. In: *Phys. Rev. Lett.* 116.10, p. 103902.
- Karpov, Maxim, Hairun Guo, Arne Kordts, Victor Brasch, Martin Pfeiffer, et al. (2015). “Raman induced soliton self-frequency shift in microresonator Kerr frequency combs”. In: *arXiv preprint arXiv:1506.08767*.
- Kasting, James F, Daniel P Whitmire, and Ray T Reynolds (1993). “Habitable zones around main sequence stars”. In: *Icarus* 101.1, pp. 108–128.
- Kessler, T et al. (2012). “A sub-40-mHz-linewidth laser based on a silicon single-crystal optical cavity”. In: *Nature Photonics* 6.10, pp. 687–692.

- Kippenberg, TJ, SM Spillane, and KJ Vahala (2004). “Kerr-nonlinearity optical parametric oscillation in an ultrahigh-Q toroid microcavity”. In: *Phys. Rev. Lett.* 93.8, p. 083904.
- Kippenberg, Tobias J, Ronald Holzwarth, and SA Diddams (2011). “Microresonator-based optical frequency combs”. In: *Science* 332.6029, pp. 555–559.
- Kippenberg, Tobias J, Sean M Spillane, et al. (2004). “Theoretical and experimental study of stimulated and cascaded Raman scattering in ultrahigh-Q optical microcavities”. In: *IEEE Journal of selected topics in Quantum Electronics* 10.5, pp. 1219–1228.
- Kippenberg, Tobias J and Kerry J Vahala (2008). “Cavity optomechanics: back-action at the mesoscale”. In: *science* 321.5893, pp. 1172–1176.
- Kordts, Arne et al. (2016). “Higher order mode suppression in high-Q anomalous dispersion SiN microresonators for temporal dissipative Kerr soliton formation”. In: *Optics letters* 41.3, pp. 452–455.
- Kotani, Takayuki et al. (2014). “Infrared Doppler instrument (IRD) for the Subaru telescope to search for Earth-like planets around nearby M-dwarfs”. In: *SPIE Astronomical Telescopes+ Instrumentation*. 914714.
- Lee, Hansuek, Tong Chen, et al. (2012). “Chemically etched ultrahigh-Q wedge-resonator on a silicon chip”. In: *Nat. Photon.* 6.6, pp. 369–373.
- Lee, Hansuek, Myoung-Gyun Suh, et al. (2013). “Spiral resonators for on-chip laser frequency stabilization”. In: *Nat. Commun.* 4, p. 2468.
- Leo, François et al. (2010). “Temporal cavity solitons in one-dimensional Kerr media as bits in an all-optical buffer”. In: *Nat. Photon.* 4.7, pp. 471–476.
- Levy, Jacob S et al. (2010). “CMOS-compatible multiple-wavelength oscillator for on-chip optical interconnects”. In: *Nat. Photon.* 4.1, pp. 37–40.
- Li, Chih-Hao et al. (2008). “A laser frequency comb that enables radial velocity measurements with a precision of 1 cm/s”. In: *Nature* 452.7187, pp. 610–612.
- Li, Jiang, Hansuek Lee, and Kerry J Vahala (2013). “Microwave synthesizer using an on-chip Brillouin oscillator”. In: *Nature communications* 4.2097.
- (2014). “Low-noise Brillouin laser on a chip at 1064 nm”. In: *Optics letters* 39.2, pp. 287–290.
- Li, Jiang, Hansuek Lee, Ki Youl Yang, et al. (2012). “Sideband spectroscopy and dispersion measurement in microcavities”. In: *Optics express* 20.24, pp. 26337–26344.
- Li, Jiang, Xu Yi, et al. (2014). “Electro-optical frequency division and stable microwave synthesis”. In: *Science* 345.6194, pp. 309–313.
- Li, Jiang et al. (2012a). “Characterization of a high coherence, Brillouin microcavity laser on silicon”. In: *Optics express* 20.18, pp. 20170–20180.

- Li, Jiang et al. (2012b). “Low-pump-power, low-phase-noise, and microwave to millimeter-wave repetition rate operation in microcombs”. In: *Phys. Rev. Lett.* 109.23, p. 233901.
- Li, Qing et al. (2015). “Octave-spanning microcavity Kerr frequency combs with harmonic dispersive-wave emission on a silicon chip”. In: *Frontiers in Optics*. Optical Society of America, FW6C–5.
- Liang, W, D Eliyahu, et al. (2015). “High spectral purity Kerr frequency comb radio frequency photonic oscillator”. In: *Nat. Commun.* 6, p. 7957.
- Liang, W, AA Savchenkov, et al. (2011). “Generation of near-infrared frequency combs from a MgF₂ whispering gallery mode resonator”. In: *Opt. Lett.* 36.12, pp. 2290–2292.
- Liu, Junqiu et al. (2016). “Frequency-comb-assisted broadband precision spectroscopy with cascaded diode lasers”. In: *Optics Letters* 41.13, pp. 3134–3137.
- Liu, Yang et al. (2014). “Investigation of mode coupling in normal-dispersion silicon nitride microresonators for Kerr frequency comb generation”. In: *Optica* 1.3, pp. 137–144.
- Loh, William et al. (2015). “Dual-microcavity narrow-linewidth Brillouin laser”. In: *Optica* 2.3, pp. 225–232.
- Lu, Tao et al. (2011). “High sensitivity nanoparticle detection using optical microcavities”. In: *Proceedings of the National Academy of Sciences* 108.15, pp. 5976–5979.
- Lucas, Erwan, John D Jost, and Tobias J Kippenberg (2016). “Study on the detuning-dependent properties of a temporal dissipative Kerr soliton in an optical microresonator”. In: *arXiv preprint arXiv:1609.02723*.
- Lugiato, Luigi A and René Lefever (1987). “Spatial dissipative structures in passive optical systems”. In: *Physical review letters* 58.21, p. 2209.
- Manili, G et al. (2012). “Gigantic dispersive wave emission from dual concentric core microstructured fiber”. In: *Opt. Lett.* 37.19, pp. 4101–4103.
- Marcy, G and Howard. A (2011). “The astrophysics of planetary systems: formation, structure, and dynamical evolution”. In: *Proceedings IAU symposium*. Vol. 276. 3–12.
- Marin-Palomo, Pablo et al. (2016). “Microresonator solitons for massively parallel coherent optical communications”. In: *arXiv preprint arXiv:1610.01484*.
- Matsko, AB et al. (2011). “Mode-locked Kerr frequency combs”. In: *Opt. Lett.* 36.15, pp. 2845–2847.
- Matsko, Andrey B and Vladimir S Ilchenko (2006). “Optical resonators with whispering gallery modes I: basics”. In: *IEEE J. Sel. Top. Quantum Electron* 12.3, p. 3.

- Matsko, Andrey B, Wei Liang, et al. (2016). “Optical Cherenkov radiation in overmoded microresonators”. In: *Opt. Lett.* 41.13, pp. 2907–2910.
- Matsko, Andrey B and Lute Maleki (2013). “On timing jitter of mode locked Kerr frequency combs”. In: *Opt. Express* 21.23, pp. 28862–28876.
- Matsko, Andrey et al. (2016). “Cherenkov Radiation Kerr Frequency Combs Based on Mode anti-Crossings”. In: *Opt. Lett.*, Doc ID: 261524.
- McKeever, Jason et al. (2003). “Experimental realization of a one-atom laser in the regime of strong coupling”. In: *Nature* 425.6955, pp. 268–271.
- McLean, Ian S et al. (1998). “Design and development of NIRSPEC: a near-infrared echelle spectrograph for the Keck II telescope”. In: *Astronomical Telescopes & Instrumentation*. 566–578.
- Menyuk, Curtis R (1987). “Stability of solitons in birefringent optical fibers. I: Equal propagation amplitudes”. In: *Opt. Lett.* 12.8, pp. 614–616.
- Metcalf, Andrew J et al. (2013). “High-power broadly tunable electrooptic frequency comb generator”. In: *IEEE Journal of Selected Topics in Quantum Electronics* 19.6, pp. 231–236.
- Milián, Carles et al. (2015). “Solitons and frequency combs in silica microring resonators: Interplay of the Raman and higher-order dispersion effects”. In: *Phys. Rev. A* 92.3, p. 033851.
- Millot, Guy et al. (2015). “Frequency-agile dual-comb spectroscopy”. In: *Nature Photonics*.
- Mitschke, Fedor M and Linn F Mollenauer (1986). “Discovery of the soliton self-frequency shift”. In: *Optics letters* 11.10, pp. 659–661.
- Modotto, Daniele et al. (2015). “Efficiency of dispersive wave generation in dual concentric core microstructured fiber”. In: *JOSA B* 32.8, pp. 1676–1685.
- Mollenauer, Linn F, Roger H Stolen, and James P Gordon (1980). “Experimental observation of picosecond pulse narrowing and solitons in optical fibers”. In: *Phys. Rev. Lett.* 45.13, p. 1095.
- Mori, K (2005). “Supercontinuum lightwave source employing Fabry-Perot filter for generating optical carriers with high signal-to-noise ratio”. In: *Electronics Letters* 41.17, pp. 975–976.
- Morohashi, Isao, Takahide Sakamoto, Hideyuki Sotobayashi, Tetsuya Kawanishi, and Iwao Hosako (2009). “Broadband wavelength-tunable ultrashort pulse source using a Mach-Zehnder modulator and dispersion-flattened dispersion-decreasing fiber”. In: *Optics letters* 34.15, pp. 2297–2299.

- Morohashi, Isao, Takahide Sakamoto, Hideyuki Sotobayashi, Tetsuya Kawanishi, Iwao Hosako, and Masahiro Tsuchiya (2008). “Widely repetition-tunable 200 fs pulse source using a Mach–Zehnder-modulator-based flat comb generator and dispersion-flattened dispersion-decreasing fiber”. In: *Optics letters* 33.11, pp. 1192–1194.
- Murata, Hiroshi et al. (2000). “Optical pulse generation by electrooptic-modulation method and its application to integrated ultrashort pulse generators”. In: *IEEE Journal of Selected Topics in Quantum Electronics* 6.6, pp. 1325–1331.
- Murphy, MT et al. (2007). “High-precision wavelength calibration of astronomical spectrographs with laser frequency combs”. In: *Monthly Notices of the Royal Astronomical Society* 380.2, pp. 839–847.
- Mussot, Arnaud et al. (2014). “Fermi-Pasta-Ulam recurrence in nonlinear fiber optics: the role of reversible and irreversible losses”. In: *Physical Review X* 4.1, p. 011054.
- Newbury, Nathan R (2011). “Searching for applications with a fine-tooth comb”. In: *Nat. Photon.* 5.4, pp. 186–188.
- Oh, Dong Yoon et al. (2014). “Supercontinuum generation in an on-chip silica waveguide”. In: *Opt. Lett.* 39.4, pp. 1046–1048.
- Osterman, Steve et al. (2007). “A proposed laser frequency comb-based wavelength reference for high-resolution spectroscopy”. In: *Optical Engineering+ Applications*. 66931G.
- Osterman, S et al. (2011). “A near infrared laser frequency comb for high precision Doppler planet surveys”. In: *EPJ Web of Conferences*. Vol. 16. 02002.
- Pan, Shilong and Jianping Yao (2009). “A wavelength-switchable single-longitudinal-mode dual-wavelength erbium-doped fiber laser for switchable microwave generation”. In: *Optics express* 17.7, pp. 5414–5419.
- Papp, Scott B, Katja Beha, et al. (2014). “Microresonator frequency comb optical clock”. In: *Optica* 1.1, pp. 10–14.
- Papp, Scott B, Pascal Del’Haye, and Scott A Diddams (2013). “Parametric seeding of a microresonator optical frequency comb”. In: *Opt. Express* 21.15, pp. 17615–17624.
- Papp, Scott B and Scott A Diddams (2011). “Spectral and temporal characterization of a fused-quartz-microresonator optical frequency comb”. In: *Phys. Rev. A* 84.5, p. 053833.
- Pepe, Francesco, David Ehrenreich, and Michael R Meyer (2014). “Instrumentation for the detection and characterization of exoplanets”. In: *Nature* 513.7518, pp. 358–366.
- Perryman, Michael (2011). *The exoplanet handbook*. Cambridge university press.

- Pfeifle, Joerg et al. (2014). "Coherent terabit communications with microresonator Kerr frequency combs". In: *Nature photonics* 8.5, pp. 375–380.
- Pillet, Grégoire et al. (2008). "Dual-frequency laser at $1.5 \mu\text{m}$ for optical distribution and generation of high-purity microwave signals". In: *Journal of Lightwave Technology* 26.15, pp. 2764–2773.
- Plavchan, Peter P, Guillem Anglada-Escude, et al. (2013). "Precision near-infrared radial velocity instrumentation I: absorption gas cells". In: *SPIE Optical Engineering+ Applications*. 88641J.
- Plavchan, Peter P, Michael Bottom, et al. (2013). "Precision near-infrared radial velocity instrumentation II: noncircular core fiber scrambler". In: *SPIE Optical Engineering+ Applications*. 88640G.
- Quinlan, F et al. (2010). "A 12.5 GHz-spaced optical frequency comb spanning > 400 nm for near-infrared astronomical spectrograph calibration". In: *Review of Scientific Instruments* 81.6, p. 063105.
- Ramelow, Sven et al. (2014). "Strong polarization mode coupling in microresonators". In: *Optics letters* 39.17, pp. 5134–5137.
- Razzari, L et al. (2010). "CMOS-compatible integrated optical hyper-parametric oscillator". In: *Nat. Photon.* 4.1, pp. 41–45.
- Renninger, William H and Frank W Wise (2013). "Optical solitons in graded-index multimode fibres". In: *Nat. Commun.* 4, p. 1719.
- Rohde, Ulrich L (1997). *Microwave and wireless synthesizers: theory and design*. John Wiley & Sons.
- Rokhsari, Hossein et al. (2005). "Radiation-pressure-driven micro-mechanical oscillator". In: *Optics Express* 13.14, pp. 5293–5301.
- Rolland, Antoine et al. (2011). "Non-linear optoelectronic phase-locked loop for stabilization of opto-millimeter waves: towards a narrow linewidth tunable THz source". In: *Optics express* 19.19, pp. 17944–17950.
- Saha, Kasturi et al. (2013). "Modelocking and femtosecond pulse generation in chip-based frequency combs". In: *Opt. Express* 21.5668, pp. 1335–1343.
- Sakamoto, Takahide, Tetsuya Kawanishi, and Masayuki Izutsu (2007). "Asymptotic formalism for ultraflat optical frequency comb generation using a Mach-Zehnder modulator". In: *Optics letters* 32.11, pp. 1515–1517.
- Santhanam, J and Govind P Agrawal (2003). "Raman-induced spectral shifts in optical fibers: general theory based on the moment method". In: *Optics Communications* 222.1, pp. 413–420.
- Savchenkov, Anatoliy A, Andrey B Matsko, Vladimir S Ilchenko, et al. (2008). "Tunable optical frequency comb with a crystalline whispering gallery mode resonator". In: *Phys. Rev. Lett.* 101.9, p. 093902.

- Savchenkov, Anatoliy A, Andrey B Matsko, Dmitry Strekalov, et al. (2004). “Low Threshold Optical Oscillations in a Whispering Gallery Mode C a F 2 Resonator”. In: *Phys. Rev. Lett.* 93.24, p. 243905.
- Schneider, Garrett J et al. (2013). “Radiofrequency signal-generation system with over seven octaves of continuous tuning”. In: *Nature Photonics* 7.2, pp. 118–122.
- Seeds, Alwyn J and Keith J Williams (2006). “Microwave photonics”. In: *Journal of Lightwave Technology* 24.12, pp. 4628–4641.
- Sinkin, Oleg V et al. (2003). “Optimization of the split-step Fourier method in modeling optical-fiber communications systems”. In: *Journal of lightwave technology* 21.1, p. 61.
- Soto-Crespo, Jose M and Nail Akhmediev (2002). “Composite solitons and two-pulse generation in passively mode-locked lasers modeled by the complex quintic Swift-Hohenberg equation”. In: *Physical Review E* 66.6, p. 066610.
- Spillane, SM, TJ Kippenberg, and KJ Vahala (2002). “Ultralow-threshold Raman laser using a spherical dielectric microcavity”. In: *Nature* 415.6872, pp. 621–623.
- Steinmetz, Tilo et al. (2008). “Laser frequency combs for astronomical observations”. In: *Science* 321.5894, pp. 1335–1337.
- Suh, Myoung-Gyun et al. (2016). “Microresonator soliton dual-comb spectroscopy”. In: *Science*, doi: 10.1126/science.aah6516.
- Suzuki, Shota et al. (2013). “12.5 GHz Near-IR Frequency Comb Generation Using Optical Pulse Synthesizer for Extra-Solar Planet Finder”. In: *Nonlinear Optics*. NM3A–3. Optical Society of America.
- Swann, William C et al. (2011). “Microwave generation with low residual phase noise from a femtosecond fiber laser with an intracavity electro-optic modulator”. In: *Optics express* 19.24, pp. 24387–24395.
- Taylor, J et al. (2011). “Characterization of power-to-phase conversion in high-speed PIN photodiodes”. In: *IEEE Photonics Journal* 3.1, pp. 140–151.
- Thorpe, Michael J et al. (2006). “Broadband cavity ringdown spectroscopy for sensitive and rapid molecular detection”. In: *Science* 311.5767, pp. 1595–1599.
- Tokunaga, Alan T et al. (1990). “Design for a 1–5-um cryogenic echelle spectrograph for the NASA IRTF”. In: *Astronomy’90, Tucson AZ, 11-16 Feb 90.* 131–143.
- Udem, Th, Ronald Holzwarth, and Theodor W Hänsch (2002). “Optical frequency metrology”. In: *Nature* 416.6877, pp. 233–237.
- Vahala, Kerry J (2003). “Optical microcavities”. In: *Nature* 424.6950, pp. 839–846.
- Vollmer, Frank and Stephen Arnold (2008). “Whispering-gallery-mode biosensing: label-free detection down to single molecules”. In: *Nature methods* 5.7, pp. 591–596.

- Vollmer, Frank and Lan Yang (2012). “Review Label-free detection with high-Q microcavities: a review of biosensing mechanisms for integrated devices”. In: *Nanophotonics* 1.3-4, pp. 267–291.
- Wabnitz, Stefan (1993). “Suppression of interactions in a phase-locked soliton optical memory”. In: *Opt. Lett.* 18.8, pp. 601–603.
- Wai, PKA et al. (1986). “Nonlinear pulse propagation in the neighborhood of the zero-dispersion wavelength of monomode optical fibers”. In: *Opt. Lett.* 11.7, pp. 464–466.
- Wang, Christine Y et al. (2013). “Mid-infrared optical frequency combs at $2.5\text{ }\mu\text{m}$ based on crystalline microresonators”. In: *Nature communications* 4, p. 1345.
- Wang, Pei-Hsun et al. (2016). “Intracavity characterization of micro-comb generation in the single-soliton regime”. In: *Opt. Express* 24.10, pp. 10890–10897.
- Wang, Shaofei et al. (2014). “Broadband Kerr frequency combs and intracavity soliton dynamics influenced by high-order cavity dispersion”. In: *Opt. Lett.* 39.10, pp. 2880–2883.
- Wiersig, Jan (2006). “Formation of long-lived, scarlike modes near avoided resonance crossings in optical microcavities”. In: *Phys. Rev. Lett.* 97.25, p. 253901.
- Wildi, François et al. (2010). “A Fabry-Perot calibrator of the HARPS radial velocity spectrograph: performance report”. In: *SPIE Astronomical Telescopes+ Instrumentation*. 77354X.
- Wilken, Tobias et al. (2012). “A spectrograph for exoplanet observations calibrated at the centimetre-per-second level”. In: *Nature* 485.7400, pp. 611–614.
- Xue, Xiaoxiao et al. (2015). “Mode-locked dark pulse Kerr combs in normal-dispersion microresonators”. In: *Nature Photonics* 9.9, pp. 594–600.
- Yang, Qi-Fan et al. (2016). “Spatial-mode-interaction-induced dispersive-waves and their active tuning in microresonators”. In: *Optica* 3, pp. 1132–1135.
- (2017). “Stokes solitons in optical microcavities”. In: *Nature Physics* 13, pp. 53–57.
- Yang, Ki Youl et al. (2016). “Broadband dispersion-engineered microresonator on a chip”. In: *Nat. Photon.* 10.5, pp. 316–320.
- Yang, Ki Y et al. (2016). “Ultra-High-Q Silica-on-Silicon Ridge-Ring-Resonator with an Integrated Silicon Nitride Waveguide”. In: *CLEO: QELS_Fundamental Science*. Optical Society of America, JTh4B–7.
- Yao, Jianping (2009). “Microwave photonics”. In: *Journal of Lightwave Technology* 27.3, pp. 314–335.
- Yariv, Amnon (1976). “Introduction to optical electronics”. In:

- Ycas, Gabriel G et al. (2012). “Demonstration of on-sky calibration of astronomical spectra using a 25 GHz near-IR laser frequency comb”. In: *Optics Express* 20.6, pp. 6631–6643.
- Ycas, Gabriel, Steve Osterman, and Scott Diddams. “Generation of a 650 nm–2000 nm laser frequency comb based on an erbium fiber laser”. In: *2012 Conference on Lasers and Electro-Optics (CLEO)*.
- Yi, Xu, Qi-Fan Yang, Ki Youl Yang, Myoung-Gyun Suh, et al. (2015). “Soliton frequency comb at microwave rates in a high-Q silica microresonator”. In: *Optica* 2.12, pp. 1078–1085.
- Yi, Xu, Qi-Fan Yang, Ki Youl Yang, and Kerry Vahala (2016a). “Active capture and stabilization of temporal solitons in microresonators”. In: *Opt. Lett.* 41.9, pp. 2037–2040.
- (2016b). “Theory and measurement of the soliton self-frequency shift and efficiency in optical microcavities”. In: *Opt. Lett.* 41.15, pp. 3419–3422.
- Yi, Xu, Qi-Fan Yang, Xueyue Zhang, et al. (2016). “Single-mode dispersive waves and soliton microcomb dynamics”. In: *Nature Communications* 14869.
- Yi, X et al. (2016). “Demonstration of a near-IR line-referenced electro-optical laser frequency comb for precision radial velocity measurements in astronomy”. In: *Nature communications* 7.10436.
- Young, BC et al. (1999). “Visible lasers with subhertz linewidths”. In: *Physical Review Letters* 82.19, p. 3799.
- Yu, Mengjie et al. (2016). “Breather soliton dynamics in microresonators”. In: *arXiv preprint arXiv:1609.01760*.
- Zhang, Lin et al. (2014). “Self-frequency shift of cavity soliton in Kerr frequency comb”. In: *arXiv preprint arXiv:1404.1137*.

INDEX

F

figures, 19–25, 27–29, 31–33, 35, 38, 44, 45, 48–52, 59, 60, 64, 67–69, 76, 79–84, 92, 93, 96–100, 102, 103, 105, 106, 108, 109, 114–118, 123–126